University of **Strathclyde**

Strathclyde institute of Pharmacy and Biomedical Sciences (SIPBS)

DYSREGULATION OF CONNEXIN-43 (Cx43) IN DOXORUBICIN-INDUCED CARDIOTOXICITY
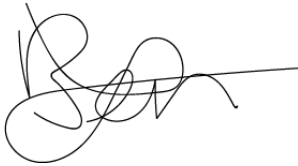
B.E.P. Veerman

A thesis submitted in fulfilment of the requirements for the degree of Doctor of Philosophy

2023

I. COVID IMPACT STATEMENT

This Covid-19 impact statement highlights the specific challenges and mitigations relating to Covid-19 restrictions.

The investigation of this project involved the research of the anthracycline drug doxorubicin and its related cardiotoxic effect. The effects of doxorubicin are associated with the gap-junctional protein connexin-43 within the heart. The effects were evaluated within different cardiac cell types and revealed a decline of the total protein level. This novel data could contribute to the knowledge of the adverse cardiac effects of doxorubicin.. The collected data would have been applied to an animal model to compare whether similar effects would be observed in relation to the previous cellular research. The initial data were promising as the connexin-43 protein levels were elevated and re-localised. These changes could be linked to changes in metabolic activity within different cardiac cell types and tissue. In order to measure metabolic changes in response to doxorubicin, the original research plan aimed to evaluate changes using time-of-flight secondary ion mass spectrophotometry, better known as ToF-SIMS. Prior to the pandemic, optimisations were carried out and in alignment with our collected data, this technique would have been a critical feature to further analyse the adverse cardiotoxic effects in cardiac and vascular cells. The ToF-SIMS is facilitated within the Technology Innovation Centre (TIC) which was closed during Covid-19 lockdown and no access was provided to use the instrument.

Moreover, ToF-SIMS training which would have been given by the IONTOF manufacturer in Münster (Germany) was also cancelled and all travel plans and registration for training was refunded. This essential training was postponed and provided in an online format 18 months after the initial course was scheduled in 2020
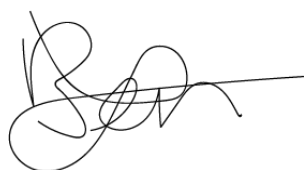
at the start of the pandemic. The information and knowledge from the training was too late in timescale of the PhD. The plan was to carry out ToF-SIMS on doxorubicin-treated cardiac cell types, 3D cardiac spheroids, and as well as Langendorff perfused rat heart samples.

All animal-related work was impacted as a result of Covid-19. No access was initially granted to the Biological Procedures Unit (BPU) within the University of Strathclyde and therefore no training could be provided. Upon reopening of the facility, social distancing and restrictions led to further delay in training and access thereby impacted the amount of work that could be conducted involving Langendorff perfusion of rat hearts.

The discussed impacts regarding ToF-SIMS and animal-related work were a result of Covid-19 which limited the amount of collected data, reduced datasets, and shortened result chapters. During Covid-19 other skills were developed in terms of learning programming languages and Adobe Illustrator & Premier Pro for the generation of illustrations and videos. In addition, public datasets were analysed in order to create an overview of connexin-43 expression throughout the human body and comparison studies of cell viability on cancer cell types in response to doxorubicin. This data has been included in the thesis in sections.
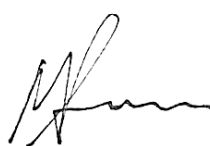

Signature student: B.E.P. Veerman   Signature supervisor: M.R. Cunningham

Date: 26-04-2023   Date: 28-04-2023

II. ACKNOWLEDGEMENTS

I have had a wonderful time in the lab with you all: Nick, Marco, Zainab, Chiara, and Lidia. Thank you for providing me with an unforgettable experience! Conducting research in the lab with disco lights and good tunes was very enjoyable! The one-pint Fridays, or often turning into many pints as was usually the case, provided me with the chance to unwind from work and switch into social mode! It was wonderful to share drinks with Graeme, Calum, Nick, Marco, Chiara, Lidia, Matthew, Mirna, Ashley, Rachel, Sandy, and of course Neil.

I have experienced an incredible three-month period in Coimbra at the Faculty of Medicine, University of Coimbra (FMUC), with the GUIC lab (Group of Ubiquitin-dependent Proteolysis and Intercellular Communication). Henrique, Tania, Maria, and Theresa, thank you so much! Getting to know everyone has been a pleasure. I feel truly honoured to have been a part of your lab, even for this short period, and it's all thanks to your exceptional hospitality that made me feel at home from day one.

My dear friends back home in the Netherlands were incredibly important to me. They offered much-needed distractions when I required them, inviting me for drinks, board games, and various other social activities. To the 'kitties,' Niels, and all the others, I am truly grateful. I want to extend a special thank you to one friend in particular: Frank. Your consistent support and assistance have been incredibly valuable to me, and I deeply appreciate your help in completing the most beautiful game in the world, Crash Bandicoot!

Those who truly play a vital role in my life are my family. I want to express my sincere gratitude to my parents, Pa and Ma, as well as my sisters Marijke and Kelly. Thank you so much. And last but certainly not least, Hilleen, I want to express my

heartfelt gratitude to you for affording me the opportunity to live abroad for several years and for the support you have always provided me.

III. PUBLICATIONS

Original Articles:

Brown, R. D. R., **Veerman, B. E. P.,** Oh, J., Tate, R. J., Torta, F., Cunningham, M. R., Adams, D. R., Pyne, S., & Pyne, N. J. (2021). A new model for regulation of sphingosine kinase 1 translocation to the plasma membrane in breast cancer cells. Journal of Biological Chemistry, [100674]. https://doi.org/10.1016/j.jbc.2021.100674.

Conference abstracts:

Veerman, B., McGivern, S-J., Dempsie, Y., Martin, P. E. M., Johnston, B., Currie, S., & Cunningham, M. R. (2020). Dysregulation of endothelial cell connexin-43 localisation in response to doxorubicin. Heart, 106(1), [11]. https://doi.org/10.1136/heartjnl-2020-SCF.11.

Written blogs:

Meet the Researcher Showcase Event: Inspiring with Biomedical Sciences (2019).https://www.strath.ac.uk/science/ourscienceblog/inspiringwithbiomedicalscience/.

Cell Block Science (2019): SIPBS brings science to HM Prison Low Moss. The blog I wrote in this regard, could not be published because of the protection of the vulnerable learners.

Abstract of the 23rd annual meeting of the Scottish Cardiovascular Forum in collaboration with McMullen, C. J. https://www.bps.ac.uk/publishing/pharmacology-matters/april-2020/the-23rd-annual-meeting-of-the-scottish-cardiovasc/.

IV.   COMMUNICATIONS

Meeting Communication:

McMullen, C. J., **Veerman, B.E.P.,** Safar, M., Currie, S. & Cunningham, M. R. (2020). Pharmacology Matters Article - 'The 23rd annual meeting of the Scottish Cardiovascular Forum".

Oral communications:

Scottish Cardiovascular Forum (SCF) Annual Meeting Roger Wadsworth Prize Oral Communication Candidate (2021). **Veerman, B.E.P.,** McMullen, C., Rattray, Z., Johnston, B., Dempsie Y., Martin, P., Currie, S., and Cunningham, M. R. Novel off-target effects of doxorubicin on cardiovascular gap-junctional proteins.

Nachwuchsgruppe Life Science Hamburg seminar (2021). Presentation for master students studying biomedical sciences concerning our PhD projects and doing a PhD in collaboration with McMullen, C.

Novel off-target effects of anti-cancer drug on cardiovascular gap-junctional proteins (2021). Strathclyde Institute for Pharmacy and Biomedical Sciences (SIPBS).

Poster communications:

The International Gap Junction Conference (IGJC) A Coruña, Spain (2022). **Veerman, B.E.P.,** Martins-Marques, T., Macquaide, N., Girao, H., Currie, S., and Cunningham, M.R., Identifying the role of connexin-43 in doxorubicin mediated cardiotoxicity by using in vitro, ex-vivo, and human cardiac spheroid models.

The 3rd ERNEST Conference (Online, 2020) Poster presentation - ECR Prize winner. **Veerman, B.E.P.,** *McMullen, C., Rattray, Z., Johnston, B., Currie, S., Cunningham, M. R. P2.5.6 - Novel off-target effects of anti-cancer drugs on cardiovascular gap-junctional proteins.*

British Pharmacological Society (BPS) Annual Meeting (2020). **Veerman, B.E.P.,** *Dempsie, Y., Martin, P., Rattray, Z., Johnston, B., Currie, S., and Cunningham, M. R., P011 - Endothelial connexin-43 dysregulation in response to the anthracycline doxorubicin.*

V. COURSES

IONTOF Users School (2021).

Data analysis with surface lab 7 and beyond, sample preparation – navigation – automation, using multivariate statistical analysis (MVSA features) in surface lab, imaging I and II.

Practical Python for beginners: a Biochemist's guide (2021).

Masterclass: How to write a thesis by Professor M.C. Watson (2020).

Covering thesis structure, format and content chapter-specific content, presentation of results, and how to help the examiners.

MATLAB Deep Learning Onramp (2019).

Using Pretrained Networks, Managing Collections of Data, and Performing Transfer Learning.

MATLAB Onramp (2019).

Commands, Vectors and Matrices, Importing Data, indexing into and Modifying Arrays, Array Calculations, Calling Functions, Obtaining Help, Plotting Data, Review Problems, MATLAB Scripts, Logical Arrays, and Programming.

R for Biochemists 101 (2019).

Learning the basics of programming in R software.

Laser Safety Training (2019).

Gaining knowledge of laser safety and University policy and procedures.

Biological Safety Training (2019).

Gaining knowledge of biological safety and University policy and procedures.

VI. FUNDING SECURED

VII.   ABSTRACT

The chemotherapeutic drug doxorubicin (DOX) is widely used in the treatment of cancer; however patients experience dose-dependent cardiotoxicity that can manifest acute, early- and late-onset chronic and is associated with a decreased contractility and dilated cardiomyopathy. Similar effects have been reported during cardiac malfunction, which have been linked with a disorganisation and dysfunction of gap junctions called connexins in the heart. Here, we examine the effects of the anthracycline DOX on the expression and localisation of connexin-43 (Cx43) in rodent and human cardiac cells and cells of the vasculature to identify if drug treatment impacts this important cardiac connexin.

Through investigating the cardiotoxic effects of DOX, this project has shown that total Cx43 protein levels were reduced in human coronary artery endothelial cells (HCAECs), AC16 cardiomyocytes, human umbilical vein endothelial cells (HUVECs), and human cardiac fibroblasts (hCFs) in response to DOX. Interestingly, Langendorff perfusion of rat hearts with clinically relevant concentrations of DOX resulted in increased Cx43 expression in the left ventricle, with lateralisation of Cx43 in ventricular cardiomyocytes. Further investigation of these effects was explored using human 3D cardiac spheroids comprising HUVECs, hCFs, and iCell cardiomyocytes. Unlike the monolayer studies, Cx43 expression levels were not reduced when the cells were co-expressed in the 3D cell model. However, these spheroids were capable of spontaneous contraction and pilot studies using contractile 3D human iCell cardiomyocytes highlighted a change in contractility and calcium handling in spheroids in response to DOX.

Interestingly, parallel studies in cancer cells did not reveal significant changes in Cx43 expression in response to DOX, which may indicate that these effects are cardiac and vascular-cell specific. More recently, there has been a growing number of publications focusing on exosomal Cx43 as a biomarker for DOX-induced cardiotoxicity in cancer patients. The potential for indirect DOX effects on the heart mediated through the release of extracellular vesicles (EVs) from cancer cells is in its infancy as most studies have focussed upon direct drug effects on cardiac function. Nanoparticle tracking analysis of DOX-treated MDA-MB-231 cells did indeed result in significantly increased EVs released with no change in particle size (120-250nm). Challenges were experienced when investigating the exosomal Cx43 during DOX treatment therefore independent funding was secured during the PhD period to go on secondment to the Faculty of Medicine at University of Coimbra (FMUC) to work with Professor Henrique Girão, an expert in exosomal Cx43 biology during cardiotoxicity. During this period, molecular and cellular tools were optimised to permit the future study of Cx43 using their established Cx43 knock out and Cx43-GFP cell models. Establishing these models in Strathclyde Institute of Pharmacy & Biomedical Sciences (SIPBS), will now pave the way for more meaningful interrogation of the functional role of Cx43 doxorubicin-induced cardiotoxicity that was unfortunately beyond the timescale of the current investigation.

Collectively, the data generated in this thesis suggest that alterations in Cx43 protein expression and subcellular re-localisation, along with alterations in cardiomyocyte calcium handling may contribute to the detrimental effects of DOX on the heart. This research has ignited new venues for follow-up investigation of Cx43 at the molecular level to understand more fully the implications of the direct and indirect

effects of DOX upon Cx43 expression, localisation and activity in the cancer and cardiac niche.

VIII.   GRAPHICAL ABSTRACT

Thesis background

Cancer survivors

DOX-induced cardiotoxicity
Cardiovascular complications

Acute	< 2 weeks treatment	Decrease contractility
Early-onset chronic	< 1 year after completion	Dilated cardiomyopathy
Late-onset chronic	> 1 year after completion	Dilated cardiomyopathy

Cx43 remodelling

| Arrythmias | Hypertrophic cardiomyopathy |
| | Ischaemic Cardiomyopathy |

Is Cx43 affected to DOX exposure?

Novel thesis findings

Direct effect of DOX

Toxicity

| | hCF | HCAEC | AC16 | HUVEC | MDA | Cardiac spheroid | Rat heart |
| Cx43 | ↓ | ↓ | ↓ | ↓ | = | = | ↑P1/P2 Lateralisation |

Indirect effect of DOX

Cancer cells

EVs ↑ Cx43?

EV/exosome release

??

Coronary artery

Cardiotoxic effect?
Work in progress

Future directions

iCell cardiomyocytes

Cx43 phosphorylation & lateralisation?

TOF-SIMS

Measure metabolic changes
* Cardiac cells
* Spheroids
* Cardiac tissue

IX.   TABLE OF CONTENTS

X. LIST OF FIGURES

CHAPTER FOUR:

CHAPTER FIVE:

CHAPTER SIX:

XI. LIST OF TABLES

XII.   LIST OF EQUATIONS

CHAPTER ONE:

Not applicable

CHAPTER TWO:

CHAPTER THREE:

Not applicable

CHAPTER FOUR:

Not applicable

CHAPTER FIVE:

Not applicable

CHAPTER SIX:

Not applicable

XIII.   LIST OF MOVIES

Figure 43 - Optimisation of culturing iCell cardiomyocytes

https://youtu.be/Y02MLvBFqF4

Figure 43 - Optimisation of culturing iCell cardiomyocytes

https://youtu.be/wmu2V1IxXYc

Figure 44 - Calcium imaging on iCell cardiomyocytes in response to DOX

https://youtu.be/2vUUP0f7xCw

Figure 45 - Comparison of brightfield versus Cal520

https://youtu.be/MO06PGTQ12k

Figure 46 - Effect of DOX on iCell spheroid contractility

https://youtu.be/TeOBQpbBHpM

Figure 51 - DOX-mediated EV-release in MDA-MB-231 cells

https://youtu.be/B8g6h_EPkjI

XIV.   ABBREVIATIONS

AA	Amino acid
ACE	Angiotensin-converting enzyme
ADP	Adenosine diphosphate
AIDS	Acquired Immune Deficiency Syndrome
AKDR	AK detection reagent
ANOVA	Analysis of variance
APS	Ammonium persulfate
ATM	Ataxia telangiectasia-mutated
ATR	Ataxia telangiectasia and rad3-related
ATP	Adenosine triphosphate
ATPIF-1	Mitochondrial ATPase inhibitory factor 1
BCA	Bicinchoninic acid
Bi3$^+$	Bismuth (3+)
BNF	British National Formulary
BSA	Bovine serum albumin
CaMKII	Calmodulin-dependent protein kinase II
CDK	Cyclin-dependent kinase
CHK	Checkpoint kinases
CI	Confidence interval
CIMP	Chemotherapy-induced cardiomyopathy
CM	Cardiac myocyte
CO$_2$	Carbon dioxide
CRISPR	Clustered regularly interspaced short palindromic repeats
cTn	Cardiac troponin

Cx	Connexin
DALYs	Disability-adjusted life years
DAPI	4',6-diamidino-2-phenylindole
DDR	DNA damage response
DEX	Dexrazoxane
DLG	Discs large
DMEM	Dulbecco's modified eagle's medium
DMSO	Dimethyl sulfoxide
DOX	Doxorubicin
DSB	Double-strand break
DTT	Dithiothreitol
e.g.	Exempli gratia (for example)
EC	Endothelial cell
EC50	Half maximal effective concentration
ECL	Enhanced chemiluminescence
EDTA	Ethylenediamine tetra-acetic acid
EHA	European Haematology Association
EL	Extracellular loop
Em	Emission
EMA	European Medicines Agency
eNOS	Endothelial nitric oxide synthase
ESC	European Society of Cardiology
ESTRO	Therapeutic Radiology and Oncology
EU	European Union
Ex	Excitation
FB	Fibroblast

FBS	Fetal bovine serum
FCS	Fetal calf serum
FSP	Fibroblast specific protein
FWHM	Full width half maximum
GAPDH	Glyceraldehyde 3-phosphate dehydrogenase
GEJ	Gastroesophageal
GFP	Green fluorescent protein
HBSS	Hank's balanced salt solution
HCAEC	Human coronary artery endothelial cell
HEPES	N-2-hydroxyethylpiperazine-N-ethanesulfonic acid
HER-2	Human epidermal receptor 2
hERG	Human ether-à-go-go-related gene
HPMA	N-(2-Hydroxypropyl) methacrylamide
hiPSCs	human-induced pluripotent stem cells
HRP	Horseradish peroxidase
IC50	Half-maximal inhibitory concentration
IC-OS	International Cardio-Oncology Society
IF	Immunofluorescence
JM	Juxtamembrane
kDa	Kilo Dalton
KeV	Kiloelectron volts
KO	Knockout
LA	Left atrium
LAS X	Leica application suite X
LV	Left ventricular
MARTA	Myocyte automatic retrieval and tissue analyser

M/z	Mass per charge
mCx43	Mitochondrial connexin 43
MCGM	MesoEndo cell growth medium
MDA-MB	M.D. Anderson Metastasis Breast cancer
MDC	Mediator of DNA damage checkpoint protein
MDT	Multi-disciplinary team
mHz	Milli hertz
mPTP	Mitochondrial permeability transition pores
MTT	3-(4,5-dimethylthiazol-2-Yl)-2,5-diphenyltetrazolium bromide
MRN	MRE11–RAD50–NBS1
N	Number of replicates
NICE	National Institute for Health and Care Excellence
NLM	National library of medicine
Nm	Nanometre
NO	Nitric oxide
Ns	Not significant
nTPM	Normalised transcript per million
OCT	Optimal cutting temperature compound
OLV	Oligolamellar liposomes
pA	Power amplifier
PAGE	Polyacrylamide gel electrophoresis
PARP	Poly (ADP-ribose) polymerase
PBS	Phosphate buffered saline
PDGF	Platelet-derived growth factor
PDZ	PSD-95 DLG-A ZO-1
PH	Power of hydrogen

PhD	Doctor of Philosophy
PI	Propidium iodide
PIHCA	Polyisohexylcyanoacrylate
PK1	Prague-Keele 1
PKA	Protein kinase A
PKC	Protein kinase C
PKG	Protein kinase G
PMs	Polymeric micelles
PSD	Post-synaptic density protein
PSF	Point spread function
RA	Right atrium
RFU	Relative fluorescent unit
RNS	Reactive nitrogen species
ROS	Reactive oxygen species
RV	Right ventricular
TBS	Tris-buffered saline
Scr	Proto-oncogene tyrosine-protein kinase
SDS	Sodium dodecyl sulphate
SSB	Single-strand break
SV40	Simian virus 40
TAT	Tyrosine aminotransferase
TEMED	Tetramethylethylenediamine
TKI	Tyrosine kinase inhibitors
TNTs	Tunnelling nanotubes
ToF-SIMS	Time of flight secondary ion mass spectrophotometry
Top	Topoisomerase

TP53	Tumour antigen p53
USA	United States of America
VEGF	Vascular endothelial growth factor
vWF	Von Willebrand Factor
WPB	Weibel-Palade bodies
WT	Wild type
ZO	Zona occludens

CHAPTER ONE:

INTRODUCTION

1.1 *Drug associated cardiotoxicity*

1.1.1 *Overview of prevalence and contributing factors*

Early detection and understanding of the mechanisms underlying chemotherapeutic cardiotoxicity are key to identifying life-prolonging cardioprotective options for cancer patient survivors. Insights from the 2018 Global Burden of Disease study have revealed cardiovascular diseases (CVDs) and cancer as the two major causes of death worldwide, with over 18 million and 10 million deaths respectively each year (Ritchie and Spooner et al., 2018). An overview of the global causes of death in 2019 is shown in Figure 1A. As well as the high number of deaths, cardiovascular disease and cancer also comprise the leading global disease burden (Roser and Ritchie et al., 2021). The global disease burden is a standardized metric expressed in Disability-Adjusted Life Years (DALYs), which represents one lost year of healthy life.

A)

Cause	Deaths
Cardiovascular diseases	18.56 million
Cancers	10.08 million
Respiratory diseases	3.97 million
Digestive diseases	2.56 million
Lower respiratory infections	2.49 million
Neonatal disorders	1.88 million
Dementia	1.62 million
Diabetes	1.55 million
Diarrheal diseases	1.53 million
Liver diseases	1.47 million
Kidney diseases	1.43 million
Road injuries	1.2 million
Tuberculosis	1.18 million
HIV/AIDS	863,837
Suicide	759,028
Malaria	643,381
Homicide	415,180
Parkinson's disease	362,907
Nutritional deficiencies	251,577
Drowning	237,242
Meningitis	236,222
Protein-energy malnutrition	212,242
Maternal disorders	196,471
Alcohol use disorders	168,015
Drug use disorders	128,083
Fire	111,292
Hepatitis	79,176
Poisonings	77,162
Conflict	62,985
Heat (hot and cold exposure)	47,461
Natural disasters	6,076

Axis: 0   2 million   6 million   10 million   14 million   18 million

B)

Cause	Percentage
Cardiovascular diseases	15.52%
Cancers	9.93%
Neonatal disorders	7.33%
Respiratory infections and TB	6.04%
Other NCDs	6.02%
Musculoskeletal disorders	5.89%
Mental disorders	4.92%
Diabetes and kidney diseases	4.44%
Respiratory diseases	4.09%
Unintentional injuries	4.08%
Neurological disorders	3.84%
Enteric infections	3.82%
Digestive diseases	3.51%
Transport injuries	3.06%
Sense organ diseases	2.59%
Malaria & neglected tropical diseases	2.48%
HIV/AIDS and STIs	2.22%
Nutritional deficiencies	1.95%
Skin diseases	1.68%
Substance use disorders	1.38%
Self-harm	1.35%
Interpersonal violence	1.06%
Maternal disorders	0.5%
Conflict & terrorism	0.25%
Natural disasters	0.04%

Axis: 0%   2%   4%   6%   8%   10%   12%   14%

Figure 1 - Overview causes of death & total disease burden globally in 2019

A) Number of deaths by cause (in millions) in 2019. This figure is adapted from (Hannah Ritchie and Fiona Spooner et al., 2018). *B) Percentage (%) of global disease burden, measured in Disability-Adjusted Life Years (DALYs). Blue; non-communicable diseases, red; maternal, communicable, neonatal, and nutritional diseases, grey; injuries. This figure is adapted from (Roser and Ritchie et al., 2021).*

Breast malignancies are the most common type of cancer, with an estimated risk of risk of 15% in females within the UK (*Cancer Research UK*, 2018). Improvement in the early detection and treatment of breast cancer patients has resulted in better prognosis and life expectancy. Between 2016 and 2018, there was an estimated survival rate of nearly 90% for breast cancer patients at 5 years post-diagnosis within the UK (*Cancer Research UK*, 2018). While relative survival depends upon stage of diagnosis, an emerging cause of death among breast cancer survivors is CVD (Coughlin *et al.*, 2020). Generally, cancer patients have over a two-fold increased likelihood of developing CVD mortality (Stoltzfus *et al.*, 2020). Pre-existing cardiovascular risk factors may account for adverse cardiovascular outcomes, however cardiotoxicity in response to cancer treatment remains a significant factor in the long-term outcome of cancer survivors even in patients with no pre-existing cardiovascular risk (Mamas and Matetic, 2022).

In 2022, a paper was published that conducted a systematic analysis of drug-associated myocarditis that was reported on the World Health Organisation (WHO) pharmacovigilance database (Nguyen *et al.*, 2022). Over a span of 21 million individual-case-safety reports were used from 2020 and identified 62 drugs that were associated with myocarditis. In recent decades, anti-cancer therapies have dramatically improved with increased survival rates of patients after diagnosis (Debela *et al.*, 2021; Miller *et al.*, 2022; Zhou and Li, 2022). In 2019, a study with large-scale electronic health records data from multiple linked UK databases used this to assess the risk of developing specific cardiovascular diseases across a wide range of cancers (Strongman *et al.*, 2019). These datasets revealed elevated risk of venous thromboembolism for at least 5 years after diagnosis in cancer survivors, mostly pronounced in patients receiving chemotherapy. Furthermore, chemotherapy is a key

driver of heart failure or cardiomyopathy risk after breast cancer. Different anti-cancer drugs are associated with cardiovascular complications, including tyrosine kinase inhibitors (TKI) and anthracyclines. However, the biomolecular complexity of the underlying mechanisms in long term cardiovascular complications introduced by anti-cancer drugs remain to be fully understood and requires more research. This project focuses on the anthracycline family member Doxorubicin (DOX), a drug that is frequently documented as a chemotherapeutic agent with a high incidence of cardiovascular-associated toxicities (Agrawal, 2019).

1.1.2 Different types of drugs are associated with cardiotoxicity

Many different types of drugs have been withdrawn from the market due to cardiovascular complications (Mamoshina and Rodrigues et al., 2021). This is a growing concern for safety pharmacology across the pharmaceutical industry. Drug-induced cardiotoxicity can arise through a disruption of mitochondrial function, contractility, electrophysiology, growth factor regulation, and microvascular injury (Wilkinson and Sidaway et al., 2016; Mamoshina and Rodriguez et al., 2021).

The human ether-à-go-go-related gene (hERG)-encoded channels are expressed within the cardiac tissue which include the delayed rectifier potassium channels (I_{Kr}) that play a critical role in cardiac repolarisation and proarrhythmic events (Sanguinetti *et al.*, 1995). The hERG channels were therefore a valuable therapeutic target in order to study adverse cardiac effects (Friedrichs and Patmore et al., 2005). hERG inhibitors have commonly off-target effects on other channels, but new studies significantly improved the prediction of their toxic effects (Mirams *et al.*, 2011; Passini *et al.*, 2017).

Drugs have also shown to have an impact on the cardiac contractility. The gap-junctions between the cardiomyocytes and calcium handling are important in intercellular communication and a synchronised cardiac contraction. Calmodulin-dependent protein kinase II (CaMKII) is a regulator of calcium cycling through phosphorylation on other cellular targets. Inhibiting CaMKII has been shown to serve potentially as a therapeutical target for antiarrhythmic therapy (Mustroph and Neef et al., 2017). Chemotherapeutic drugs, including TKIs are associated with an upregulation of CaMKII levels and activity (Mooney *et al.*, 2015). Moreover,

anthracyclines treatments have been characterised to elevate CaMKII levels (Tscheschner *et al.*, 2019).

The mitochondria are cellular organelles that play a vital role in the generation of energy and are therefore critical for cardiac contraction. Different types of drugs, including anthracyclines and TKIs, have been shown to impact mitochondrial function which could lead to cardiomyocyte and endothelial cell death with a consequence on cardiovascular function (Varga *et al.*, 2015). A loss of mitochondrial function could be as a result of increased levels of ROS (reactive oxygen species) or RNS (reactive nitrogen species) which could lead to a loss of mitochondrial membrane potential (Varga *et al.*, 2015). Moreover, local anaesthetics could interact with phospholipids and cholesterol within the mitochondrial membrane which potentially could disrupt the electron transport chain as well as increasing membrane permeability (Tsuchiya and Mizogami, 2013).

Vascular endothelial growth factor (VEGF) regulates vascularisation, angiogenesis, and promotes cardiomyocyte survival (Braile *et al.*, 2020). Therefore is VEGF signalling a valuable therapeutical target, however the designed drugs are associated with cardiotoxicity (Chen and Ai, 2016; Touyz and Herrmann, 2018). In addition, platelet-derived growth factor (PDGF) targeted by TKIs also cause cardiotoxicity (Chen and Ai, 2016). The human epidermal receptor 2 (HER-2) is crucial in cardiac development and function (Negro and Brar et al., 2004). The anti-apoptotic properties of HER-2 makes it an interesting target, but drugs like trastuzumab have cardiotoxic side effects (Pondé and Lambertini et al., 2016).

Most studies focus on the cardiotoxic effects of drug on the cardiomyocytes. However, studies have previously been shown that anti-cancer agents trastuzumab and anthracyclines have an impact on the microvascular endothelial barrier formation which results in increased drug permeability (Wilkinson and Sidaway et al., 2016).

An overview of different drug associated cardiotoxicities is shown in Figure 2 and examples of drugs with corresponding potential cardiotoxicity are displayed in Table 1.
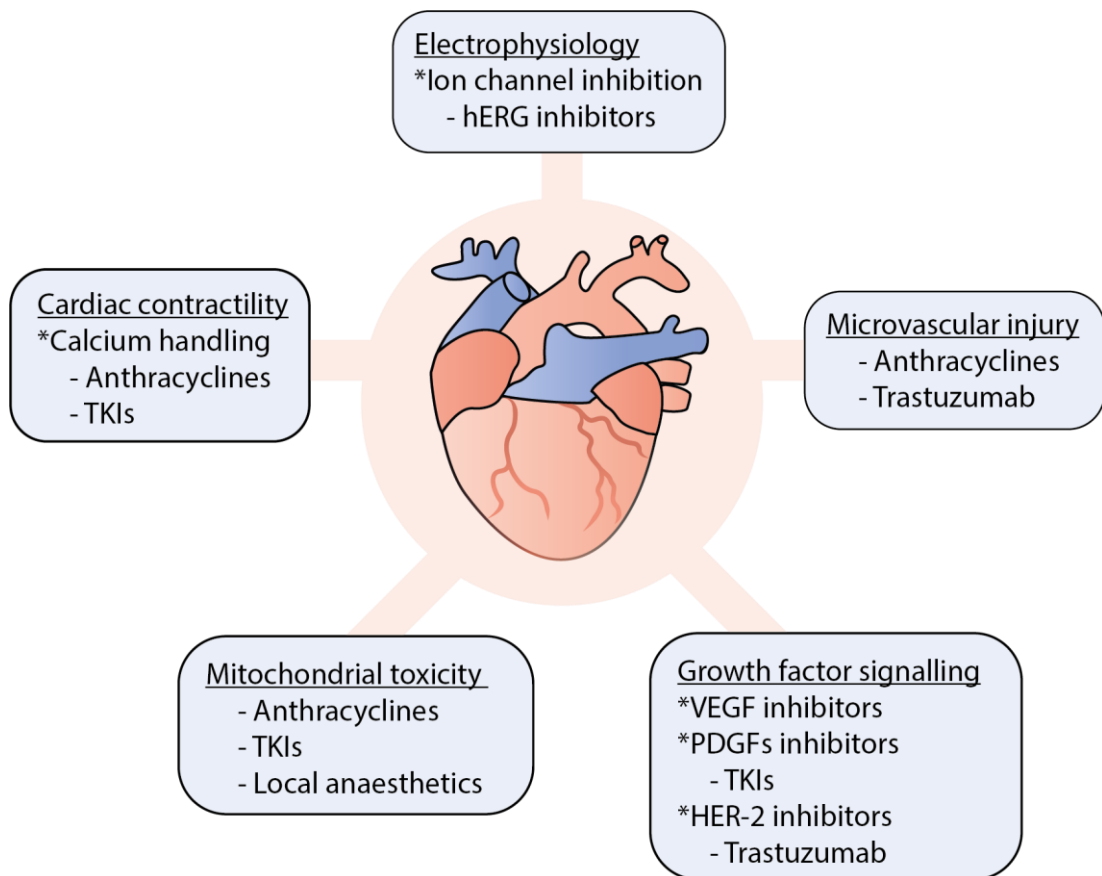
Figure 2 - Examples of drug-induced cardiotoxicity

Drug-induced cardiotoxicity could be caused through disruption of mitochondrial function, contractility, electrophysiology, cytokine, and growth factor regulation. Abbreviations: HER-2; human epidermal receptor-2, PDGF; platelet-derived growth factor, TKI; tyrosine kinase inhibitor, VEGF; vascular endothelial growth factor. This figure is adapted from (Mamoshina et al., 2021).

Table 1 - Examples of antineoplastic agents causing cardiotoxicity

Drug	Type of drug	Cardiotoxic effect	Reference
Daunorubicin	Anthracycline	- Arrythmias - Heart failure	(Druhan., 2015; Bloom *et al.*, 2016)
Doxorubicin	Anthracycline	- Arrythmias - Heart failure - Left ejection fraction - Left ventricular dysfunction	(Armenian *et al.*, 2015; Bloom *et al.*, 2016; Koene *et al.*, 2016; Mitry and Edwards, 2016; Zamorano *et al.*, 2016; Feijen *et al.*, 2019)
Idarubicin	Anthracycline	- Arrythmias - Heart failure	(Bloom *et al.*, 2016)
Imatinib	Tyrosine kinase inhibitor	- Systolic heart failure - Heart failure - Left ventricular dysfunction	(Xu *et al.*, 2009; Chakravarthy *et al.*, 2022)
Sunitinib	Tyrosine kinase inhibitor	- Long QT - Left ejection fraction - Left ventricular dysfunction - Myocardial infarction	(Chu *et al.*, 2007; Telli *et al.*, 2008; Force and Kolaja, 2011)
Trastuzumab	Monoclonal antibody	- Heart failure - Tachycardia	(Zeglinski *et al.*, 2011; Pondé et al, 2016)

Anthracycline, tyrosine kinase inhibitors, and monoclonal antibody antineoplastic agents with corresponding potential cardiotoxicity. This table is adapted from (Mamoshina et al., 2021).

The most prevalent cardiotoxic effects induced by chemotherapies manifest as left ventricular (LV) systolic dysfunction or chemotherapy-induced cardiomyopathy (CIMP). These symptoms can vary, ranging from mild asymptomatic myocardial injury, characterized by elevated troponin levels, to a reduction in left ventricular ejection fraction (LVEF), indicating contractile dysfunction. The development of CIMP worsens the patient's overall prognosis through the detrimental effects on the heart. The option of switching to less cardiotoxic cancer treatments could unfortunately contribute to a decrease of survival of the cancer patient (Stone *et al.*, 2021). Early detection of cardiotoxicity is therefore key to improving cardioprotective therapies and to improve the recovery of the LV function (Cardinale and Sandri, 2010). The European Society for Medical Oncology 2020 and European Society of Cardiology (ESC) guidelines recommend LV function determination, even if the accumulated dose is <300 mg/m^2, and follow-up surveillance with echocardiography at 1 and 5 year for patients that received more than 300 mg/m^2 (Ponikowski *et al.*, 2016; Zamorano *et al.*, 2016; Curigliano *et al.*, 2020).

Various imaging methods can be employed to monitor the development of CIMP. Nuclear cardiac imaging, in the form of multigated acquisition scans have been used to assess CIMP with accuracy and reproducibility (Gottdiener *et al.*, 1981). Due to radiation exposure during the acquisition, and limited information involving only LVEF and volume, CIMP has been superseded by echocardiography. Echocardiography is a method which is widely available, safe to use, accurate, reproducible, and can now be improved by using intravenous image enhancers and 3D echocardiography (Zamorano *et al.*, 2016). Cardiac magnetic resonance imaging (MRI) is currently the best non-invasive method to determine LV volumes and LVEF. Strain imaging has been shown to detect early myocardial dysfunction before a

decrease in LVEF occurs due to anthracyclines and/or trastuzumab (Curigliano *et al.*, 2020). The parameter global longitudinal strain (GLS) is used in strain imaging and a change of >15% is showing clinical significance (Lang *et al.*, 2015). Cardiac imaging is the main method to determine LVEF for CIMP.

1.2 Anthracycline-induced cardiotoxicity

1.2.1 General overview of anthracyclines

Anthracyclines are a class of antibiotics which were discovered from a mutated strain of *Streptomyces peucetius* in the 1960s (Grein et al., 1963). The first discovered anthracycline, namely daunorubicin (trade name Daunomycin) was followed by DOX (trade name Adriamycin®). Both were proven to have tumour-growth-inhibiting properties (Bonadonna et al., 1969). Other members of the anthracycline family are epirubicin, idarubicin, mitoxantrone, and valrubicin. Anthracyclines are used in the treatment of both adult and paediatric cancers, including lung, breast, ovarian, gastric, thyroid, lymphoma, multiple myeloma, and sarcoma cancers (Thorn et al., 2011).

1.2.2 Anthracycline-induced cardiotoxicity

Back in the 1980s a classification of anthracycline-induced cardiotoxicity was developed by studies on paediatric and young adult cancer survivors that developed cardiovascular complications (Steinherz *et al.*, 1991; Giantris *et al.*, 1998; Grenier and Lipshultz, 1998) (Table 2). The classification included three different groups of anthracycline-induced cardiotoxicity including: acute, that could occur after a single dose or course with symptoms within 14 days which is usually reversible; early-onset chronic, development of dilated cardiomyopathy within 1 year after treatment; late-onset chronic, development of dilated cardiomyopathy after 1 year after treatment completion. Chronic cardiotoxicity is usually irreversible due to the dilated cardiomyopathy that could progress into heart failure (Cardinale and Iacopo et al., 2020). The anthracycline-induced cardiotoxicity classification was not based on adult cancer survivors and has therefore limited clinical relevance. Diagnosis of "late" cardiotoxicity may take years as the onset of symptoms develop at a later stage. Conversely, 'early' cardiotoxicity could become evident within months due to a

reduction in left ventricular ejection fraction (LVEF). The "acute" cardiotoxicity could be detected at an early stage as circulating biomarkers could indicate myocardial damage (Cardinale *et al.*, 2015, 2017; Cardinale and Cipolla, 2016).

Two of the most common cardiac biomarkers for indication of cardiac damage are the brain natriuretic peptide (BNP) and cardiac troponin (cTn) (Tan and Lyon, 2018). The timing of cTn detection is important, as it has been demonstrated to increase in plasma levels immediately after a high-dose of chemotherapy delivery (33-53%) (Cardinale et al., 2000, 2004). The BNP, NT-proBNP or MR-proBNP, and cTn levels should be measured in suspected acute heart failure cases (Felker *et al.*, 2015; Zamorano *et al.*, 2016).

Anti-cancer therapy related side effects have an impact on the survival of the patients, also in the long-term mortality and morbidity outcomes. It is important to manage cancer as well as CVD side effects of treatment. This combined approach has emerged into a new discipline, named cardio-oncology (Ponikowski et al., 2016; Lancellotti et al., 2019). Recently, the ESC published guidelines on cardio-oncology which were developed in collaboration with the European Haematology Association (EHA), the European Society for Therapeutic Radiology and Oncology (ESTRO), and the International Cardio-Oncology Society (IC-OS) (Lyon *et al.*, 2022). A baseline risk of cancer patients with cardiovascular complications before treatment is graded into elevated, moderate, high, and very high by the Heart Failure Organisation (HFO) and the IC-OS (Lyon *et al.*, 2020; Battisti *et al.*, 2021). It is important to examine patient-specific risk prior to treatment. Factors included as part of the risk assessment are: age; sex; physical examination; genetics; previous cardiovascular disease and cardiotoxic therapies; lifestyle risk factors; medical cardiovascular risk factor;

electrocardiogram (ECG), transthoracic echocardiography (TTE), and biomarker abnormalities (Lyon *et al.*, 2022).

Gene and genome studies have identified mutations which are linked to anthracycline-induced cardiac dysfunction (Blanco *et al.*, 2012; Aminkeng *et al.*, 2015; Garcia-Pavia *et al.*, 2019). The role of genetics in anthracycline-induced cardiomyopathy in cancer survivors has recently been reviewed (Bhatia, 2020). Moreover, the incidence of the side effects of DOX can be dependent upon several underlying conditions, including hypertension, diabetes mellitus, and obesity (Qiu *et al.*, 2021). Due to the adverse cardiac effects of anthracycline treatment, it is critical to evaluate the baseline cardiovascular toxicity risk level. Patients that are at substantial risk to develop cardiotoxicity include those with previous cardiovascular disease such as heart failure, cardiomyopathy, cancer therapy-related cardiac dysfunction, severe valvular heart disease, myocardial infarction, percutaneous coronary intervention, coronary artery bypass graft, and stable angina. Other factors include a reduced LVEF (<50%), age (>65 years), previous anthracycline and/or radiotherapy to the left chest (Lyon et al., 2022). For the surveillance of anthracycline treatment, it is important to have a baseline screening with ECG, TTE, and biomarker levels of cTn and natriuretic peptide (NPs) should be done prior to the anthracycline cycles (C1-C6). Patients that are at considerable risk should be assessed for cTn and NPs after every cycle and 3-12 months after treatment completion. In addition, TTE imaging should be conducted after every 2 cycles and 3-12 months after treatment completion (Lyon et al., 2022). An overview of the baseline cardiovascular risk factors of anthracyclines by the Heart Failure Association-International Cardio-Oncology Society is shown in Table 3. The recommendations of anthracycline treatment surveillance are displayed in Table 4.

Table 2 - Classification of anthracycline-induced cardiotoxicity

Classification	Acute	Early-onset chronic	Late-onset chronic
Onset	< 2 weeks treatment	< 1 year after completion	> 1 year after completion
Dose-dependent	Unknown	Yes	Yes
Cardiac effect	Decrease contractility	Dilated cardiomyopathy	Dilated cardiomyopathy
Reversibility	yes	no	no

This table is adapted from (Cardinale and Iacopo et al., 2020).

Table 3 - Baseline cardiovascular risk factors of anthracyclines

Baseline cardiovascular toxicity risk factors	Risk level
Previous cardiovascular disease	
Heart failure / cardiomyopathy / cancer therapy-related cardiac dysfunction	4
Severe valvular heart disease	3
Myocardial infarction / percutaneous coronary intervention / coronary artery bypass graft	3
Stable angina	3
Cardiac Imaging	
LVEF <50%	3
LVEF 50-54%	1
Cardiac biomarkers	
Elevated baseline cTn (> reference range)	1
Elevated baseline BNP and NT-proBNP (> reference range)	1
Age and cardiovascular risk factor	
Age ≥ 80 years	3
Age 65–79 years	2
Hypertension (Systolic BP > 140 mmHg / diastolic BP > 90 mmHg / on treatment)	1
Chronic kidney disease (eGFR > 60 mL/min/1.73m[Ref])	1
Diabetes Mellitus (HbA1c >7.0% / > 53 mmol/mol / on treatment)	1
Previous exposure	
Anthracycline	3
Radio therapy to left chest / mediastinum	3
Non-anthracycline chemotherapy	1
Lifestyle risk factors	
Current smoker or significant smoking history	1
Obesity (BMI > 30 kg/m[Ref])	1

Overview of baseline cardiovascular toxicity risk level. 1-elevated risk; 2-moderate risk; 3-high risk; 4-very high risk. Ref = (Herrmann et al., 2014). This table is adapted from (Lyon et al., 2022).

Table 4 - Surveillance of anthracycline treatment

	Measurement	Baseline	C1	C2	C3	C4	C5	C6	3M-post	12M-post
Low risk	ECG	3								
	TTE	3				1				3
	Markers	2		1		1		1	1	
Moderate risk	ECG	3								
	TTE	3				2				3
	Markers	2		2		2		2	2	
High and very high risk	ECG	3								
	TTE	3		3		3		3	3	3
	Markers	3	3	3	3	3	3	3	3	3

The assessment of biomarker plasma levels and TTE imaging should be done prior to the anthracycline cycles (C1-C6). In moderate-risk patients, TTE should be considered with a dose of ≥ 250 mg/m^2 and in low-risk patients may be considered. The markers, including cTn and NPs, should be measured every 2 cycles and 3 months after completion in moderate-risk patients. 1-may be considered; 2-should be considered; 3-recommended or indicated. This table is adapted from (Lyon et al., 2022).

1.2.3 Patient treatments with Doxorubicin

Patients treated with DOX show dose-dependent cardiotoxicity that can manifest as arrhythmias, ischemia, cardiomyopathy, systolic dysfunction and heart failure (Mitry and Edwards, 2016). The first case describing DOX-induced cardiotoxicity in the literature was dated from 1971, from a 23-year-old female with osteosarcoma and therefore treated for 9 months with DOX with a total dose of 720 mg/m^2. The patient died one month after the end of the treatment due to the development of congestive heart failure (Lefrak et $al.$, 1973). The incidence of DOX induced cardiotoxicity is 3% at 400 mg/m^2, 7% at 500 mg/m^2, and 18% at 700 mg/m^2 (Koene et $al.$, 2016). The suggested monitoring threshold is a cumulative dose higher than 250 mg/m^2. The cumulative dose of 250 mg/m^2 or higher of DOX should be considered higher risk to developing cardiovascular complications (Armenian et $al.$, 2015; Feijen et $al.$, 2019). DOX is administered via an intravenous injection over 5 minutes. The dosage of the drug is dependent on the body surface area with a recommended starting dose of 60 mg/m^2 for adults. These doses result in DOX plasma levels that do not exceed 6.7 μM with an estimated half-life of 14 hours (Liston and Davis, 2017). The dosage and administration frequency depends upon various factors, such as the type of cancer and cancer history, hepatic and cardiovascular dysfunction, and drug combinations. A cumulative dose of 400 mg/m^2 DOX has a frequency of heart failure of 3-5%. With a high accumulative dose of 700 mg/m^2 complication frequencies can occur in 18 to 48% of cases (Zamorano et $al.$, 2016). In order to limit the adverse cardiac effects, recommends the British National Formulary (BNF), provided by the National Institute for Health and Care Excellence (NICE), to use a limited cumulated dose of 450 mg/m^2 with 21-day intervals (BNF, 2023). A report in 2022, revealed long-term cardiovascular complications in breast cancer patients with an incidence of 16.5% at 4.5 years (Caballero et $al.$, 2022).

It is often advised that patients with breast cancer do not receive DOX alone but in combination with other drugs and radiation, which can also contribute to side effects such as cardiotoxicity (Kim *et al.*, 2019; Correia, Gärtner and Vale, 2021).

1.3   *Cellular mechanisms of DOX-dependent cardiovascular toxicity*

1.3.1   *Topoisomerase inhibition and DNA intercalation*

The main considered molecular target of DOX is DNA topoisomerase (Top)-2, an enzyme that introduces double-strand breaks in the DNA template strand (Chen *et al.*, 1984; Tewey *et al.*, 1984). Anthracyclines, such as DOX, stabilise the intermediate where the DNA strand is cleaved and covalently linked to Top-2, termed the DNA-Top-2 cleavage complex (Top-2cc). The stabilisation of the Top-2cc complex could lead to apoptosis when DNA cuts become irreversible at regions of active DNA synthesis (Marinello, Delcuratolo et al., 2018).

Two different Top-2 isoforms are expressed throughout the human body, namely Top-2α and Top-2β. A study in mice tissues revealed that Top-2β is expressed across all tissues and Top-2α typically in high proliferating tissues such as bone marrow and spleen (Capranico *et al.*, 1992). Top-2α is frequently overexpressed in aggressive or rapidly proliferating tumours, whereas it is not detected in differentiated and quiescent cells (Sandri *et al.*, 1996; Turley *et al.*, 1997). Top-2β is highly expressed across normal tissues, but expression levels are elevated in tumours and proliferating cells (Turley *et al.*, 1997; Padget et al., 2000). As anthracyclines increase Top-2 mediated DNA damage, proliferating cells are more susceptible to DOX-induced toxicity in comparison to post-mitotic cells (Marinello, Delcuratolo et al., 2018)

1.3.2   *The cellular targets of DOX*

As well as targeting Top-2α, Top-2β (Top-2B) and the DNA, DOX also exerts detrimental effects on cardiac cells through the formation of reactive oxygen species (ROS), RNS, impaired calcium handling, lipid peroxidation, and apoptosis (Mobaraki and Faraji et al., 2017). Transcription of endothelial nitric oxide synthase (eNOS) is

upregulated through elevated ROS levels and is required for the synthesis of nitric oxide (NO) (Drummond *et al.*, 2000; Kalivendi *et al.*, 2001). NO combined with ROS could cause the formation of RNS, which are both toxic species that could potentially induce apoptosis by triggering the release of cytochrome C from the mitochondria, subsequently activating caspases to initiate the breakdown of cellular structures (Kotamraju *et al.*, 2000). An overview of the described targets of DOX is illustrated in Figure 3.
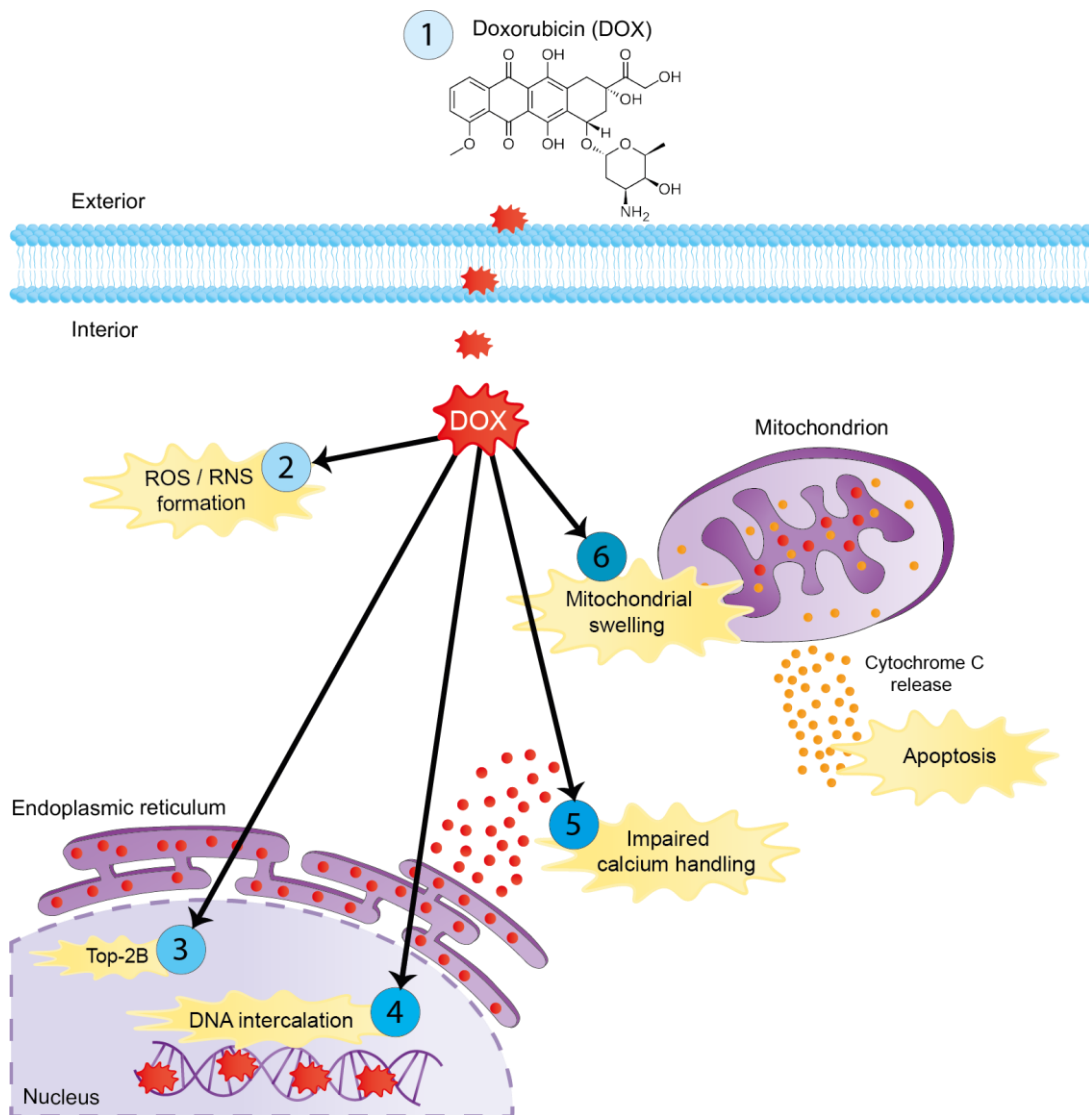
Figure 3 - Overview of the cellular targets of DOX

(1) DOX enters the cytosol of the cell through passive diffusion, causing the generation of ROS and RNS (2), inhibition of Top-2B (3), intercalates within the DNA (4), impairs calcium handling (5), and causes mitochondrial swelling which finally results in cellular apoptosis (6). This figure is adapted from (Mobaraki and Faraji et al., 2017).

1.3.3 The underlying mechanism of DOX in cancer cells

As previously described, DOX is the most effective drug used for cancer treatment. Nevertheless, the precise underlying mechanism of DOX's effect on cancer cells remains unknown. A recent comprehensive review summarized previous findings regarding the effects of DOX on cancer cells (Kciuk *et al.*, 2023).

One of the key targets of DOX is DNA, attained through intercalation between the major groove of guanine-cysteine and the minor groove of the adenine-tyrosine base pairs (Howerton, Nagpal and Williams, 2003). The exact mechanism remains unclear. Evidence indicates a role of positive supercoiling and nucleosome turnover around promotors inducing alterations in DNA topology (Yang, Kemp and Henikoff, 2013). The formation of DOX-DNA adducts could initiate the DNA damage response (DDR) pathway activation (Forrest *et al.*, 2012). The DDR response involves ataxia-telangiectasia-mutated (ATM) and ataxia telangiectasia and rad3-related (ATR) kinases (Awasthi, Foiani and Kumar, 2015). Furthermore, the ATM and ATR can also be activated through the downstream effects of topoisomerases.

The physiological roles of Top-1 and Top-2 are to introduce single-strand breaks (SSBs) or double-strand breaks (DSBs), respectively (Roca and Wang, 1994; Capranico, Marinello and Chillemi, 2017). The SSB are recognised by poly (ADP-ribose) polymerase 1 (PARP1) which plays a central role in the response to SSBs through binding and recruitment of DNA repair factors, including tumour antigen p53 (TP53) (Pleschke *et al.*, 2000). The DSBs are detected and regulated by the MRE11–RAD50–NBS1 (MRN) complex which leads to ATM recruitment (Lamarche, Orazio and Weitzman, 2010). The MRN complex promotes recruitment of mediator of DNA damage checkpoint protein (MDC)-1 and subsequently ATM kinase (Ruff *et al.*, 2020).

The ATR and ATM could both either phosphorylate checkpoint kinases (CHK-1 and CHK-2), which play a central role in the DDR downstream effects. CHK-1/2 phosphorylation limits its cellular function, leading to cell-cycle arrest and promotes apoptosis (Amani *et al.*, 2021; Kciuk *et al.*, 2022). The treatment of DOX has been shown to promote the ATR and ATM downstream signalling and thereby apoptosis of cancer cells (Kurz, Douglas and Lees-Miller, 2004; Ghelli Luserna Di Rorà *et al.*, 2021).

1.4 Cardioprotective strategies in response to DOX

1.4.1 Current cardioprotective strategies

Cardioprotective therapies during anthracycline treatments could potentially limit the risk of LVEF reduction. Examples of cardioprotective drugs include β-blockers and angiotensin-converting enzyme (ACE) inhibitors (Bosch *et al.*, 2013; Akpek *et al.*, 2015; Gulati *et al.*, 2017; Avila *et al.*, 2018; Cardinale *et al.*, 2018). A meta-analysis revealed a significant reduction in the drop of the LVEF in response to anthracyclines (Xu *et al.*, 2020). The β-blockers carvedilol and nebivolol had shown to serve a role in cardioprotection, but more scientific evidence to routinely apply these drugs for prevention of anthracycline induced cardiotoxicity is mandatory (Barbosa *et al.*, 2018). The exact underlying mechanism of how β-blockers are associated with a protective role in anthracycline-induced cardiotoxicity remains unknown. Moreover, the ACE inhibitor enalapril has previously been shown to reduce cardiotoxicity after anthracycline administration (Gupta *et al.*, 2018). Similar to β-blockers, the mechanism of the ACE inhibitors-mediated cardioprotection during anthracycline treatment is unclear.

The only FDA and European Medicines Agency (EMA) approved drug to prevent DOX induced cardiotoxicity is dexrazoxane (DEX) which is also known as ICRF-187 or Zinecard (Buss and Hasinoff, 1993). DEX is used by the National Health Service (NHS) in the UK (NHS England, 2020) as adjuvant in children and patients under 25 years receiving high-dose anthracyclines. The use of DEX requires a multi-disciplinary team (MDT) for each patient. The dose should be ten times the DOX-equivalent dose and is administered by a 15-minute infusion, 30 minutes prior to anthracycline administration. Most paediatric cancer treatments limit high accumulative doses of DOX, but in a few cases a high dose is required with a

concomitant increased risk of cardiotoxicity. Symptomatic cardiac events have been observed in around 1 out of 10 childhood cancer survivors receiving a high-dose DOX (Shaikh *et al.*, 2016). DEX has not been shown to have a negative impact on the long-term mortality or second cancer risk of patients (Chow *et al.*, 2022).

The exact mechanism of DEX remains unclear. However, DEX has strong iron chelating abilities and limits DOX-induced ROS generation and inhibits the interaction between non-heme iron and thereby reduces the formation of mitochondrial oxidative stress (Buss and Hasinoff, 1993; Kwok and Richardson, 2000). Conversely, DEX can interact to the Top-2 ATP binding sites, potentially impeding the binding of DOX (Classen et al., 2003). A more recent study strongly supports that DEX is a cardioprotective agent against anthracycline induced cardiotoxicity through interactions with Top-2B and not as a result of its iron chelating properties (Jirkovský *et al.*, 2021). The administrations of DEX as an adjuvant to DOX therapy identified a reduced risk of developing clinical heart failure without impacting the cancer outcomes (Dalen *et al.*, 2011; Macedo *et al.*, 2019).

1.4.2   Alternative strategies for DOX treatment

Other strategies to minimise "off target" effects include the use of more selective delivery methods, for example liposomes, micelles, dendrimers, and nanoparticles (Khan and Gurav, 2017). For example, liposomes with DOX loaded as cargo and with surface expression of aspartate and folate could potentially be used for dual-targeting, where aspartate prefers the resorption in bones and folate selectively targets tumour cells (Ke *et al.*, 2017). Developments have been made to use DOX as a precision medicine by using nanotechnology-based techniques, the

most relevant are discussed in this section (Duggan *et al.*, 2011; Barenholz Y., 2012; Regenold *et al.*, 2022).

The first nanotechnology-based DOX was liposomal DOX, created in the 1980s which comprise negatively charged oligolamellar liposomes (OLV) used to encapsulate DOX, these particles are known as OLV-DOX. The clinical trials of OLV-DOX were cancelled due to inferior therapeutic efficacy as the DOX was quickly released from the liposomes and they were rapidly removed by the liver (Gabizon *et al.*, 1989). In 1995, the same researchers released a PEGylated lipid nano system to prevent the rapid DOX release and particle degradation by the liver to extend its lifetime. This drug is known in the United States of America (USA) as Doxil® and Caelyx® in the European Union (EU) (Barenholz Y., 2012). Doxil has been used in the treatments of acquired immune deficiency syndrome (AIDS) related Kaposi's, recurrent ovarian cancer, metastatic breast cancer, and multiple myeloma (Duggan *et al.*, 2011). A non-PEGylated version of Doxil, named Myocet®, previously known as Cephalon®, was approved by the EMA in the year 2000 (Swenson *et al.*, 2001). Myocet® had shown in Phase III clinical studies to reduce the frequency of cardiac events. However, no increased survival rate was observed in metastatic breast cancer patients in comparison to conventional DOX (Harris *et al.*, 2002; O'Brien *et al.*, 2004)

Polymer-drug conjugates have been used to encapsulate DOX through its hydrophobic core to prevent a rapid drug release within circulation (Fang *et al.*, 2016). Prague-Keele 1 (PK1), also known as FCE28068 was developed by Pfizer and entered Phase II clinical trials (CRUKD/97/016) (Schütz *et al.*, 2013). PK1 uses the copolymer N-(2-Hydroxypropyl) methacrylamide (HPMA) which is covalently linked to DOX through a peptide linker. The linking peptide is cleaved by lysosomal enzymes

upon entering the malignant cells, initiating drug release at the tumour site. In a Phase I clinical study performed in different types of resistant cancers, a three times clearance was identified in comparison to free DOX and no congestive heart failure was detected (Vasey et al., 1999). In a Phase II clinical study where patients with either breast, colorectal and non-small-cell lung cancer (NSCLC) were treated, a partial response in breast and colorectal cancers was observed, but no effect in NSCLC cancers was identified (Seymour *et al.*, 2009). Next to PK1, is PK2 (FCE28069) also a HMPA based polymer-drug conjugate and is linked to galactosamine residues (Julyan *et al.*, 1999). Primary metastatic liver cancer was treated in a Phase I clinical trial where approximately 17% of the drug reached the liver, and in the free DOX trials no drug observed in the liver (Seymour *et al.*, 2002). However, the development of PK2 discontinued due to a lack of drug supply.

Thermosensitive liposomes have also been generated, which are lipid-based nanoparticles that release their content in a temperature sensitive manner. These particles can be loaded with DOX which is then named ThermoDox®. The lipid bilayer composition is critical in order to release the drug at the desired temperature as mild hyperthermic particles are activated between 39-45°C (Landon *et al.*, 2011) (Regenold *et al.*, 2022). Patients with primary and metastatic liver cancer were treated with ThermoDox alongside radiofrequency ablation (RFA) with success in 2007 (Celsion, 2005, NCT00441376). In 2009, a Phase III clinical trial was initiated (NCT00617981), however, no progression-free survival and ultimately encountered failure (Dou et al., 2017). Furthermore, in the year 2014, a subsequent Phase III clinical trial was initiated (NCT02112656). However, this trial also did not have a favourable outcome.

Another type of nanotechnology-based therapy involves the use of polymeric micelles (PMs). These have an inner hydrophobic core and an outer hydrophilic corona with encapsulated DOX. These PMs have the ability to release the drug in a temperature, and or pH-dependent manner (Torchilin, 2001, 2002; Z. Zhang *et al.*, 2014). There are two important PMs that reached clinical trials, namely NK911 and SP1049C. The Phase I clinical trial concerned the treatment of adenocarcinoma in the oesophagus and the gastroesophageal junction (GEJ) and showed a slower clearance in comparison to free DOX, but anti-tumour activity was observed in some patients with advanced resistant sold tumours (Danson *et al.*, 2004). However, in a Phase II clinical trial a high level of toxicity and disease progression was shown in the treatment of patients with advanced adenocarcinoma of the oesophagus and GEJ. The LVEF was decreased in the patients (Valle *et al.*, 2011).

Furthermore, a DOX-loaded nanoparticle created with polyisohexylcyano-acrylate (PIHCA), also known as Livatag®, was generated in 2011 and is currently in Phase III clinical trials. In the Phase II clinical trial patients suffering from liver cancer were treated with Livatag® which resulted in an increased survival in comparison to free DOX (Alphandéry *et al.*, 2015).

Unfortunately, as of 2023, Lipo-DOX® has been discontinued in the USA due to an elevated 11% risk of developing cardiomyopathy with a cumulative dose of 450-550 mg/m2. Additionally, 11% of patients treated for solid tumours experienced acute infusion-related reactions (Drugs.com, 2023). The historical events of DOX and nanotechnology-based alternatives for DOX treatments are shown in Figure 4.
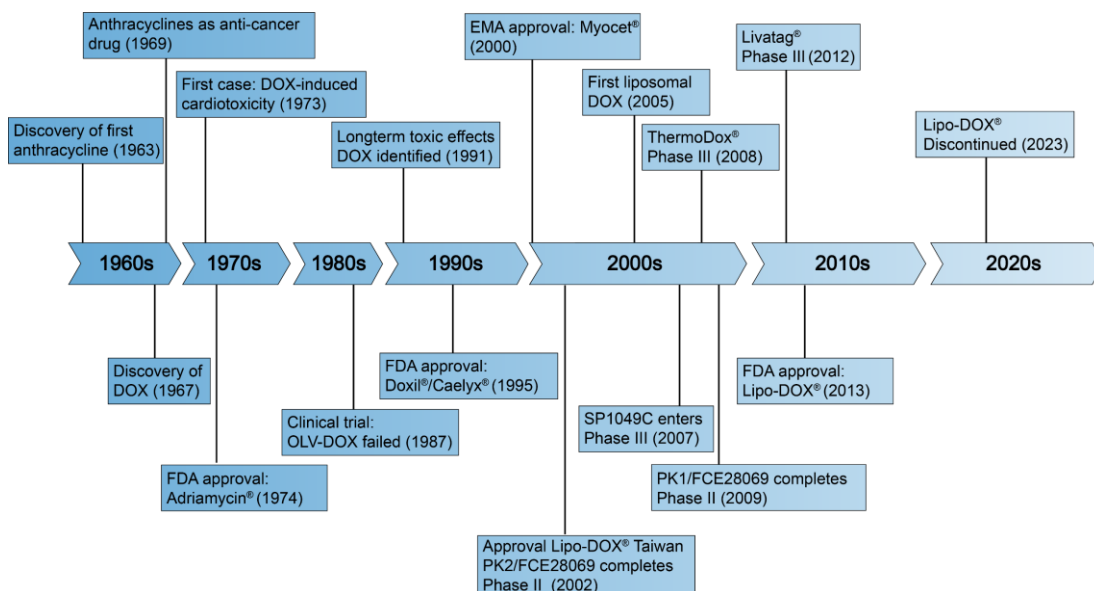
Figure 4 - History of DOX and evolution of related nanotechnological strategies

The first anthracycline was discovered in 1963 and applied as an anti-cancer agent in 1969. The first case of DOX-induced cardiotoxicity was observed in 1973, the FDA shortly thereafter approved DOX. The first clinical trial of a liposomal DOX, named OLV-DOX, failed in 1987. In 1995, PEGylated liposomal Doxil®/Caelyx® reached the market. Myocet® was approved by the EMA in 2000. Two years later, Lipo-DOX® was approved in Taiwan and PK2 (FCE28069) completed Phase II clinical trial. The first liposomal DOX dates from 2005, and the polymeric micelle SP1049C entered Phase III clinical trials in 2007. ThermoDox® entered Phase III clinical trials in 2008. PK1 (FCE28068) entered Phase II clinical trials in 2009, and the Livatag® nanoparticle Phase III in 2012. Lipo-DOX® was FDA approved in 2013. In 2023, Lipo-DOX® was discontinued in the USA. This figure is adapted from (Cagel et al., 2017).

The sheer number of failing clinical trials trying to combat DOX-induced cardiotoxicity has motivated renewed interest in the investigation to discover new mechanisms into the regulation critical cardiac events during cancer treatment. For this reason, more mechanistic insight is required to understand cardiotoxicity and to develop more effective ways to treat and to preserve cardiovascular function in patients. Preservation of cardiac contraction and function is highly organised through gap-junctions between the cardiomyocytes (Severs *et al.*, 2004; Severs, 2009; Stroemlund *et al.*, 2015). The next section will describe the role of gap-junctions involving connexins.

1.5 *Connexins and their role in cell-to-cell communication in the heart*

1.5.1 *The structure and physiological function of connexins*

The first association of direct intercellular communication between neighbouring cells dates back to the mid-1930s (Schmidtmann, 1925). The first time gap-junctions were visualised was in the 1950s in mouse and guinea pig heart sections (Sjöstrand et al., 1958) and later intercellular channels in hexagonal structures were identified by electron microscopy (Revel and Karnovsky, 1967; Gilula and Reeves et al., 1972). Connexins are widely expressed in cells throughout the human body, for example in smooth muscle cells, vascular cells, follicular dendritic cells, epithelial cells, cardiomyocytes and myoblasts (Laird, 2006). Genetic linkage analysis has associated connexins to at least 30 human diseases with a wide variety of phenotypes, including skin disease, lymphedema, neuropathies, cataracts, deafness, syndactyly, developmental defects, and cardiac dysfunction (Guo and Yang, 2022; Laird and Lampe, 2022). The focus of this thesis involves connexins in the cardiac niche.

The connexin family consists of a total of twenty-one different genes, each coding for a transmembrane protein, which is composed of four α-helical transmembrane domains (TM1-TM4), two extracellular loops (EL1-EL2), a cytoplasmic loop (CL) connecting TM2 and TM3, and N-terminal and C-terminal domains. Interaction of six homomeric or heteromeric channels leads to the formation a hexameric structure, namely a hemichannel or connexon (Laird, 2006). Connexins can be classified on gene structure, homology and sequence, and length of the C-terminal region in five sub-families: GJA, GJB, GJC, GJD, and GJE (Laird, 2006).

The created hemichannels are transported and embedded into the plasma membrane, where they interact with other hemichannels on adjacent cells to form gap junction channels and allow paracrine signalling of small molecules (<1kD) such as Ca^{2+}, secondary messengers such as cAMP and ATP, microRNAs, and other metabolites (Evans and Martin, 2002; Aucher, Rudnicka and Davis, 2013; Leybaert *et al.*, 2017). This process is also known as gap junction intercellular communication (GJIC) and plays a role in physiological processes in the heart such as electric conduction to allow cardiac contraction (Severs *et al.*, 2004; Severs, 2009; Stroemlund *et al.*, 2015). Connexins that are expressed in cancer cells act as tumour suppressors or promoters depending on the connexin isoform, post-translational modification, cancer stage and type of tissue (Aasen *et al.*, 2019). An overview of the connexin structure is provided in Figure 5.
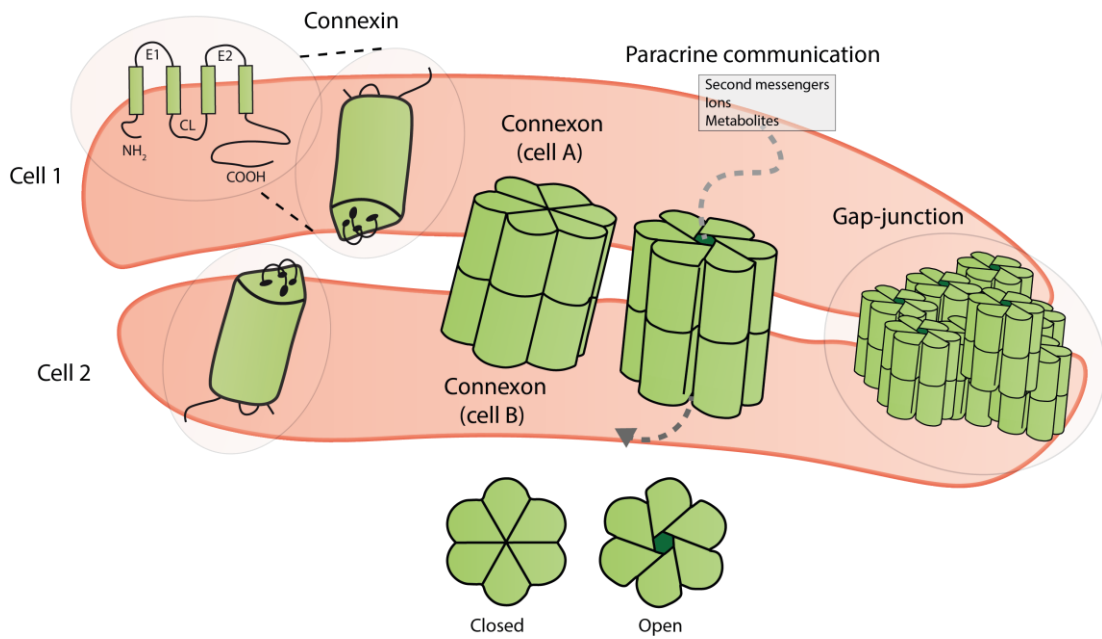
Figure 5 - Overview of connexin structure and communication

Connexins consist of N-terminal and C-terminal regions with two extracellular and a single cytoplasmic loop. Six connexin proteins compose a connexon that can dock to a connexon on a neighbouring cell to promote paracrine communication of second messengers, ions, and other metabolites. A group of docked connexons are called a gap-junction, also known as a plaque.

1.5.2 The role of connexins within the cardiovascular system

Connexins are expressed throughout the cardiac system in different cell types including, cardiomyocytes, fibroblasts, leukocytes, endothelial and smooth muscle cells (Lambiase and Tinker, 2015). In the cardiac system, connexins are important to mediate electrical coupling between cardiomyocytes and thereby enabling synchronised contraction (Del Ry *et al.*, 2015). The gap-junctions, also known as plaques, are mainly located at the intercalated disks of cardiomyocytes (Severs, 1990; Shaw *et al.*, 2007). Within the heart, three main connexin isoforms are expressed including, Cx40, Cx43, and Cx45. The Cx40 isoform is mainly expressed in atrioventricular node, bundle of His, atrial, and ventricular myocytes. Cx45 is expressed in the sinoatrial node and the atrioventricular node (Jansen *et al.*, 2010). The most well-known isoform is Cx43, which is the most widely studied and is the most highly expressed connexin in atrial and ventricular myocytes (Lampe and Lau, 2004). An overview of connexin expression within the different regions of the heart is provided in Figure 6. Connexins play a role in a variety of cellular processes and are important for healthy functioning of the cardiovascular system. The functional role of connexins have been identified through genetic diseases as a cause of mutations within the protein sequence (Srinivas, Verselis and White, 2018).

A protective role of gap-junctional protein connexin-43 (Cx43) has been associated in DOX-induced cardiotoxicity. Changes of Cx43 expression results in a loss of its protective role (Pecoraro *et al.*, 2015). The alterations of Cx43 expression coincide with changes in Ca^{2+} homeostasis (Pecoraro *et al.*, 2017). In addition, cardiovascular diseases have been associated with dysfunction and disorganisation of Cx43 (Michela *et al.*, 2015). A schematic overview of Cx43 in heart disease is provided in Figure 7.
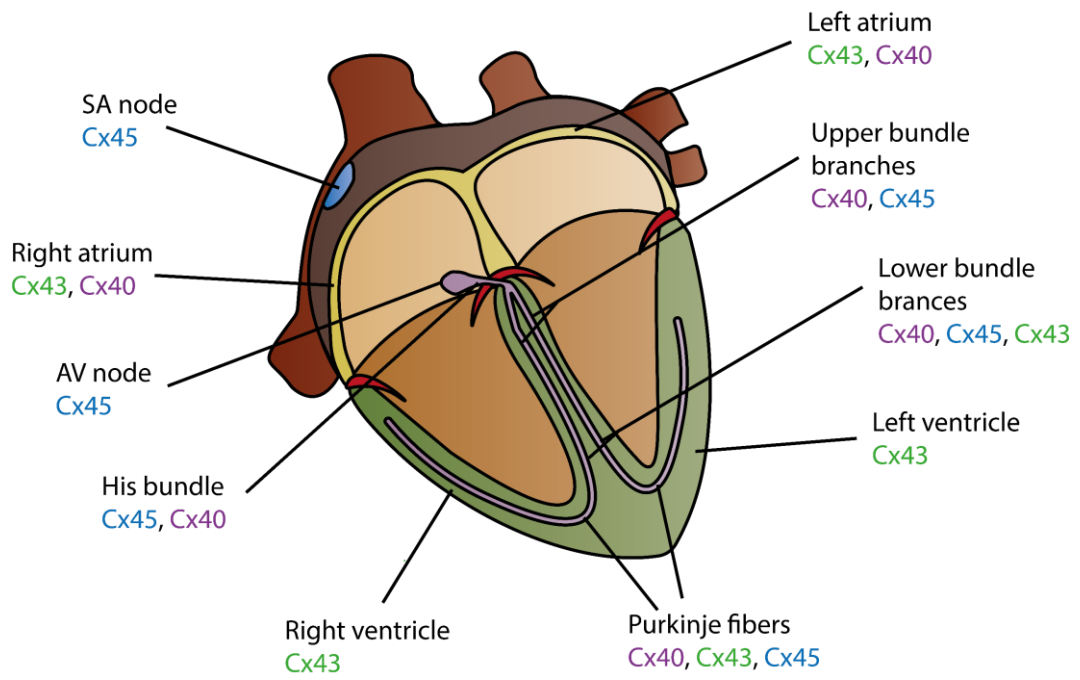
Figure 6 - Connexin expression within the heart

Expression of Cx40, Cx43, and Cx45 throughout different regions of the heart. AV; atrioventricular node, SA; sinoatrial node. This figure is adapted from (Desplantez, 2017).
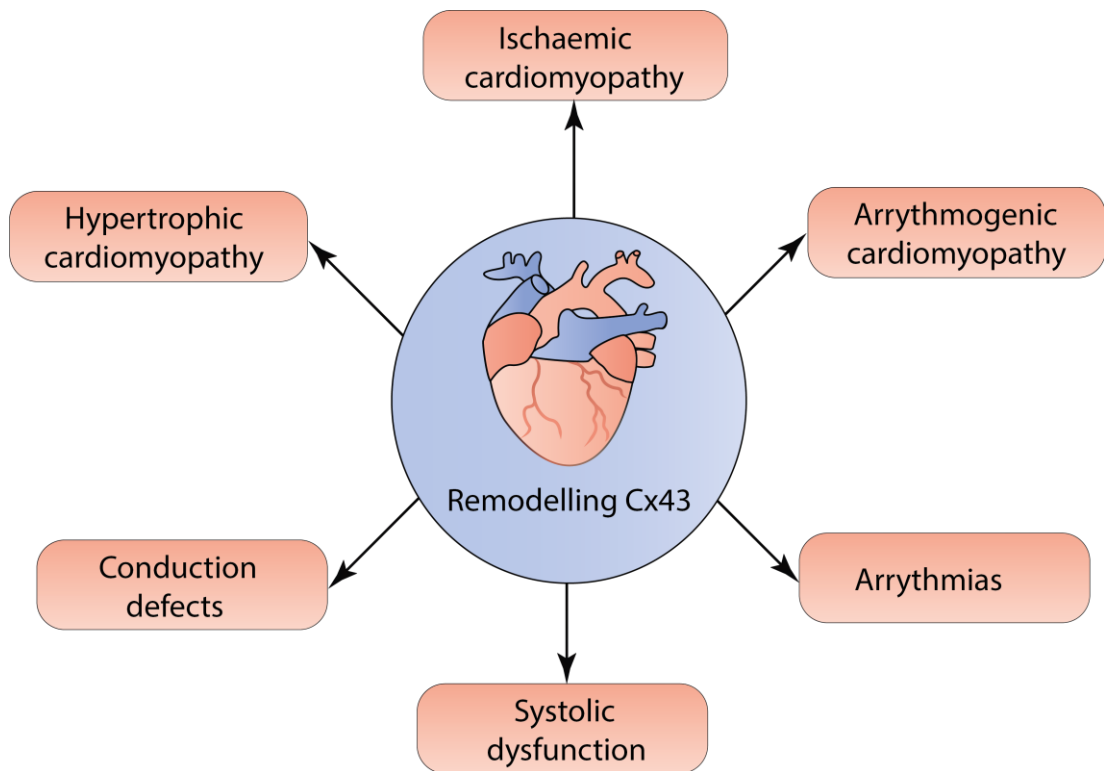
Figure 7 - Cx43 associated with cardiac dysfunction

Dysfunction and disorganisation of Cx43 participates in arrhythmias, systolic dysfunction, conduction defects, hypertrophic and ischaemic cardiomyopathy. This figure is adapted from (Michela et al., 2015).

1.5.3 *The structure and function of Cx43*

Cx43 remains monomeric in the endoplasmic reticulum and Golgi, thereafter hexamerization is established in the trans-Golgi and then the protein is transported in vesicles along microtubules and actin filaments towards the plasma membrane. (Musil and Goodenough, 1993; Epifantseva and Shaw, 2018). Hemichannels on the plasma membrane are normally in their "closed state" through two mechanisms: membrane potential and the intra- and extracellular Ca^{2+} concentration. The closed state of the hemichannel is maintained by a negative membrane potential (V_m) as well as by 1-2mM extracellular Ca^{2+} concentration (Trexler *et al.*, 1996; Contreras *et al.*, 2003; Verselis *et al.*, 2009; Leybaert *et al.*, 2017). In addition, the intercellular Ca^{2+} flow can be regulated by the C-terminal region of Cx43 through its binding site for calmodulin (Ahmad et al., 2001). Next to the binding motif for calmodulin there is the C-terminal region of Cx43 comprising a large interactome with over 50 different proteins (Leithe et al., 2018). The Cx43 amino-acid structure and its C-terminal phosphorylation sites is provided in Figure 8.
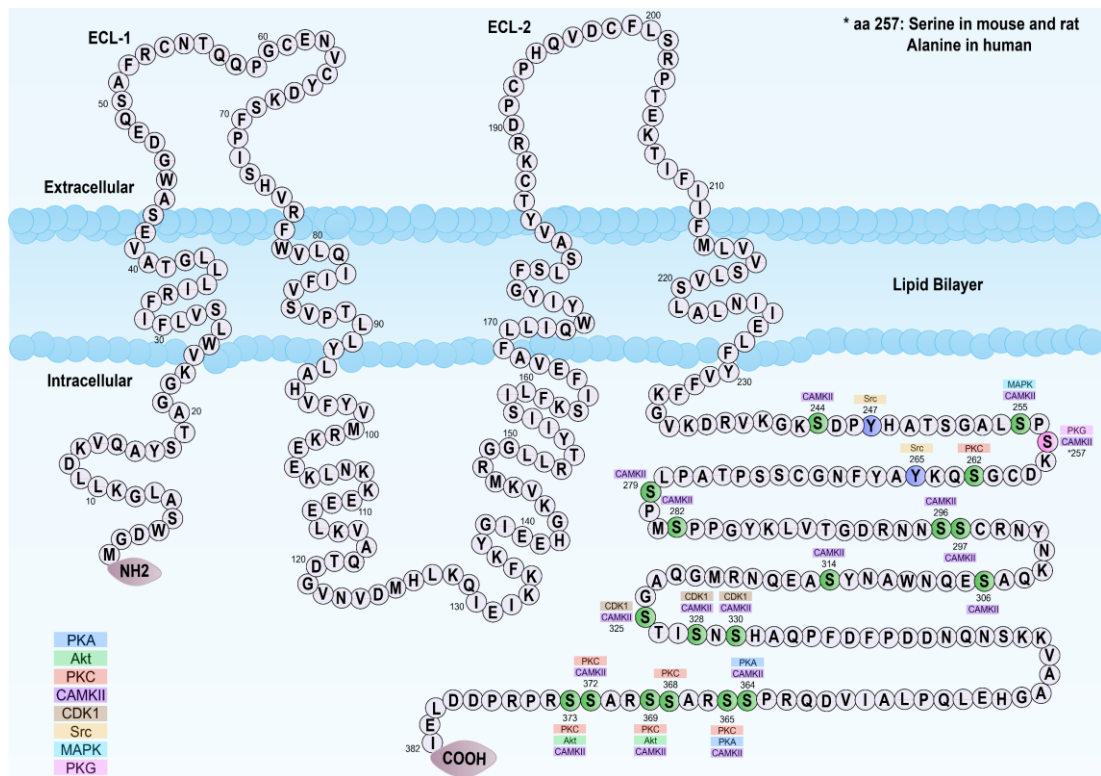
Figure 8 - Cx43 structure and phosphorylation sites

Overview of the Cx43 structure including the phosphorylation sites at the C-terminal region. PKA; Protein kinase A, Akt; Protein kinase B, PKC; Protein kinase C, CAMKII; Calmodulin kinase, CDK; Cyclin-dependent kinase, Src; proto-oncogene tyrosine-protein kinase, MAPK; Mitogen-activated protein kinase, PKG; Protein kinase G; ECL; extracellular loop, aa; amino acid.

The C-terminal region is highly involved in the turnover of Cx43 as Src activation promotes internalisation of the gap junctions through ERK-mediated phosphorylation at Ser-279 and Ser-282 (Solan and Lampe, 2020). The recruitment of hemichannels to the gap junctions is a highly organised event that involves interaction with a scaffolding protein named zonula occludens (ZO-1). ZO-1 is connected to Cx43 and F-actin, and interacts through its post-synaptic density protein (PSD)-95/ discs large (DLG)-A/ZO-1 (PDZ)-2 domain with Cx43 (Hunter *et al.*, 2005). The formation of gap junctions are regulated by protein kinase B (PKB) which is responsible for the phosphorylation of Ser-372 or Ser-373 and this affects the interaction between Cx43 and ZO-1 (Hunter *et al.*, 2005). In addition to this, casein kinase (CK)-1 has been shown to phosphorylate Ser-325, Ser-328, and Ser-330 to promote gap junction formation, and supports gap junction opening (Thévenin *et al.*, 2013). Thus, ZO-1 and Cx43 are important in gap junction formation, as well as endothelial barrier function and vascular permeability to promote a pro-inflammatory response.

HYPOTHESIS AND AIMS

The overall hypothesis of this project is that altered gap junction is a critical factor involved in the cardiotoxic effects of the anti-cancer drug DOX and that dysregulation of Cx43 leads to altered cardiac cell contractility.

The aims of this project are to:

1) Provide evidence in cardiac cells that doxorubicin treatment leads to changes in Cx43 expression.

2) Show that Cx43 changes in primary cardiac cell models translate to whole heart using isolated rodent heart Langendorff perfusion models.

3) Investigate whether DOX impacts Cx43 expression in human 3D cardiac cell spheroid models leading to changes in contractility and calcium handling.

Experimental work impacted because of laboratory closures and delay with the pandemic.

Originally, the plan was to investigate the effects of DOX on cardiac cell and vascular cells using mass spectrometry imaging (MSI) using Time-of-Flight Secondary Ion Mass Spectrometry (ToF-SIMS). The aim was to detect critical cell surface metabolite shifts in response to DOX. Pilot data was generated, however, incomplete due to laboratory closure during the pandemic (see Covid Impact statement). This has been included in the thesis General Discussion chapter.

CHAPTER TWO:

MATERIAL AND METHODS

2.1 Materials

This paragraph provides an overview of the used chemicals sorted by company (Table 5) and a list of prepared solutions/buffers with its corresponding recipe (Table 6).

Table 5 - List of materials

Company	Chemicals
Acros Organics (Geel, Belgium)	2-Methylbutane
Carl Roth (Karlsruhe, Germany)	Acrylamide 30% (w/w)
Cell Applications (San Diego, USA)	MesoEndo Cell Growth Medium (MCGM)
Covetrus (Dumfries, UK)	Dolethal (200 mg/mL) Heparin (5000U/mL)
GE Healthcare Life Sciences (Chicago, USA)	Amersham hybond hydrophilic polyvinylidene fluoride (PVDF) membrane (0.45 µm pore size)
Gibco® (Carlsbad, USA)	Minimum Essential Medium (MEM) Non-Essential Amino acids NEAA) Dulbecco's Modified Eagle Medium (4.5g/L Glucose, 0,11g/L Pyruvate, [-] Glutamine) (DMEM 1x) TrypLE™ Express
Santa Cruz Technology (Dallas, USA)	UltraCruz® Autoradiography film blue
Sigma-Aldrich (Missouri, USA)	N,N,N',N'-Tetramethylethylenediamine (TEMED) 2-methylbutane Ammonium formate β-mercaptoethanol cOmplete™ Protease Inhibitor Cocktail Calcium chloride solution in H_2O D-(+)-Glucose Dithiothreitol (DTT) Doxorubicin hydrochloride DMSO Glycerol HEPES Hydrogen peroxide L-Glutamine solution Luminol Magnesium chloride

	Magnesium sulphate p-coumaric acid Peel-A-Way embedding moulds (square S-22) Potassium chloride Phosphatase Inhibitor Cocktail Set V Protease Inhibitor Cocktail Set V (EDTA-Free) Tris base Triton x100 Tween 20 Thiazolyl Blue Tetrazolium Bromide
Thermo Fischer Scientific (Massachusetts, USA)	Bovine Serum Albumin (BSA) Di-Sodium hydrogen orthophosphate anhydrous Fluo-4 AM Glycine NuPAGE LDS sample buffer (4x) Phosphate buffered saline (PBS) tablets Potassium chloride Pierce™ BCA protein assay kit Sodium chloride (NaCl) Sodium dodecyl sulphate (SDS)
Merck (Darmstadt, Germany)	Mowiol® 4-88
VWR international (Leuven, Belgium)	Optimal cutting temperature compound (OCT)

Table 6 - List of prepared solutions

Solution	Recipe
Phosphate-buffered saline (PBS)	1x PBS tablet per 100 mL dH_2O (pH 7.4)
Buffer 1 (for resolving gel)	1.5 M tris base, 0.5 M SDS, pH 8.8 in dH_2O
Buffer 2 (for stacking gel)	0.5 M tris base, 14 mM SDS, pH 6.8 in dH_2O
Hank's Buffered Salt Solution (HBSS)	137 mM NaCl, 5.4 mM KCl, 0.25 mM Na_2HPO_4, 5.6 mM D-glucose, 0.44 mM KH_2PO_4, 1.0 mM $CaCl_2$, 1.0 mM $MgSO_4$, 4.2 mM $NaHCO_3$, 250 µM probenecid and 0.1% (v/v) Pluronic acid
Running Buffer	3.5 mM SDS, 192 mM glycine and 25 mM tris base in dH_2O
Stripping Buffer	31 mM tris base, 35 mM SDS, pH 6.7 in dH_2O
Transfer Buffer	192 mM glycine, 25 mM tris base, 20% (v/v) methanol in dH_2O
Tris-buffered saline (TBS)	20 mM tris base and 150 mM NaCl in dH_2O (pH 7.5)
TBS-Tween 20 (TBS-T) (0.1%)	TBS buffer and 0.1% (v/v) Tween 20
Lysis Buffer	50 mM tris (pH 7.4), 0.5% (v/v) triton x100 in dH_2O + cOmplete™ Protease Inhibitor tablet (1 per 10mL)
Homogenisation Buffer	20 mM Tris (pH7.4), 1mM DTT, 1X protease inhibitor cocktail (500 µM AEBSF, 150 nM Aprotinin, 1µM E-64, 1 µM Leupeptin) 1X phosphatase inhibitor cocktail (5 mM NaF, 1 mM Na_3VO_4, 1 mM NaPP, 1 mM β-glycerophosphate)
ECL-1	100 mM Tris base (pH 8.5), 250 mM luminol (in DMSO), and 250 mM p-coumaric acid (in DMSO) in dH_2O
ECL-2	100 mM tris base, and 9.8 mM H_2O_2 in dH_2O

Tyrode's buffer	1 mM CaCl, 137 mM NaCl, 20 mM HEPES, 5.4 mM KCl, 1.2 mM Na$_2$HPO$_4$, 1.2 mM MgSO$_4$.7H$_2$O, and 15 mM L-glucose in ddH$_2$O (pH 7.54). Solution stored overnight at 4°C. 15 mM D-(+)-glucose added before experiment.
Versene	0.48 mM EDTA in PBS

2.2   Animal ethics

All procedures were performed under sterile conditions and conformed to the Guide for the Care and Use of Laboratory Animals published by the US National Institutes of Health (NIH Publication No. 85-23, revised 1996) and Directive 2010/63/EU of the European Parliament. All animals used in this project were adult male Sprague-Dawley rats (248-315 grams, 7-9 weeks).

2.3   Tissue Culture

Cell morphology and growth was monitored by using a Nikon Eclipse (TE300) inverted microscope (Nikon, Tokyo, Japan) and a Leica EC3 digital camera affixed to a Leica DM IL LED inverted microscope (Leica Biosystems, Wetzlar, Germany). Imaging was conducted with a 10- or 20-times magnification.

2.3.1   Culturing of HUVECs

Human Umbilical Vein Endothelial Cells (HUVECs) (Promocell – C-12203) were cultured in MCGM and maintained in a humidified atmosphere at 37°C with 5% CO_2 with media replaced every second day. At 70-90% confluence, cells were detached by using TrypLE^{TM} Express and then passaged.

2.3.2   Culturing of HCAECs

Human Coronary Artery Endothelial Cells (HCAEC) (Merck) were cultured in MesoEndo Cell Growth Medium (MCGM) and maintained in a humidified atmosphere at 37°C with 5% CO_2 with media replaced every second day. At 70-90% confluence, cells were detached by using TrypLE^{TM} Express and then passaged.

2.3.3 Culturing of hCFs

Human Cardiac Fibroblasts (hCFs) cells (Promocell – C12375) are from ventricular origin and were cultured in fibroblast growth medium 3 kit (Promocell – C23130) and maintained in a humidified atmosphere at 37°C with 5% CO_2 with media replaced every second day. The culture flasks and well plates were coated with 1% gelatine in ddH_2O for 0.5 – 4 hours. The gelatine was removed prior to plating cells. At 70-90% confluence, cells were detached by using TrypLE™ Express and then passaged.

2.3.4 Culturing of AC16 human cardiomyocyte cell line

Proliferating AC16 human cardiomyocyte cell line (Cat. # SCC109 – Sigma Aldrich) were cultured in DMEM/F12 (Sigma Cat. No. D6434) containing 2 mM L-Glutamine (EMD Millipore Cat. No. TMS-002-C), 12.5% fetal bovine serum (FBS, EMD Millipore Cat. No. ES-009-B), and 1X Penicillin-Streptomycin solution (EMD Millipore Cat. No. TMS-AB2-C). The cells were grown at 37°C in a humidified incubator with 5% CO_2. When the cells reached 90-95% confluence, they were detached with accutase (EMD Millipore Cat. No. SM-20030C) and then passaged with a split ratio of 1:5.

2.3.5 Culturing of iCell cardiomyocytes

The iCell cardiomyocytes (iCell Cardiomyocytes², 11713, FUJIFILM Cellular Dynamics) are cells from a <18 year old female donor from a fibroblast tissue source with no associated disease. The cells were defrosted in a 37°C water bath for 4 minutes. The content was transferred into a 50mL falcon tube in droplets of every 4 to 5 seconds by continuous swirling with a 1 mL pipette. Thereafter, 1 mL of plating media in droplets of 4 to 5 seconds was added to the vial in order to collect the residual

cells. The residual cells were added to the cells in the 50 mL falcon tube in in droplets of 4 to 5 seconds through continues swirling. The cells were resuspended by slowly adding plating medium (room temperature) to the 50 mL falcon tube over 30 to 60 seconds by swirling continuously. The tube was inverted 2 to 3 times and centrifuged at 180 x g for 5 minutes in order to remove the residual DMSO. The cell pellet was resuspended in the desired volume. The plating efficiency of the cells varied by batch. For example, for a plating efficiency of 50%, double the number of required cells were seeded. 2.1 million cells were resuspended in 2100 μL plating medium, resulting in 100,000 cells per 100 μL. 100,000 cells were then plated per well in a 96-well plate for experiments. The cells were incubated at 37°C and 5% CO_2. The plating medium was replaced by maintenance medium 10 hours after seeding and every 2 days. The cells were cultured for a maximum of 10 days.

2.3.6   Culturing of MDA-MB 231 cells

M.D. Anderson Metastasis Breast Cancer (MDA-MB) 231 cells (ATCC-HTB-26[TM]) were cultured in Dulbecco's Modified Eagle Medium (DMEM) (250mM glucose, 1 mM sodium pyruvate, 4 mM L-glutamine, 10% fetal calf serum (FCS) , 1% MEM NEAA, 1% penicillin/streptomycin) and maintained in a humidified atmosphere at 37°C with 5% CO_2 with media replaced every second day. At 70-90% confluence, cells were detached by using versene and then passaged.

2.3.7   Culturing of SUM-159 WT/KO cells

SUM-159 cells were from mesenchymal triple-negative breast cancer origin. The wild type (WT) as well as the clustered regularly interspaced short palindromic repeats (CRISPR) Cx43 knockout (KO) cells were derived from Dr. T. Aasen (Vall d'Hebron Research Institute, Barcelona). The cells were cultured in DMEM (250 mM

glucose, 1 mM sodium pyruvate, 2 mM L-glutamine, 10% FCS, 1% MEM NEAA, 1% penicillin/streptomycin) and maintained in a humidified atmosphere at 37°C with 5% CO_2. At 70-90% confluence, cells were detached by using TrypLE™ Express and passaged 1:6 every 2-3 days.

2.3.8 Culturing of HEK293

The Human Embryonic Kidney (HEK) cells with an epithelial morphology. The cells were cultured in DMEM (250mM glucose, 1 mM sodium pyruvate, 2 mM L-glutamine, 10% FCS, 1% MEM NEAA, 1% penicillin/streptomycin) and maintained in a humidified atmosphere at 37°C with 5% CO_2. At 70-90% confluence, cells were detached by using TrypLE™ Express and passaged 1:6 every 2-3 days.

2.3.9 Cryopreservation and re-establishment

For storage, cells were cryopreserved in FCS containing 10% (v/v) DMSO and stored at -80°C, prior to transfer to liquid nitrogen for long term storage. To re-culture, the cells were rapidly defrosted and re-suspended in designated medium. Cells were then centrifuged at 1500 rpm for 5 minutes as to remove the DMSO and the pellet re-suspended in medium and thereafter cultured as described for each specific cell type.

2.4 Spheroid culture

Homogeneous cell culture has limitations by lacking paracrine communication of different cell types, therefore spheroid models have been established. Research conducted by the Polonchuk group, showed cardiac spheroids models consisting of human cardiac myocytes, endothelial cells, and fibroblasts (Polonchuk *et al.*, 2017). Spheroids containing two different cardiac cell types have been shown to respond differently in response to DOX and show cells could either serve a protective or a

more damaging role within the cell population. A simplified overview is illustrated in Figure 9. All cell types used were split at the same time and thereafter cell counting was performed by using a haemocytometer to seed the desired cell number and ratio into an ultra-low attachment polystyrene 96 well plate (Costar®).
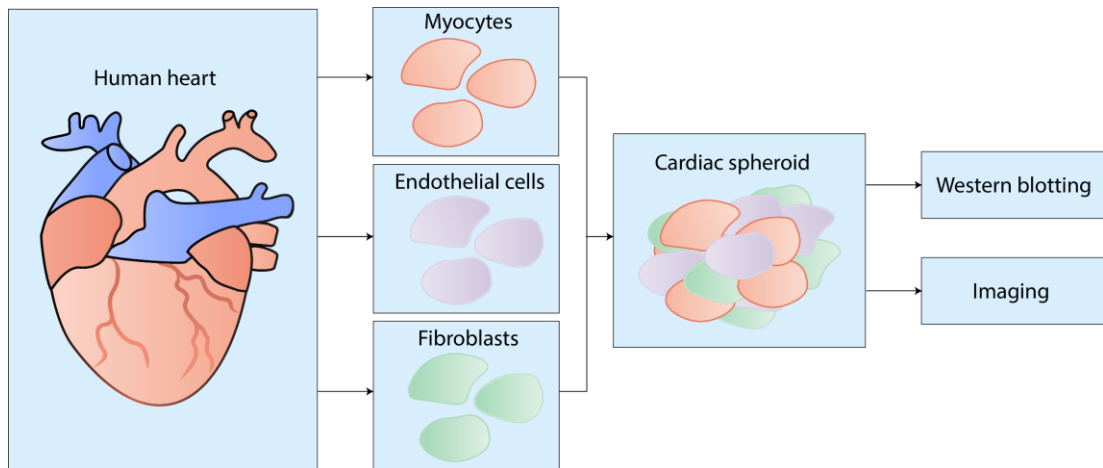
Figure 9 - Flowchart of cardiac spheroids

Schematic overview of spheroids culturing with human cardiac cells, including endothelial cells (HCAECs or HUVECs), fibroblasts (hCFs), and AC16 or iCell cardiomyocytes. The spheroids were analysed through imaging and SDS-PAGE with Western blot.

2.5   *Langendorff perfusion*

Adult male Sprague-Dawley rats (248 – 315 grams, 7-9 weeks) were given an overdose of Dolethal (0.7 ml/kg (200 mg/mL)) and 0.1 mL heparin (5000 U/mL). Following confirmation of loss of pedal reflexes, the heart was rapidly excised, washed in Tyrode's and cannulated on to the perfusion system via the aorta. It was then perfused retrogradely with oxygenated Tyrode's at a flow rate of ~3.2mL/min^{-1} and 37°C for the first 5 minutes, followed by 1 hour perfusion with 1.0 μM DOX or vehicle (DMSO) diluted in Tyrode's. After perfusing, the heart was weighed and cut with a scalpel along the short-axis (mid-section) so that, the upper half included the atria and half of the ventricles, and the lower part (apex) included the other half of both ventricles. The lower part of the heart was fixed in a Peel-A-Way embedding mould (square S-22) filled with optimal cutting temperature compound (OCT) on dry ice and stored at -20°C. The top part was further dissected, to collect the left ventricle (LV), right ventricle (RV), left atrium (LA), and right atrium (RA). Firstly, both atria were removed, followed by the right ventricle, the septum was taken from the underlying tissue of the RV, and finally the LA. The post-processing of these tissues is described in section 2.6.2 and in 2.9.2. An overview of the Langendorff perfusion system is displayed in Figure 10. The age and the weight of the heart and compartments is shown in Table 7.
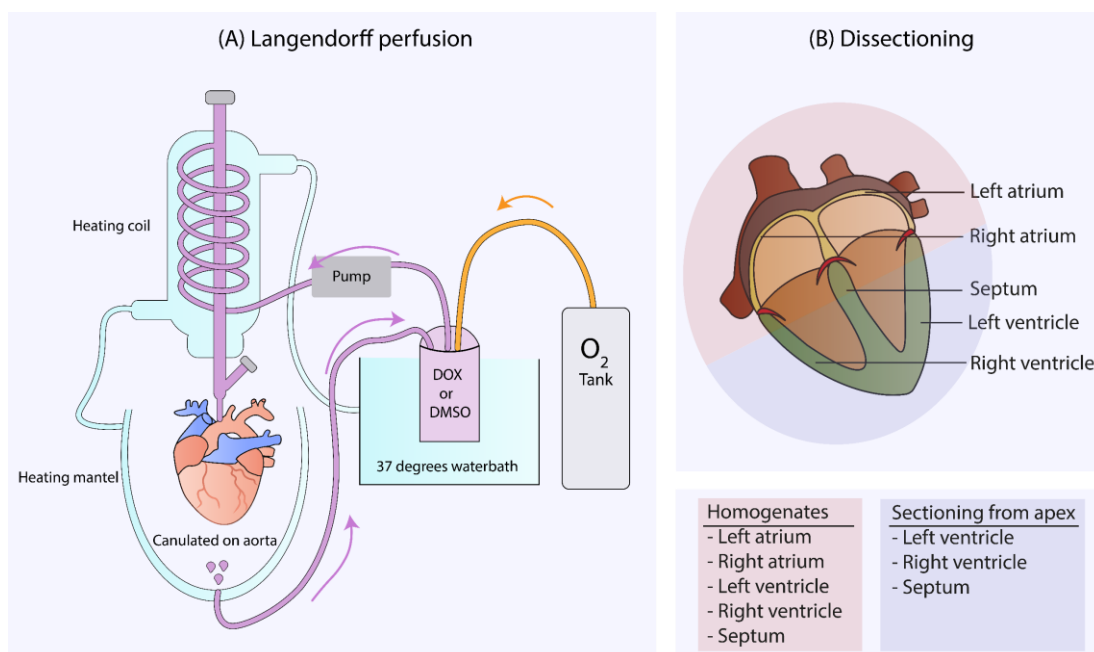
Figure 10 - Overview Langendorff perfusion set-up

A) The drug or vehicle is diluted in Tyrode's in a 100 mL cylinder (37°C). The solution is oxygenated and is pumped through a glass heating coil (maintained at physiological temperature of 37°C), and then through the cannulated heart. Upon drug or vehicle addition, the solution is re-circulated. **B)** The tissue of the lower part of the ventricles was used for tissue sectioning and the upper part of the ventricles, atria and septum were homogenised.

Table 7 - Overview of Langendorff perfusion experiments.

Age (weeks)	Treatment	Rat (g)	Heart (g)	LV (g)	RV (g)	LA (g)	RA (g)	Septum (g)
8.0	DMSO	315	1.90	0.292	0.142	0.050	0.042	0.134
7.0	DOX	270	1.52	0.345	0.095	0.032	0.047	0.084
7.5	DMSO	248	1.57	0.482	0.164	0.045	0.054	0.163
8.0	DOX	287	1.51	0.341	0.179	0.049	0.036	0.168
9.0	DMSO	308	1.36	0.268	0.131	0.040	0.041	0.118
9.0	DOX	310	1.50	0.361	0.147	0.033	0.034	0.177
8.0	DMSO	272	1.72	0.163	0.174	0.038	0.063	0.103
8.0	DOX	302	1.54	0.398	0.064	0.038	0.023	0.054
9.0	DMSO	320	1.58	0.155	0.111	0.031	0.029	0.085
9.0	DOX	295	1.44	0.114	0.180	0.070	0.029	0.072

2.6   Lysing samples and protein normalisation

2.6.1   Lysing cells

Cells were lysed and transferred into Eppendorf tubes prior to 1 hour rotation at 40rpm at 4°C. The lysates were centrifuged at 10,000 rpm for 5 minutes at 4°C and the supernatant was transferred into a new Eppendorf tube. Lysates were stored at -20°C. Protein concentrations of cell lysates were determined by using bicinchoninic acid assay (BCA).

2.6.2   Homogenising tissue

All tissue sections were weighed and homogenised in homogenisation buffer. The ventricles were homogenised in five times weight/volume and the atria in 10x weight/volume. The tissues were firstly minced into small pieces and then homogenised with an Ultra-Turrax T8. Samples were aliquoted and stored at -80°C. BCA protein assays were conducted prior to protein normalisation.

2.6.3   Protein normalisation

To normalise the protein concentration within the sample set, three calculations were required. Firstly, the sample volume was calculated by using Equation 1 with the input of the desired final protein concentration and volume, as well as the protein concentration of that specific sample. 4x sample buffer (with 200 µM dithiothreitol (DTT)) volume was calculated with Equation 2, in order to achieve 1x sample buffer in the sample. The used diluent was lysis buffer, the volume required could be calculated by using Equation 3. The process of protein normalised was streamlined by a python script whereby the input of desired protein concentration and volume is required. The programme conducts the calculation for each individual sample. The script is shown in appendix I.

Cell lysates of DOX-treated cells were normalised to the lowest protein concentration within the sample set, as DOX induced cell death, the highest possible protein concentration is achieved. Tissue homogenates were normalised to 500 µg/µL. Samples were heated to 95°C for 5 minutes and stored at -20°C prior to sodium dodecyl sulphate (SDS) polyacrylamide gel electrophoresis (PAGE) and Western blotting.

Equation 1 - Sample volume calculation

$$sample\ vol. = \frac{desired\ protein\ conc.\ (\mu g/\mu L) * desired\ vol.(\mu L)}{sample\ protein\ conc.\ (\mu g/\mu L)\ * 0.75} = \ ...\mu L$$

Equation 2 - Sample buffer volume calculation

$$sample\ buffer\ vol.(4x) = 0.25 * desired\ vol.\ (\mu L) = \ ...\mu L$$

Equation 3 - Lysis buffer volume calculation

$$lysis\ buffer\ vol. = desired\ volume - [SB\ vol.\ +\ sample\ vol.(\mu L)] = \ ...\mu L$$

2.7   List of used antibodies and stains

The antibodies that were used for Western Blotting and Immunofluorescence staining is shown in Table 8. An overview of the stains that were applied with IF is shown in Table 9.

Table 8 - List of antibodies

Antibody	Ref ID	Type	Concentration	Immunofluorescence	Western blotting
ATPIF-1	AB_110277	Mouse	1.0 mg/mL	1/200 in 1% BSA (in PBS)	N/A
Vimentin (Sigma-Aldrich)	V5255	Mouse	1.0 mg/mL	1/400 in 1% BSA (in PBS)	1/80.000 in 0.5% BSA (in TBS-T)
von Willebrand Factor (Abcam)	ab6994	Rabbit	10.5 mg/ml	1/100 in 1% BSA (in PBS)	1/100.000 in 0.5% BSA (in TBS-T)
α smooth muscle actin (Abcam)	ab7817	Mouse	1.0 mg/mL	1/200 in 1% BSA (in PBS)	1/80.000 in 0.5% BSA (in TBS-T)
Connexin 43 (Sigma-Aldrich)	C6219	Rabbit	0.5 – 0.8 mg/mL	1/1000 in 1% BSA (in PBS)	1/20.000 in 0.3% BSA (in TBS-T)
Connexin 43 (Sigma-Aldrich)	MAB3067	Mouse	1.0 mg/mL	1/200 in 1% BSA (in PBS)	N/A
Phospho-Connexin 43 (Ser368) (Cell Signalling Technologies)	3511S	Rabbit	Not provided	N/A	1/1000 in 0.3% BSA (in TBS-T)
α-Tubulin (Sigma-Aldrich)	T5168	Mouse	3.0 – 7.0 mg/mL	N/A	1/60.000 in 0.5% BSA (in TBS-T)
GAPDH (Abcam)	ab8245	Mouse	2 mg/mL	N/A	1/60.000 in 0.3% BSA (in TBS-T)
Alexa Fluor 555 goat anti-rabbit IgG (Invitrogen)	A21428		2.0 mg/mL	1/100 in 1% BSA (in PBS)	N/A
Alexa Fluor 488 goat anti-rabbit IgG (Invitrogen)	A11008		2.0 mg/mL	1/100 in 1% BSA (in PBS)	N/A

Alexa Fluor 555 goat anti-mouse IgG (Invitrogen)	A21422		2.0 mg/mL	1/100 in 1% BSA (in PBS)	N/A
Alexa Fluor 488 goat anti-mouse IgG (Invitrogen)	A11001		2.0 mg/mL	1/100 in 1% BSA (in PBS)	N/A
Donkey Anti-Mouse IgG (H+L) (Jackson immunoresearch)	AB_2340770		0.8 mg/ml	N/A	1/7.500 in 0.3% BSA (in TBS-T)
Goat Anti-Rabbit IgG (H+L) (Jackson immunoresearch)	AB_2307391		0.8 mg/ml	N/A	1/7.500 in 0.3% BSA (in TBS-T)

Table 9 - Immunofluorescent stain list

Stain	Ref ID	Concentration	Dilution
DAPI (Sigma)	D-9542	1 mM aliquots	1/2000 in PBS
Fluorescein phalloidin (ThermoFisher)	F432	300 U	1/40 in PBS
Rhodamine phalloidin (ThermoFisher)	R415	300 U	1/40 in PBS
Wheat Germ Agglutin 488 (ThermoFisher)	W11261	1 mg/mL	1/1000 In media
CellMask Orange (ThermoFisher)	C10045	5 mg/mL	1/1000 In media

2.8 SDS-PAGE, Western blotting, membrane reprobing and analysis

2.8.1 SDS-PAGE

The resolving gel (10% (v/v) acrylamide, 60mM tris-base, 0.6mM SDS, 0.13% (w/v) ammonium persulfate (APS), 0.13% (v/v) tetramethylethylenediamine (TEMED) was prepared with 0.1% (w/v) SDS layered on top of the gel for 15 minutes to remove air bubbles and avoid evaporation during polymerisation. The stacking gel (3% (v/v) acrylamide, 20 mM tris-base, 0.6 mM SDS, 0.13% (w/v) APS, 0.13% (v/v) TEMED) was added on the resolving gel with a Teflon comb inserted and left to polymerize for 15 minutes. PageRuler Plus Prestained protein ladder (Thermo Scientific) was loaded on the gel alongside 10-50µL of cell sample. Gel electrophoresis was performed in a Bio-Rad Mini-PROTEAN II™ electrophoresis tank topped up with running buffer. Electrophoresis was conducted at 120 V for 110 minutes.

2.8.2 Western blotting

The transfer cassette, prepared with two sponges, two 0.92mm cellulose chromatography paper grade filters (Whatman®), one nitrocellulose membrane with a 0.45 µm pore size (GE Healthcare Life Sciences) and gel were placed in a Bio-Rad Mini Trans-Blot™ tank topped with transfer buffer and ran at 300mA for 110 minutes. The tank was cooled with an ice tray during the process. The membrane was blocked with 3% bovine serum albumin (BSA) in TBS-T buffer to avoid non-specific binding. The primary antibody (see Table 8) was added to the membrane and overnight, followed by three TBS-T washes with 5-minute intervals and incubated with the required secondary antibody for 2 hours. After incubation, the membrane was washed three times with TBS-T. The horseradish peroxidase (HRP) conjugate was activated by a 2-minute incubation with enhanced chemiluminescence (ECL)-1 and ECL-2 with a 1:1 ratio. The membranes were transferred to an exposure cassette and exposed

to Ultra Cruz® Autoradiography film blue and developed using automatic X-ray film processor model JP-33.

2.8.3   Stripping and reprobing Western blot membranes

Membrane bonded antibodies were removed by 15 minutes incubation with stripping buffer and 14mM β-mercaptoethanol (100 rpm at 60°C). The stripping buffer was removed by three 5-minute TBS-T washes before 2 hours of blocking in 3% (w/v) BSA in TSB-T. The membrane was then incubated with a primary antibody (e.g. glyceraldehyde 3-phosphate dehydrogenase (GAPDH) and further protocol was performed as previously described in section 2.8.2.

2.8.4   Densitometry analysis of Western blots

The autoradiography films obtained from the Western blot membrane development, were scanned with a HP Deskjet 2540, using 600dpi and greyscale. The file was saved as a TIF format. The band intensities were measured with Fiji software. The colour of the film was firstly inverted by using "Invert" and the region of interest (ROI) was selected by using "Rectangle" and the mean intensity was measured with "Measure". The obtained "mean" value is the average intensity of all pixels within the selected region of interest. The intensity of each pixel could vary from 0 (black) to 255 (white), which accounts for saturated signal. The background signal (ROI-2) is subtracted from the band of interest (ROI-1), which is repeated for each band individually. Thereafter, the same procedure was conducted for the reference protein (e.g. GAPDH). The data was normalised to the control (untreated), in order to calculate the fold change. Figure 11 displays the selection of the ROI's and the calculation prior fold-change is displayed in Equation 4.

A)

B)

	Mean	StdDev	Mode
1	85.249	25.743	71
2	69.975	3.466	69
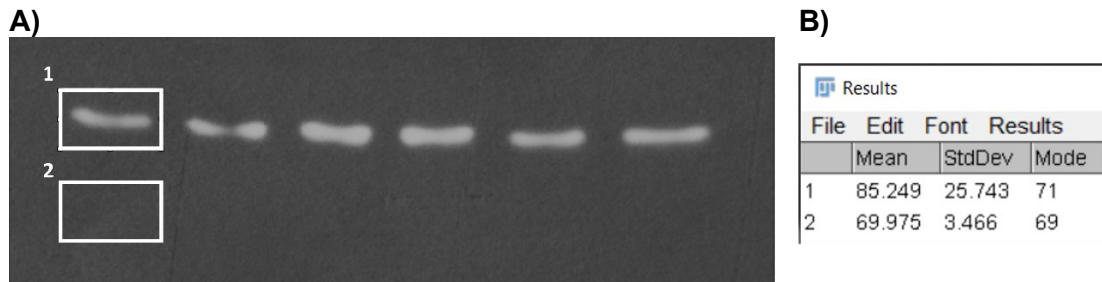
Figure 11 - Densitometry analysis of Western blot

*Densitometry analysis of developed Western blots was conducted by using ImageJ. **A)** The band of interest (1) as well as the background (2) were selected by a region of interest (ROI). **B)** The mean pixel intensities were obtained for further calculations.*

Equation 4 - Fold change calculation of Western blots

$$Fold\ change = \frac{Protein\ interest * reference\ protein\ (sample)}{Protein\ interest * reference\ protein\ (untreated)}$$

2.9 Immunohistochemistry on cells and tissues

2.9.1 Indirect immunofluorescence on cells

Cells were grown on 13mm coverslips to 90% confluence. The coverslips were washed twice in PBS and fixed with 3.6% (v/v) paraformaldehyde in PBS for 10 minutes. Residual paraformaldehyde was removed, and the coverslips were carefully washed with PBS and permeabilised with 0.25% (v/v) Triton-X-100 in PBS for 10 minutes. The coverslips were blocked in 1% (w/v) BSA in PBS for one hour and incubated with the primary antibody (Table 8) in a humidified atmosphere overnight at room temperature . Residual antibody was removed by three PBS washes, prior to a second block step with 1% (w/v) BSA in PBS for 30 minutes. The cells were incubated with the required secondary antibody for 2 hours in the dark as due to light sensitivity. Cells were then given three PBS washes to remove excess antibody. Rhodamine phalloidin or Fluorescein green staining was performed with a 20-minute incubation, followed by two washes in PBS. 4',6-diamidino-2-phenylindole (DAPI) was used with a concentration of 0.5 µM and diluted in PBS as a nuclear counterstain was added to the cells for 5 minutes. The DAPI was removed, followed by a single PBS wash. Each coverslip was placed with the cell-side-down on a glass slide with 20 µL mowiol mounting medium and dried overnight in the dark at room temperature. The slides were stored at 4°C.

Images were acquired on a Leica Confocal SP8 microscope using licensed Leica Application Suite X (LAS X) software. Images were also obtained by using EVOS FL Auto system. Post-processing was conducted with ImageJ and PowerPoint 2016 software (Microsoft Office). Red was converted into magenta to accommodate for colour to avoid colour-blindness (Wong, 2011).

2.9.2 Indirect immunofluorescence on tissue sections

Cardiac tissue embedded in OCT was sectioned on the Shandon SME Cryotome Cryostat or the Leica CM1950 apparatus with a set temperature of -20°C and a cutting temperature of -20°C. Sections were acquired, starting from the apex with a thickness of 12 microns. The sectioned tissue was placed on a microscopic slide and dried overnight prior to immunofluorescent staining.

The OCT was removed from the tissue by two 5-minute washes with PBS in Coplin jars. The tissue was fixed with 3.6% (v/v) paraformaldehyde in PBS for 10 minutes. The paraformaldehyde was removed by two washes with 5-minute intervals, with PBS and permeabilised with 0.25% (v/v) Triton-X-100 in PBS for 10 minutes. The Triton-X-100 was removed by two 5-minute washes with PBS and thereafter blocked in 1% (w/v) BSA in PBS for one hour and incubated with the primary antibody (Table 8) in a humidified atmosphere overnight at room temperature. Residual antibody was removed by three PBS washes with 5-minute intervals, prior to a second block step with 1% (w/v) BSA in PBS for 30 minutes. The tissue was incubated with the required secondary antibody for 2 hours in the dark as due to light sensitivity. The tissue was then given three 5-minute washes in PBS to remove excess antibody. Rhodamine phalloidin staining was performed with a 20-minute incubation, followed by two 5-minute washes in PBS. DAPI (0.5 µM in PBS) as a nuclear counterstain was added to the cells for 5 minutes. The DAPI was removed, followed by three 5-minute PBS washes. Mowiol mounting media was added on top of the tissue and covered by a 0.13-0.17 mm thick cover glass and dried overnight in the dark at room temperature. The slides were thereafter stored at 4°C. The images were acquired on a Leica Confocal SP8 microscope using licensed LAS X software. Post-processing was conducted with ImageJ and PowerPoint 365 software (Microsoft Office).

2.9.3 Quantification of nuclear accumulation of DOX

The auto fluorescent properties of DOX allowed for subcellular localisation and was shown to accumulate in the nucleus. The intensities of DAPI (blue) and DOX (magenta) were quantified using the ImageJ tools "selection tool brush" to select the nuclear area, followed by selecting the plugin "RGB histogram". The RGB histogram tool measures the intensity for red, green, and blue for each pixel in the selected area. The rMean (red mean) and bMean (blue mean) values were used for further processing. The rMean and bMean were measured for the same number of nuclei for each specific treatment. An example to measure the rMean and bMean is shown in Figure 12.
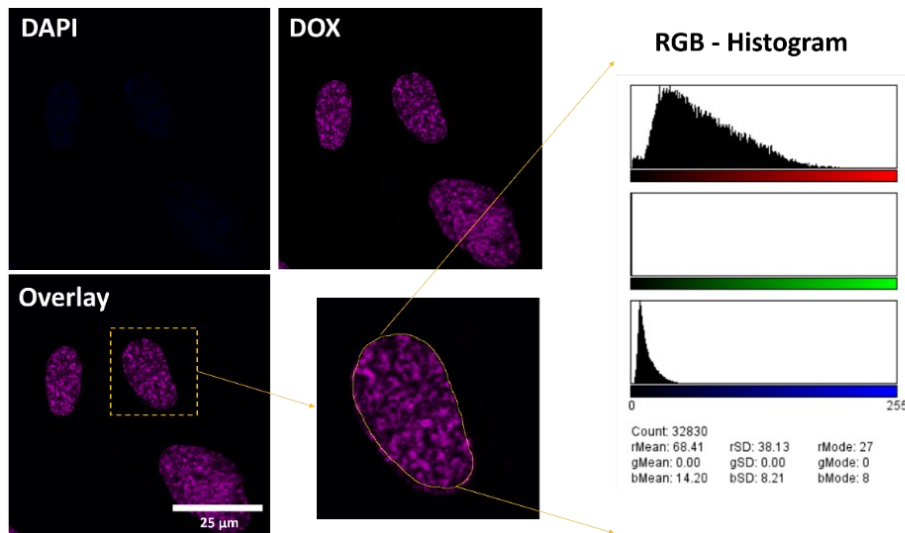
Figure 12 - Measuring of rMean and bMean in nuclei

To compare different n-numbers, the rMean or bMean (yMean) across all nuclei within the same sample set were averaged. This was conducted for each of the data sets (yMean average X) and all measurements normalised to the dataset with the highest average (yMean average H), shown in Equation 5.

Equation 5 - Normalisation of yMean

$$\frac{yMean}{yMean\ average\ X} * yMean\ average\ H$$

2.9.4 Colocalization analysis

The colocalization analysis has been conducted by using Coloc 2 plugin from ImageJ. Two images in an 8-bit format were selected prior to colocalization by using Costes threshold regression (Point Spread Function (PSF): 3.0; Costes randomisations: 10). The Pearson's R value indicates the linear relationship between the two channels. R of -1 indicates no and 1 a perfect positive linear relationship. The raw data from the scatterplot was re-plotted by using python. The scatterplot is heatmap based, showing the overlay of pixels of both channels.

2.10   Calcium assays

2.10.1 Fluo-4 calcium assay

Cells were seeded into a 96-well black polystyrene microplate (Corning®, Sigma Aldridge) and incubated at 37°C and 5% CO_2, until confluent. Fluo-4 Direct protocol was followed according to manufacturer's instructions. Briefly, Fluo-4 calcium dye solution was prepared in Hank's balanced salt solution (HBSS). Media was removed from the plates and 50 µL of the Fluo-4 dye was added to each well prior to a 1-hour incubation at 37°C with the plate protected from light. After incubation, the Fluo-4 dye was removed from the cells and replaced with 80 µL HBSS. Assays were performed on a Flexstation 3 Multi-Mode Microplate Reader and the assay performed (Excitation λ = 494nm, Emission λ = 516 nm) with data acquisition through SoftMax Pro 5 (Molecular Devices) software. Calcium signalling was measured for doxorubicin hydrochloride (0-100 µM) and thrombin (0-10 U/mL). Data was transferred to Microsoft Excel 2016 and dose-response curves performed using GraphPad Prism 8 non-linear regression curve fitting (variable slope).

2.10.2 Cal-520 calcium imaging

The cells were washed with PBS and the cal-520 dye was incubated for 20 minutes at 37°C. The cal-520 dye was removed with PBS and covered in DMEM prior imaging. Cal-520 calcium and brightfield imaging was performed on a confocal machine with an acquisition time of 50 frames per second. The acquired stacked data was processed in ImageJ by using the plot Z-axis profile tool which measures overall pixel intensity changes. The raw data was collected and further processed in OriginPro 2022 software. Baseline was firstly subtracted (see Figure 13A) and thereafter the data was normalised to 1 (F/F0), allowing further post-analysis and data comparison. An example for baseline correction is showed in Figure 13A. The time

required for the response to rise from 10% to 90% of the highest value is called the rise time. The full width half maximum (FWHM) duration between two independent variables between the half maximum (f_{max} / 2) value. The rise time and the FWHM are illustrated in Figure 13B, both were calculated within the OriginPro 2022 software. The altitude is the maximum value (f_{max}) of the peak. The frequency is the duration between the maximum value of two peaks, calculated by 1 / duration (seconds). The altitude and frequency are illustrated in Figure 13C.
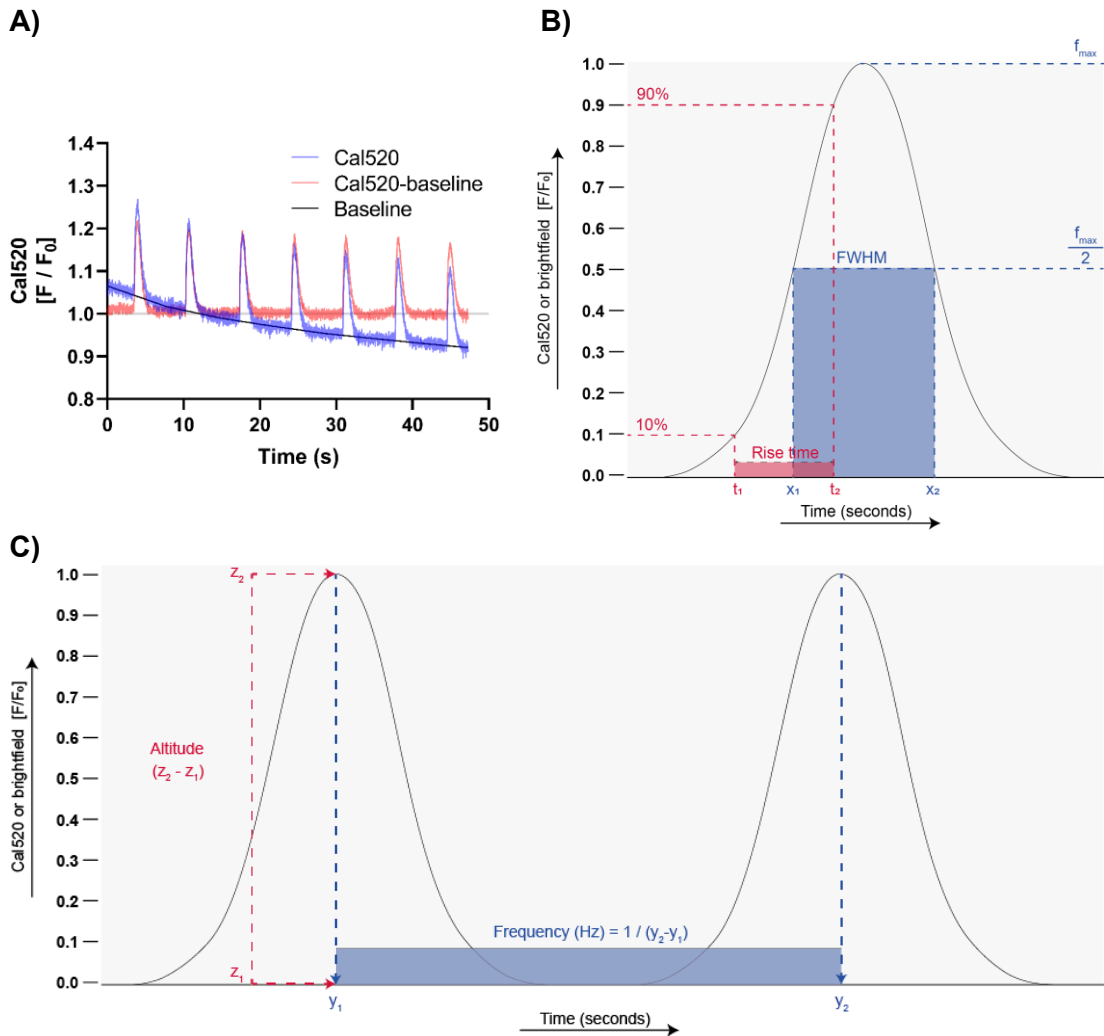
Figure 13 - Illustrative explanation of the rise time and FWHM

A) *Example of a baseline correction. The blue line is the curve with the raw data, the black line is the background, and the red represents the curve with subtracted baseline.* ***B)*** *The time between 10% (t_1) and 90% (t_2) of the peak altitude is called the rise time. The half of f_{max} (f_{max} / 2) from x_1 to x_2 is the full width half maximum (FWHM) duration.* ***C)*** *The altitude is the height of the peak from the baseline to the top (z_2-z_1). The frequency (in Hz) is the time between the peaks, calculated by 1 / (y_2-y_1).*

2.11   Cell viability assays

2.11.1 MTT assay

The   3-(4,5-Dimethylthiazol-2-Yl)-2,5-Diphenyltetrazolium   Bromide   (MTT) assay has been performed to measure cell viability. Cells were cultured in a 96-well plate and maintained at 37°C and 5% CO_2, until confluent. The media was removed, and the cells were washed once with PBS and thereafter incubated for 3 hours at 37°C with 100 µL thiazolyl blue tetrazolium bromide (1mM in PBS). As thiazolyl blue tetrazolium bromide is light sensitive, the plate was wrapped in tin foil. After incubation, thiazolyl blue tetrazolium bromide was replaced with 100 µL DMSO to allow the formed formazan crystals to dissolve. Each treatment and/or control was conducted in triplicate. The absorbance was measured at 570 nm by using a Flexstation 3 Multi-Mode Microplate Reader and data acquisition through SoftMax Pro 5 (Molecular Devices) software. The data was further analysed by using Excel 365 (Microsoft Office) and GraphPad Prism 8 software.

2.11.2 Toxilight viability assay

The Toxilight bioassay kit (Lonza Biosciences, USA) was used to measure cellular toxicity in response to treatments from collected media. The reagents within the kit were equilibrated at room temperature for 15 minutes and the AK Detection Reagent (AKDR) was reconstituted in assay buffer. 20 µL from the media was transferred into a 96 well plate and 100 µL of AKDR was added to each well and incubated for 5 minutes at room temperature. The luminescence was read at 540nm by using was a Flexstation 3 Multi-Mode Microplate Reader and data acquisition through SoftMax Pro 5 (Molecular Devices) software. The data was further analysed by using Excel 365 (Microsoft Office) and GraphPad Prism 8 software.

2.12   Isolation of extracellular vesicles

MDA-MB-231 cells were grown in three T75 flasks and were serum starved overnight prior to treatment. The media was replaced with serum free media with a total volume of 10 mL and treated with 1.0 µM DOX or DMSO (vehicle) for 24 hours. To isolate the extracellular vesicles, the media was collected into 15mL falcon tubes and centrifuged at 3,500 x g for 10 minutes. The supernatant was transferred into 1.5mL Eppendorf tubes and centrifuged at 10,000 x g for 20 minutes. The supernatant was centrifuged at 100,000 x g for 60 minutes on the Optima™ TLX or on the Optima™ MAX-XP Ultracentrifuge. The pellet was resuspended in sterile PBS and re-centrifuged at 100,000 x g for 60 minutes. The pellet was resuspended in 150 µL PBS and aliquoted into three 50 µL in 0.5 mL Eppendorf tubes. The extracellular vesicle extract was stored at -80°C prior to experimental use.

2.13   Nanoparticle tracking analysis

The extracellular vesicle size and concentration were determined by Nanoparticle Tracking Analysis (NTA). The extracellular vesicle isolate was diluted 1 in 1000 µL PBS and was loaded into the sample chamber of a LM10 unit (NanoSight, Malvern, UK). Five 60-second videos were acquired of each sample by using NTA 3.1 software (NanoSight).

2.14   Lipofectamine 2000 & 3000 transfection

HEK293 or AC16 cells were passaged and grown in 24-well plates to reach 70% confluence. The cells were transfected on the day after with 0.5 µg pEGFP C1 Cx43 DNA vector. By using lipofectamine 2000 (Lipo2000), the plasmid DNA was diluted in 25 µL Opti-MEM medium and the Lipo2000 was added to 25µL Opti-MEM

medium in a separate tube. By using Lipo3000, 0.75 µL of Lipo3000 reagent was diluted in 25 µL Opti-MEM medium and vortexed. The plasmid DNA was diluted in 25 µL Opti-MEM medium and 0.5 µL P3000 reagent. The content of both suspensions was gently mixed and incubated for 20 minutes. The suspension was added to the cell culture, the medium was replaced after 6 hours of incubation. The cells were lysed for Western blotting or fixed for immunohistochemistry staining after 24 hours.

2.15   Time of Flight Secondary Ion Mass Spectrophotometry

2.15.1 Methodology of TOF-SIMS

Time of Flight Secondary Ion Mass Spectrophotometry (ToF-SIMS) 5 from IONTOF GMBH (Münster, Germany) in collaboration with CMAC (Glasgow, UK) was used for analysis. HCAECs were cultured on 50 µm thick silicon wafers (Mi-Net Technology) in a humidified atmosphere of 37°C and 5% CO_2, until 80% confluent. The silicon wafers were washed once with PBS and then incubated with ammonium formate (150 mM) for 2 minutes. The silicon wafers were transferred in 2-methylbutane and cryofixed in liquid nitrogen (-196°C) for 2 minutes, followed by 24 hours of freeze drying at -50°C and 0.003 Torr vacuum in a 2.5 L freeze dry system (Labconco FreeZone).

The negative and positive ion spectra and images were obtained with a pulsed current of 0.26-0.32 power amplifier (pA) using 30 kiloelectron volts (KeV) $Bi3^+$. Area of analysis for mass spectra is a field of view of 500 x 500 $µm^2$ with 512 x 512-pixel raster size. Cycle time of 130 microseconds was used and resulted in a mass range of $1 \leq$ mass per charge (m/z) ≤ 1500. For all experiments, ion dose density was kept below 5×10^{11} ions/cm^2 to avoid saturated signals. The negative and positive ion spectra were calibrated using $C1^-$, $C2^-$, $C3^-$, $C4^-$ and CH_3^+, $C_2H_3^+$, $C_3H_7^+$, $C_5H_9^+$ peaks, respectively. For each sample, a minimum of three different mass spectra were collected. Acquired ToF-SIMS data was analysed by SurfaceLab version 7.0. Theoretical m/z values of spectra were extracted from SurfaceLab version 7.0.

2.16 Re-analysis of published datasets

2.16.1 Proteomic data re-analysis of human heart biopsies for GJA-1

To investigate potential variations in physiological GJA-1 levels between human atrial and ventricular tissue, we utilized a proteomic dataset containing over 7000 proteins (Linscheid *et al.*, 2020). The proteomic data from both atrial and ventricular tissues were re-plotted using -Log P and Log2 fold change values for all proteins, including GJA-1.

2.16.2 Human protein atlas data

The human protein atlas was consulted to acquire information of GJA-1 throughout different organs, tissues, and 69 different cell types. The protein expression scores were based on the best estimation from a knowledge-based annotation. The tissue-specific cell types and heart muscle data were measured in enrichment scores. These enrichment scores represent a comparison to other cell types within the tissue and are classified into three different categories: >0.35; very high, >0.25; high, and >0.15; moderate. The RNA-specific cell types were plotted using RNA expression levels in normalized transcripts per million (nTPM), which represent values from transcriptomic data clusters based on gene expression.

2.16.3 Protein sequence alignment of Cx43 antibodies

The protein sequence of Cx43 was compared between distinct species, including human, mouse, and rat. The amino-acid sequences were collected from the National Library of Medicine (NLM) and processed with ClustalW2 (RRID:SCR_001591) software. The targets on Cx43 anti-mouse and anti-rabbit antibodies were highlighted within the amino-acid sequence.

2.17 Statistical analysis

All statistics were calculated using GraphPad Prism version 8. P-values <0.05 were considered significant, confidence intervals represent the +/- standard error of the mean (SEM), and n stand for the number of replications of the experiment.

2.18 Analysis software

The different types of software's for sequence alignments, illustrative images and videos, calcium peak analysis, reference manager, and data analysis are displayed in Table 10.

Table 10 - Software's used within thesis

Software	Applications
Adobe Illustrator	Illustrative images
Adobe Premier Pro	Creating/editing video files
ClustalW2	Multiple sequence alignments
GraphPad prism 8	Volcano plot
	Dose-response curves
	Dot-plots
	Statistical analysis
ImageJ	Western blot quantification
	Confocal image composition
	Colocalization analysis (Coloc 2 plugin)
Mendeley	Reference manager
Microsoft PowerPoint	Used for figure composition
NTA 3.1 software	Acquisition NTA videos
Origin pro	Calcium peak analysis
Python & Anaconda	Generation of scripts

CHAPTER THREE:

INVESTIGATING THE EFFECT OF DOX ON CX43

EXPRESSION IN CARDIAC CELLS

3.1 Introduction

The aim of this chapter was to provide evidence in cardiac cells that DOX treatment leads to changes in Cx43 expression. DOX, also known under the brand name Adriamycin, is a family member of the anthracyclines and has transformed cancer therapy since its FDA approval in 1974. DOX is used as a chemotherapeutic drug for the treatment of many different types of cancer, including breast cancer (Thorn *et al.*, 2011). The use of DOX has limitations, as the drug is associated with cardiotoxicity which manifests in the clinic as arrhythmias, ischemia, cardiomyopathy, systolic dysfunction and heart failure (Mitry and Edwards, 2016). Cx43 expression in the heart is normally recognised at the intercalated discs of the cardiomyocytes to preserve a synchronised cardiac contraction (Hesketh *et al.*, 2010). Changes in Cx43 expression has been linked to cardiac dysfunction (Rucker-Martin *et al.*, 2006; Fontes *et al.*, 2012; Michela *et al.*, 2015). For example, an occurrence known as lateralization, involving the redistribution of cardiomyocytes from intercalated disks to the lateral side, has been noted in cases of atrial fibrillation (Kim *et al.*, 2011; Takahashi *et al.*, 2012).

The aim of the first results chapter is to investigate the effect of DOX on Cx43 expression in cardiac cells. Firstly, the database of the protein atlas was used to get an indication of the Cx43 expression throughout the human body, tissue, and cell types. The inherent fluorescent properties of DOX were determined and its cellular localisation after treatment. The experimental results provided in this chapter include the morphological assessment of HUVECs, HCAECs, human cardiac fibroblasts (hCFs), and AC16 cardiomyocyte-related cells. The cytotoxic effect of DOX on the cardiac cells was assessed and the endogenous protein levels and cellular localisation of Cx43 were evaluated.

3.2   The Human Protein Atlas and Cx43

The Human Protein Atlas is a Swedish online database that started in 2003 with the aim of mapping human proteome on cellular, tissue, and organ level through the use of omic technologies. To appreciate the extent of Cx43 expression throughout the human body, the human protein atlas was consulted. Figure 14A-B describes a male and female display and shows the variety of Cx43 expression, and the highest amount of protein expression is located in the brain, endocrine tissue, genitals, skin, bone marrow & lymphoid tissues, and muscle tissues. This shows that Cx43 plays a role throughout the human body, and it is known to preserve a synchronous contraction of the heart. Comparison between tissue specific cell types reveal the highest enrichment scores were identified in the cardiomyocytes (Figure 14C). Interestingly, enrichment scores from cardiac cells show scores of <0.3 in endothelial cells and fibroblasts (Figure 14D). However, different studies have shown that Cx43 plays an important role in the maintenance of the normal vascular function and is involved in pathological disorders (Liao *et al.*, 2001; Wang *et al.*, 2008). In addition, Cx43 in fibroblasts plays a role, for example in the transformation into the myofibroblast phenotype (Schultz *et al.*, 2019). The normalised RNA expression levels indicate prominent levels of Cx43 in HUVEC cells (Figure 14E).

A proteomic data-analysis on human heart biopsies from atrial and ventricular tissue was conducted and detected over 7000 different proteins (Linscheid *et al.*, 2020). This was in 2020 the largest *in vivo* cardiac protein expression dataset from human origin. This dataset was used to perform analysis on the expression levels of Cx43 as they have included GJA-1. A volcano plot was generated to compare the levels of atrial and ventricular Cx43. However, no statistically significant differences were observed between the two distinct regions (Figure 14F).

17)

Body heatmap

Female   Male

B)

RNA expression   Protein expression

Brain
Eye
Endocrine tissue
Respiratory system
Proximal digestive tract
Gastrointestinal tract
Liver & Gallbladder
Pancreas
Kidney & Bladder
Male tissues
Female tissue
Muscle tissues
Heart
Skeletal
Smooth
Connective & Soft tissue
Skin
Bone marrow & Lymphoid tissues

C)

Tissue specific cell types

Enrichment

- Adipocytes
- Specialized epithelial cells
- Glandular epithelial cells
- Endocrine cells
- Glial cells
- Undifferentiated cells
- Muscle cells
- Blood & immune cells
- Squamous epithelial cells
- Pigment cells
- Germ cells

Leydig cells, Cardiomyocytes, Ductal cells, Sertoli cells, Spermatogonia, Mesothelial cells, Outer root sheath cells, Thyroid glandular cells (Skin), Cholangiocyte, Inner root sheath cells, Mitotic cells (Heart), Peritubular cells, Hair cortex cells, Breast myoepithelial cells, Melanocytes, Spermatocytes, Alpha cells, Keratinocyte (other), Alveolar cells type 1, Podocytes, Mitotic cells (Colon), Skeletal myocytes

D)

Heart Muscle

Enrichment

- Muscle cells
- Undifferentiated cells
- Endothelial cells
- Mesenchymal cells
- Blood & immune cells

Cardiomyocytes, Smooth muscle cells, Macrophages, Plasma cells, Mitotic cells (Heart), Endothelial cells, Fibroblasts

E)

RNA-levels cell types

nTPM

- Brain
- Liver & Gallbladder
- Gastrointestinal tract
- Pancreas
- Male reproductive system
- Kidney & Urinary bladder
- Skin
- Eye
- Proximal digestive tract
- Female reproductive system
- Endothelial
- Muscle
- Mesenchymal
- Lymphoid
- Myeloid

F)

Cardiac protein expression

-Log P

GJA1

Log2 fold change
(Ventricular / Atrial)

Figure 14 - Expression GJA-1 throughout the human body

A-B) *A female (left) and male (right) organ display of GJA-1 expression levels throughout the human body.* **C)** *Enrichment scores of GJA-1 in tissue specific cell types allowing cross comparison between tissues. A larger symbol size correlates*

*with increased GJA-1 enrichments in different cell types. **D)** Enrichment scores of cells specifically from the heart. **E)** Normalised RNA expression (in normalised transcripts per million, nTPM) of individual tissue culture cell lines. **F)** Volcano plot of ventricular and atrial GJA-1 expression. The figures A-E were obtained from the Human Protein Atlas proteinatlas.org. A-B: https://www.proteinatlas.org/ENSG00000152661-GJA1/tissue; C-D: https://www.-proteinatlas.org/ENSG00000152661-GJA1/tissue+cell+type; E: https://www.protein-atlas.org/ENSG00000152661-GJA1/cell+line. Figure F is adapted from* (Linscheid *et al.*, 2020)*. The data from the protein atlas was accessed in June 2022.*

3.3   *Characterisation of HUVECs and selecting Cx43 antibody*

A well-established endothelial originated cell model are human umbilical vein endothelial cells, also known as HUVECs. HUVECs were isolated in the 1970s by Jaffe and other researchers and can be easily maintained and cultured for *in vitro* based experiments (Jaffe *et al.*, 1973). The cells were morphologically characterised by a well-known cobblestone structure and grew in a monolayer with no overlapping layers (Figure 15A). HUVECs are a well-established subset of macrovascular endothelial cells commonly used to evaluate the function and pathology of endothelial cells which makes them an ideal model for studying the effects of DOX upon vascular endothelium in this study (Medina-Leyte *et al.*, 2020).

A frequently used marker for identifying the phenotype of endothelial cells is von Willebrand Factor (vWF), a protein which is expressed within Weibel-Palade bodies (WPB) (Haberichter *et al.*, 2005). WPB are cigar-shaped secretory endothelial cell specific organelles that are generated in a wide range of sizes with lengths between 0.5 to 5.0 µm (Ferraro *et al.*, 2016). vWF plays a critical role within the regulation of haemostasis and acts upon vascular damage through platelet activation and plug formation. Intracellular punctae of vWF were observed and are WPB, which thereby support its endothelial phenotype (Figure 15B). As well as vWF, the HUVECs also showed expression of vimentin. Next to actin filaments and microtubules, vimentin intermediate filaments are also part of the cellular cytoskeleton and play a role within e.g. cell migration (Battaglia *et al.*, 2018). Vimentin expression was identified as intracellular fibers throughout the cell and convey the impression that it is present in the entire population.

To exclude the presence of smooth muscle cells within the cell population, the cells were stained for α-smooth muscle cell actin (α-SMC). A-SMC is expressed in smooth muscle cells (Pokrywczynska *et al.*, 2016; Sugita *et al.*, 2019) as well as in transformed fibroblasts, namely myofibroblasts (Hinz *et al.*, 2001; Liu *et al.*, 2017). No α-SMC positive cells were characterised within the cell population (Figure 15C).
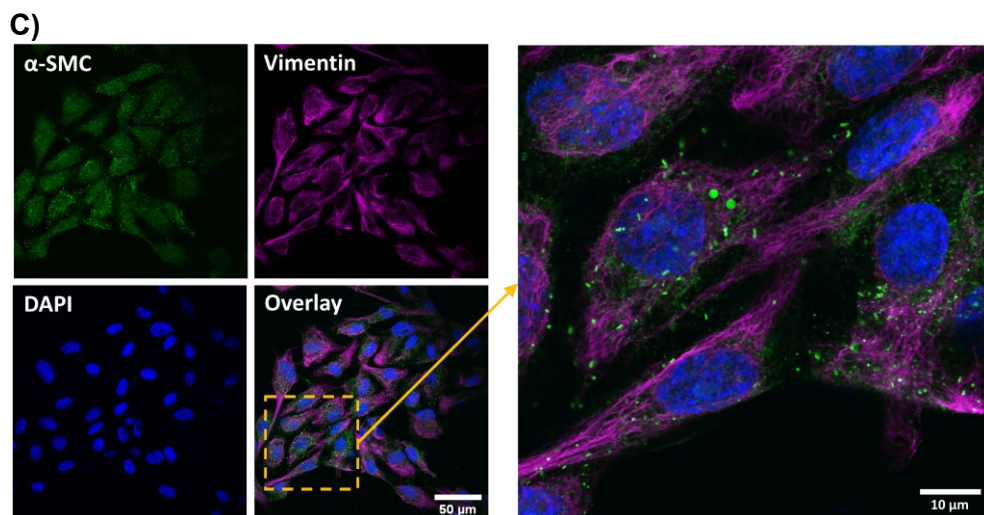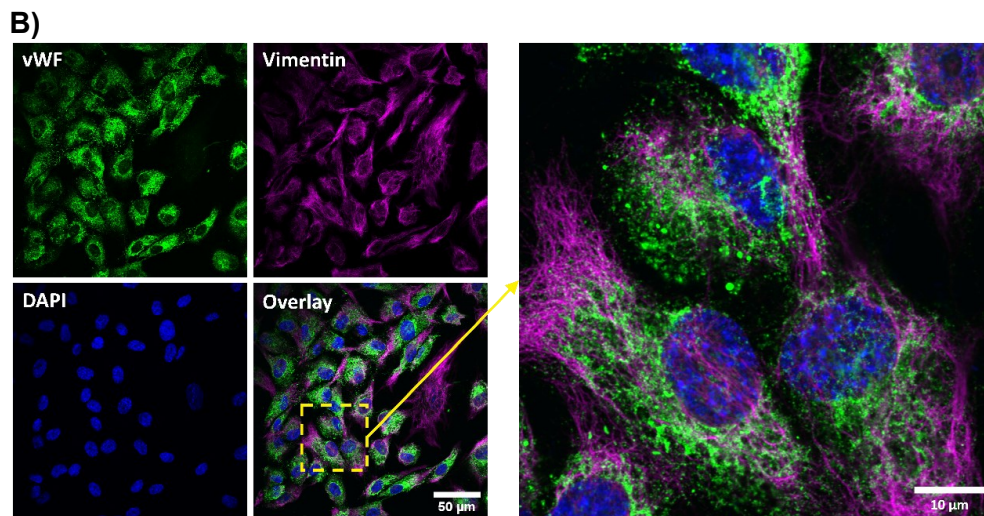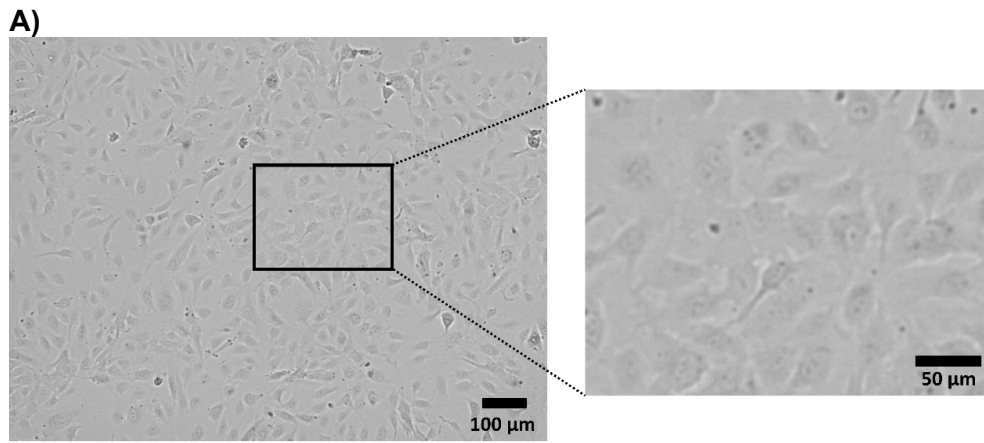
Figure 15 - Characterisation of HUVECs

A) Brightfield image to visualise the morphology of HUVEC cells. B) Indirect immunofluorescent staining of vWF (green), vimentin (magenta), and counterstained with DAPI (blue). n=5.

In the confocal images throughout the result chapters, was DAPI used as a nuclear counterstain. DAPI (4′,6-diamidino-2-phenylindole) can cross the membrane of cells and interacts within the adenine-thymine regions of the DNA. DAPI was synthesised in 1971 by Otto Dann for the purpose of trypanosomiasis treatment (Dann *et al.*, 1971). The drug was identified to contain fluorescent properties and was therefore firstly considered as a DNA marker in 1975 (Hajduk, 1976).

HUVECs have previously been used to study the role of Cx43 within the endothelium. Examples of studies are the investigation of its role in monocyte adhesion (Yuan et al., 2015), angiogenesis (Koepple et al., 2021), apoptosis regulating through influencing mitochondrial functions (Ma et al., 2020), and TGF-β signalling (Shi, Li and Yang, 2022). Another study showed the importance of Cx43 in the endothelium in order to maintain normal cardiac function (Liao et al., 2001).

It was important to consider selection of the best antibody targeting Cx43 for the duration of this project. The anti-Mouse antibody recognises the 252-270 amino acid residues on the carboxyl terminal region of Cx43. Conversely, the anti-Rabbit antibody binds to the end of the carboxyl terminal region, to the 363-382 amino acid residues. The regions of antibody recognition are illustrated in Figure 16A. In order to identify the localisation of Cx43 the anti-Mouse as well as anti-Rabbit antibodies used for indirect immunohistochemistry studies (Figure 16B). Interestingly, colocalization analysis resulted in a Pearson R value of 0.59 (Figure 16C). The correlation indicates a degree of overlap in Cx43 expression, however, the anti-Mouse antibody shows a more perinuclear localisation in comparison to the anti-Rabbit. The alignment of cross-species were important, as distinct species were used within the project. Therefore, a comparison of amino acid sequence was conducted between human,

rat, and mouse species (Figure 16D). Differences were observed, especially between human and the rodents. These differences contain two single amino acids within the binding region of the anti-Mouse antibody. No differences were identified within the anti-Rabbit binding region and therefore future experiments were conducted using the anti-Rabbit antibody.

A)

C-terminal region

anti-Mouse: 252 - 270

anti-Rabbit: 363 - 382

B)

Cx43 (R) Cx43 (M)
DAPI Overlay
50 µm

Cx43 (R) Cx43 (M)
DAPI Overlay
10 µm

C)

Pearson R value: 0.59

D)

```
HUMAN   MGDWSALGKLLDKVQAYSTAGGKVWLSVLFIFRILLLGTAVESAWGDEQSAFRCNTQQPG   60
MOUSE   MGDWSALGKLLDKVQAYSTAGGKVWLSVLFIFRILLLGTAVESAWGDEQSAFRCNTQQPG   60
RAT     MGDWSALGKLLDKVQAYSTAGGKVWLSVLFIFRILLLGTAVESAWGDEQSAFRCNTQQPG   60
        ************************************************************

HUMAN   CENVCYDKSFPISHVRFWVLQIIFVSVPTLLYLAHVFYVMRKEEKLNKKEEELKVAQTDG   120
MOUSE   CENVCYDKSFPISHVRFWVLQIIFVSVPTLLYLAHVFYVMRKEEKLNKKEEELKVAQTDG   120
RAT     CENVCYDKSFPISHVRFWVLQIIFVSVPTLLYLAHVFYVMRKEEKLNKKEEELKVAQTDG   120
        ************************************************************

HUMAN   VNVDMHLKQIEIKKFKYGIEEHGKVKMRGGLLRTYIISILFKSIFEVAFLLIQWYIYGFS   180
MOUSE   VNVEMHLKQIEIKKFKYGIEEHGKVKMRGGLLRTYIISILFKSVFEVAFLLIQWYIYGFS   180
RAT     VNVEMHLKQIEIKKFKYGIEEHGKVKMRGGLLRTYIISILFKSVFEVAFLLIQWYIYGFS   180
        ***.*********************************************************

HUMAN   LSAVYTCKRDPCPHQVDCFLSRPTEKTIFIIFMLVVSLVSLALNIIELFYVFFKGVKDRV   240
MOUSE   LSAVYTCKRDPCPHQVDCFLSRPTEKTIFIIFMLVVSLVSLALNIIELFYVFFKGVKDRV   240
RAT     LSAVYTCKRDPCPHQVDCFLSRPTEKTIFIIFMLVVSLVSLALNIIELFYVFFKGVKDRV   240
        ************************************************************

                             Anti-Mouse 252-270
HUMAN   KGKSDPYHATSGALSPAKDCGSQKYAYFNGCSSPTAPLSPMSPPGYKLVTGDRNNSSCRN   300
MOUSE   KGRSDPYHATTGPLSPSKDCGSPKYAYFNGCSSPTAPLSPMSPPGYKLVTGDRNNSSCRN   300
RAT     KGRSDPYHATTGPLSPSKDCGSPKYAYFNGCSSPTAPLSPMSPPGYKLVTGDRNNSSCRN   300
        **.*******.* ***.***** *************************************

HUMAN   YNKQASEQNWANYSAEQNRMGQAGSTISNSHAQPFDFPDDNQNSKKLAAGHELQPLAIVD   360
MOUSE   YNKQASEQNWANYSAEQNRMGQAGSTISNSHAQPFDFPDDSQNAKKVAAGHELQPLAIVD   360
RAT     YNKQASEQNWANYSAEQNRMGQAGSTISNSHAQPFDFPDDNQNAKKVAAGHELQPLAIVD   360
        ***************************************.**.**.**************

               Anti-Rabbit 363 - 382
HUMAN   QRPSSRASSRASSRPRPDDLEI   382
MOUSE   QRPSSRASSRASSRPRPDDLEI   382
RAT     QRPSSRASSRASSRPRPDDLEI   382
        **********************
```

Figure 16 - Comparison of Cx43 anti-rabbit and mouse antibody epitopes.

***A)** Illustration of the Cx43 structure with a region zoomed in on the C-terminal. Anti-Cx43 anti-Mouse binds between the amino acids 252-270 (showed in magenta) and anti-Rabbit binds at the end of the C-terminal region between amino acids 363-382 (showed in green). **B)** Indirect immunofluorescent staining of Cx43 anti-rabbit (green) and anti-mouse (magenta). **C)** The Pearson correlation coefficient was 0.59. **D)** Protein sequence comparison between human, rat, and mouse species with anti-Cx43 anti-Mouse and anti-Rabbit regions. * identical amino acid; mutation human vs mouse (highlighted in red); mutation between human vs mouse & rat (highlighted in blue rectangular boxes). N = 1.*

To determine the Cx43 localisation in HUVECs the cells were counterstained with rhodamine phalloidin, a filamentous actin stain to visualise the structure of the cells. Phalloidin is a phallotoxin, originated from the death cap mushroom (Amanita phalloides). The toxin was first discovered by Feodor Lynen and Ulrich Wieland in 1937 (Lynen and Wieland, 1937), and acts through binding and stabilising filamentous actin (F-actin). The phalloidin can be fluorescently labelled with for instance rhodamine to use for imaging purposes. The Cx43 protein was majorly expressed in the perinuclear region of the HUVEC (Figure 17).
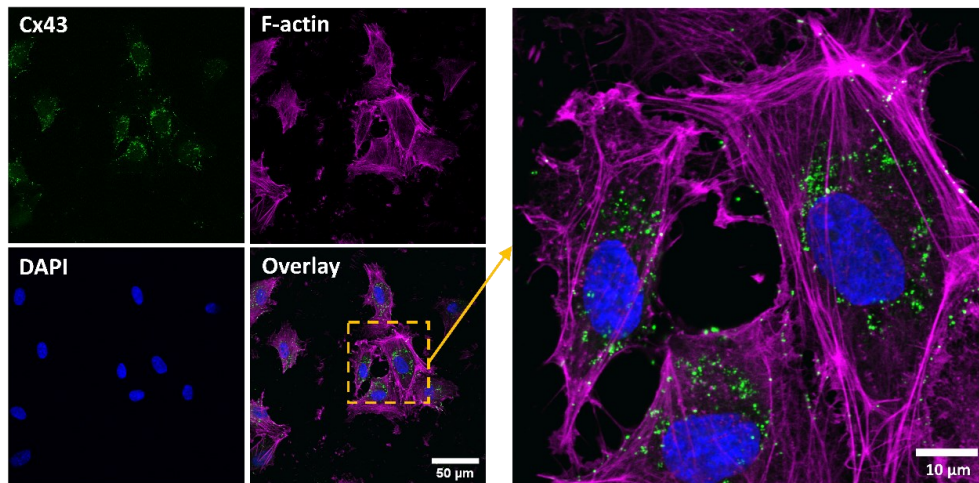
Figure 17 - Cx43 expression and localisation in HUVECs

Indirect immunofluorescence staining for Cx43 (green), rhodamine phalloidin stain for F-actin (magenta), and DAPI nuclear counterstain (blue). n = 1,

3.4   Nuclear localisation of DOX in HUVECs

DNA intercalation of DOX has previously been studied by different groups (Agudelo *et al.*, 2014; Yao *et al.*, 2015; Silva *et al.*, 2017) and has extensively been reviewed (Cutts *et al.*, 2005; Agudelo *et al.*, 2016). DOX has previously been characterised to have inherent fluorescent properties (Vigevani and Williamson, 1981; Duray, Cuono and Madri, 1986; Karukstis *et al.*, 1998), and could therefore be used in fluorescence-based assays in biological systems (Kauffman *et al.*, 2016). Immunofluorescent microscopy strategies have confirmed the nuclear localisation of DOX in treated cells (Shen *et al.*, 2018; Li *et al.*, 2019; Rembiałkowska *et al.*, 2020; Guo *et al.*, 2021). During our studies we have identified comparable results. DOX treated HUVEC cells reveal nuclear localisation (Figure 18A). These findings support the action of DOX within the nucleus and interacting with the DNA (Figure 18B). Interestingly, increasing concentrations of DOX result in a significant elevation of its nuclear localization, while the DAPI intensity significantly decreases at increasing concentrations of DOX in comparison to the control group (Figure 18C).
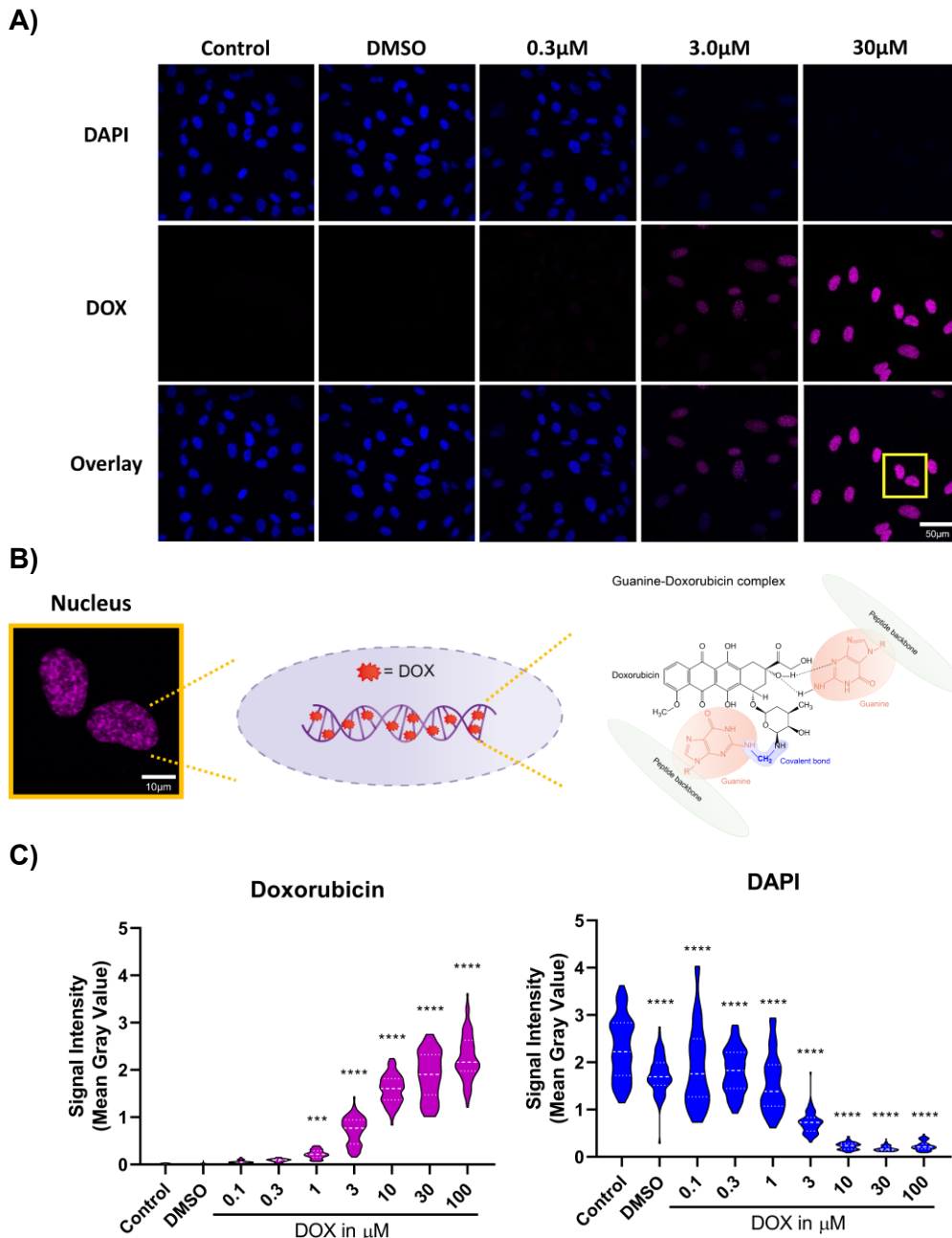
Figure 18 - Nuclear accumulation of DOX identified in HUVECs

A) *Immunofluorescent images of HUVECs counterstained with DAPI (blue) and treated with DOX (magenta, 0-100 µM). The auto fluorescence of DOX is visualised and showed in magenta.* **B)** *A region zoomed in on the nucleus from the overlayed 30 µM image and illustrates the DNA binding capability of DOX.* **C)** *Quantified signal intensity as the mean grey value of DAPI and DOX in the nuclear region in response to DOX. Data is presented in a violin plot. Statistical analysis was conducted by an ordinary one-way ANOVA, Post-hoc Tukey test. ****p < 0.0001; ***p < 0.001, compared to the control group. n=3 (27 individual cells per independent biological replicate).*

3.5   *Limitation of DOX-autofluorescence*

Previous studies have identified that both DOX and thrombin cause increases in intracellular calcium levels (Kim *et al.*, 2006; Aziz *et al.*, 2019). In the current study, calcium flux was assessed. Increasing concentrations of thrombin (0-10U/mL) resulted in a dose-dependent increase in Fluo-4 AM calcium response (half maximal effective concentration (EC50) 0.36 U/mL). When human coronary artery endothelial cells (HCAECs) were treated with increasing concentrations of DOX (0-100 µM), intracellular calcium released was highest at 10 µM, 30 µM and 100 µM (EC50 4.71 µM) (see Figure 19A). Raw calcium traces are shown in Figure 19B, where 0.3U/mL thrombin and 10 µM DOX was shown to trigger a comparable increase in calcium response. One of the properties of the DOX that make interpretation of fluorescent based assays most challenging is the natural fluorescent properties of the drug. Whilst other studies have implicated DOX in calcium handling (Y. Zhang *et al.*, 2014; Pecoraro *et al.*, 2017), the concentration range where our studies indicated calcium flux, were also those that were identified to result in highest detection in the nucleus in confocal microscopy studies (shown in Figure 19 previously). Experiments were conducted to identify if the calcium signals observed were an artefact of the fluorescent properties of the drug. To do this, increasing concentrations of the drug (0-100 µM) were added to 96 well black plates in the absence of cells. As shown in Figure 19C, fluorescence was detected using cellular calcium dyes with excitation (Ex) / emission (Em) wavelengths of Ex 494/Em (Fluo4-AM) and Ex 540/Em 590 (Cal590). Based on the calcium studies in HCAEC cells (panel A and B) where this relative fluorescent units (RFU) (max-min) signal was ~100 RFU, here this data confirms that the fluorescent responses measured are an artefact of the natural fluorescent properties of the drug being detected in the Ex 494/Em 525 range. The

autofluorescence is even higher in the Ex 540/Em 590 wavelength range, which rules

out the use of Cal590 too.
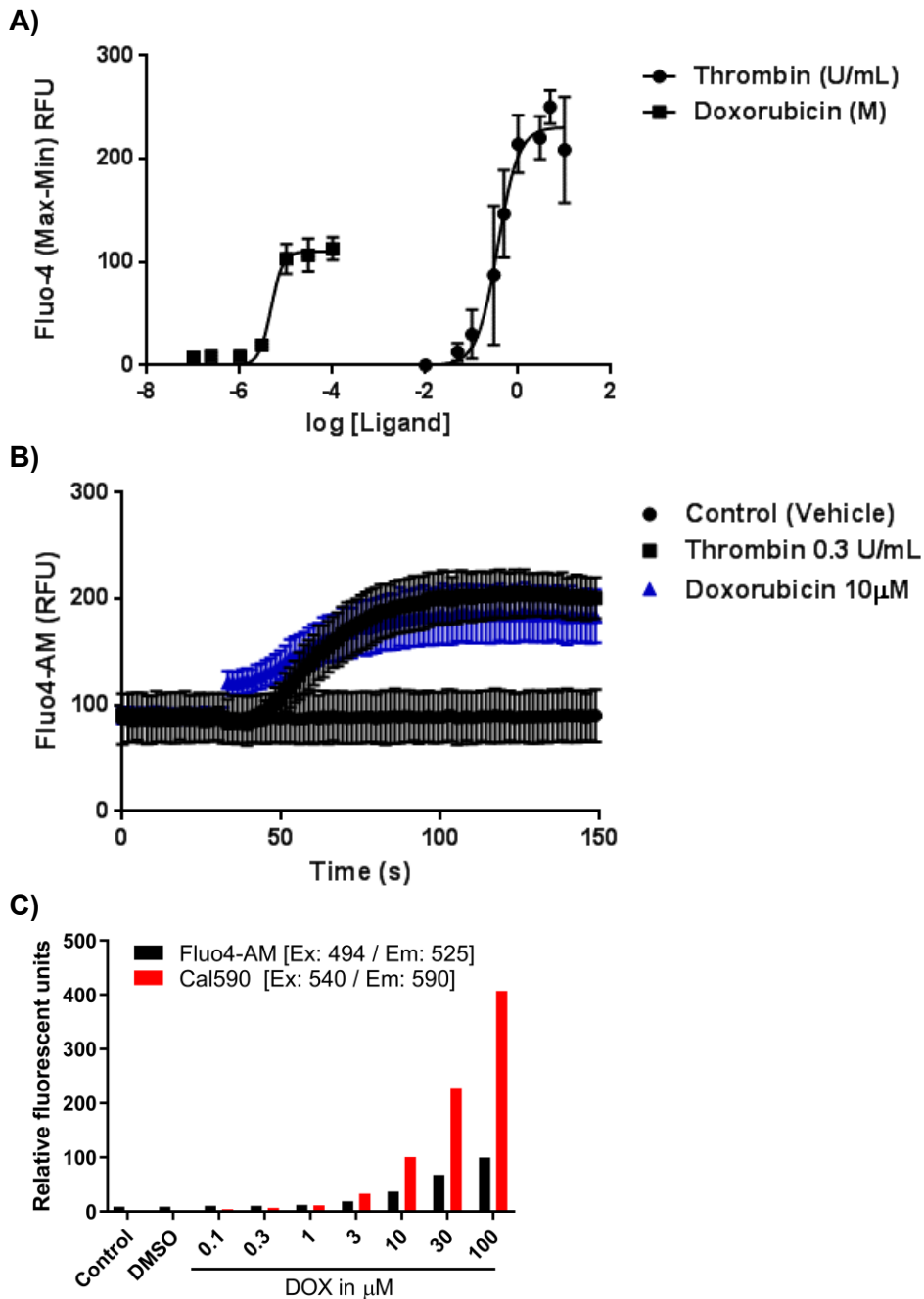
Figure 19 - Calcium response to thrombin and doxorubicin in HCAEC cells.
A) HCAEC cells were treated with thrombin (0-10 U/mL) and DOX (0-100 μM) showing a dose-response curve with a EC50 of 0.36 U/mL and 4.71 μM for thrombin and DOX, respectively. B) Raw calcium traces of thrombin (0.3 U/mL) and DOX (10 μM) show comparable increase in calcium response. C) Fluorescence detection of DOX (0-100 μM) background by using Fluo4-AM (Ex:494 / Em:525) and Cal590 (Ex:540 / Em:590) which increased upon higher concentration. n = 1.

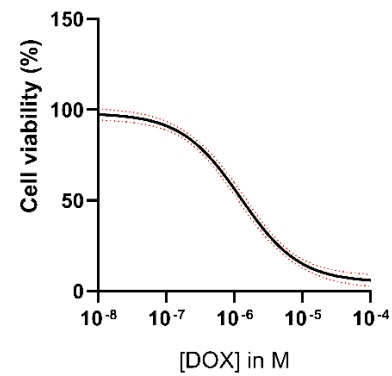## 3.6   Effect of DOX on cell viability and Cx43 expression in HUVECs

The morphology of HUVECs changes in response to DOX. The cobblestone structure of the cells disappears coinciding with a loss of cells (Figure 20A). The loss of cells was thought to be a result of cell death, therefore 3-(4,5-dimethylthiazol-2-yl)-2,5-diphenyl tetrazolium bromide (MTT) and ToxiLight[TM] cytotoxicity assays were conducted. ToxiLight[TM] cytotoxicity assay is based on the release of the enzyme adenylate kinase from the cell in response to toxic agents such as DOX. The activity of adenylate kinase can be measured by a bioluminescent luciferase reaction through the conversion of ADP to ATP (Jacobs *et al.*, 2013; Pabst *et al.*, 2016). Conversely, the MTT assay leverages the enzymatic activity of succinate dehydrogenase (SDH) within the mitochondria, resulting in the transformation of 3-(4,5-dimethylthiazol-2-yl)-2,5-diphenyl tetrazolium bromide (MTT) into purple formazan crystals. The absorbance of the formazan crystals can be measured (Mosmann, 1983; Denizot and Lang, 1986).

The results show a higher sensitivity of the MTT assay as a decrease of cell viability was observed at a lower concentration of DOX. A significant decrease of cell viability was observed at 1.0 µM in comparison to the control group. A dose-response curve resulted in a log half-maximal inhibitory concentration (IC50) of -5.910 ± 0.08 M, equivalent to 1.23 µM (Figure 20B). A dose-response curve with the ToxiLight[TM] assay resulted in a EC50 value of 0.82 µM (0.54-1.24 µM) (Figure 20C). The MTT-assay will be used as standard future cytotoxicity assays due to its higher sensitivity in response to DOX. The mechanism of the ToxiLight[TM] and MTT is illustrated in Figure 20D. Method comparison of both assays, resulted in a squared correlation coefficient (R^2) of 0.6158 with a p-value of <0.0001, indicating that both assays had decreased cell viability at increasing concentrations of DOX (Figure 20E)

D)

E)
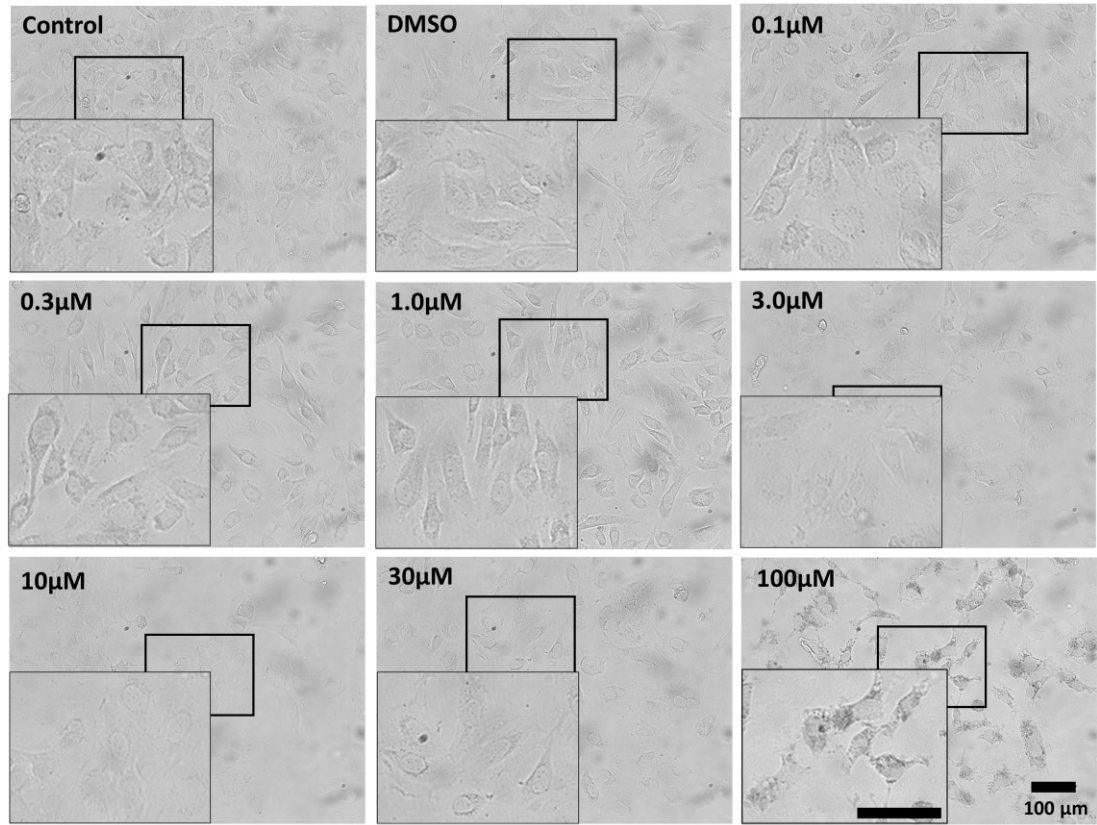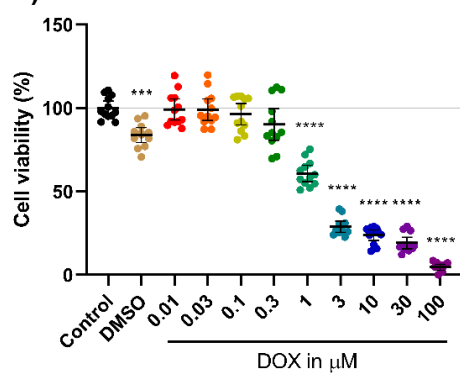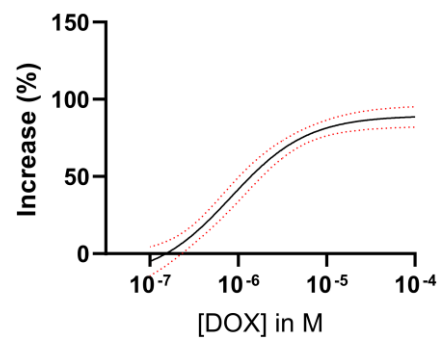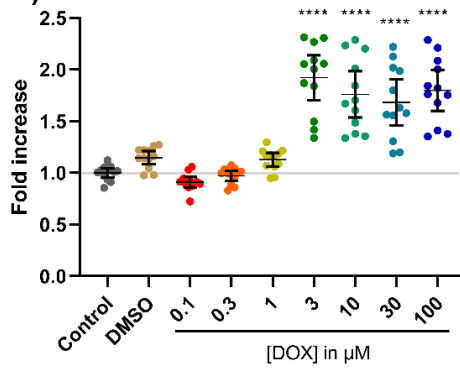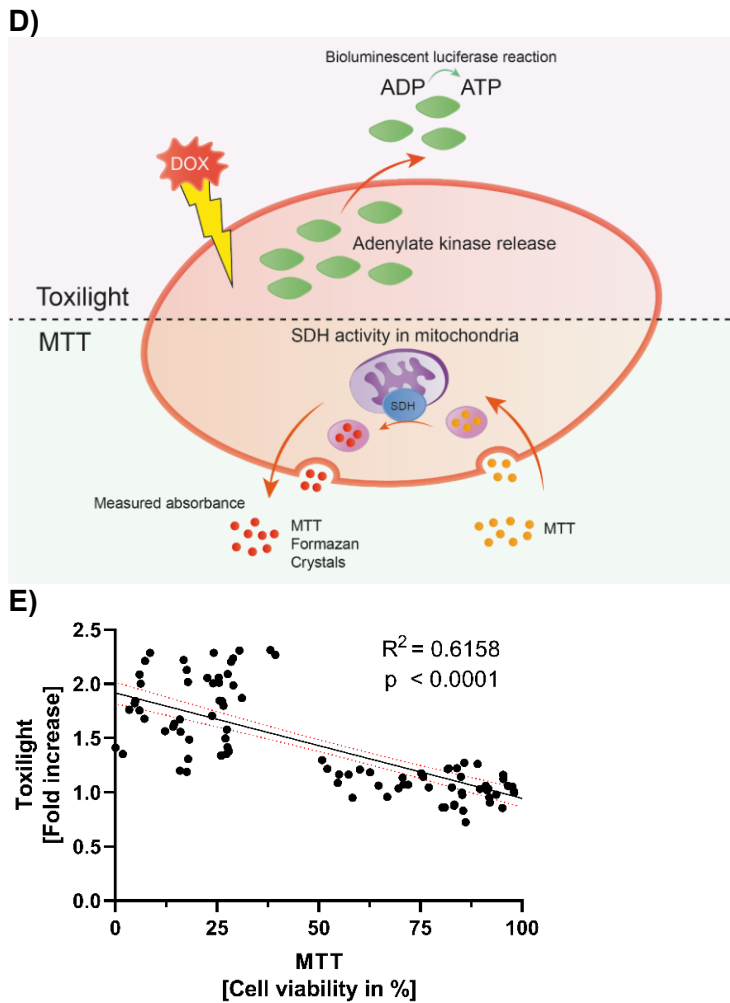
Figure 20 – Effect of DOX on HUVEC cell viability

A) Brightfield images of HUVEC cells treated with DOX (0-100 µM) show a change in cell morphology at concentrations of 1.0 µM and higher, characterized by a decrease in cell volume due to apoptosis. B) MTT assay dot-plot with cell viability (in %) normalised to control and the dose-response curve of the MTT assay resulted in a IC50 value of 1.23 µM (1.01-1.50 µM). C) Toxilight assay dot-plot with values (fold increase) normalised to control and the dose-response curve of the toxilight assay resulted in a EC50 value of 0.82 µM (0.54-1.24 µM). D) Illustrative overview of cell viability assays ToxiLight^{TM} and MTT. E) Linear regression of toxilight (fold increase) and MTT (cell viability in %) assays in HUVECs in response to DOX (0-100 µM). R-square (R2) is 0.6158; p < 0.0001; 95% confidence interval (CI). Four independent assays, conducted in triplicate, were used for analysis. Statistical analysis was conducted by an ordinary one-way ANOVA, Post-hoc Tukey test. Error bars represent the mean ± 95% confidence interval. ****p < 0.0001; ***p < 0.001; ***p < 0.01; *p < 0.05, compared to the control group. n=4, conducted in triplicate.

The cytotoxic effects of DOX have been evaluated in the HUVECs. To determine the effects of DOX on the Cx43 expression, indirect immunofluorescence and Western blotting was performed in DOX treated HUVECs. The nuclear localisation of DOX in the nucleus is observed by immunofluorescent imaging which is shown in Figure 21A. The localisation of Cx43 seems unaltered in response to DOX. However, the total Cx43 protein levels were downregulated with increasing concentrations (Figure 21B). These observational changes have been discovered in the HUVECs and has to be translational to cardiac endothelial cells. Therefore, the experimental design was repeated in the more physiological relevant HCAECs.

DOX has previously been shown to impact the cellular cytoskeleton (Wei *et al.*, 2015). Therefore, no cytoskeletal proteins were used as loading controls for Western blotting. Whereas β-actin and tubulin were inconsistent in animal models of myocardial ischemic infarction, was GAPDH shown to be an appropriate marker (Nie *et al.*, 2017). GAPDH is a glycolytic enzyme which plays a role in energy metabolism, cell proliferation, tumorigenesis, and is constitutively expressed (Nicholls, Li and Liu, 2012). For this reason, GAPDH was chosen as the designated loading control.

A)
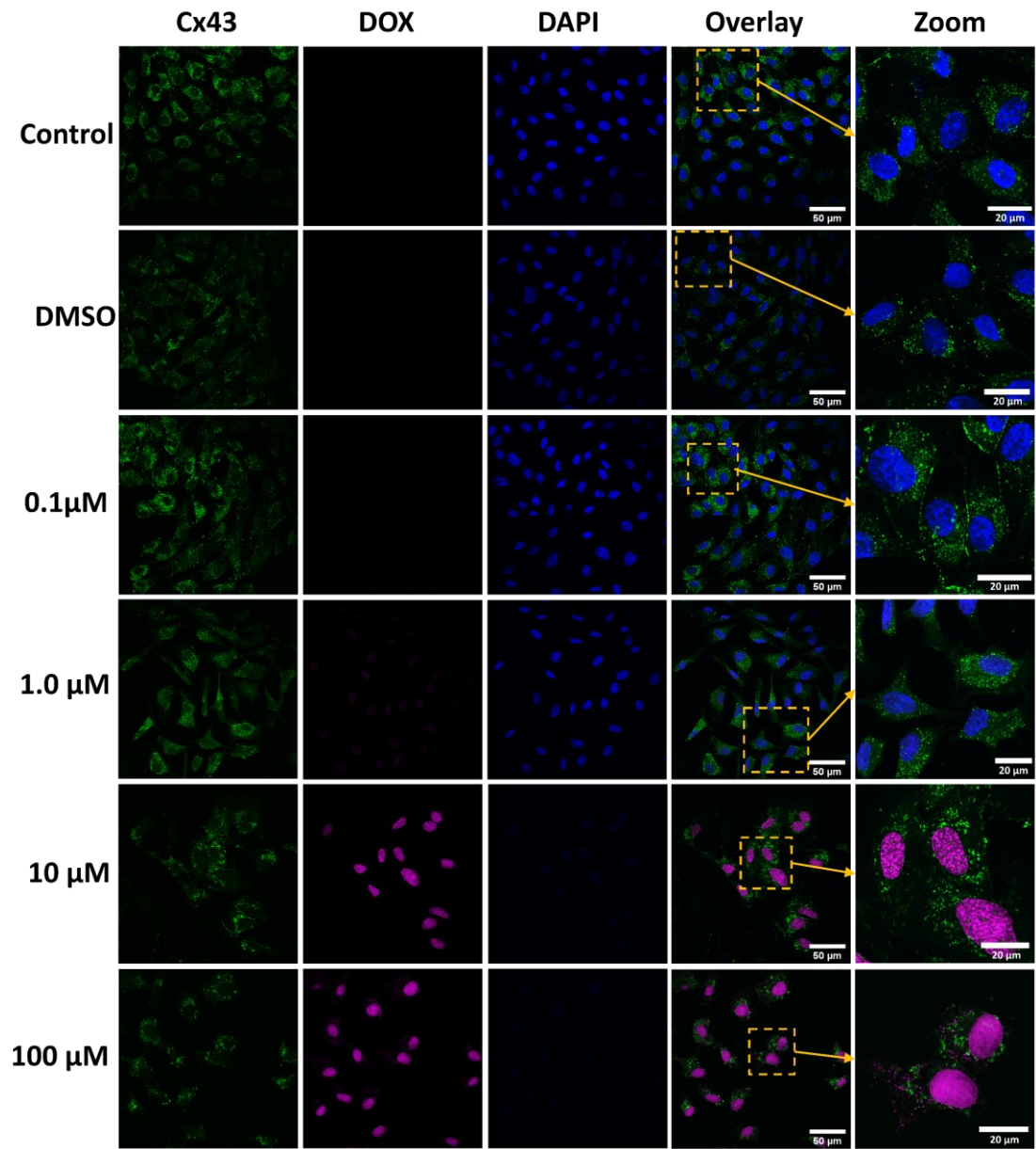
B)
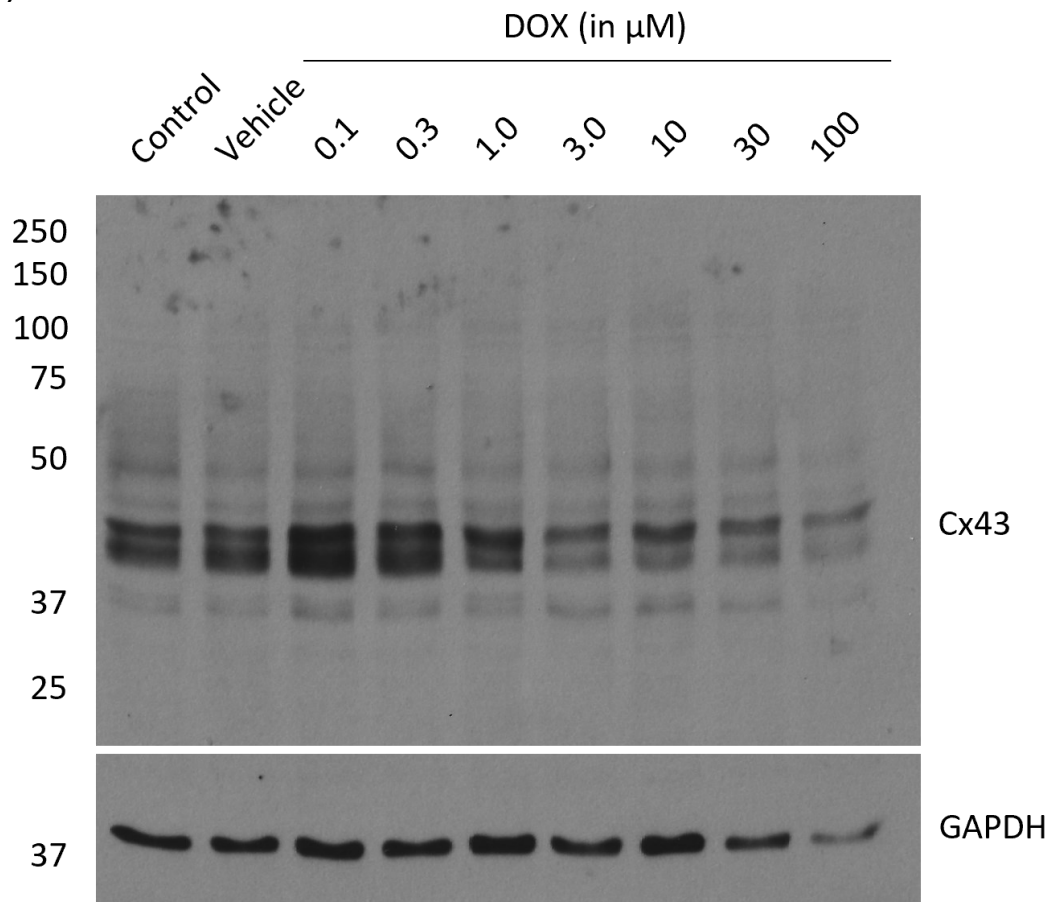
Figure 21 - Effect of DOX on Cx43 expression localisation

A) Indirect immunofluorescent imaging shows Cx43 expression (green) in response to DOX and show no changes in localisation. B) Total Cx43 protein expression by Western blotting and show a decrease in response to DOX. GAPDH was used as loading control. n = 1.

3.7   Characterisation of human coronary artery endothelial cells

The HUVECs are non-cardiovascular endothelial cells. To determine the effects on endothelial cells with a cardiac origin, HCAECs were selected. HCAECs are isolated cells from the coronary artery from single donors and have previously been used to study Cx43 (Zhang *et al.*, 2016; Smit *et al.*, 2018). HCAECs are proliferative endothelial cells with a "cobblestone phenotype" on the surface, typical for endothelial cells in 2D cell culture (Figure 22A). The tissue culture of HCAECs at higher passages resulted in a change of cellular phenotype (Figure 22B).
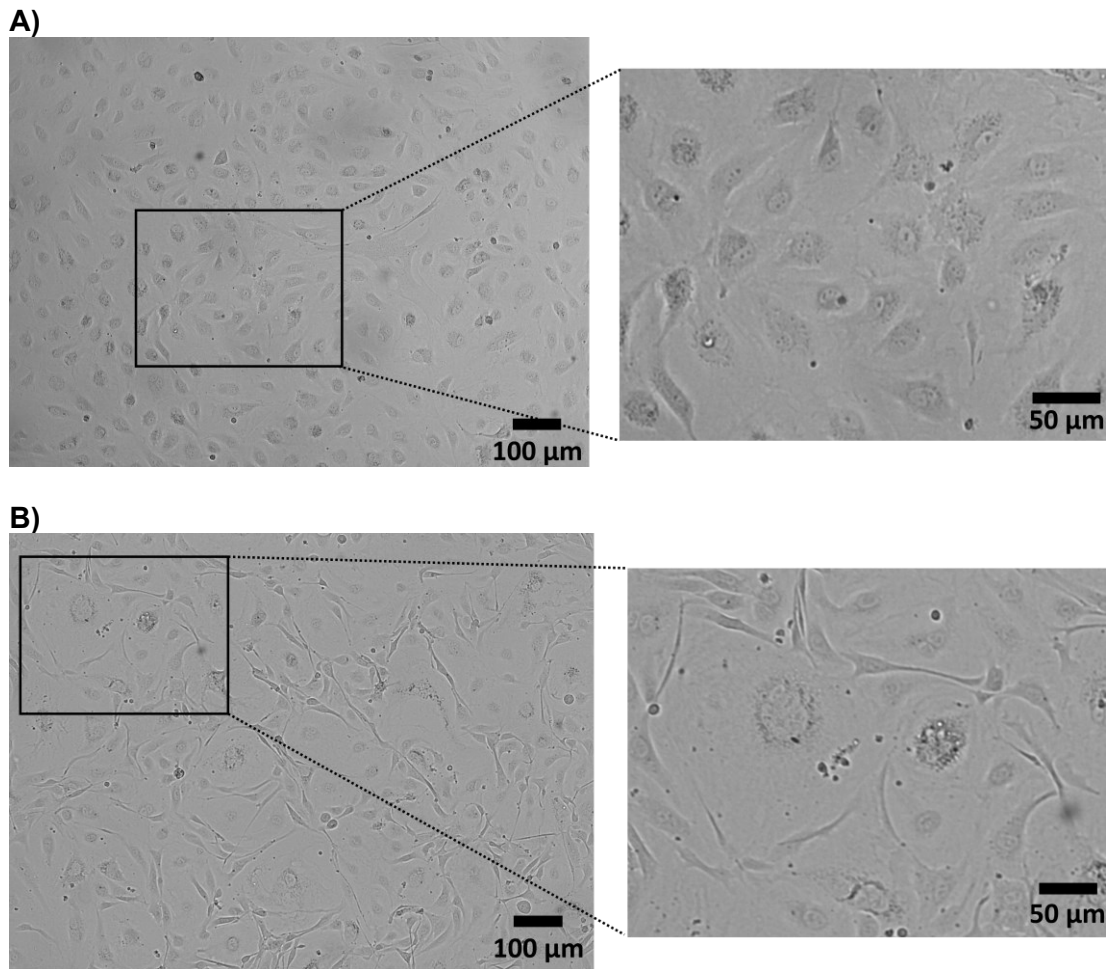
Figure 22 - Phenotype of HCAECs in tissue culture.

Brightfield images were acquired to assess the morphology of HCAEC cells in culture. **A)** HCAECs at low passage number had a cobblestone-like shape. **B)** At higher passages, the cells had a decreased growth rate and larger non-endothelial looking cells appeared within culture. Scalebars are 100 μm and 50 μm for zoomed in areas.

To determine the presence of other cell types in the HCAEC primary culture a screening with vWF, vimentin, α-SMC was conducted by using immunohistochemistry and confocal/EVOS microscopic techniques. All cells were identified with vimentin expression, and most cells expressed vWF (Figure 23A). No cells were stained positive for α-SMC, indicating that no smooth muscle cells or myofibroblasts were present (Figure 23B). The same samples were used to conduct EVOS microscopy in order to optimise the pace and reduce the costs to quantify the number of positive stained cells for each marker (Figure 23C). The same markers were used with the characterisation of HUVECs described in section 3.3. Initially, the quantified data obtained through confocal microscopy was compared to that acquired using the EVOS microscope method, and no statistically significant difference was observed (Figure 23D). The quantified data revealed a 100% expression of vimentin, 72% vWF, and 0% α-SMC within the HCAEC culture (Figure 23E).

A)

vWF | Vimentin

vWF + / Vimentin +

DAPI | Overlay

vWF - / Vimentin +

100 µm | 25 µm

B)

α-SMC | vWF

DAPI | Overlay

vWF + / α-SMC -

100 µm | 25 µm
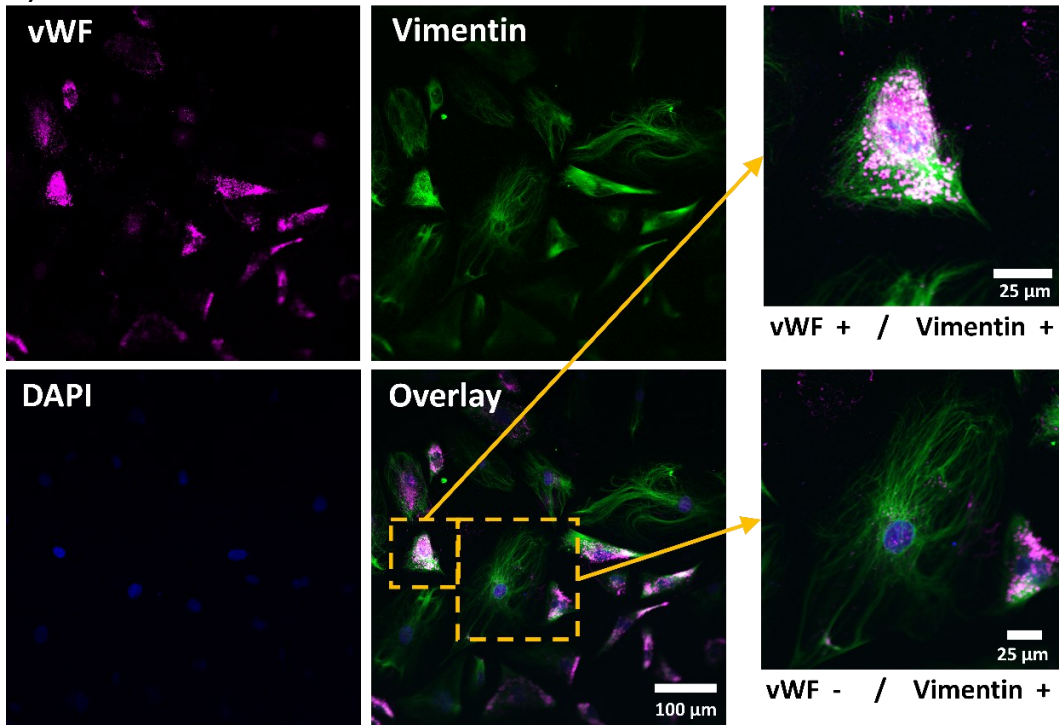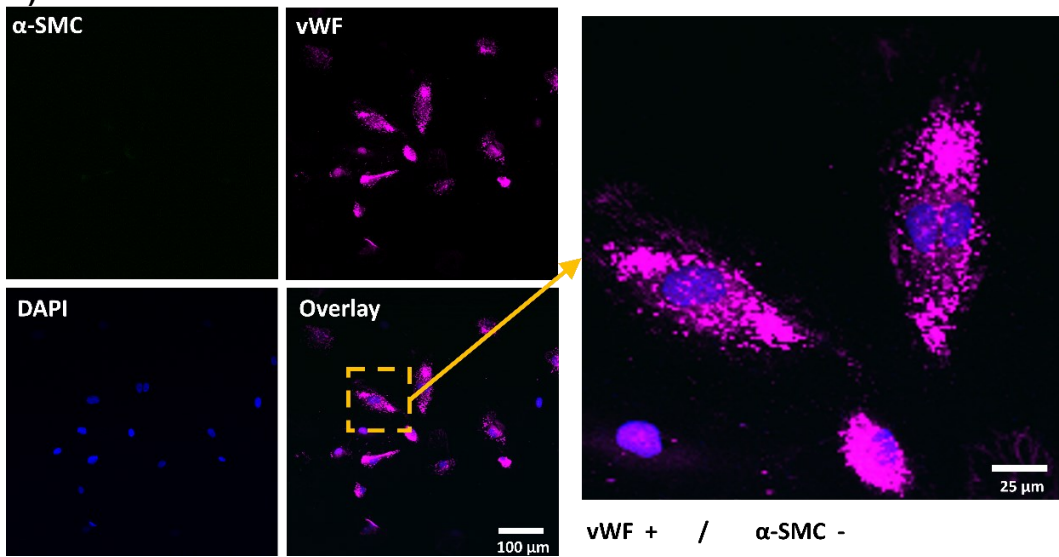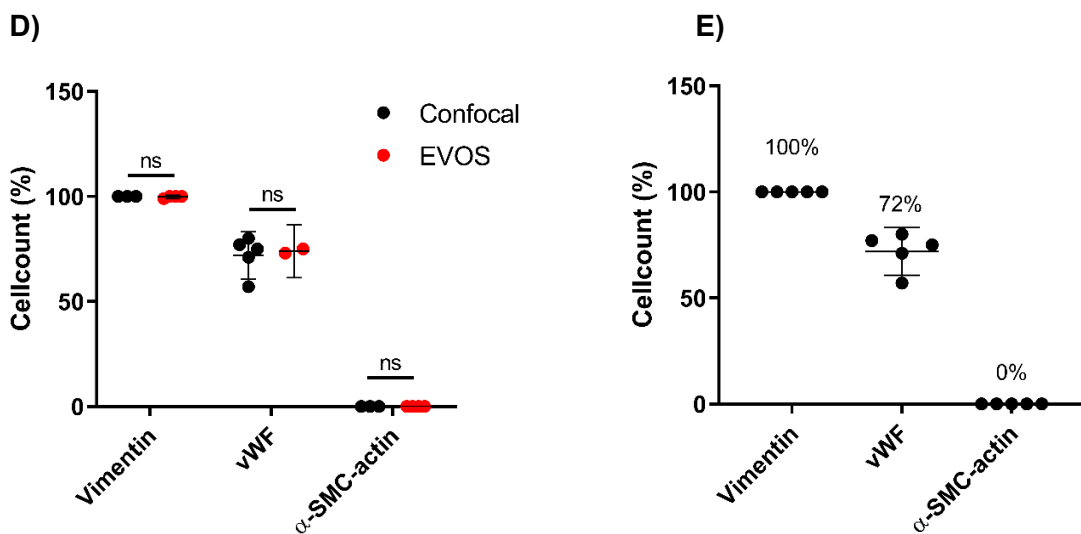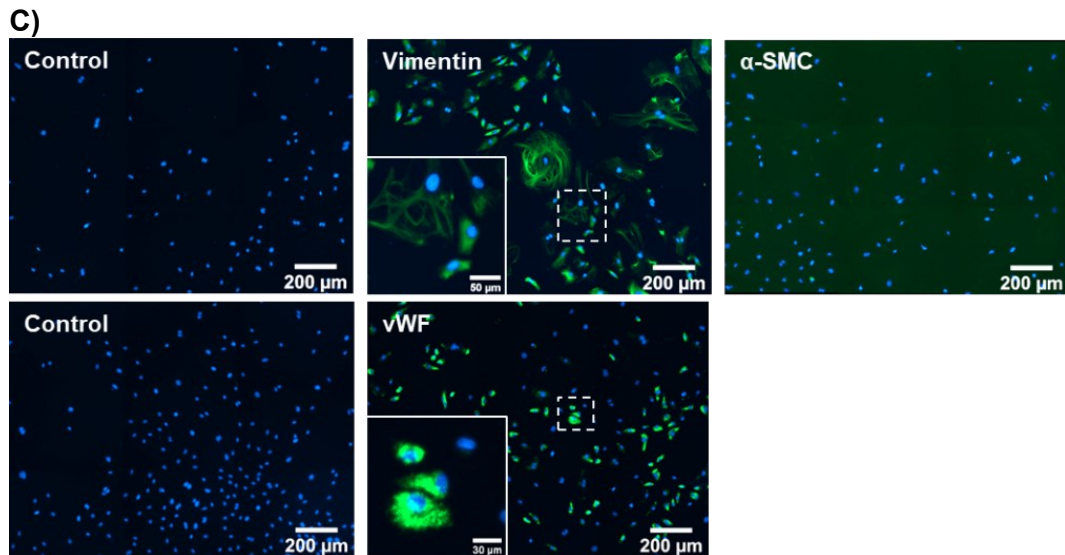
Figure 23 - Indirect immunofluorescent imaging of vWF, vimentin and α-SMC.
A) Confocal microscopic immunofluorescent images show consistent vimentin expression (green), regular vWF expression (magenta), however, no α-SMC was observed (B). Scalebar is 100 μm and 25 μm for zoomed in areas. C) EVOS images show vWF, vimentin, and no α-SMC expression. D) Method comparison between confocal and EVOS showed no significance different (ns) by a student's t-test. Scalebar is 200 μm and 30 μm for zoomed in areas. E) Quantitative analysis indicates 72% ± 3% vWF, 100% vimentin, and no α-SMC expression. Cell count was normalised against cell number (132 cells average). Error bars represent the mean ± 95% confidence interval (n=5).

The phenotype of the HCAECs were altered in response to DOX. The "cobblestone structure" of the cells was affected in response to DOX as well as a loss of cells (Figure 24A). The toxic effect of DOX on the HCAECs was determined with a MTT-assay. A significant decrease of cell viability was observed at 1.0 µM DOX in comparison to the control group (Figure 24B). An IC50 value of -6.264 ± 0.107 M, equivalent to 0.54 µM was obtained (Figure 24C).

A)

Control

DMSO

0.1µM

1.0µM

10µM
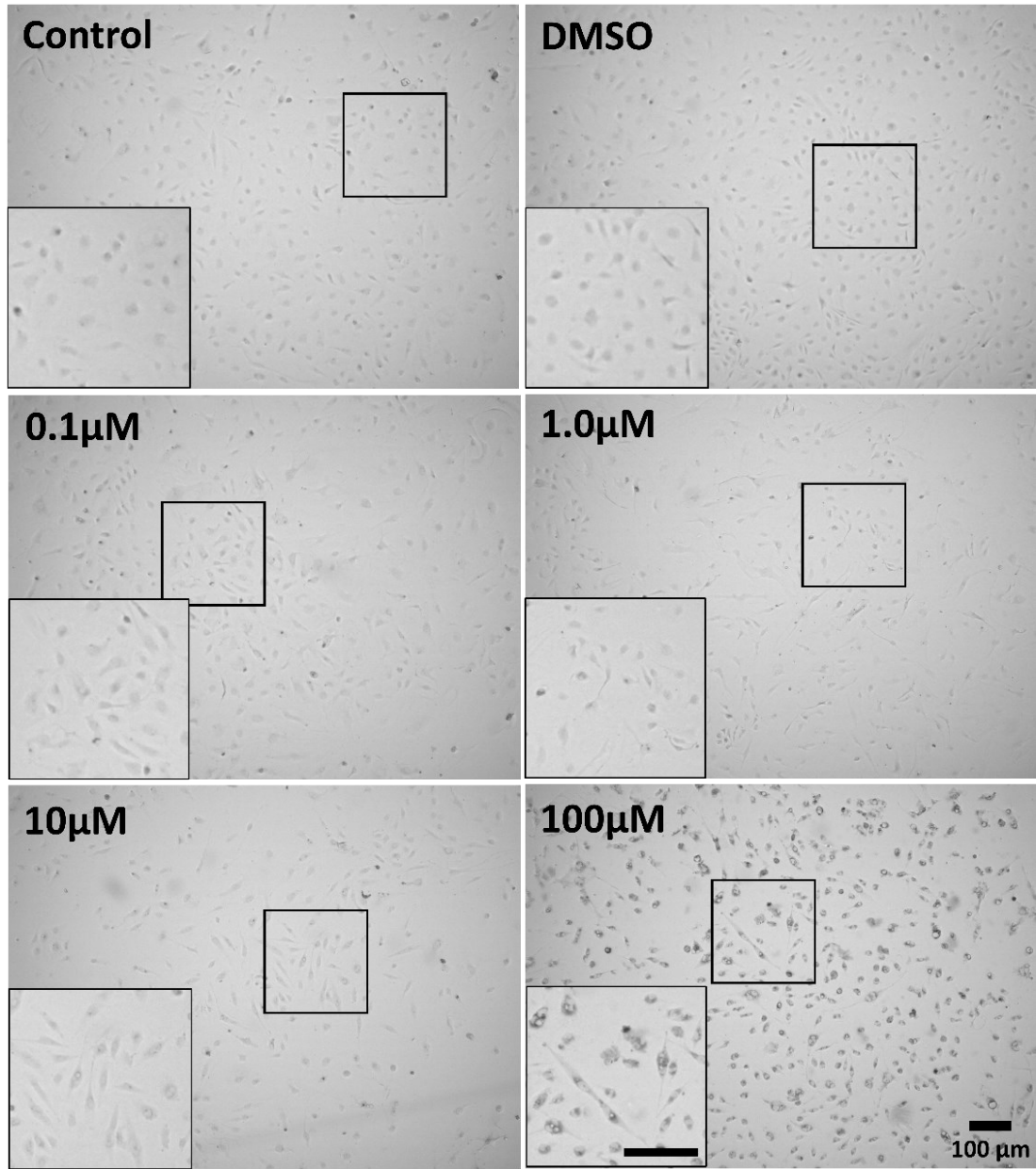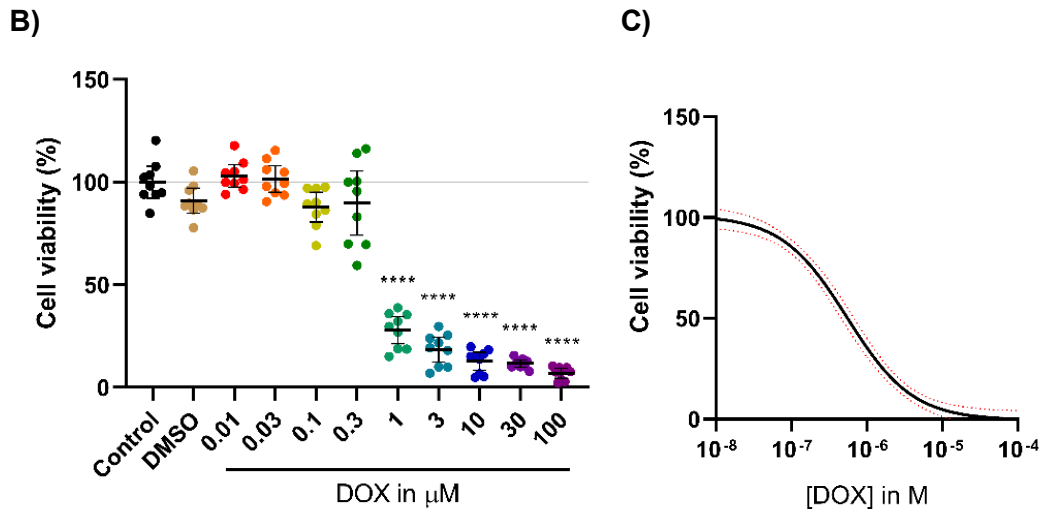
100µM

100 µm

Figure 24 - DOX decreases cell viability in HCAECs

A) Brightfield images of HCAEC cells treated with DOX (0-100 µM). B) MTT assay dot-plot with cell viability (in %) normalised to control. C) Dose-response curve of the MTT assay resulted in a log IC50 of -6.264 ± 0.107. Statistical analysis was conducted by an ordinary one-way ANOVA, Post-hoc Tukey test. Error bars represent the mean ± 95% confidence interval. ****p < 0.0001, compared to the control group. n=3, conducted in triplicate.

Following brightfield imaging and cell viability assays, the DOX-treated HCAECs were also used for fluorescent imaging, similar to the HUVEC characterisation in described in section 3.4. The cells were additionally stained with fluorescein phalloidin which is similar to rhodamine phalloidin and has a strong affinity to F-actin, but green instead of red to see the structure of the cells simultaneously. The confocal imaging revealed a nuclear accumulation of DOX which is a similar finding with the DOX treated HUVECs (Figure 25A). The yellow-coloured line scan shows the intensity of each pixel of the blue and red channel across the line. At concentrations of 1.0 µM and higher show overlap of the blue and red channel, confirming the presence of DOX in the nucleus. Quantifications of the nuclear area shows an increase at 0.1 µM DOX and becomes significant at >1.0 µM in comparison to the control group ($p < 0.0001$, Figure 25B).
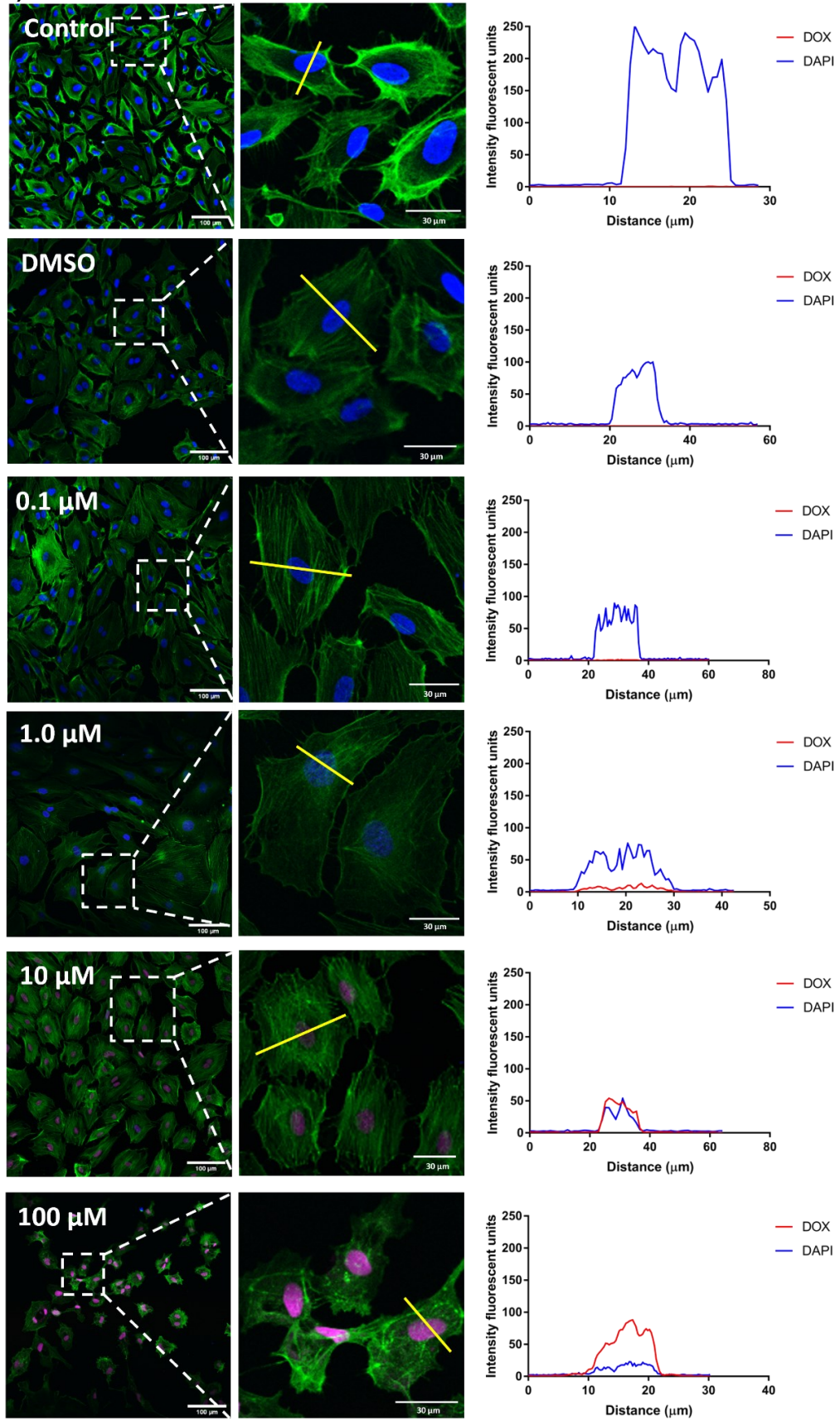
B)
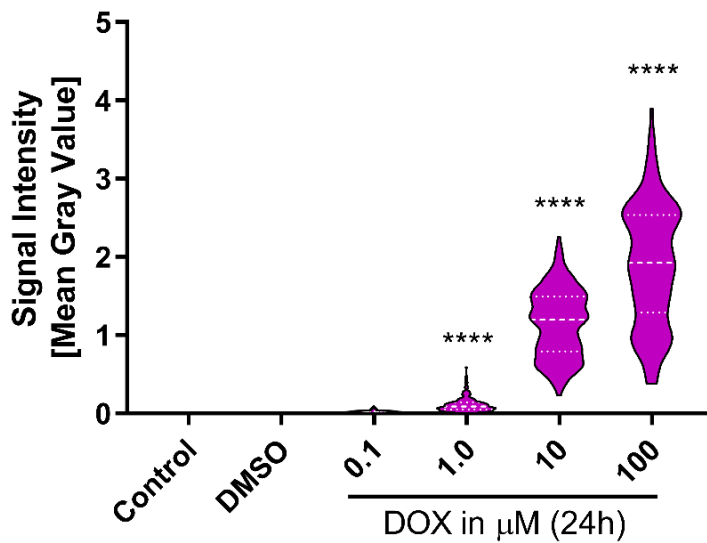
Figure 25 - Nuclear accumulation of DOX in HCAECs.

A) Immunofluorescent images of HCAECs treated with DOX (0-100 μM). F-actin was stained with fluorescein green (green), and the nucleus was counterstained with DAPI (blue). The auto fluorescent properties of DOX were shown in magenta. A line scan (yellow line) measured the pixel intensity of the blue and magenta and shows increasing DOX fluorescent signals in the nuclear area. B) Quantified signal intensity as the mean grey value of DAPI and DOX in the nuclear region in response to DOX. Data is presented in a violin plot. ****p < 0.0001, compared to the control group. n=4, each n-number represents 40 individual cells.

Indirect immunofluorescent imaging was performed to determine the presence and cellular localisation of Cx43 in HCAECs. The expression of Cx43 is detected by using a specific Cx43 antibody (C6219) directed to the C-terminal domain and shows majorly membranous expression in the form of punctae, indicating clustering of Cx43 to support gap junction formation (Figure 26A). The observed localisation of Cx43 expression is supported by previous studies that were conducted by using this antibody (Singh *et al.*, 2005; Press *et al.*, 2017; Kotini *et al.*, 2018). Furthermore, F-actin staining reveals intercellular structures between adjacent cells with expression of Cx43. This could be referring to tunnelling tubes which are known to facilitate crosstalk between adjacent cells (Wang *et al.*, 2010). Moreover, Cx43 expression was also observed at the perinuclear region of the HCAECs.

Next to the nuclear accumulation of DOX, Cx43 was characterised to have altered localisation within the HCAECs (Figure 26B). The localisation of Cx43 appears to be increased at the plasma membrane at 10 µM and more internalised at 100 µM in intracellular vesicles. After examining relocalisation the total protein levels measured of Cx43 in response to DOX were assessed. A significant reduction of total Cx43 levels were identified in response to >1.0 µM DOX in comparison to the control group ($p < 0.05$, Figure 26C-D).

C)

[DOX] in µM

Control DMSO 0.1 1.0 10 100

250
150
100
75
50
37 — Cx43
25

50 — GADPH

D)

Relative density [Cx43 / GAPDH]

DOX in µM (24h)
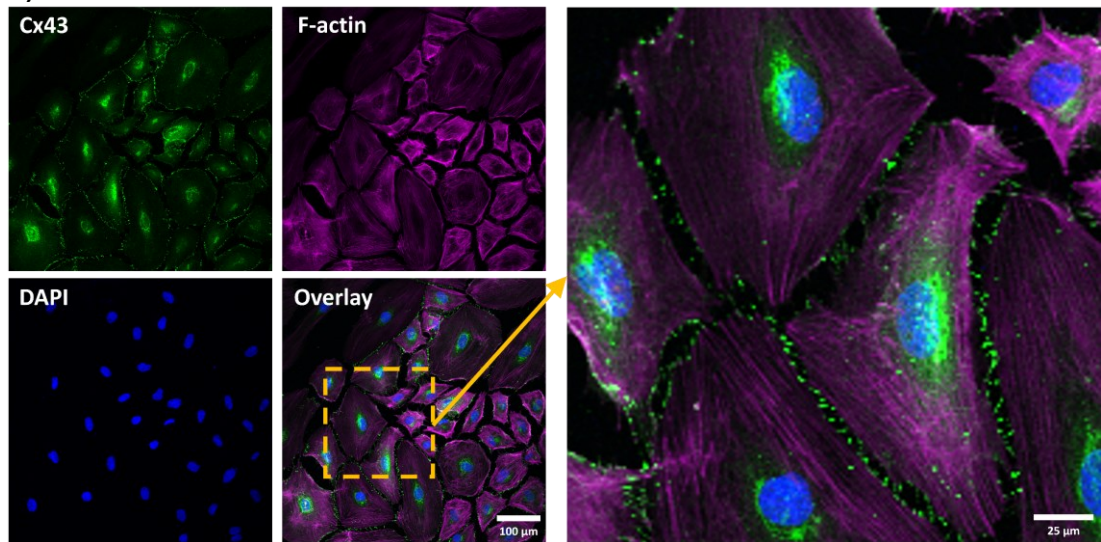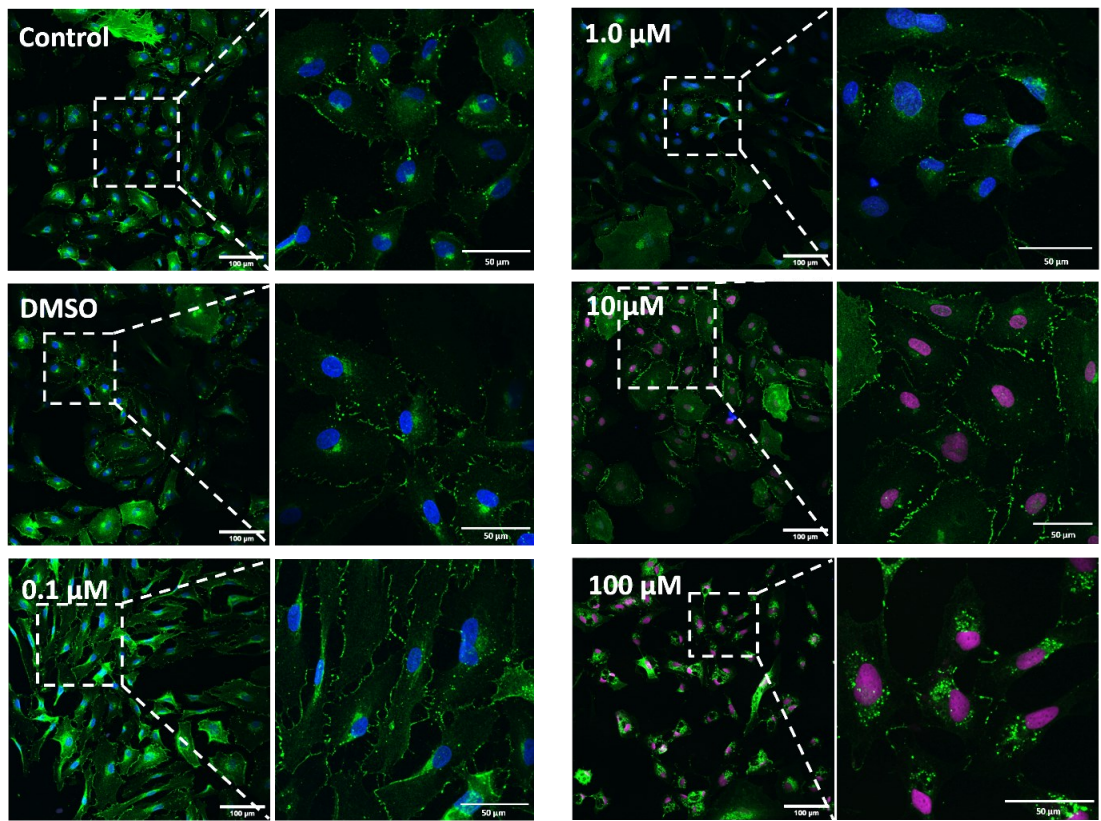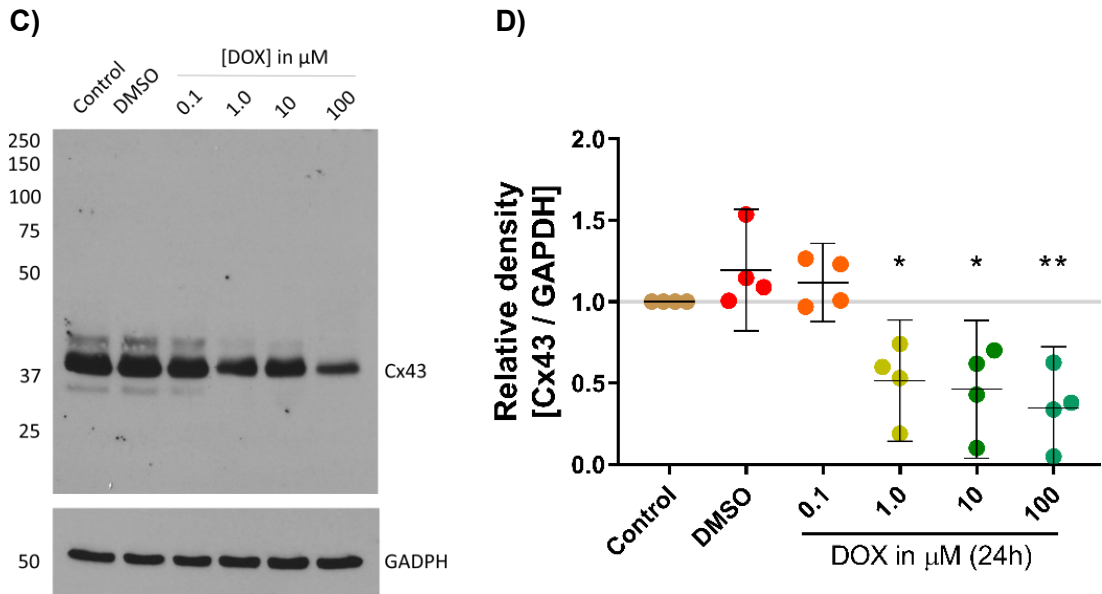
Figure 26 - Reduction of Cx43 and re-localisation in HCAECs by DOX.

A) *Indirect immunofluorescence staining of Cx43 (green) with a rhodamine phalloidin stain for F-actin (magenta) and a DAPI nuclear counterstain (blue) in HCAECs (n=3). Cx43 is majorly localised at the perinuclear region as well as the plasma membrane to form gap junctions with adherent cells.* ***B)*** *HCAECs treated with DOX (0-100 µM for 24h) show a re-localisation of Cx43.* ***C)*** *Western blot for Cx43 and GAPDH of DOX treated HCAECs resulting a reduction of total protein expression.* ***D)*** *Relative density (Cx43 / GAPDH) plot shows a significant reduction of total Cx43 protein levels. Statistical analysis was conducted by an ordinary one-way ANOVA, Post-hoc Tukey test. *p < 0.05; **p < 0.01, compared to the control group. n=4, error bars represent the mean ± 95% confidence interval.*

3.8 Characterisation of primary human cardiac fibroblast cells

Next to the cardiac myocytes and endothelial cells, another cell type which is present within the cardiac tissue is the mesenchymal originated fibroblast. Primary cardiac fibroblasts isolated from the ventricles of the human heart (hCFs) were used during this project. The morphology of cardiac fibroblasts was characterised by a flat, elongated, and spindle-shaped structure (Figure 27A). Once the cell culture reached a confluent monolayer, the cells started to change into long stretched shape (Figure 27B). The cardiac fibroblasts play a protective and reparative role in the response upon cardiac infarction through pro-inflammatory responses and the production of extracellular matrix (ECM). During cardiac injury, fibroblasts can undergo transformation into a myofibroblast phenotype. The transformation of fibroblasts into myofibroblasts can be stimulated by the transforming growth factor beta (TGF-β) cytokine which plays an important role in immunologic responses, angiogenesis, and wound healing (Petrov, Fagard and Lijnen, 2002). Myofibroblasts are a larger phenotype in comparison to cardiac fibroblasts (Figure 27C).
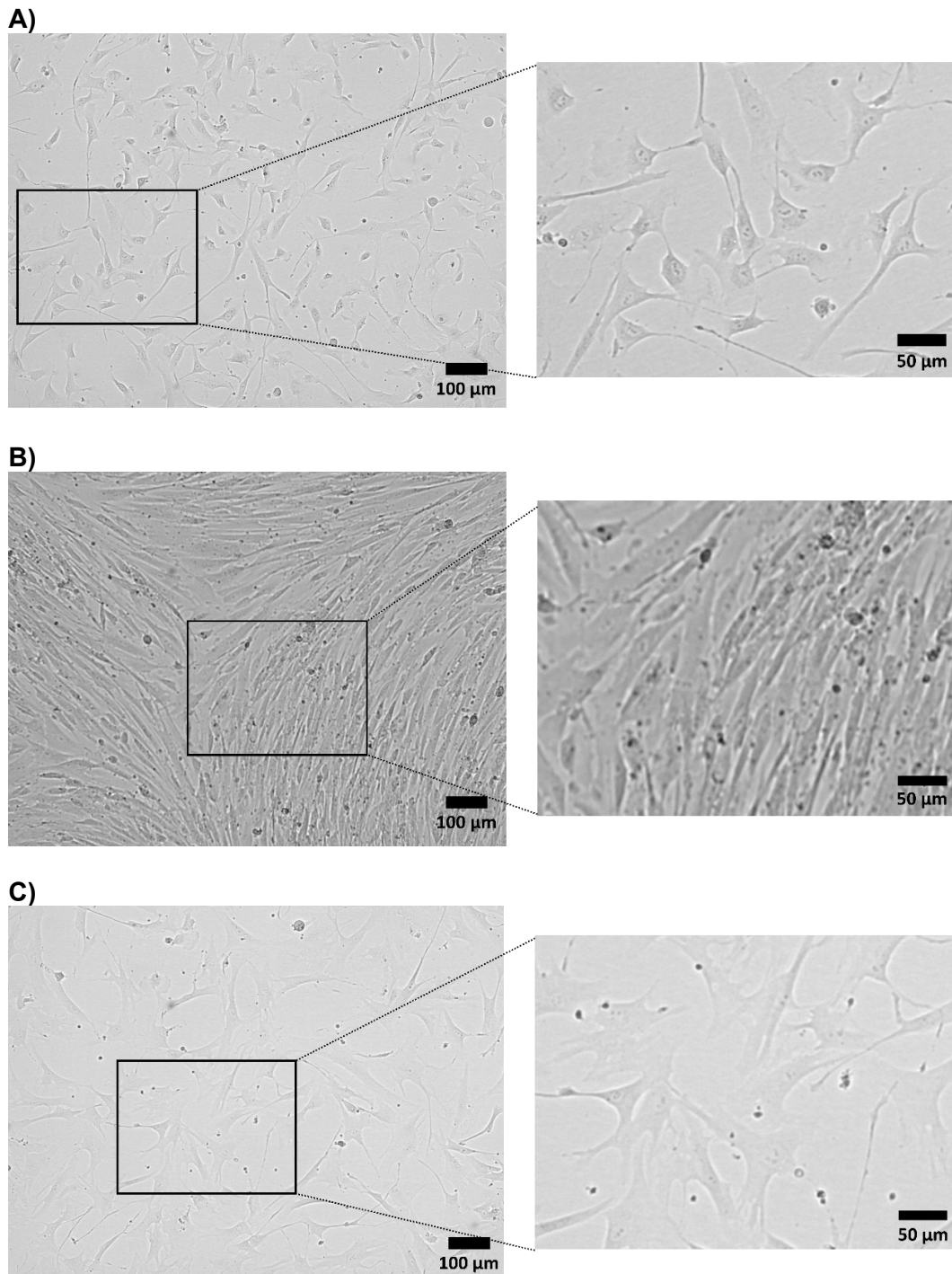
Figure 27 - Morphological changes of hCFs in culture.

A) Brightfield images of hCFs in culture show a spindle-shaped structure. B) The morphology of the cells changes at 100% confluence into long-elongated cells and loses its spindle-shaped structure. C) Cultured hCFs at low confluence resulted in a transformation into a myofibroblast phenotype. Scalebar is 100 μm for original sized images and 50 μm for zoomed areas.

To rule out the presence of endothelial, smooth muscle cells, and to identify the phenotype of the human cardiac fibroblasts (hCFs) the cells were used for immunohistochemistry experiments. The cells were stained for the endothelial marker vWF, smooth muscle cell and myofibroblast marker α-SMC actin. As expected, there were no typical WPB with vWF expression observed within the cell population, confirming the absence of endothelial cells (Figure 28A). Normally hCFs express no α-SMC actin proteins, but conversely, the transformed fibroblast phenotype myofibroblasts do express α-SMC actin (Sousa *et al.*, 2007). No α-SMC actin expression was observed in the hCF population (Figure 28A). As shown in Figure 27C, hCFs were stressed to induce transformation into the myofibroblast phenotype. Unlike hCFs, the myofibroblasts were characterised with α-SMC actin expression in fibre-like structures and thereby support its phenotype (Figure 28B). Vimentin, a well-known fibroblast marker was identified in all cells within the cell population (Figure 28C). The subcellular localisation of Cx43 in hCFs was localised as hemichannels at the plasma membrane at a few places but is mainly expressed throughout the cell (Figure 28D).

Lysates of different hCF passages and the transformed myofibroblasts were evaluated by SDS-PAGE and Western blotting to assess the total Cx43 and vimentin expression (Figure 28E). The Cx43 expression band pattern indicates a change between the hCFs and myofibroblasts as a band appeared with an approximate size of 70 kilo Dalton (kDa). Vimentin levels were also identified with bands at approximate 50kDa.

.

D)

Cx43 | F-actin
DAPI | Overlay
100 µm
25 µm

E)

Passage number

| 3 | 4 | 5 | 6 | 7 | 8 | 9 | 10 | TF |

100
75
50
37

Cx43

100
75
50
37

Vimentin

37

GAPDH
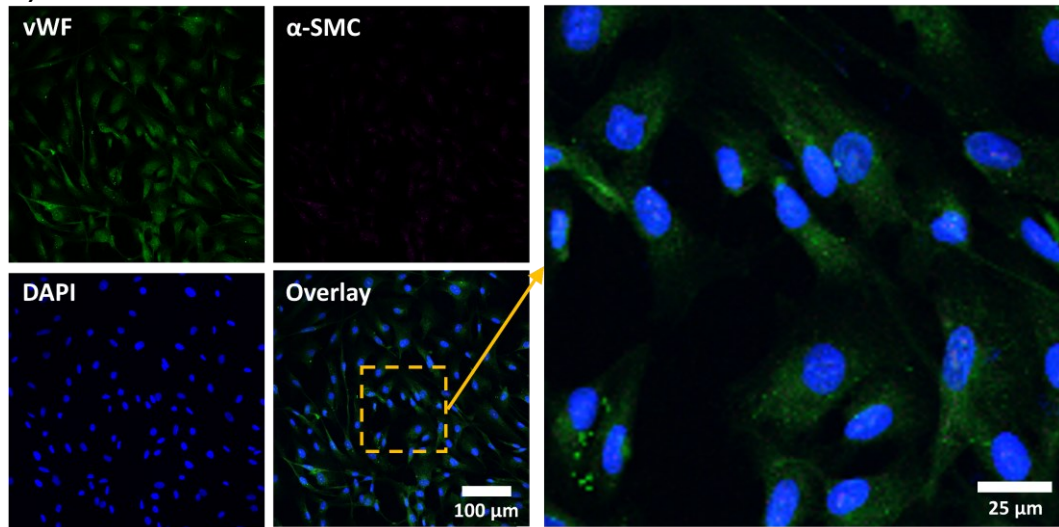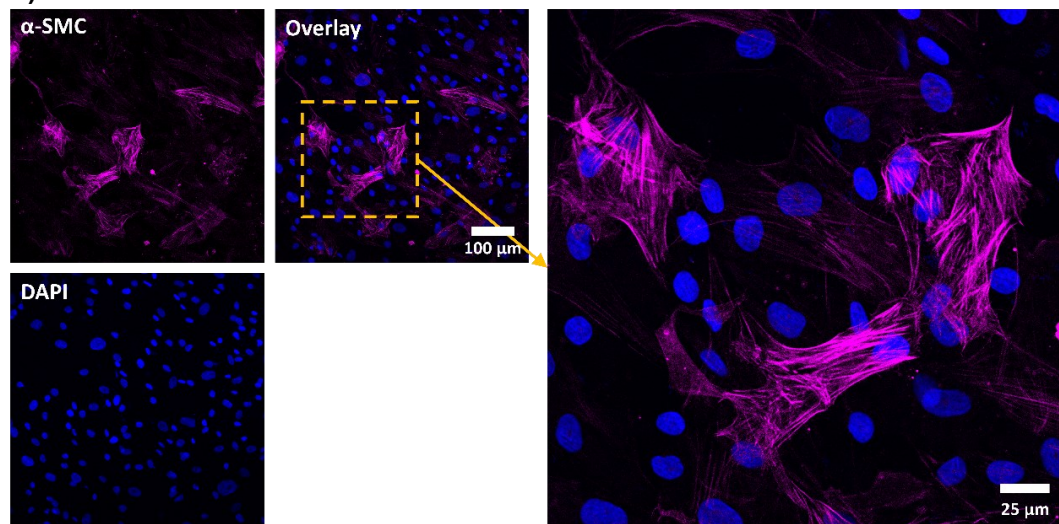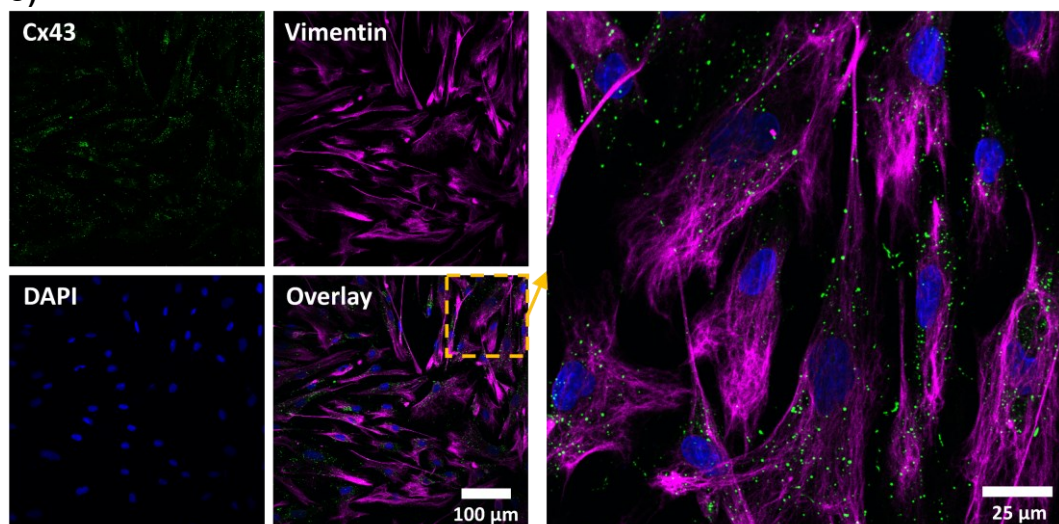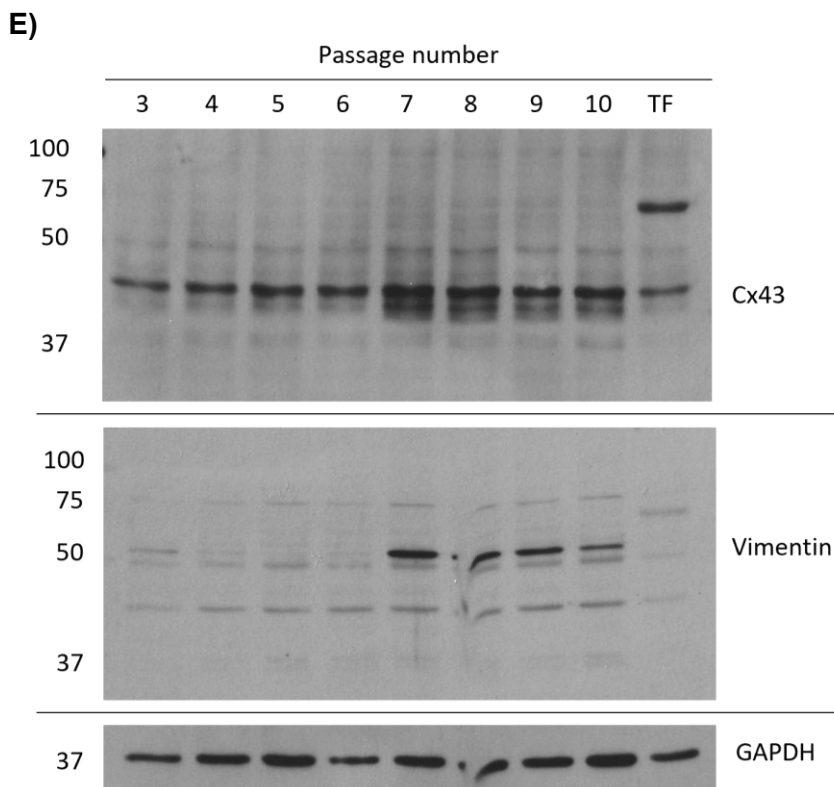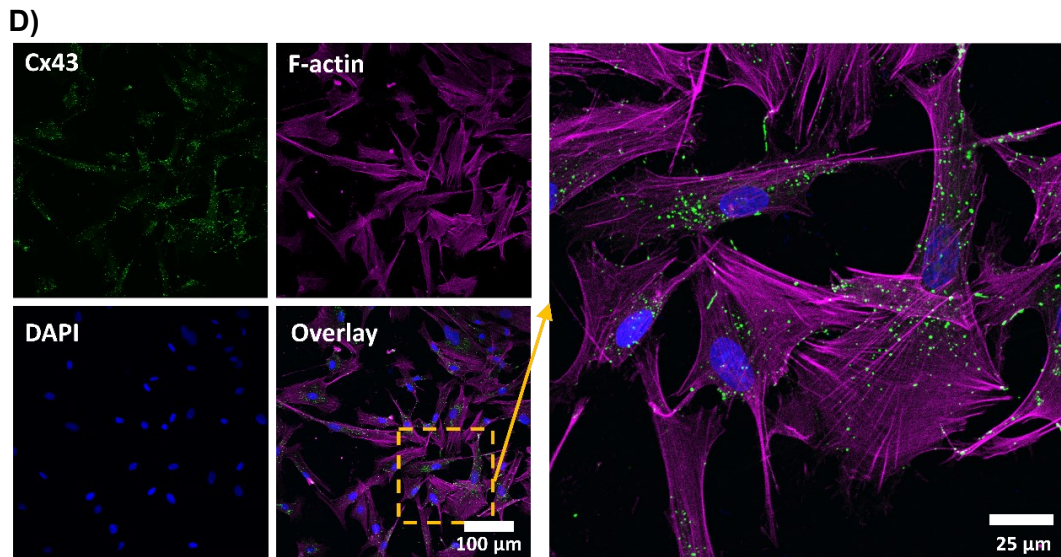
Figure 28 - Characterisation of hCF cells

A) *No typical vWF and α-SMC actin expression was observed in hCFs.* ***B)*** *Myofibroblasts show positive staining for α-SMC actin.* ***C)*** *The fibroblast marker vimentin is present in all cells within the population.* ***D)*** *Cx43 expression was identified and localised throughout the cells.* ***E)*** *Western blots showing total Cx43 and Vimentin levels of different passages (3-10) and the transformed (TF) myofibroblasts with GAPDH as reference protein.*

After the characterisation of the phenotype of the hCFs the cells were treated with DOX. The morphology of the cells was assessed upon treatments and showed no significant shape change, but a loss of cells was observed in response to DOX (Figure 29A). The observation of a loss of cells was followed up by cell viability assays to identify the toxic effect of DOX on the hCFs. A significant reduction of cell viability was identified at 0.1 µM DOX in comparison to the control ($p < 0.001$, Figure 29B). A dose-response curve was generated and resulted in an IC50 log value of -6.427 (± 0.167), equivalent to 0.37 µM DOX (Figure 29C). The high sensitivity of hCFs to DMSO and DOX might be attributed to their role within the cardiovascular system, where they exhibit rapid responses to stress.
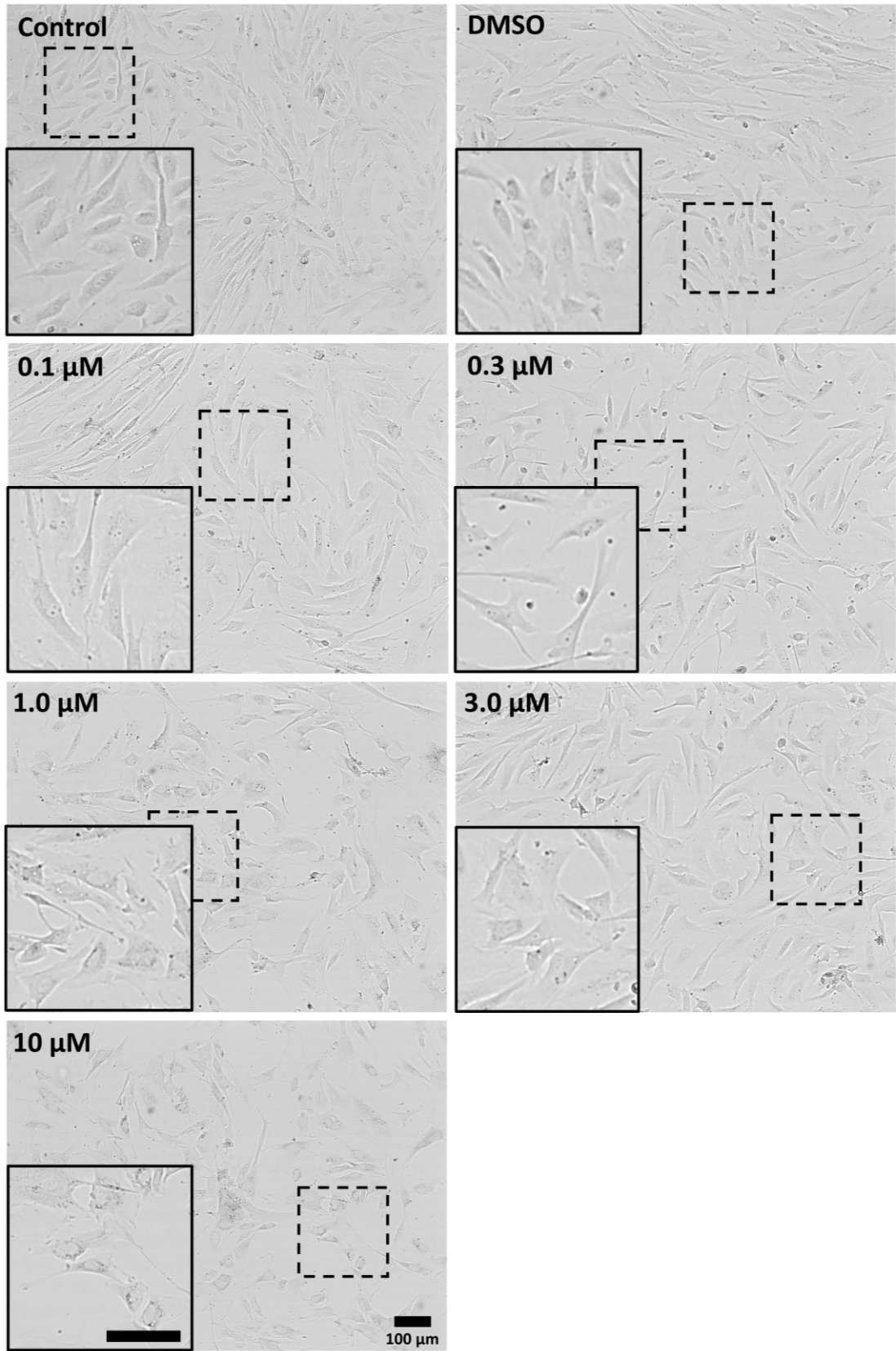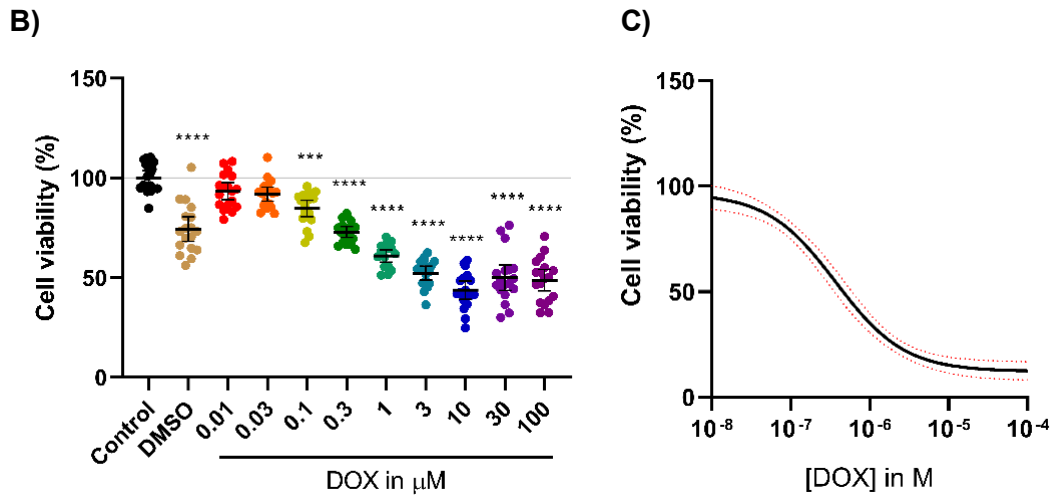
Figure 29 - Effect of DOX on hCF morphology and cell viability

*A) Brightfield images show the morphology of the hCFs in response to DOX. **B)** MTT assay dot-plot with cell viability (in %) normalised to control. **C)** Dose-response curve of the MTT assay resulted in a log IC50 of -6.427 ± 0.167. Statistical analysis was conducted by an ordinary one-way ANOVA, Post-hoc Tukey test. Error bars represent the mean ± 95% confidence interval. ****p < 0.0001; ***p < 0.001; compared to the control group. n=4, conducted in triplicate.*

After the determination of the cell viability the research was followed up to identify the effects of DOX on the Cx43 expression in the hCFs. Similar results were obtained in comparison to the HCAECs as a reduction in the total Cx43 protein levels was revealed in response to DOX (Figure 30A). Quantification of the band intensities of Cx43 and normalisation with the reference protein GAPDH, resulted in a decreased signal at 1.0 µM (Figure 30B).

To measure the effect on Cx43 localisation in hCFs DOX treated cells were stained for Cx43 (Figure 30C). In the hCFs DOX was visualised within the nucleus at concentrations of 1.0 µM and higher. As well as the nuclear accumulation of DOX, changes in Cx43 localisation were observed, particularly at 3.0 µM DOX were an increased Cx43 localisation at the plasma membrane was observed between neighbouring cells.
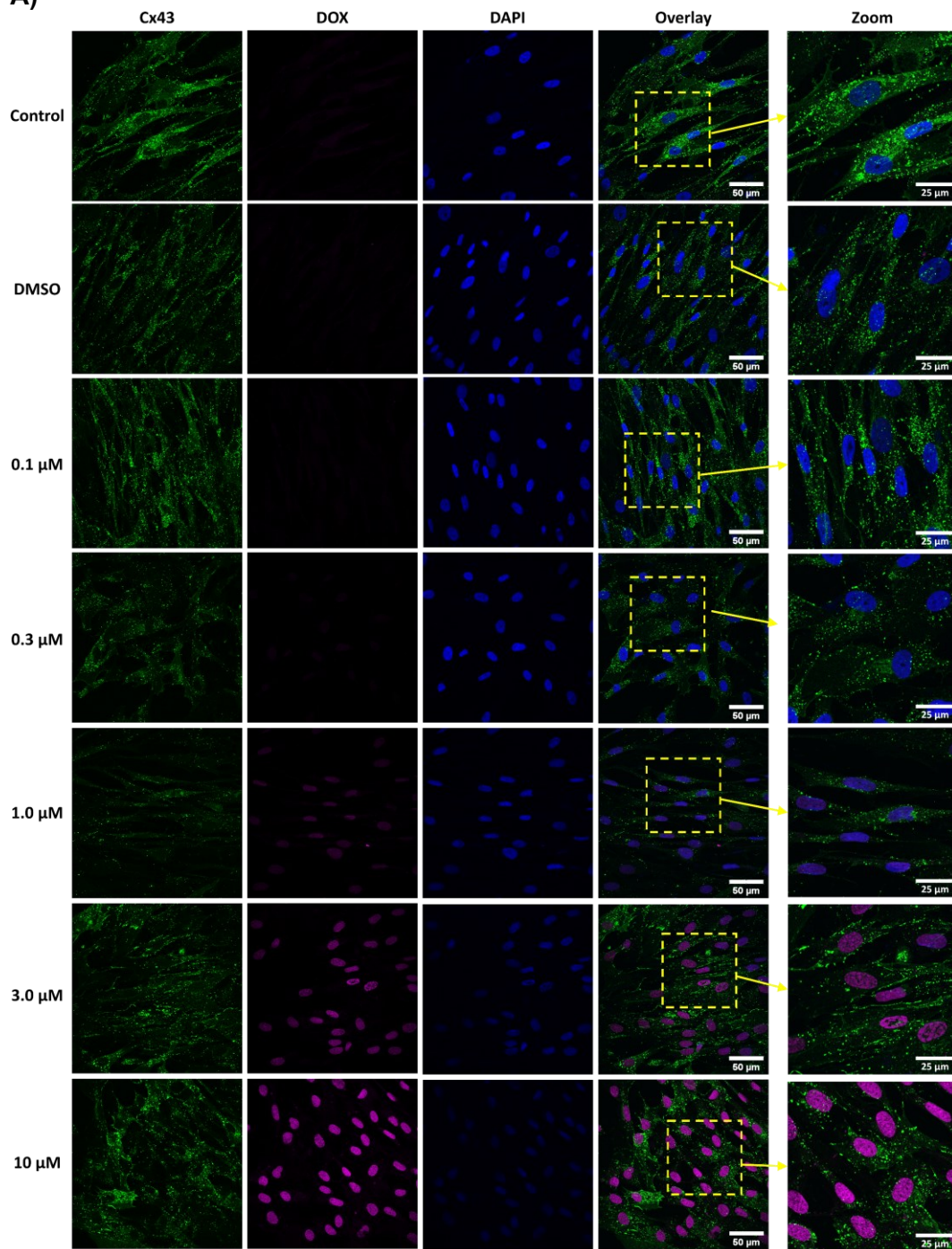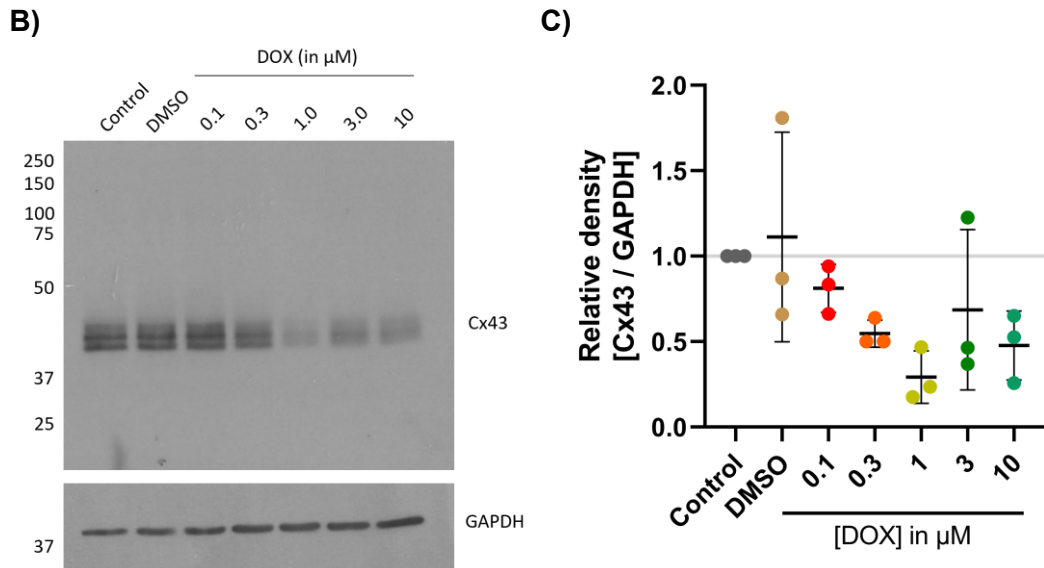
Figure 30 - Effect of DOX on Cx43 expression in hCFs

A) *Immunohistochemistry staining of Cx43 (green), DOX (magenta) showed nuclear accumulation, and DAPI (blue) was used as nuclear counterstain.* **B)** *Western blot of total Cx43 expression in response to DOX in hCFs.* **C)** *Quantified and normalised protein expression of total Cx43 levels which are normalised to GAPDH expression which did not result in a significant difference in comparison to the control group ($p > 0.05$, n=3). Statistical analysis was conducted by an ordinary one-way ANOVA, Post-hoc Tukey test. Error bars represent the mean ± 95% confidence interval.*

3.9   *Characterisation of AC16 cardiomyocyte cells*

There are limitations when using primary adult cardiac myocytes, the main one being the inability to culture these cells for long-term study. Challenges are therefore to create cardiomyocyte-like proliferative cells for *in vitro* research. Davidson et al. published a paper regarding the establishment of a novel cell line from human ventricular cardiomyocytes (Davidson *et al.*, 2005). Primary cells were isolated from human ventricular tissue and fused with a fibroblast cell type. The fibroblast, from human skin origin (DWFB1), was lacking mitochondrial DNA and was transformed with a simian virus 40 (SV40). The SV40 is an oncogenic DNA virus and important for the selection process of fused cells with uridine. This resulted in four different clones, namely AC1, AC10, AC12, AC16, which all expressed the SV40 large T-ag, and characteristic cardiomyocyte markers β-myosin heavy chain (β-MHC) and Cx43. The AC16 cells were the most characterised and lacked sarcomeres and intercalated discs and were devoid of vimentin and fibroblast specific protein (FSP) 1. In addition, mitochondria, gap junctions, calcium handling proteins, and troponin-I were also identified. Conversely, the DWFB1 cells showed a positive stain for vimentin and FSP1. Another study confirmed the Cx43 expression levels in the AC16 cell line (Thakur *et al.*, 2021) and therefore these cells were used for this investigation.

To assess the morphology of the AC16 cells brightfield images were acquired (Figure 31A). The phenotype of the AC16 cells was determined in a similar way as the previously described cell lines. Firstly, the cells were stained for vWF, α-SMC actin, vimentin, and of course Cx43. As expected, there was no typical vWF expression observed within the cell population (Figure 31B). This data suggests that no cells from endothelial origin are present in the culture. Furthermore, no α-SMC actin expression was identified (Figure 31C). However, despite the AC16 cells being

derived from a fibroblast-like cell type, there was no expression of vimentin observed (Figure 31D). Cx43 expression showed a perinuclear region, at the plasma membrane, and also in the tunnelling nanotubes (TNTs) (Figure 31E).

To assess if Cx43 expression was localised within the mitochondria, the cells were co-stained with mitochondrial ATP synthase inhibitory factor 1 (ATPIF-1). (Figure 31F). ATPIF-1 revealed the localisation of the mitochondria within the AC16 cells but showed a low level of colocalization with a Pearson R value of 0.09 (Figure 31G).

D)

Vimentin | F-actin

DAPI | Overlay

50 µm

10 µm

E)

Cx43 | F-actin

DAPI | Overlay

50 µm

10 µm

F)

Cx43 | Mitochondria

DAPI | Overlay

25 μm

10 μm

G)

Pearson R value: 0.09
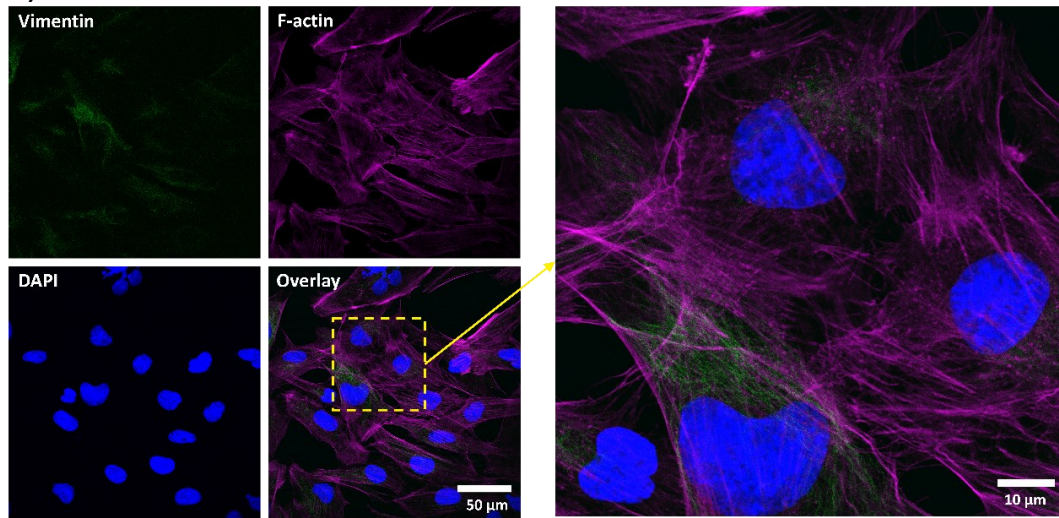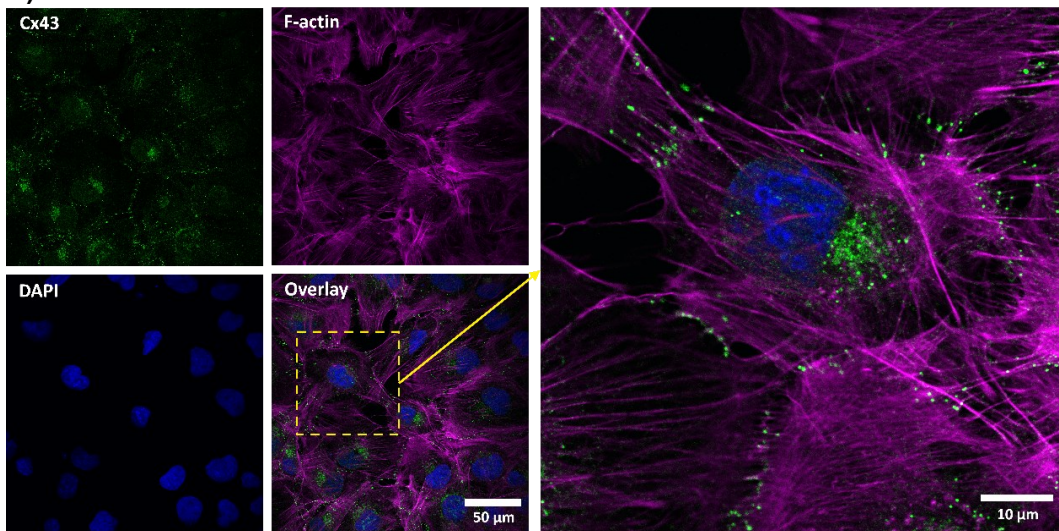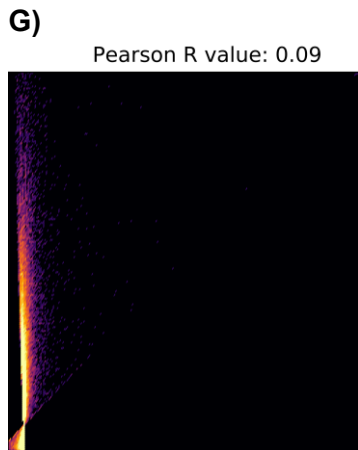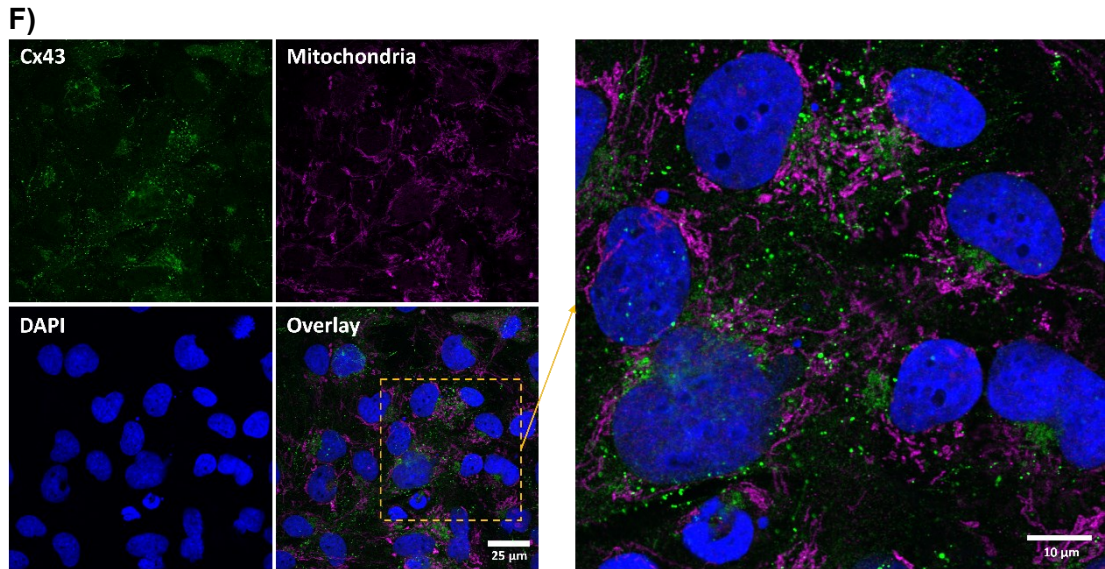
Figure 31 - Characterisation of AC16 cardiomyocyte cells

A) Brightfield image of AC16 cell to show its morphology (Scalebar is 200 μm and for zoomed areas 100 μm). B) Indirect immunostaining for vWF (green), rhodamine phalloidin stain for F-actin (magenta), and a DAPI nuclear counterstain (blue). No typical vWF expression was observed, and no α-SMC (C) and vimentin (D) expression was discovered. E) Cx43 expression is showed at the perinuclear region, plasma membrane, and also in the nano tunnelling tubes. F) Cx43 (green) with ATPIF-1 (magenta) resulted in a Pearson R value of 0.09 (G). Scalebar is 50 μm and for zoomed areas 10 μm.

The effects of DOX on the morphology of the AC16 cells was identified by using brightfield microscopy. The treatment of DOX resulted in a loss of cells at 1.0 µM and higher as more gaps between the cell clusters was observed (Figure 32A). To investigate cell death, cell viability assays were performed. The MTT assay resulted in a significant cell death at 0.1 µM DOX ($p < 0.001$) with an IC50 log value of -5.973 (±0.090M), equivalent to 1.06 µM (Figure 32B-C). The MTT results were compared to the cell viability assay toxilight. The toxilight assay resulted in an increase of cell death at 1.0 µM of DOX and significant at > 3.0 µM to the control group ($p < 0.0001$, Figure 32D). The dose-response curve of the toxilight assay resulted in an EC50 log value of -5.317 (±0.175), equivalent to 4.82 µM. The correlation between the MTT and toxilight assay resulted in a R^2 of 0.8395. The Cx43 total protein levels were evaluated in response to DOX with a significant reduction was observed at 1.0 µM in comparison to the control group ($p < 0.05$).

A)

Control

DMSO

0.1 µM

0.3 µM

1.0 µM

3.0 µM

10 µM

100 µm

G)

DOX (in µM)

Control Vehicle 0.1 0.3 1.0 3.0 10

250
150
100
75

50

Cx43

37

25

37   GAPDH

H)

[DOX] in µM
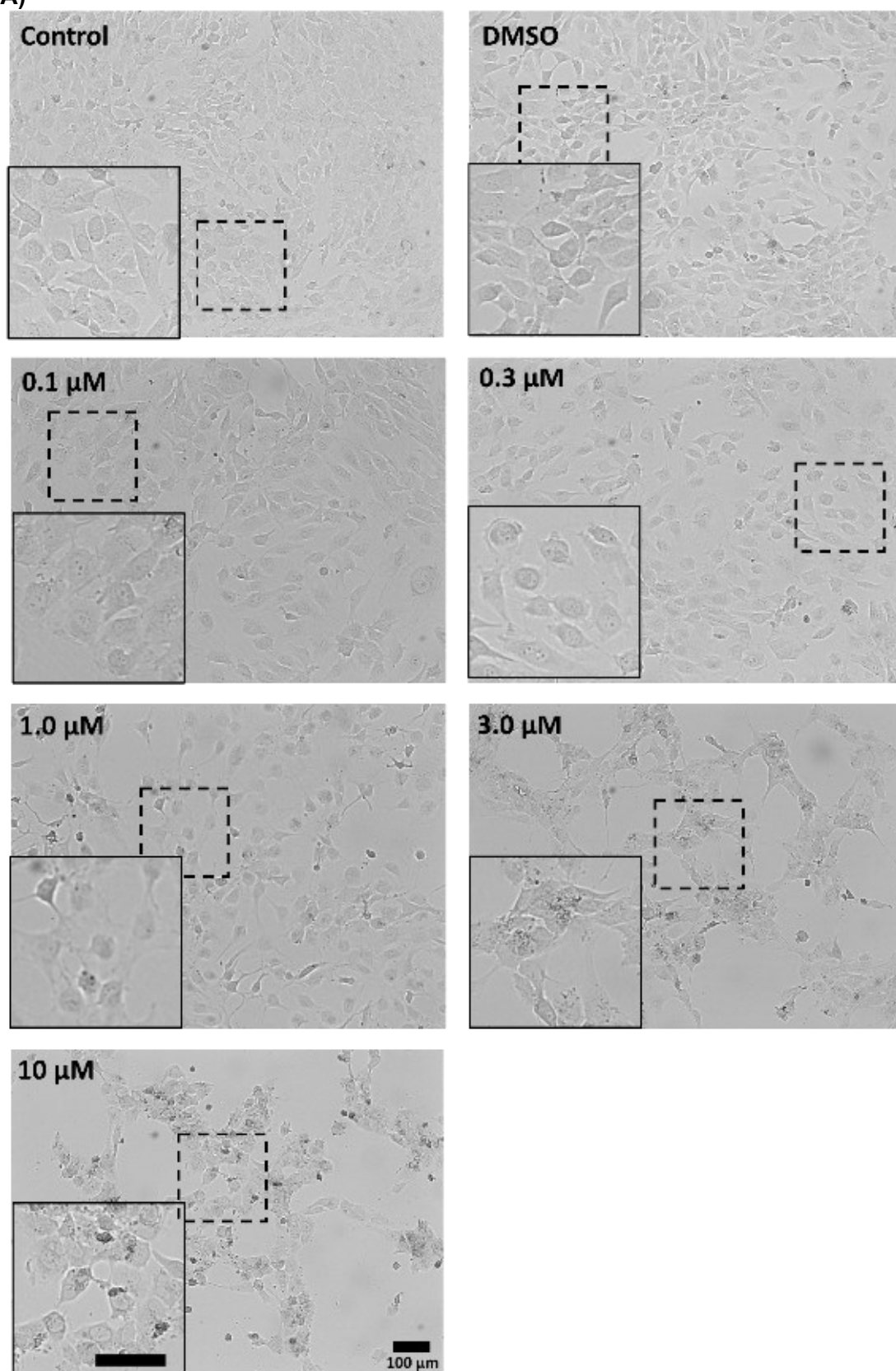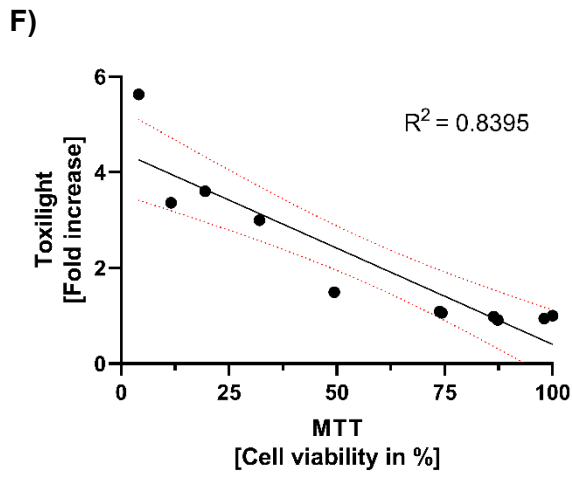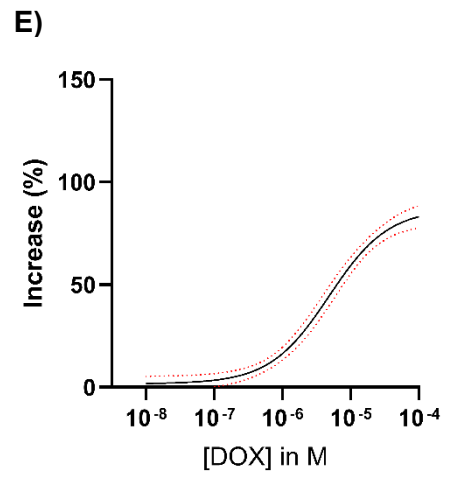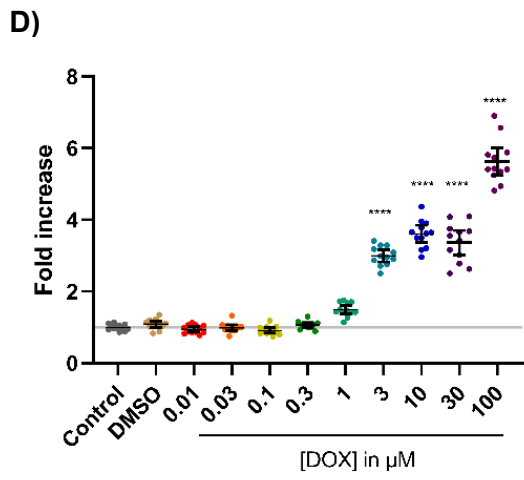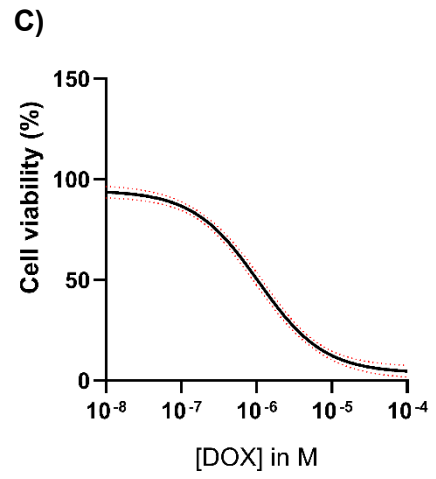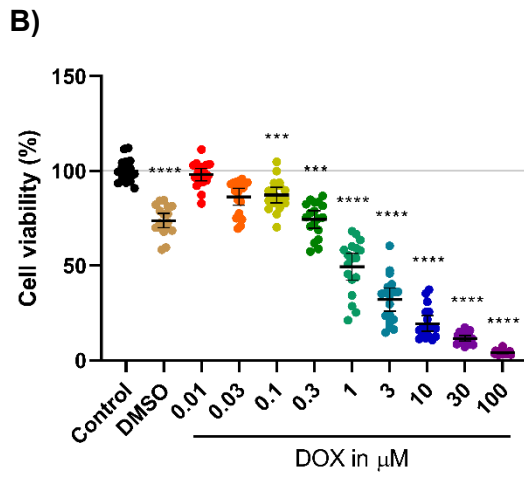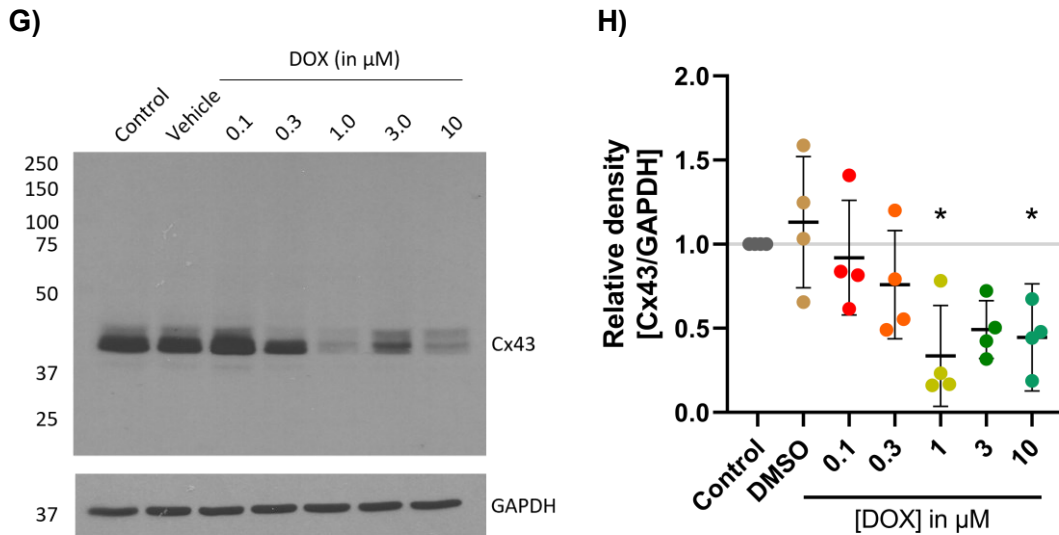
Figure 32 - DOX decreases cell viability in AC16 cells

A) *Brightfield images of AC16 cells treated with DOX (0-10 µM) show the morphology cells.* ***B)*** *MTT assay dot-plot with cell viability (in %) normalised to control.* ***C)*** *Dose-response curve of the MTT assay resulted in a log IC50 of -5.973 ± 0.090 M.* ***D)*** *Toxilight assay dot-plot with values (fold increase) normalised to control.* ***E)*** *Dose-response curve of the toxilight assay resulted in a log EC50 of -5.317 ± 0.175 M.* ***F)*** *Correlation of MTT vs Toxilight cell viability resulted in a R^2 of 0.8395.* ***G)*** *Western blots of Cx43 and GAPDH on DOX treated AC16 cells.* ***H)*** *Relative density of Cx43 protein levels of the Western blot. Statistical analysis was conducted by an ordinary one-way ANOVA, Post-hoc Tukey te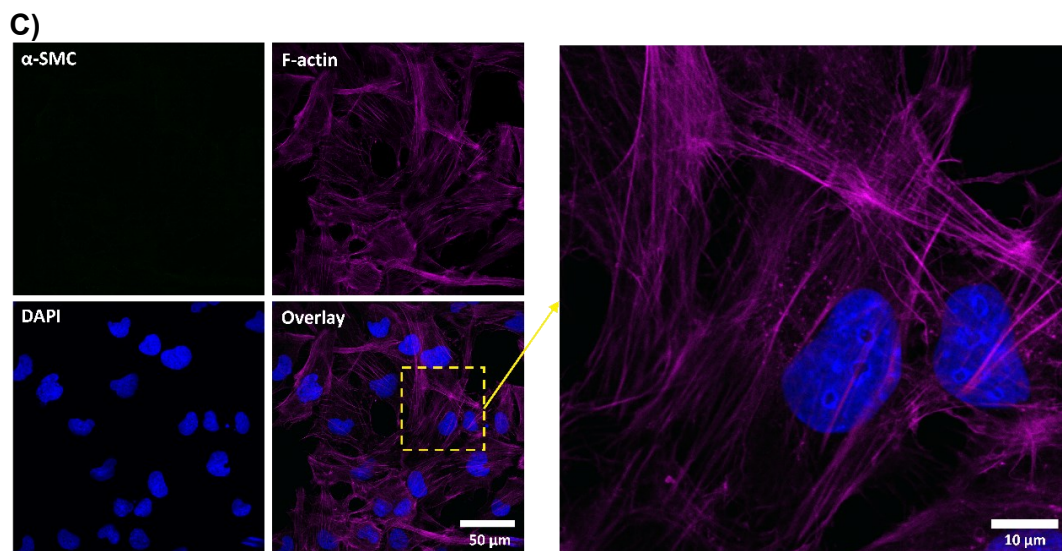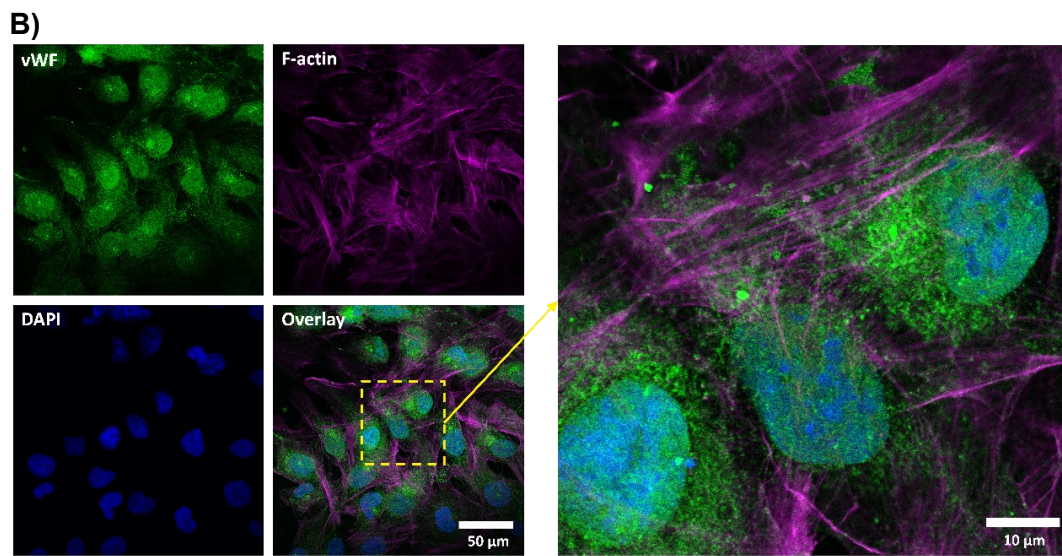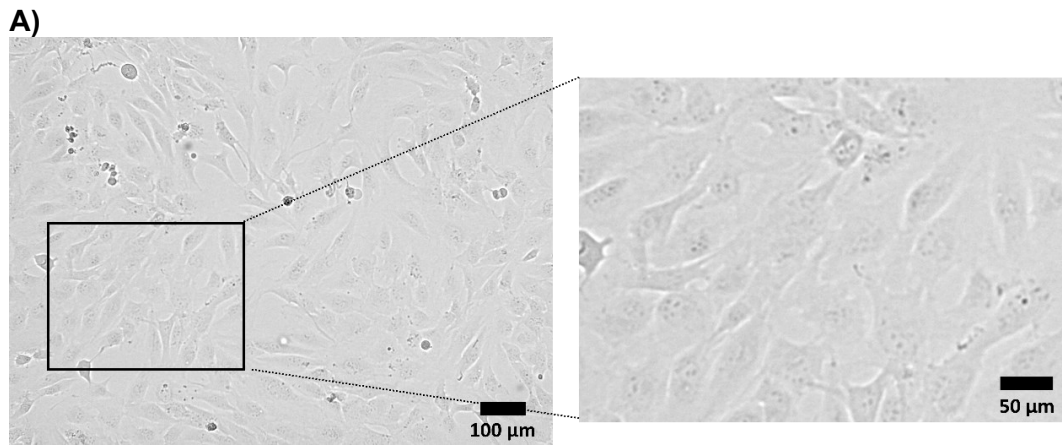st. Error bars represent the mean ± 95% confidence interval. ****$p < 0.0001$; ***$p < 0.001$, compared to the control group. n=4, conducted in triplicate.*

3.10   Discussion

This chapter focused on the characterisation of a range of human cardiovascular cells and to discover the effect of DOX on the cell viability as well as the Cx43 protein expression. These cells involved HUVECs, HCAECs, hCFs, and AC16 cardiomyocyte-like cells.

Unfortunately, limited studies have investigated the effect of DOX on the cellular viability in cardiovascular cell types. Most researchers study the detrimental effects on the cardiomyocytes, but other studies have shown effects of DOX on the microvasculature and fibroblast transition (Bielak-Zmijewska *et al.*, 2014; Wojcik *et al.*, 2015; Yin *et al.*, 2016; Narikawa *et al.*, 2019; Bosman *et al.*, 2021; Galán-Arriola *et al.*, 2022). In our studies, we have conducted cell viability assays with DOX on HUVECs, HCAECs, hCFs, and AC16. Differences in IC50 cell viabilities were observed which were: hCF, 0.37 µM; AC16, 1.06 µM; HCAECs, 0.54 µM; HUVECs, 1.23 µM. The dose-response curves and their associated IC50 values are shown in Figure 33 and their corresponding IC50s were compared to published pharmacological values, which are shown in **Error! Reference source not found.**. The only IC50 value that was discovered within the literature concerned the HUVECs, with a value of 0.75 µM (Abou El Hassan *et al.*, 2003). The IC50 value is lower when compared to our data. However, there is a lack of reliability when comparing IC50 values (Paolini, Lyons and Laflin, 2010; Damiani *et al.*, 2019). This could be due to a different methodology of the cell viability assay, culture differences, drug concentrations, time of stimulation or other parameters that could contribute. As no other studies have investigated the toxicity profile on the studied cell types, therefore could our data contribute to get a better understanding of DOX in cardiotoxicity.

Table 11 - IC50 values compared to published pharmacological values

Cell line	IC50 (DOX in µM)	Published pharmacological values (µM)	Reference
HUVEC	1.23 (1.01-1.50)	0.75	(Abou El Hassan *et al.*, 2003)
HCAEC	0.54 (0.42-0.70)	Not identified	N/A
hCF	0.37 (0.29-0.48)	Not identified	N/A
AC16	1.06 (0.86-1.31)	Not identified	N/A

Figure 33 - Comparison of dose-response curves and IC50 values

*A) Dose-response curve of MTT cell-viability in response to DOX (cell viability in %). B) Log IC50 values in a dot-plot showing significant differences between different cell types. Statistical analysis was conducted by an ordinary one-way ANOVA, Post-hoc Tukey test. Error bars represent the mean ± 95% confidence interval. *p < 0.05; **p < 0.01. n=4, conducted in triplicate.*

A feature that was observed in this chapter were differences in subcellular localisation of Cx43 between the cell types that were used in the study. Figure 34A displays fluorescent images whereby Cx43 and rhodamine phalloidin for F-actin were imaged to show the structure and localisation. To simplify and to create a better overview of the Cx43 localisation, an illustrative schematic was created which was based on the images (Figure 34B).

Firstly, the HUVECs express Cx43 majorly at the perinuclear region of the cells and at the TNTs with neighbouring cells. The localisation in the HCAECs is different as Cx43 is mainly between adjacent cells and in the TNTs and at the perinuclear region. Conversely, Cx43 expression in hCFs was observed throughout the cell with no expression between adjacent cells. Finally, the AC16 cells show a high degree of Cx43 also at the perinuclear region and at the TNTs. The TNTs are associated with long-distance cellular communication which is linked to Cx43 expression (Valdebenito *et al.*, 2018; Asencio-Barría *et al.*, 2019; Tishchenko *et al.*, 2020; Cervantes and Zurzolo, 2021).
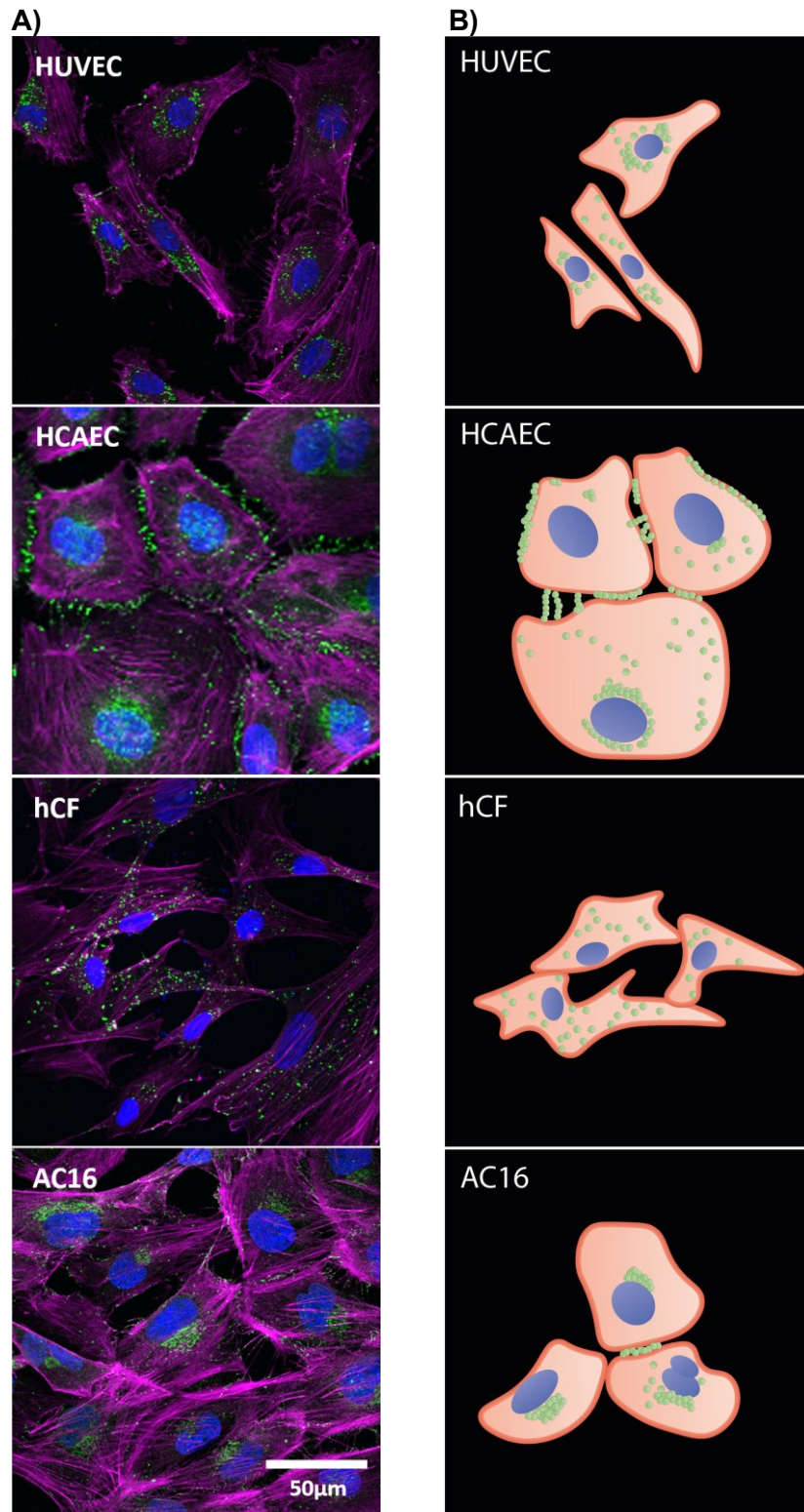
Figure 34 - Comparison of Cx43 subcellular localisation in different cell types
A) Indirect immunofluorescence staining for Cx43 (green) with a rhodamine phalloidin stain for F-actin (magenta) and a DAPI nuclear counterstain (blue). B) Illustrative overview of the localisation of Cx43 in each cell type.

Besides the identification of the subcellular localisation of Cx43 within the different cardiac cell types and HUVECs, the protein levels were also identified through conducting Western blots of cell homogenates (see section 3.6). Interestingly, next to the well-known Cx43 protein band at approximately 43kDa different bands were present. These bands migrated slower in SDS-PAGE and therefore indicate a larger protein size. Different studies associate these bands with a higher phosphorylation state of the Cx43 protein and characterise these as P0 (also known as NP), P1 and P2 (Hesketh et al., 2010; Leithe, Mesnil and Aasen, 2018; Rodríguez-Sinovas et al., 2021). Sometimes difficulties arise to discriminate the three different Cx43 bands or only identify two. For this reason, some researchers merge the P1 and P2 bands or only mention P1 (Chen et al., 2010; Dunk et al., 2012; Lee, Lin and Chang, 2013). In addition, the band profile could vary in different cell types (Musil et al., 1990). Other bands that appeared on the Western blots could be related to N-terminally truncated Cx43 isoforms in human cardiac cells include GJA1-32k, GJA1-29k, GJA1-26k, and GJA1-20k (Smyth and Shaw, 2013). The GJA1-20k fragment is the most described and the predominant isoform (Salat-Canela et al., 2014, 2015). The different N-terminally truncated isoforms of GJA1 are shown in Figure 35A-C.
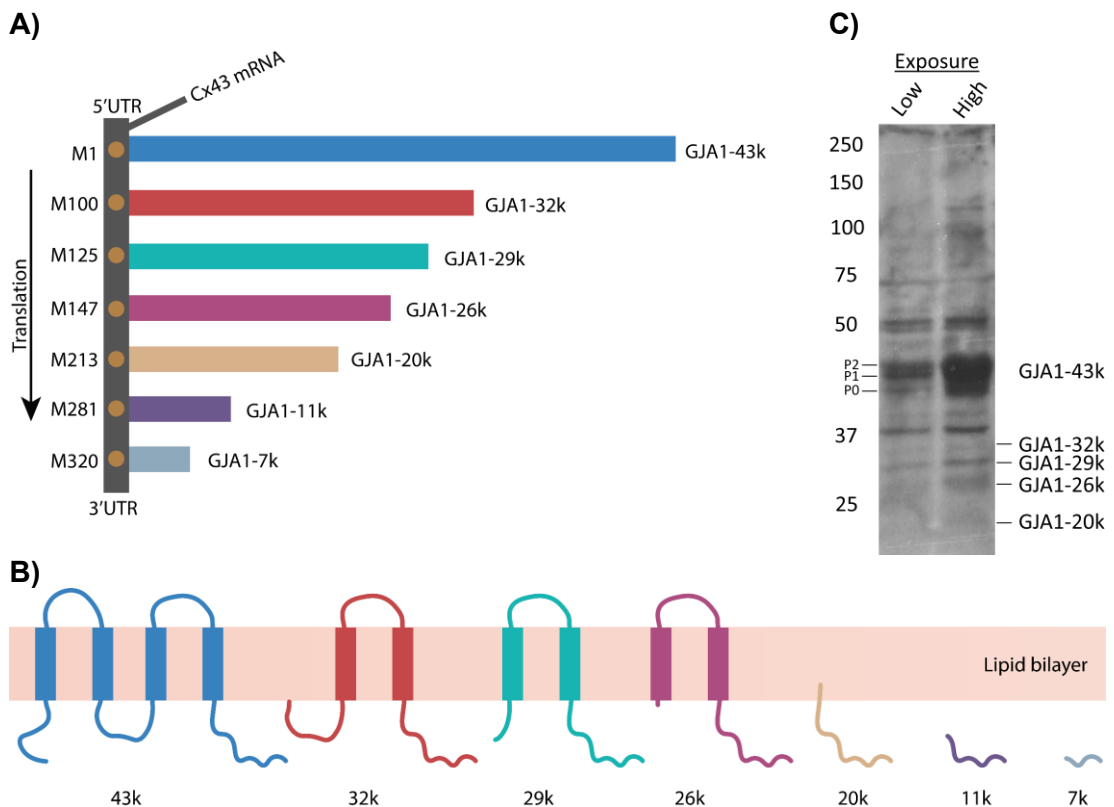
Figure 35 - Identifying different bands of Cx43 transcripts

A) Overview of the different transcripts encoding Cx43 and starting AUG codons were shown as orange circles. B) Putative truncated forms within the lipid bilayer. C) Overview of band profile of Cx43 within the rat hearts, including the different phosphorylation states P0, P1, and P2. This figure was adapted from (Salat-Canela et al., 2015; Leithe et al., 2018; Rodríguez-Sinovas et al., 2021).

3.11   Conclusion

Within this results chapter the human cardiac cell types HCAECs, hCFs, and AC16 as well as the HUVEC were characterised by cell-specific markers. For the first time, we have managed to identify the toxicity profile of DOX on different cardiac cell types, whereby hCFs showed the highest sensitivity, which was followed by HCAECs, AC16, and HUVECs, respectively. The auto-fluorescence properties of DOX confirmed its nuclear localisation in all cell types. The key results were novel findings, as a reduction of total Cx43 levels at concentrations of 1.0 µM DOX and higher were identified. This data was followed up by using ex-vivo experiments using Langendorff perfusion and 3D multicellular spheroid systems.

CHAPTER FOUR:

INVESTIGATING THE EFFECT OF DOX ON CX43 EXPRESSION IN LANGENDORFF MODEL AND 3D SPHEROIDS

4.1   Introduction

The aim of this chapter was to assess DOX-mediated Cx43 changes in primary cardiac cell models and to translate to whole heart using isolated rodent heart Langendorff perfusion models. In the previous chapter Cx43 expression was evaluated within cardiac cells and HUVECs. Research conducted within single cell type 2D monolayer culture has its limitations as no paracrine communication occurs between different cardiac cell types (Soares *et al.*, 2012). To further investigate the effects of DOX on cardiac cell function, rat hearts were used to assess the direct effect of the drug using the Langendorff perfusion method. (Watanabe and Okada, 2018). The Langendorff perfusion is an experimental procedure to perfuse the hearts of animals (ex-vivo) which was firstly described at the end of the 19th century by Oskar Langendorff (Langendorff, 1897). An oxygenated physiological buffer is perfused through the canulated aorta of the heart. The Langendorff is a well-established technique that allows direct studies on the heart without the contributions of other *in vivo* unrelated effects. Previous examples of how this technique has been used include monitoring heart function, evaluation of ischaemia-reperfusion (I/R) injury, and drug screening (Hole *et al.*, 2014; Martins-Marques *et al.*, 2015).   In this study, Langendorff was used to assess the direct effect of DOX upon the heart, with particular focus placed upon the expression and localisation of cardiac cell Cx43.

Multicellular 3D spheroids were cultured to overcome the lack of paracrine communication in the 2D cell models used previously. The 3D cardiac cell model allows crosstalk between the different cells and is also known as a "cardiac spheroid". This spheroid was composed of the three main cellular cell types of the heart in co-culture, including cardiac myocytes, fibroblasts, and endothelial cells (Sharma and Gentile, 2021). The AC16 cardiomyocyte cells have limitations as these cells have no

contractile phenotype. Therefore studies were optimised by using iCell cardiomyocytes to achieve a contractile monolayer as well as multicellular spheroids.

Cx43 expression in the heart is normally recognised at the intercalated discs of cardiomyocytes to preserve a synchronised cardiac contraction (Hesketh *et al.*, 2010). Abnormal expression of Cx43 expression within the heart has been associated with cardiovascular dysfunction (Fontes *et al.*, 2012). For example, the redistribution of Cx43 from the intercalated disks to the lateral side of the cardiomyocytes, so called lateralisation, was characterised in atrial fibrillation (Kim *et al.*, 2011; Takahashi *et al.*, 2012). Another study identified no change of Cx43 expression in atrial fibrillation, but an increased expression of Cx40 (Polontchouk *et al.*, 2001).

4.2 Physiological expression of Cx43 in the heart

To investigate the effect of DOX on Cx43 within cardiac tissue the Langendorff perfusion technique was optimised and applied in rat hearts. The hearts were canulated onto a perfusion system with Tyrode's buffer to maintain the physiological function of the cardiovascular system. The perfusion was conducted with either 1.0 µM DOX added or equivalent DMSO concentration as vehicle for a duration of one hour. Total Cx43 protein levels were detected by using Western blotting which revealed a band pattern with three distinct bands (Figure 36A). The lowest band (P0) is the lowest phosphorylated state of the protein, followed by P1 and P2 which have a higher molecular weight.

Optimisation experiments were conducted to enhance the efficiency of the Langendorff perfused hearts. Each perfused heart was initially dissected into two compartments whereby the upper part was further dissected to isolate the RA, LA, RV, and LV. The lower part was embedded in OCT medium for sectioning and immunohistochemistry staining (Figure 36B-C). As previously described, Cx43 is physiologically expressed at the intercalated disks of the cardiomyocytes to serve its role in intercellular communication (Figure 36D). The localisation of Cx43 expression was examined within the tissue by using rhodamine phalloidin which stained the F-actin within the cardiomyocyte structure. The cardiomyocytes show characteristic long striations, alongside the presence of Cx43 between neighbouring cells to form the gap-junctions (Figure 36E).

Langendorff perfused rat hearts were also used for cardiomyocyte isolation. Previous studies were successful in the isolation procedure and conducted further experiments on these (Li *et al.*, 2014; López-Dávila *et al.*, 2021). In our studies, we

have isolated the cardiomyocytes with success. The cardiomyocyte morphology showed clearly the elongated striated structure of the cells, which is shown in Figure 36F. However, some of the cardiomyocytes show a hypercontracted phenotype, this could be a result of changes of calcium levels and external stimuli (López-Dávila *et al.*, 2021). The Cx43 localisation was identified within the isolated cardiomyocytes with a rhodamine phalloidin stain, which showed the striation of the cells. Cx43 was present as punctae at the outside of the cardiomyocytes, confirming the presence at the intercalated discs Figure 36G).

A)

50
p2
p1 Cx43
p0
37

B)

Section
LV
RV

C)

RV
LV

D)

Cardiac muscle tissue

Intercalated disc

Myofibril
Gap junction
Myocyte 1
Myocyte 2
Mitochondrion
Intercalated disc

Cx43
Myocyte 1
Myocyte 2

E)

Cx43
F-actin
DAPI
Overlay
100 μm
25 μm

F)

G)
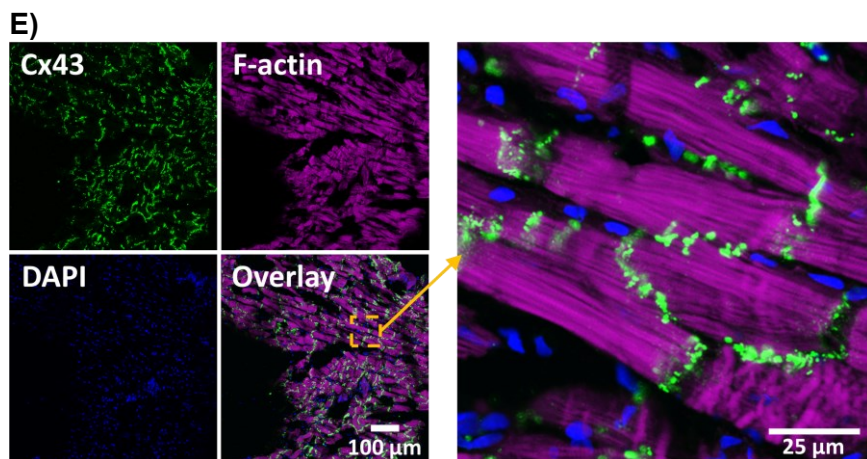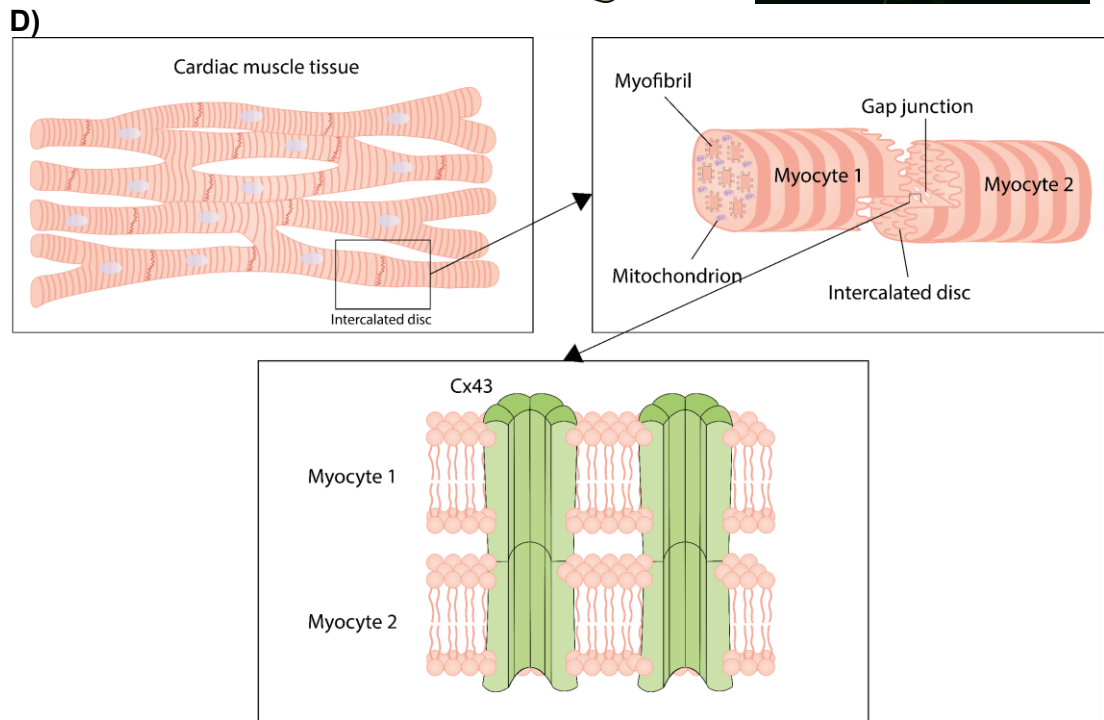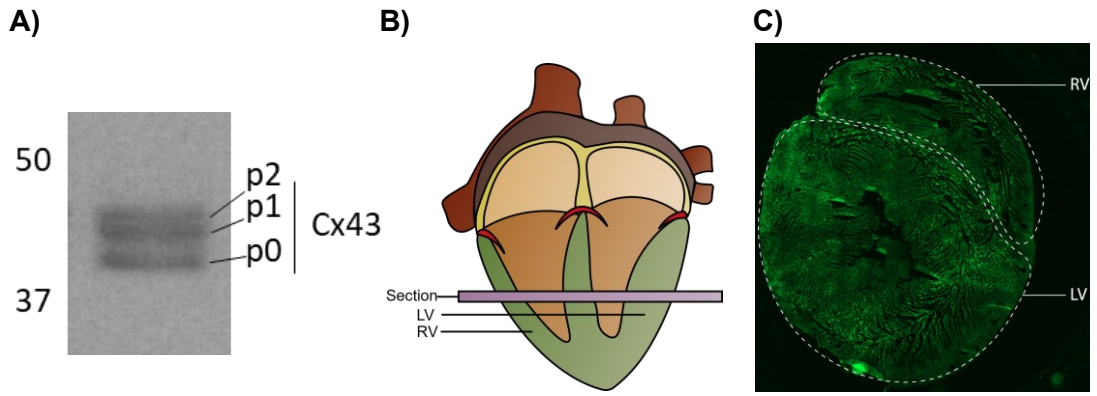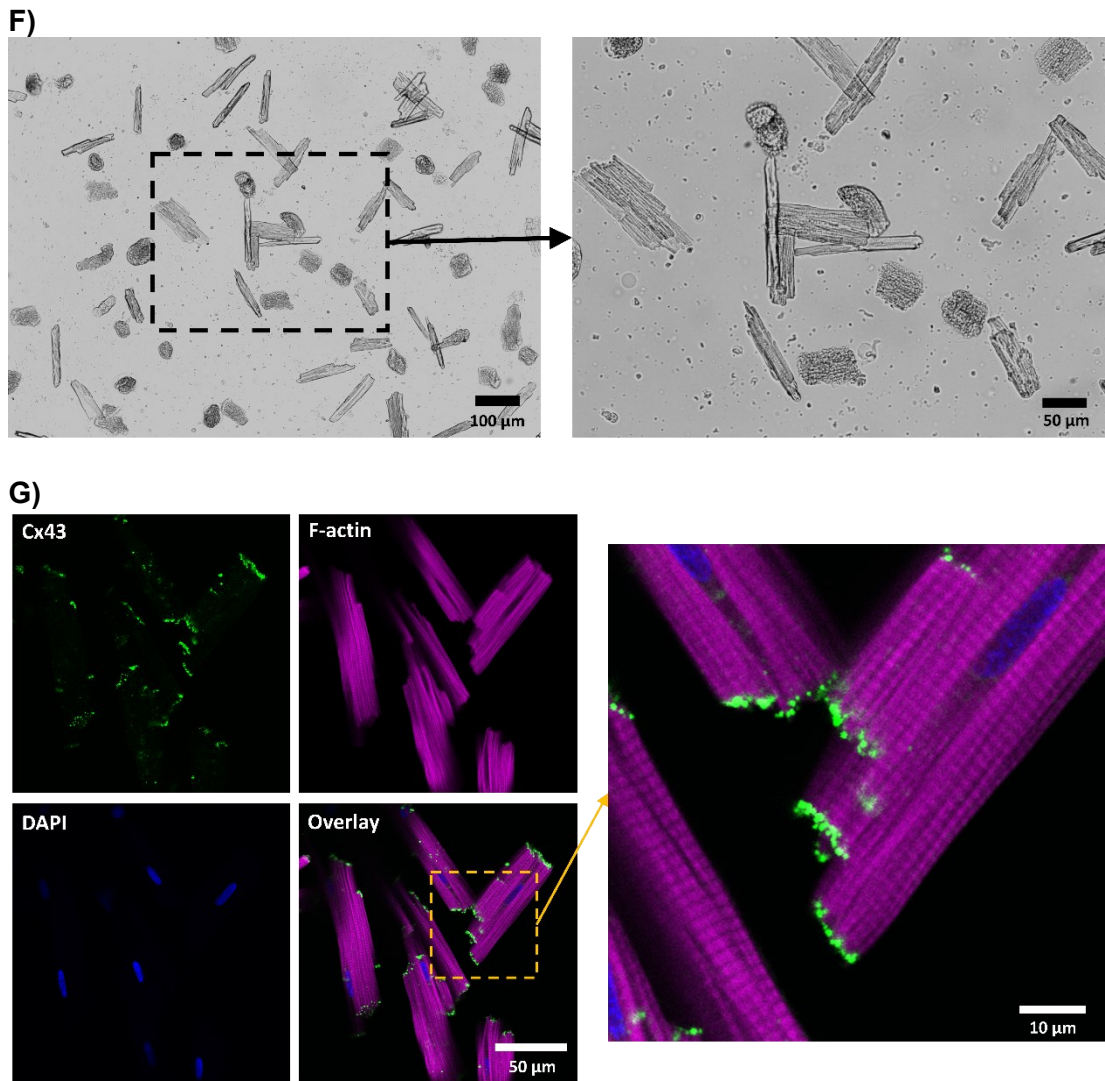
Figure 36 - Expression of Cx43 in cardiac tissue

A) Representative Western blot of Cx43 of the Langendorff perfused rat hearts. B) Illustrative image showing the sectioning of the Langendorff perfused rat heart. C) The full section with Cx43 expression (green) in the LV and RV regions. D) Illustrative overview of the cardiac muscle with the intercalated disks and Cx43 expression, adapted from (Cardiac Muscle Tissue | GetBodySmart, 2022). E) Rhodamine phalloidin stain (magenta) with DAPI (blue) as nuclear counterstain, and Cx43 (green) in a tissue section of left ventricle of the rat heart. The long-striated cardiomyocytes show expression majorly at the lateral side of the cell by forming gap junctions. F) Brightfield images of isolated cardiomyocytes. G) Isolated cardiomyocytes with a rhodamine phalloidin stain (magenta), Cx43 (green), and DAPI nuclear counterstain (blue).

4.3 Changes of Cx43 expression in response to DOX on Cx43 in rat hearts

In the previous section, optimization studies were conducted to measure total Cx43 levels and its localization using the Langendorff perfusion method, protein extraction with Western blotting, and immunohistochemistry staining on sections. This section focusses on the effect of DOX on the subcellular localisation of Cx43 within the cardiac tissue as well at the total protein levels.

The Langendorff perfused hearts with DOX show differences in comparison to the vehicle samples. Firstly, changes in the total protein levels were observed within different regions of the heart. A noticeable feature was the increase of the higher phosphorylated states the Cx43 bands in the LV and RV cardiac regions in response to DOX (Figure 37A). In addition, the total Cx43 protein level alterations show a change after normalisation with the reference protein GAPDH (Figure 37B). Immunofluorescent imaging of sections of LV tissue, showed a physiological localisation of Cx43, majorly at the intercalated discs (Figure 37C-left). However, when the hearts were perfused with DOX, a lateralisation was observed, which means more Cx43 expression was characterised on the lateral side of the cardiomyocytes (Figure 37C-right).
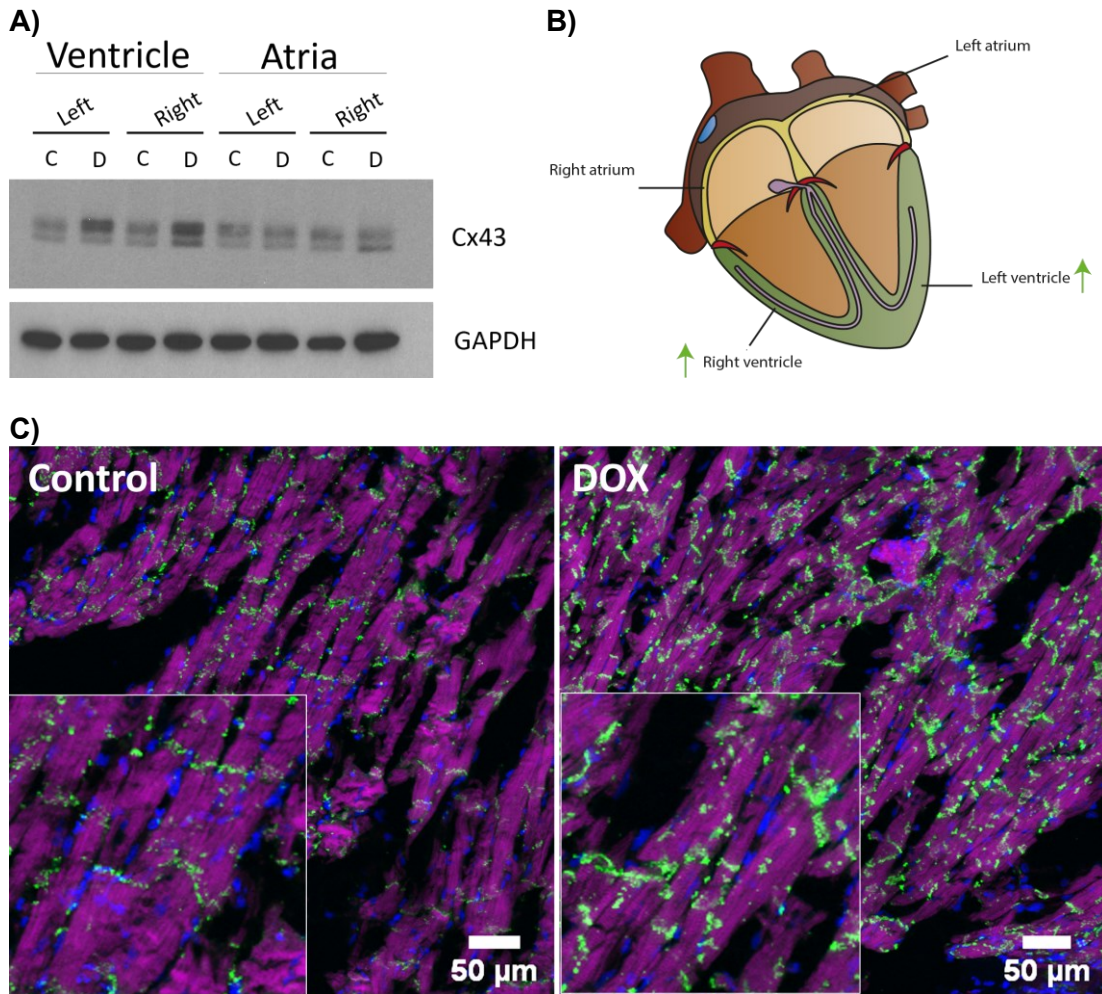
Figure 37 - Changes in Cx43 expression in the rat heart in response to DOX
A) Total Cx43 protein expression in ventricular and atrial tissue in response to DOX in comparison to control by Langendorff perfusion. **B)** Illustrative overview of the effect of DOX on Cx43 levels in tissue specific regions. **C)** Immunohistochemistry staining on left ventricular tissue for Cx43 (green), F-actin (magenta), and DAPI (blue). The left panel shows the DMSO perfused, and the right panel the DOX perfused rat heart. The DOX-treatments reveals lateralisation of Cx43. n = 2.

4.4 Optimising 3D spheroid culture

Next to the use of the Langendorff perfusion ex-vivo model, it would be advantageous to generate cardiac 3D spheroid models to overcome the lack of paracrine communication between different cell types. To allow crosstalk between different cardiac cell types by the *in vitro* model could be important to study the behaviour of Cx43 in response to DOX. The cardiac spheroids are composed of the three main cellular cell types of the heart in co-culture, including cardiac myocytes, fibroblasts, and endothelial cells (Sharma and Gentile, 2021). The advantages and limitations of 2D hiPSCs-cardiomyocyte system versus 3D culture platforms derived from hiPSCs has been recently extensively reviewed (Liu *et al.*, 2022). Another study demonstrated the use of 3D co-culture of hiPSC-DMs is superior over 2D culture conditions as these models mimic the native myocardium more closely (Beauchamp *et al.*, 2020).

Firstly, MDA-MB-231 human triple negative breast cancer cells were used to optimise spheroid culturing. MDA-MB-231 cells are from epithelial origin, obtained from a pleural effusion from a 51-year old female with a metastatic mammary adenocarcinoma (Cailleau et al., 1978). The human breast cancer cell line is triple negative, which means there is no expression of oestrogen receptor (ER), progesterone receptor (PR), and HER-2. Initially, MDA-MB-231 cells were seeded in an ultra-low attachment 96-well plate with a density of 250 to 8,000 cells. Brightfield images reveal the size and structure of the spheroids (Figure 38A). The area of the spheroid increased at higher cell densities and showed a positive correlation with growth over the numbers of days (Figure 38B).
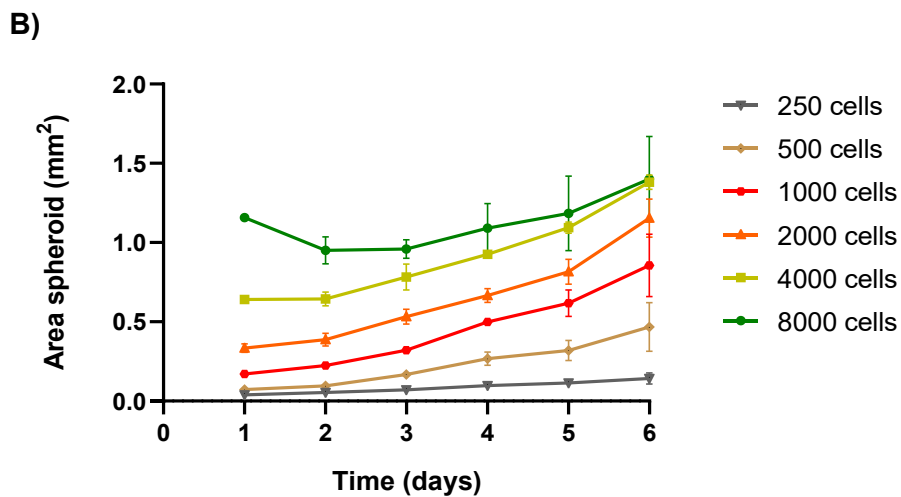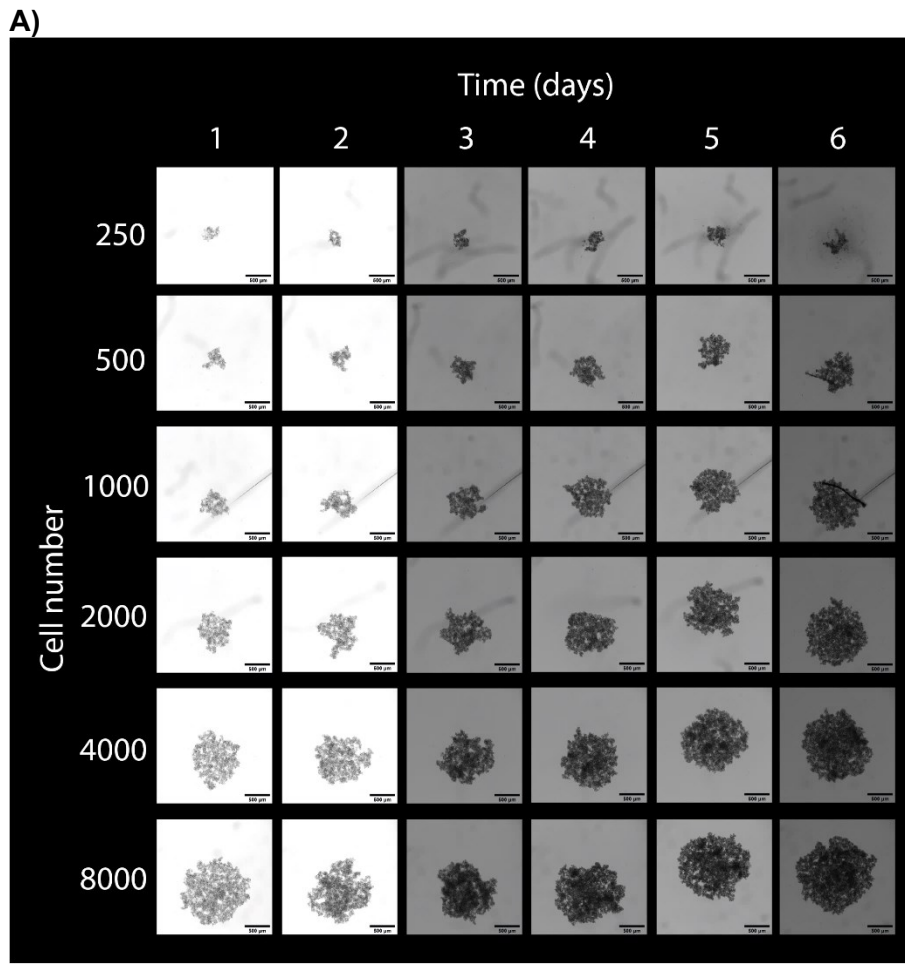
Figure 38 - Spheroid growth curve MDA-MB-231 cells

A) MDA-MB-231 spheroids with a cell density of 250-8.000 cells per well which were daily imaged up to 6 days. **B)** Quantification of area spheroids (mm^2) of the brightfield images. Scalebar is 500 μm.

After observing the growth of the MDA-MB-231 spheroids and confirming their formation, the next step was to optimize the cardiac spheroids. The cells that were used in this experiment included the AC16 cells, hCFs, and HUVECs. The spheroids were seeded with 4,000 cells with a AC16: hCF: HUVEC ratio of 2:1:1. Due to the different types of media that are used for each specific cell optimisations were performed by culturing the spheroids in endothelial (EC), fibroblast (FB), and cardiomyocyte (CM) Imedium (Figure 39A). The spheroids grown in the fibroblast medium showed a high degree of outgrowth. The outgrowth included the sprouting of cells which could occur at high proliferation and in toxic environments in response to e.g. drugs and could therefore be used as a screening method (Christoffersson *et al.*, 2018; Beauchamp *et al.*, 2020).

To investigate the effect of each cell line on the spheroid formation different combinations of the AC16, hCFs, and HUVECs were used (Figure 39B). The first observation includes the formation of the spheroids with hCFs/HUVECs as they are smaller in comparison to the other combinations and many cells did not adhere to the spheroid. However, similar results were obtained with the AC16/HUVEC spheroid combination, the area is larger. The AC16/hCF spheroid looks more rounded and had less unattached cells. The cardiac spheroid with AC16/hCF/HUVECs show a few cluster of cells that were unattached, but the roundness was also achieved.
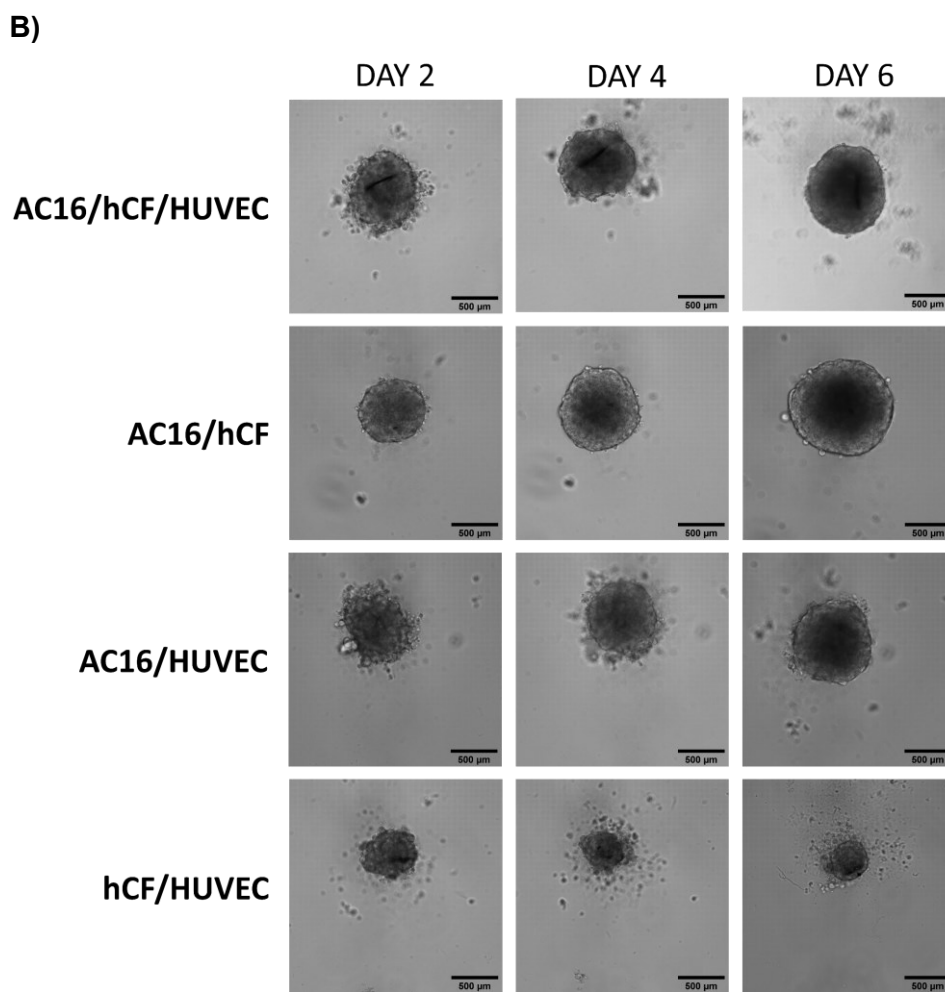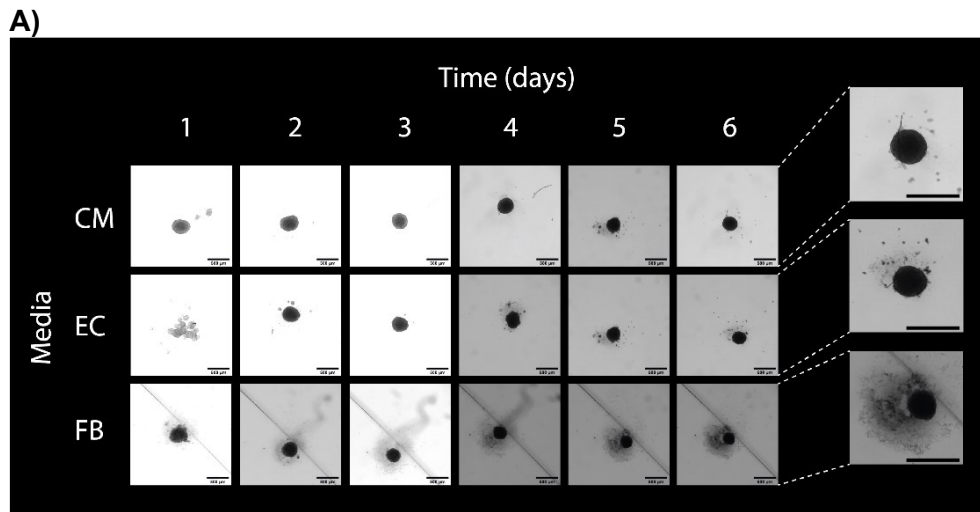
Figure 39 - Cardiac spheroid optimisation

A) Brightfield images of cardiac spheroids in endothelial (EC), fibroblast (FB), and cardiomyocyte (CM) medium over 6 days. **B)** Brightfield images of cardiac spheroids in mixed media to compare different spheroid combinations. Scalebar is 500 μm. n = 1.

The triple cell AC16/hCF/HUVEC spheroids were also used to conduct experiments concerning the optimisation for immunofluorescent staining. One of the disadvantages of the use of spheroids, is the formation of a necrotic core as a result of oxygen deprivation, also known as hypoxia (King, 2012; Acland *et al.*, 2018). For the purpose of optimisation spheroids consisting of 1000-4000 cells were used and stained with propidium iodide (PI), which is a well-known fluorescent marker for the DNA and is not membrane-permeable for viable cells. PI is membrane-permeable dye for cells in the apoptotic state (Zamai *et al.*, 1996; Suzuki *et al.*, 1997). The immunofluorescent images by using confocal microscopy show a lack of clearing and requires further optimisation (Figure 40A). A different imaging approach was undertaken by using light sheet microscopy on the cardiac spheroids with wheat germ agglutinin (WGA) and rhodamine phalloidin staining (Figure 40B). This data indicates that further optimisation of spheroid clearing is required.
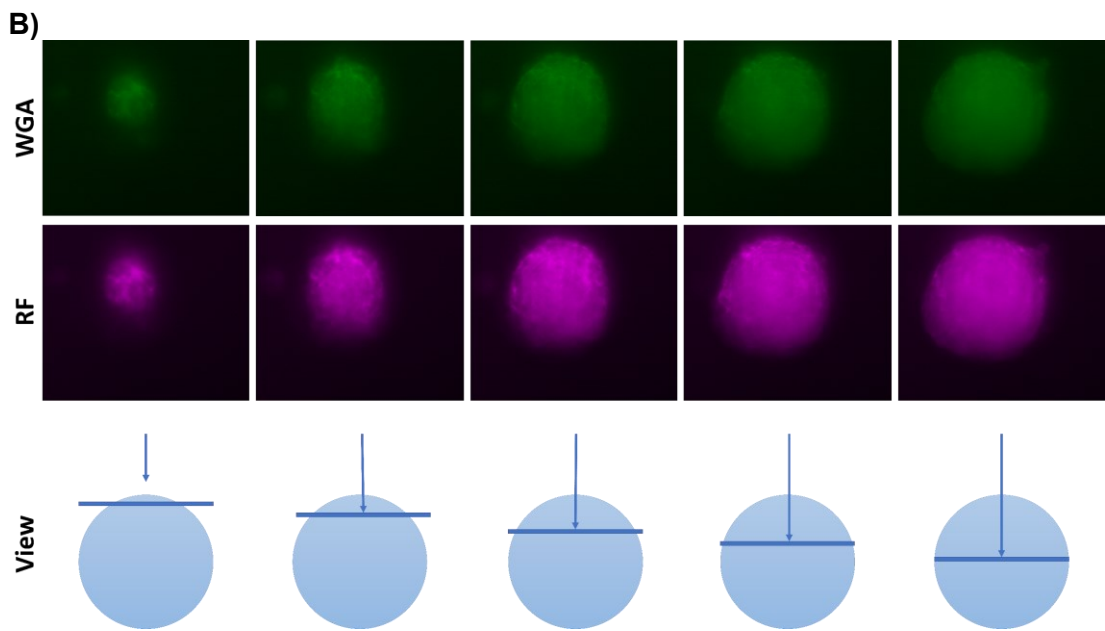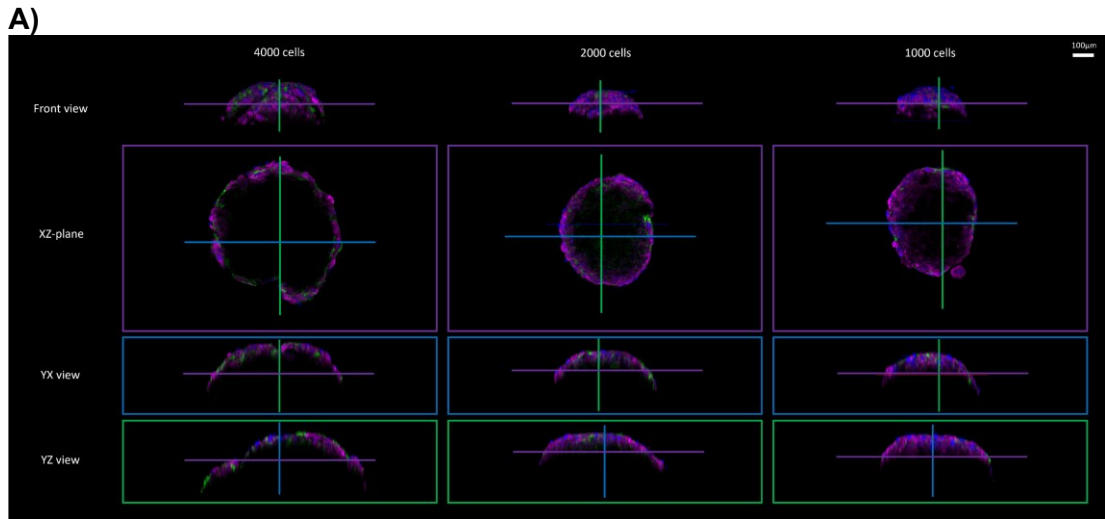
Figure 40 - Optimisation immunofluorescent imaging of cardiac spheroids

A) 3D imaging of cardiac spheroid with 1000, 2000, and 4000 total cells. The XZ-view is the magenta, and the YZ-view is the green line from the front view. The YX-view is the blue line from the XY-view. The staining was PI (magenta), F-actin (green), and DAPI (blue). The scalebar is 100 μm. B) Light sheet microscopy images of cardiac spheroids which were stained with wheat germ agglutinin (WGA, green) and rhodamine phalloidin (RF, magenta) with the illustrative plane view of each image. n = 1.

To investigate the effect of DOX on the spheroid formation brightfield images were acquired after treatment and compared to the vehicle. The images revealed that DOX induced outgrowth of the spheroid, which is shown in Figure 41A. The impact of DOX on the total Cx43 protein levels were assessed. No changes were observed between the different bands with the treated and untreated samples (Figure 41B). The GAPDH bands were oversaturated and therefore introduced limitations for quantification purposes. However, the bands were quantified in order to retrieve an indication whether DOX would have an effect on the Cx43 levels, however no statistical differences were discovered (Figure 41C).
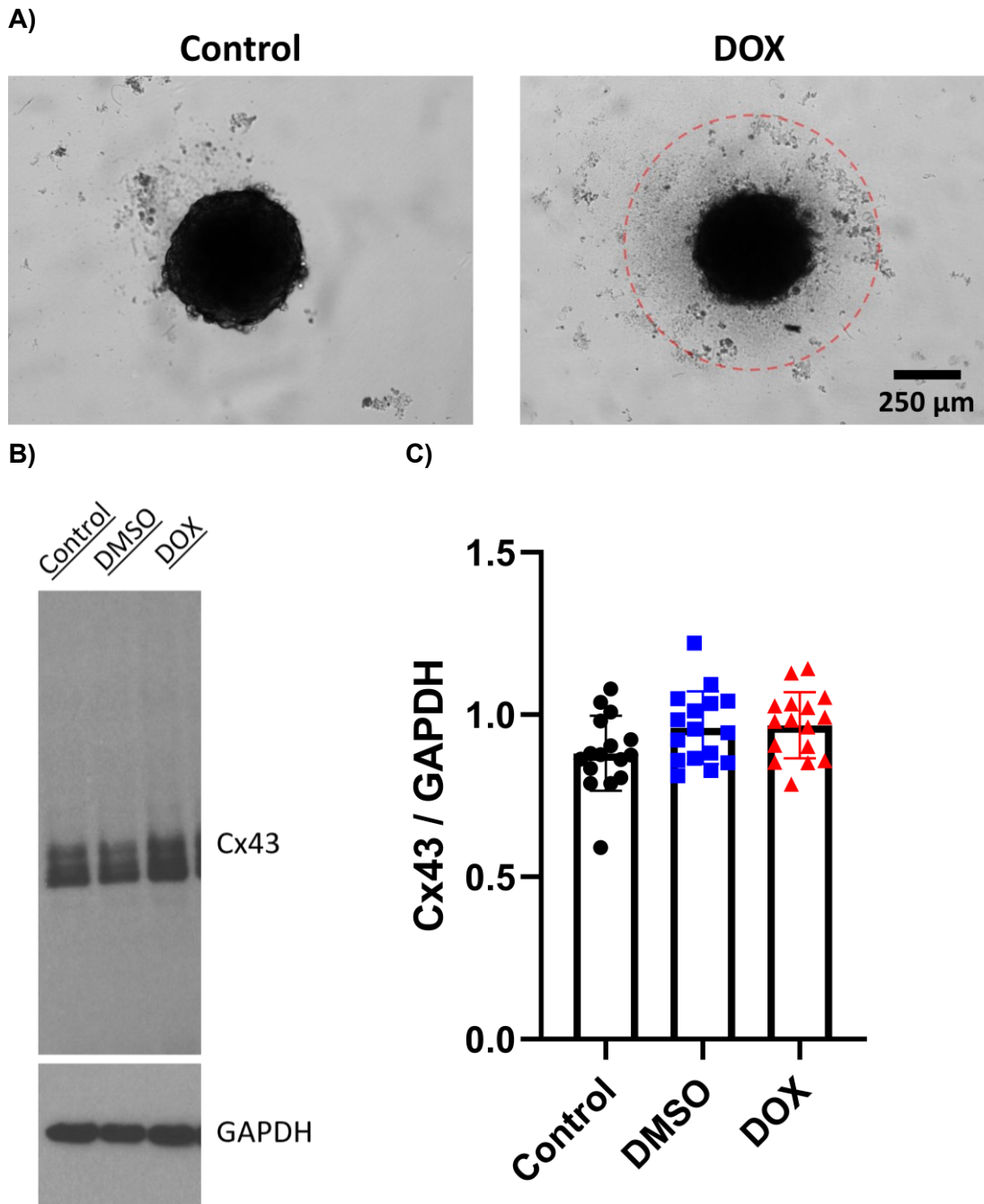
Figure 41 - Cx43 protein levels in cardiac spheroids in response to DOX

A) DOX induced outgrowth of triple cardiac spheroids AC16/hCF/HUVEC. Outgrowth is highlighted with red coloured dashed line. B) Protein bands of Cx43 and reference protein GAPDH in triple cardiac spheroids with AC16/hCF/HUVEC cells in response DOX. C) Normalised Cx43 levels to GAPDH did not show significant differences in comparison to the control group (p > 0.05). Statistical analysis was conducted by an ordinary one-way ANOVA, Post-hoc Tukey test. The error bars represent 95% CI, 16 different spheroids were used.

4.5 Optimising of culturing iCell cardiomyocytes

The AC16 cardiomyocyte-like cells have disadvantages as the cells have no contractile properties when compared to normal physiological cardiomyocytes. To overcome this disadvantage the use of human-induced pluripotent stem cells (hiPSCs) that are differentiated into functional and contractile cardiomyocytes (iCell cardiomyocytes) were used. These cells could bring the spheroid multicellular system a step closer to a "human heart in a dish". ICell cardiomyocytes have previously been used in different types of studies and could be used in disease modelling and drug discovery (Feaster *et al.*, 2021; Schmid *et al.*, 2021). The iCell cardiomyocytes are expensive and very sensitive cells. The cells need to be managed extremely carefully in order to achieve a monolayer with contractile properties. The different steps of the handling process, prior to plating, are illustrated in Figure 42A. Two different types of iCell cardiomyocytes were purchased, namely iCell cardiomyocytes (P1) and iCell cardiomyocytes[2] (P2). The P2 iCell cardiomyocytes are an enhanced version of the P1 cells and have been optimised for high-throughput assays. In addition, the P2 cells are assay-ready within four days after defrosting.

As first optimisation studies were conducted on P1 iCell cardiomyocytes as a limited number of 2.1 million cells were available in each provided vial. A plan was created in order to maximise the efficiency and generate as much data as possible. This plan included immunofluorescent imaging of the cardiomyocyte marker troponin as well as Cx43, Western blotting to determine the total Cx43 protein levels, and calcium imaging. The media would be collected from the Western blot assigned wells for toxilight assays. All of these experiments would be conducted with an untreated, vehicle, 1.0 µM, and 10 µM DOX. An illustrative overview is displayed in Figure 42B.

A) Defrost cells by 4 minutes at 37°C waterbath

1mL pipette 4/5 droplets / second
Gently shake simultaniously

Add 4 mL RT plating medium over 50-60 seconds while shaking

Invert 2-3 times gently

Centrifugation

180 x g for 5 minutes

Resuspend

Plate cells for experiments
96-well plate

50% plating efficiency

B)

	Untreated	Vehicle	1.0 µM	10 µM	Control	Untreated	Untreated	Untreated	Untreated
Immunofluorescent imaging	●	●	●	●	●	●	●	●	●
Western blotting / Toxilight	●	●	●	●					
Calcium imaging	●	●	●	●					

Figure 42 - Overview of experimental design of iCell cardiomyocytes

A) *Schematic overview of defrosting and handling steps, prior plating iCell cardiomyocyte cells.* ***B)*** *Experimental design with iCell cardiomyocytes.*

There are two types of media used for culturing iCell cardiomyocytes, including plating and maintenance medium. The plating medium is used in the process of plating the cells, which should be replaced by maintenance medium after 4 to 24 hours of incubation. In order to monitor the process of culturing the iCell cardiomyocytes brightfield images were acquired. Difficulties arose during the culture process of the P1 iCell cardiomyocytes as just a few cells attached to the bottom of the plate within 12 hours. As many cells remained detached the plating medium was not replaced with maintenance medium. In contrast, the P2 iCell cardiomyocytes attached within 12 hours after plating and resulted in a contractile monolayer within 48 hours. The brightfield images displaying the cell attachment are shown Figure 43A. Videos of the contraction differences between the P1 and P2 cells are shown in Figure 43B and illustrated in Figure 43C.

Next to the optimisation of culturing iCell monolayers, spheroids were generated with the residual cells from the defrosted vial. Spheroids consisting only P2 iCell cardiomyocytes, but also with additional hCFs and HUVECs (Figure 43D) were generated. Brightfield images of the spheroids were acquired and revealed a different shape when compared with AC16 (Figure 43E). The iCell cardiomyocyte only spheroid had no desired spherical shape in contrast to the triple cardiac spheroid consisting of iCell or AC16 / hCF / HUVEC. This data suggests the presence of other cell types are required for the development of the spherical shape. The iCell only and triple cardiac spheroids with iCells gained both contractile properties (Figure 43F)

A)

B)

C)

P1: no media replacement

Plating: 100.000 cells / well

Some cells contract but no monolayer was established after 96 hours

P2: replaced media after 12 hours

Plating: 100.000 cells / well

Most cells adhered and contracted within 24 hours

D)

iCell only

iCell / HUVEC / hCF

AC16 / HUVEC / hCF

500 µm

E)

iCell cardiomyocytes

iCell / hCF / HUVEC
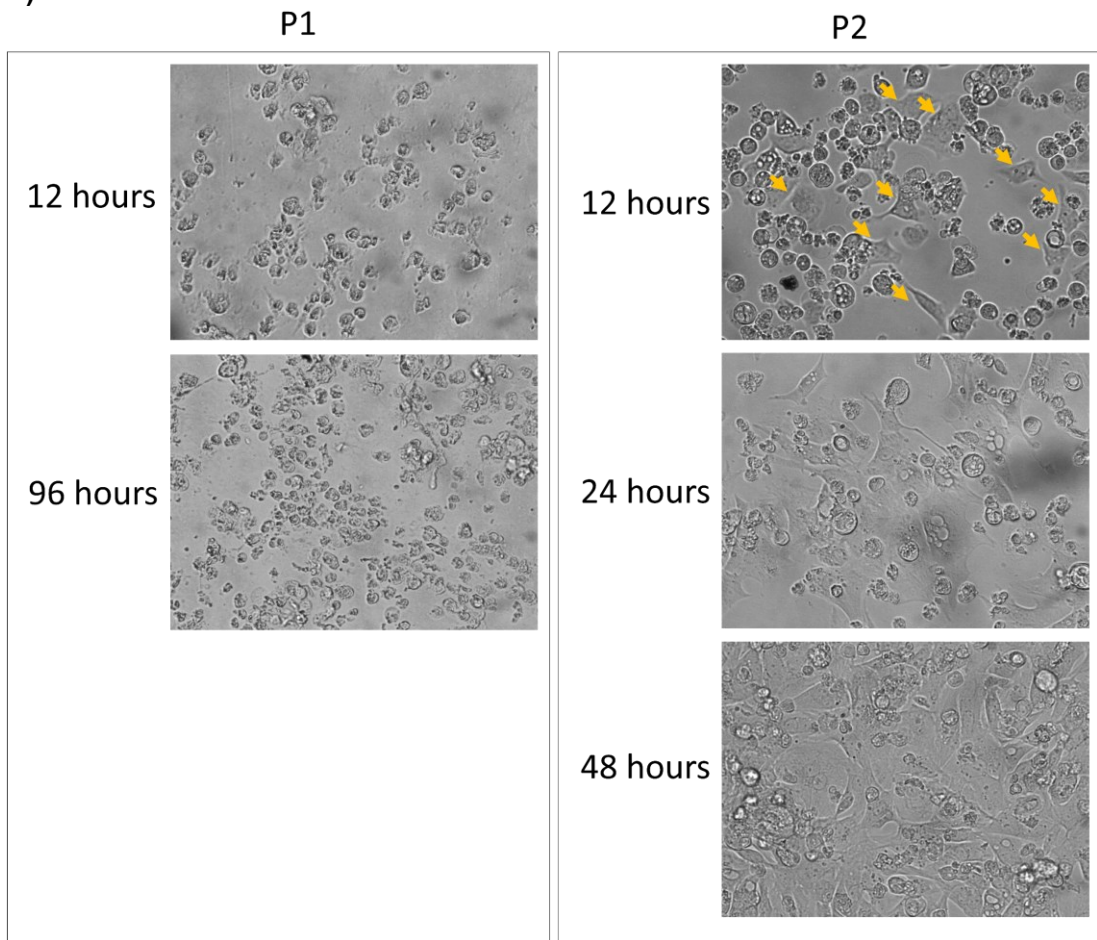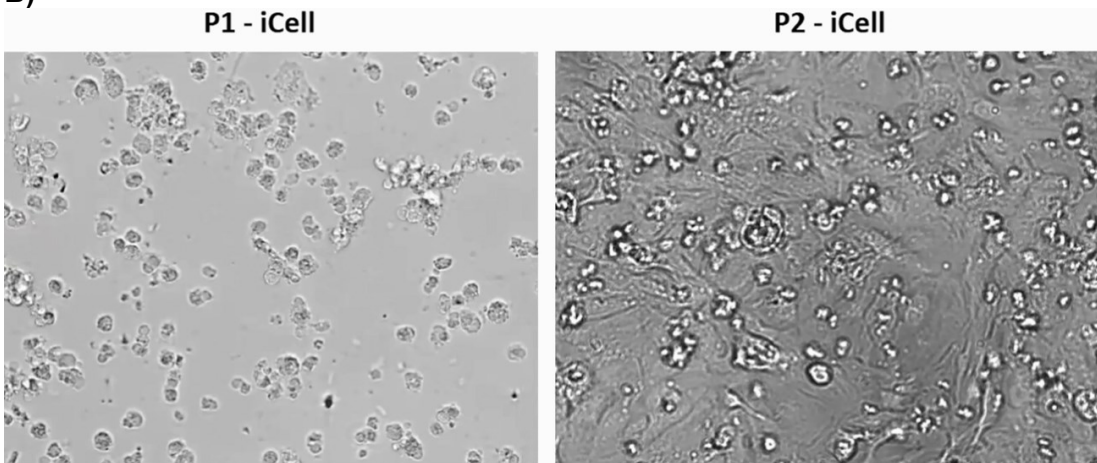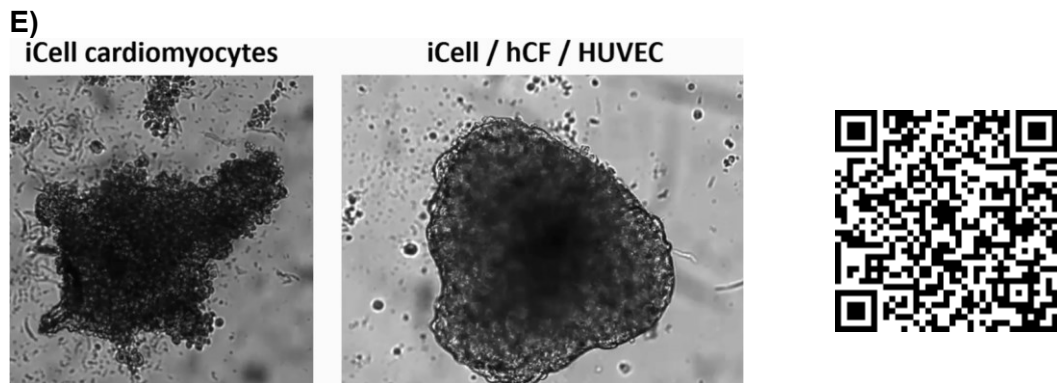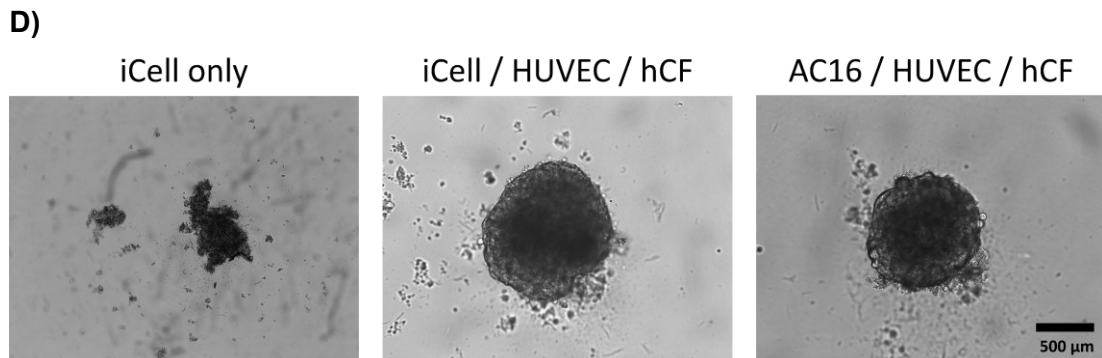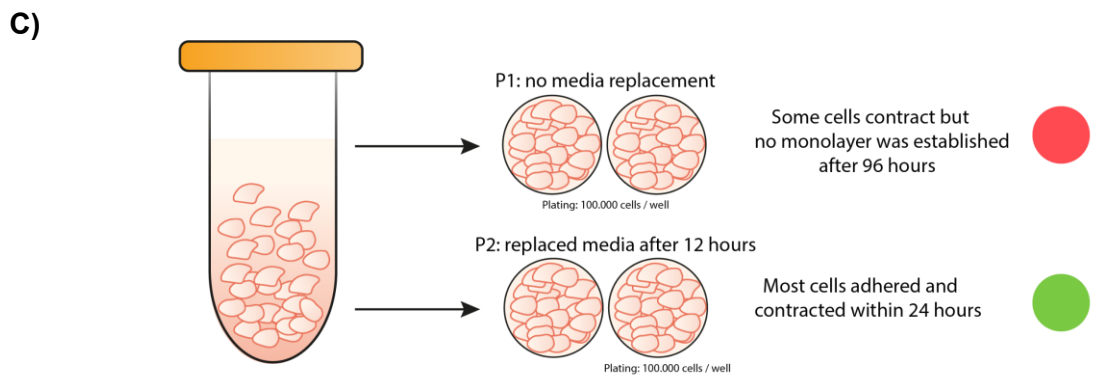
Figure 43 - Optimisation of culturing iCell cardiomyocytes

A) P1 iCell cardiomyocytes show a lower plating efficiency in comparison to the P2 cells. Attached cells are marked with orange-coloured arrows. *B)* Video showing contractility in the P2 iCell cardiomyocytes. The video is accessible through the QR-code. *C)* Illustration of plating and contractility differences between P1 and P2 iCell cardiomyocytes. *D)* Spheroid generation with iCell cardiomyocytes only, iCell / HUVEC / hCF, and AC16 / HUVEC / hCF combinations. *E)* Video of showing contractility of the spheroids. The videos are accessible through the QR-code. n = 1.

4.6 Calcium imaging of iCell monolayer

To follow-up the contractile properties of the iCell cardiomyocytes optimisation studies were performed using Cal-520 calcium imaging. Cal-520 AM is a well-known fluorogenic calcium-sensitive dye that is frequently used to study calcium signalling (Daily *et al.*, 2017; Kopljar *et al.*, 2018). The cells are pre-loaded with the Cal-520 AM which can cross the plasma membrane and is intracellularly cleaved by esterase enzymes and therefore remains within the cell. The fluorescent emission intensifies after interacting with calcium and result in a measurable signal. The P2 iCell cardiomyocytes were used to determine the effect of DOX on the intracellular calcium signalling as well as contractility. The normalised Cal520 levels were altered in response to DOX which is shown in Figure 44A. The amplitude was significantly altered ($0 < 0.05$) as a decrease observed in response to DOX (Figure 44B). In addition, the FWHM response was significantly decreased ($p < 0.0001$) in response to DOX (Figure 44C). The decrease of the FWHM correlates with a shortened duration of the calcium release and with significant increased frequency of contraction ($p < 0.0001$, Figure 44D). However, no significant changes in the rise time ($p > 0.05$) were observed that indicates the L-type calcium channels are not affected (Figure 44E). A video of the Cal520 calcium imaging is shown in Figure 44F.
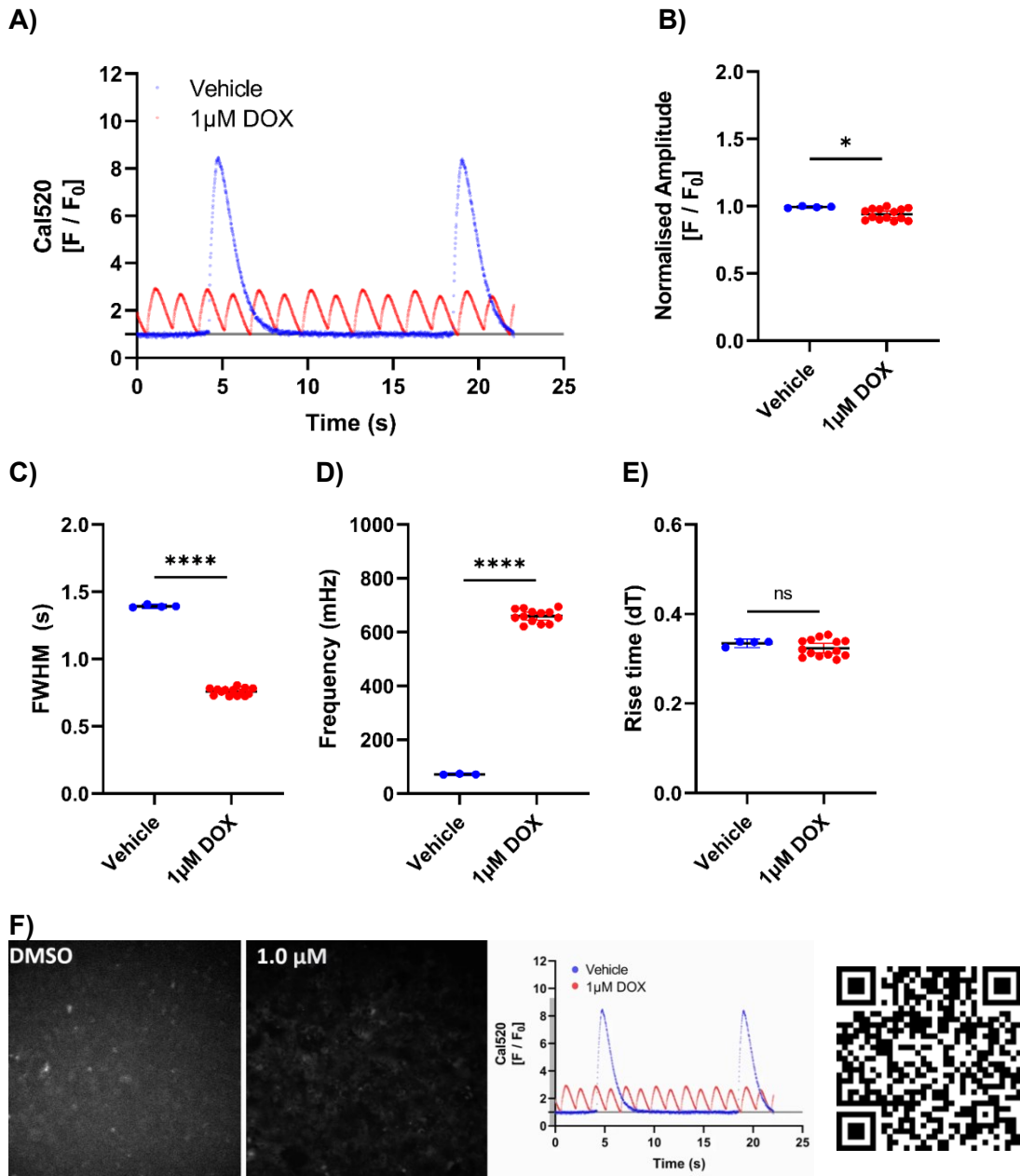
Figure 44 - Calcium imaging on iCell cardiomyocytes in response to DOX

A) Cal-520 normalised signal intensity of iCell cardiomyocytes treated with vehicle and DOX. B) Normalised amplitude. C) FWHM in seconds (s). D) Frequency of calcium oscillation in mHz. E) The rise time (dT). F) Video of calcium imaging which is accessible through the QR-code. The statistical differences were identified by using the student's T-test. **** $p < 0.0001$; * $p < 0.05$, ns = not significant, compared to the control group (n = 1).

4.7 Calcium and brightfield imaging in iCell spheroids

After conducting Cal-520 calcium imaging on iCell cardiomyocytes in a 2D monolayer system, experiments were then performed on the 3D cardiac spheroid model. For optimisation purposes, the signal of calcium fluorescence and contraction by brightfield images was compared. These experiments were conducted on iCell only spheroids. Four random regions within the spheroid were selected in order to perform post-analysis for Cal-520 and brightfield comparison (Figure 45A-B).

The overall signal intensity of Cal-520 and brightfield were normalised by F / F_0, which is shown in Figure 45C. The overall intensity of the Cal-520 calcium imaging showed a decline which had to be post-processed. The brightfield imaging results, however, revealed a notable signal-to-noise ratio. The background noise was removed when the signal intensity was analysed within the different selected regions (Figure 45D). Figure 45E identified an identical trend of decline of the signal intensity in the Cal-520 imaging from the four selected regions when compared to the overall intensity in Figure 45C.

Before the Cal-520 results could be compared the brightfield contraction was the baseline extracted from the Cal520 which is shown in Figure 45F. The Cal-520 baseline extracted data was compared to the brightfield data and as expected, no significant difference ($p > 0.05$) was identified in frequency (Figure 45G-H). Figure 45I show a video of the brightfield and Cal-520 imaging.
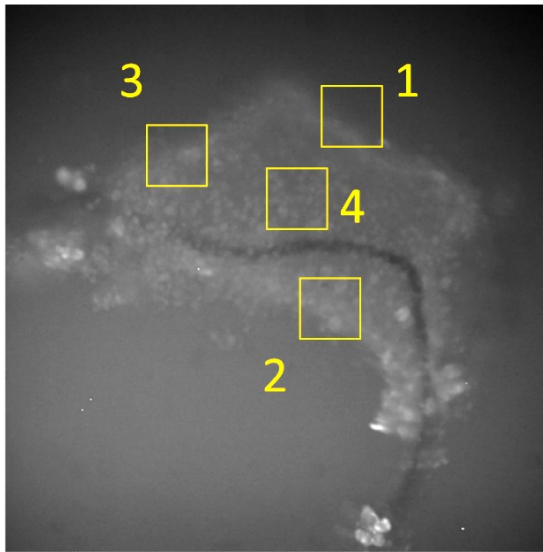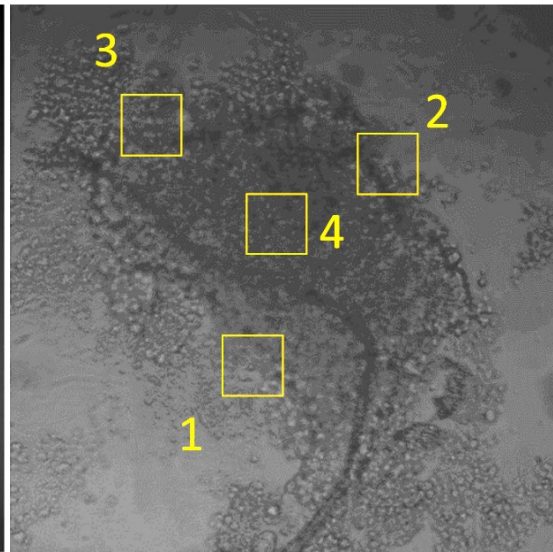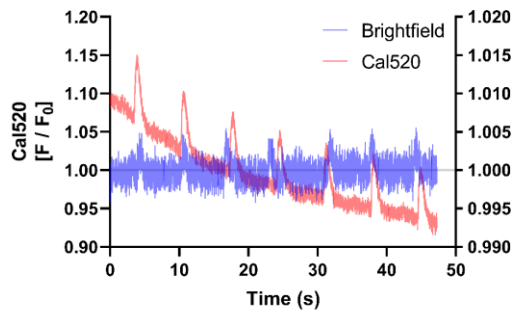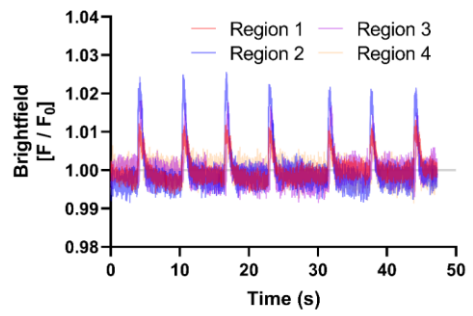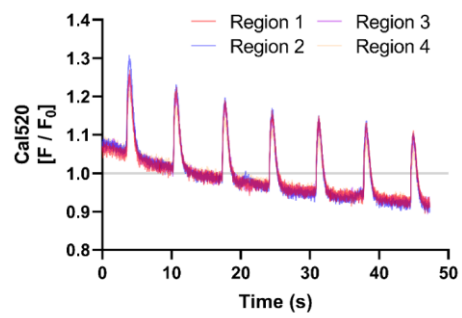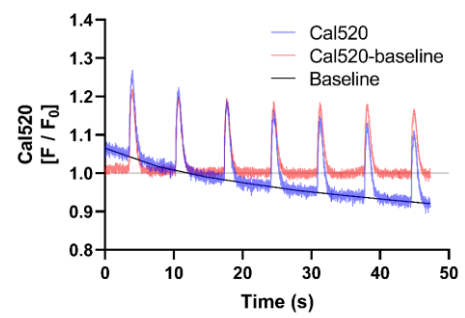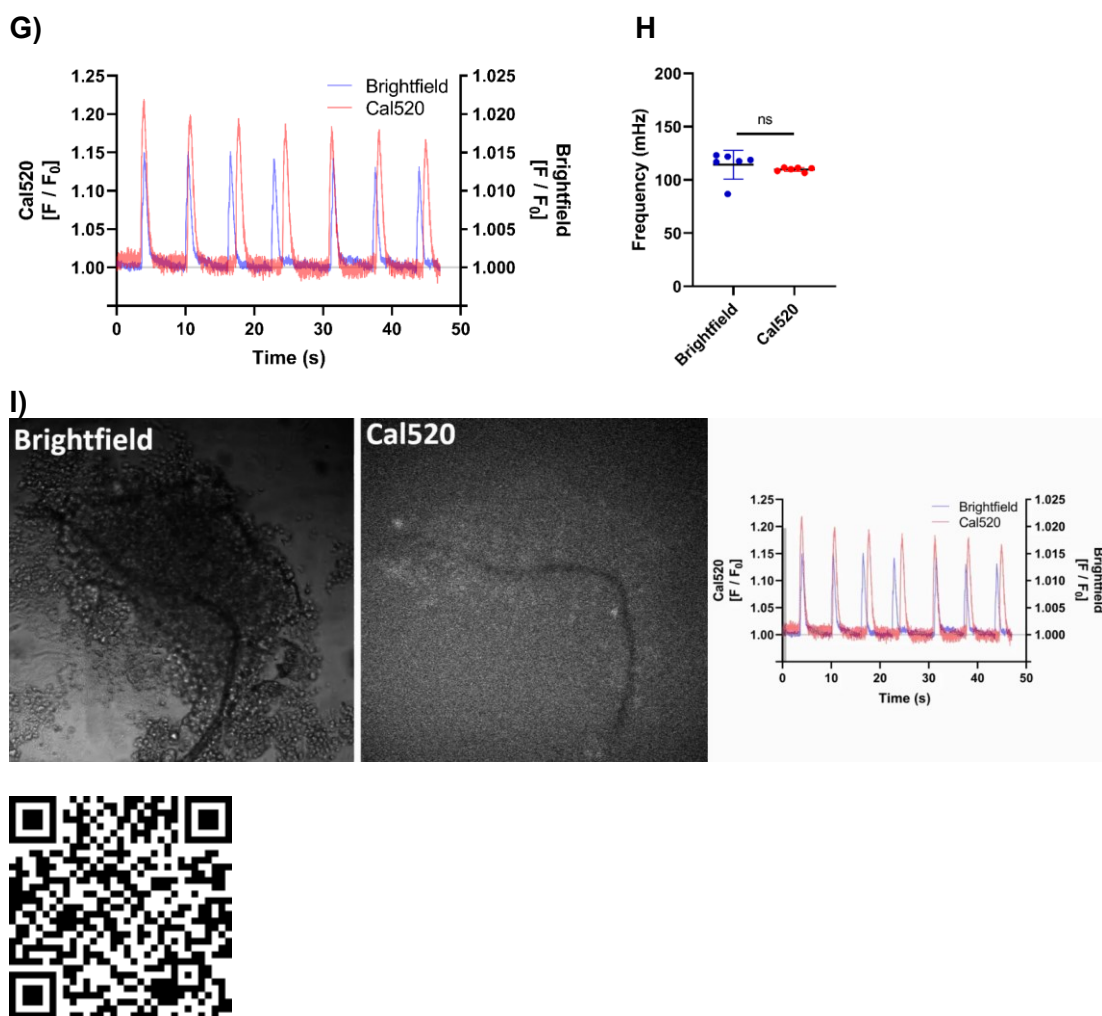
Figure 45 - Comparison of brightfield versus Cal520

A) Representative image of the spheroid during Cal520 imaging. B) Brightfield image of the spheroid. C) Total signal intensity (F/F0) of the Cal520 imaging and spheroid contraction measured by brightfield imaging. D) Contraction measured through brightfield images acquired at the four different regions, highlighted by the yellow-coloured boxes in B. E) Contraction measured through Cal520 imaging from four different regions, highlighted by the yellow-coloured boxes in B. F) Baseline extraction of the Cal520 calcium imaging intensity. G) Comparison of frequency of contraction measured by Cal520 and brightfield imaging. H) Quantified frequency in mHz of contraction by Cal520 and brightfield imaging. I) Video of brightfield and Cal520 imaging which are accessible through the QR-code. The statistical differences were identified by using the student's T-test. ns = not significant, compared to the control group. n = 1.

After comparing the Cal-520 and brightfield imaging, the iCell cardiomyocyte spheroids were treated with DOX. Brightfield images were acquired of the iCell only spheroids and were develop into a video to show the effect of DOX on the contraction (Figure 46A). Differences were identified within the contraction as the frequency was decreased in response to DOX (Figure 46B). Moreover, the rise time and FWHM response were altered as an increase was observed in comparison to the vehicle (Figure 46C-D).
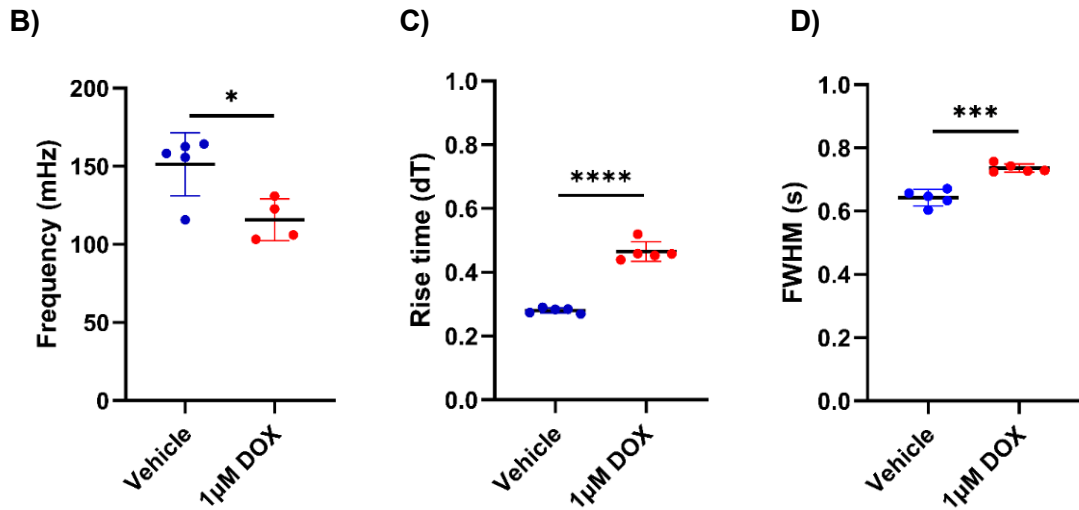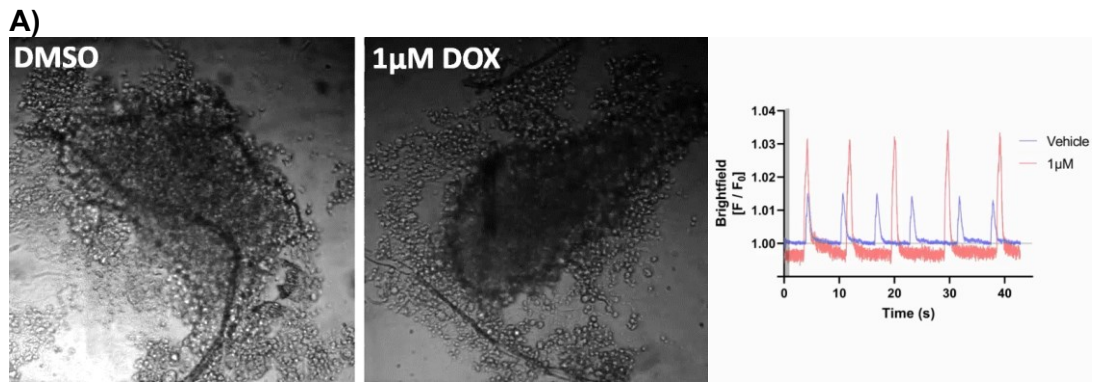
Figure 46 - Effect of DOX on iCell spheroid contractility

A) *The video of contraction by brightfield acquisition is accessible through the QR-code.* **B)** *Comparison of frequency in mHz.* **C)** *Rise time (dT).* **D)** *FWHM response in seconds. n = 1.*

4.8 Discussion

The aim of this chapter was to investigate the effect of DOX on Cx43 expression in the Langendorff model, to optimise 3D spheroid culture and post-processing. The Langendorff perfused rat hearts were treated with DOX and revealed interesting changes of Cx43.

Firstly, three different phosphorylation states of Cx43 were identified by Western blotting, namely P0, P1, and P2 which is supported by other studies (Kalcheva *et al.*, 2007; Solan and Lampe, 2007; Hesketh *et al.*, 2010; Rodríguez-Sinovas *et al.*, 2021). The DOX treatment revealed discrete changes in total Cx43 protein levels compared to vehicle-treated hearts. The P1/P2 bands were enhanced within the ventricular tissue, suggesting that DOX promotes phosphorylation of Cx43 (Hesketh *et al.*, 2010; Rodríguez-Sinovas *et al.*, 2021). The elevated Cx43 P1/P2 expression in response to DOX coincided with the lateralisation of the Cx43 protein in the cardiomyocytes. The effects of DOX on Cx43 protein expression within the Langendorff perfused rat hearts are illustrated in Figure 47. This data suggests that DOX mediates lateralisation through alteration of the Cx43 phosphorylation status. For future studies, we would suggest investigating the phosphorylation status of Ser-368 and Ser-373 initially. The phosphorylation of these sites is associated with the internalization of Cx43 (Jozwiak and Dhein, 2008; Dunn and Lampe, 2014; Del Ry *et al.*, 2015).

Control   **DOX**
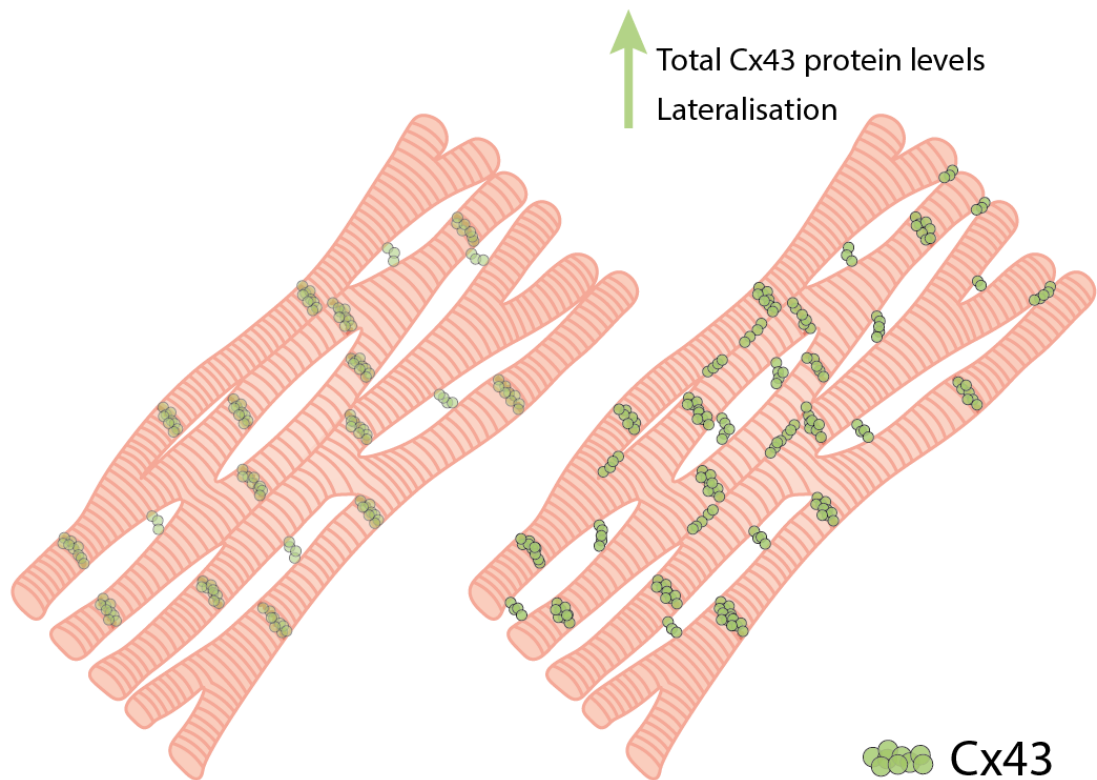
Figure 47 - Effect DOX on Cx43 in Langendorff perfused rat hearts

Illustrative overview of Langendorff perfused hearts with DOX show increased total Cx43 protein levels and caused lateralisation within the cardiomyocytes.

The results from the Langendorff perfusion led to the implementation of 3D multicellular cardiac spheroids. A study compared 2D with 3D cell cultures and described the limitations of 2D culture, which included the disturbance of interactions between cellular and extracellular environments, polarity, method of cell division as well as changes in cell morphology (Kapałczyńska *et al.*, 2018). To closer represent in-vivo, 3D cultures such as spheroids and organoids are becoming more common practice. Further benefits of 3D spheroid culture are the use of different cell types to introduce paracrine communication between cells. An example of this is the formation of 3D spheroids comprised of endothelial, fibroblast, and cardiomyocyte cells to represent a "heart in a dish" (Polonchuk *et al.*, 2017; Beauchamp *et al.*, 2020; Andrysiak, Stępniewski and Dulak, 2021). This model was used in this investigation to further assess the impact of DOX treatment upon cardiac cell Cx43 expression and localisation.

In our studies we have optimised the process for spheroid formation, culture, and maintenance. Immunofluorescent imaging was performed by using confocal as well as light sheet microscopy on the cardiac spheroids, but difficulties were identified in resolving Cx43 localisation in this model (Figure 40). No clear 3D images could be acquired on the confocal system which could be due to the limitations of the imaging system. Therefore the spheroids were additionally imaged on a light sheet microscope with limited success. Prior further imaging, the clearance and staining of the spheroids will need to be optimised first. Once optimised, the immunofluorescent imaging could be important to identify the different cell localisations within the spheroid. In our studies we have previously identified cell specific markers, which are described in Chapter 3. An overview of the different markers that were identified in each cell type, based on the work conducted in Chapter three, with corresponding literature is shown

in Table 12. In this way, the different markers could be used also to identify the number of each cell within the spheroid over time of growth. It is possible different cells have different cell replication rates and could thereby become the major cell type and change the cell ratio. These studies would be conducted once the clearance of the spheroids is optimised. A study created spheroids with endothelial cells, fibroblasts and cardiomyocytes (Polonchuk *et al.*, 2017). Their research identified vascularisation by using the endothelial marker platelet endothelial cell adhesion molecule (PECAM) to characterise the endothelial cells.

Table 12 - Overview of identified cellular markers for cardiac spheroid cell types

Cell type	Vimentin	vWF	α-SMC actin	Troponin
HUVECs	+	+	-	-
AC16	-	-	-	+[1]
hCFs	+	-	-	-
iCells	-[2]	-	-	+[3]

HUVEC; Human Umbilical Vascular Endothelial Cell, hCF ; human Cardiac Fibroblast, MFB; Myofibroblast, vWF ; von Willebrand Factor, α-SMC ; alpha Smooth Muscle Cell. [1](Davidson et al., 2005), [2](Beauchamp et al., 2020), [3](Andrysiak, Stępniewski and Dulak, 2021).

Despite the efforts on the imaging of the cardiac spheroids, we evaluated the effect of DOX on the Cx43 levels which resulted in no effect (Figure 41). Previous studies have demonstrated that Cx43 plays a role in maintaining healthy spheroids (Dovmark *et al.*, 2017, 2018; Gong *et al.*, 2022). For example, a study in cancer spheroids by the Gong group showed Cx43 involvement in glucose transfer into the core of the spheroid (Gong et al., 2022). These results contribute to overcome nutrient limitations and favour tumour sustainability and growth of the spheroids. The Cx43 protein levels were also increased in response to glucose deprivation in H9C2 cardiomyoblast cells (Wang et al., 2018). Moreover, within spheroids, Cx43 gap junction channels are proposed to play a role in facilitating the exchange of lactate from the more hypoxic inner core in glycolytic pancreatic ductal adenocarcinoma cells (Dovmark *et al.*, 2017, 2018). Therefore, Cx43 channels could be advantageous for highly proliferating cancer cells and could be a potential therapeutic target. Additionally, Cx43 is also associated with fibrosis and several mimetic peptides have been proposed as potential therapeutics, including Cx43 degenerative disorders, some even reaching human clinical trials (Marsh *et al.*, 2021). Moreover, Cx43 improves infarcted heart angiogenesis, as evidenced by higher levels of VEGF and basic fibroblast growth factor (Wang *et al.*, 2014). The coupling between fibroblasts and cardiomyocytes could be potentially used for therapeutic interventions (Ongstad and Kohl, 2016).The Figtree group demonstrated that cardiac spheroids could be used to study cardiac fibrosis and they have showed that DOX triggered apoptosis and disrupts vascular networks within cardiac spheroids models (Figtree *et al.*, 2017). Our studies could contribute to the investigation of DOX on spheroids and what the role is of Cx43 expression.

In our studies we have identified differences in spheroid contractility in response to DOX, as described in section 4.7. The measurement of contraction through brightfield imaging has been previously evaluated in other studies (Oltolina *et al.*, 2015; Richards *et al.*, 2017; Kitsuka *et al.*, 2019; Qian *et al.*, 2020). Noteworthy is the difference between the contraction frequency between the iCell cardiomyocyte monolayer and 3D cardiac spheroid in response to DOX. The contraction frequency was significantly increased in 2D monolayer iCell cardiomyocytes (Figure 44), whereas the frequency of the 3D iCell spheroid was significantly decreased (Figure 46). The controversial effect of DOX on the calcium homeostasis has been previously described (Mitry and Edwards, 2016). DOX treated hearts introduced a decreased calcium storage capacity within mitochondria through activation of calcium channels, resulting in a calcium overload. These effects could introduced mitochondrial dysfunction and cellular apoptosis (Zhou, Heller and Wallace, 2001). Calcium plays a key role within muscle contraction and therefore would a decrease of intracellular calcium levels be associated with decreased contractility.

The type of surface for culturing iCell cardiomyocytes could give rise to differences in the contraction duration. Rigid biomaterial surfaces have recently been shown to introduce unphysiological multiphasic contractions (Huethorst *et al.*, 2022). In our studies we have not identified a bi-phasic contraction, however it is key to keep in mind that different surfaces could cause alterations in contractility.

So far, we have assessed the impact of DOX on Cx43 expression in singular cardiac cell types, Langendorff perfused rat hearts, and in cardiac spheroids. Next to the cardiovascular system is Cx43 expression also associated with cancer (Teleki *et al.*, 2014; Aasen *et al.*, 2018, 2019; Mulkearns-Hubert, Reizes and Lathia, 2020). The

next chapter will focus whether similar changes occur within the cancer cell setting and if the effects of DOX on the cancer cells are associated with DOX-induced cardiotoxicity.

4.9 Conclusion

Within this chapter we have identified Cx43 lateralisation alongside increased total protein levels by performing Langendorff perfusion on rat hearts with DOX. This is novel data, therefore could our research contribute to get a better understanding of the molecular mechanisms in DOX-induced cardiotoxicity. The optimisation of the 2D monolayer and multicellular 3D spheroid system has been conducted with iCell cardiomyocytes with success as contractility was observed. These cardiac spheroid models could be used for future optimisations regarding immunofluorescent imaging and discovering the effects of DOX on the Cx43 localisation within these models. However differences in iCell cardiomyocyte contractility were observed in response to DOX, more research will be required whether to determine if these changes are 2D or 3D model dependent and to discover the role is of Cx43.

CHAPTER FIVE:

INVESTIGATING THE EFFECT OF DOX ON BREAST

CANCER CELL CELLS AND EXTRACELLULAR

VESICLE RELEASE

5.1   Introduction

The aim of this chapter was to investigate the impact of DOX on Cx43 in triple negative breast cancer cells. It is imperative, in addition to evaluating the impact of DOX on the cardiovascular system, to also conduct an assessment of DOX's influence on cancer cells. The potential contribution of DOX's effects on cancer cells to the development of cardiovascular complications in response to the drug must be thoroughly examined. As well as being linked to cardiovascular dysfunction, changes in connexin expression are also associated with cancer as these proteins have been shown to act either as tumour suppressors or tumour promoters depending on the isoform, cancer stage and tissue, ultimately resulting in either a favourable or unfavourable prognosis (Teleki *et al.*, 2014; Murphy *et al.*, 2016; Aasen *et al.*, 2019). Gap junction intercellular communication inhibitor oleamide has been shown to have anti-metastatic activity in MDA-MB-231 triple negative breast cancers cells and thereby supports a role of GJIC in cancer cell extravasation (Zibara *et al.*, 2015). In addition, Cx43 overexpression has been shown to enhance the sensitivity of DOX and to suppress tumour angiogenesis in breast cancer cells (Huang *et al.*, 2001; W. K. Wang *et al.*, 2014; Liu *et al.*, 2015). Other studies have also utilized 2D monolayer and 3D spheroid models with MDA-MB-231 cells to investigate the effect of glucose on Cx43, which could contribute to the maintenance of a healthy spheroid (Dovmark *et al.*, 2017, 2018; Wang *et al.*, 2018; Jones *et al.*, 2021; Gong *et al.*, 2022).

There is also evidence that connexins could facilitate short and long-range communication through extracellular vesicles and exosomes. For example, a study revealed a role for Cx43 in facilitating cargo transfer and internalisation (Soares et al., 2015). Extracellular vesicles are composed of a lipid-bilayer and are released from cells. They can be classified as exosomes (30-200nm) and microvesicles (100-

1000nm). Exosomes originate from the endocytic machinery, in contrast to microvesicles which bud off the plasma membrane (Gurung et al., 2021). The cargo of these extracellular vesicles include lipids, miRNAs, and nucleic acids (Becker *et al.*, 2016; Bebelman *et al.*, 2018; Zhang and Yu, 2019).

This chapter focusses on the effect of DOX on Cx43 in breast cancer cells. The MDA-MB-231 breast cancer cells were characterised on their morphology and Cx43 expression. The impact of DOX on the cell viability was investigated and resulted in a higher IC50 value when compared to the cardiac cells described in the previous chapters. Interestingly, data has shown a role for DOX in the release of extracellular vesicles and exosomes. Optimisation of Cx43 knockout and overexpression were successfully performed.

5.2   *Characterisation of MDA-MB-231 breast cancer cells*

M.D. Anderson Metastasis Breast Cancer (MDA-MB) 231 is an epithelial cell line which was obtained from a pleural effusion from a 51-year old female with a metastatic mammary adenocarcinoma (Cailleau et al., 1978). The human breast cancer cell line is triple negative, which means there is no expression of oestrogen receptor (ER), progesterone receptor (PR), and HER-2. Different types of studies have previously been conducted by other researchers on Cx43 in MDA-MB-231 cells (Zibara *et al.*, 2015; Jones *et al.*, 2021).

Firstly the morphology was assessed of the MDA-MB-231 cells. This resulted in characteristic spindle-shaped cells, but also rounded cells were observed within culture (Figure 48A). The shape of the cells was identical with the supplier ATCC (*MDA-MB-231 - HTB-26, ATCC*). The morphology characterisation was followed-up by identifying Cx43 within the MDA-MB-231 cells. Localisation studies showed the absence of Cx43 protein on the plasma membrane but appears to be present as small punctae in the cytosol of the cells (Figure 48B).
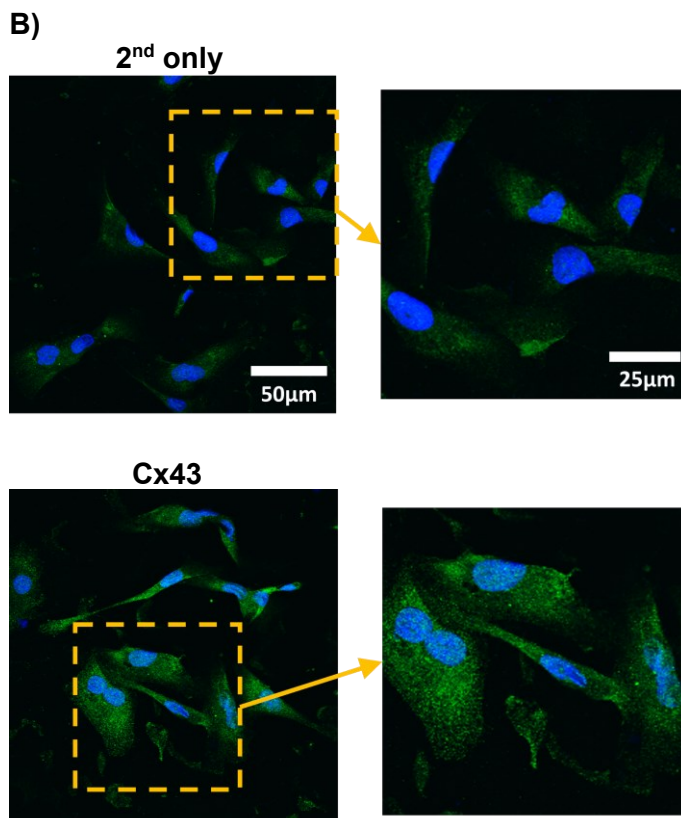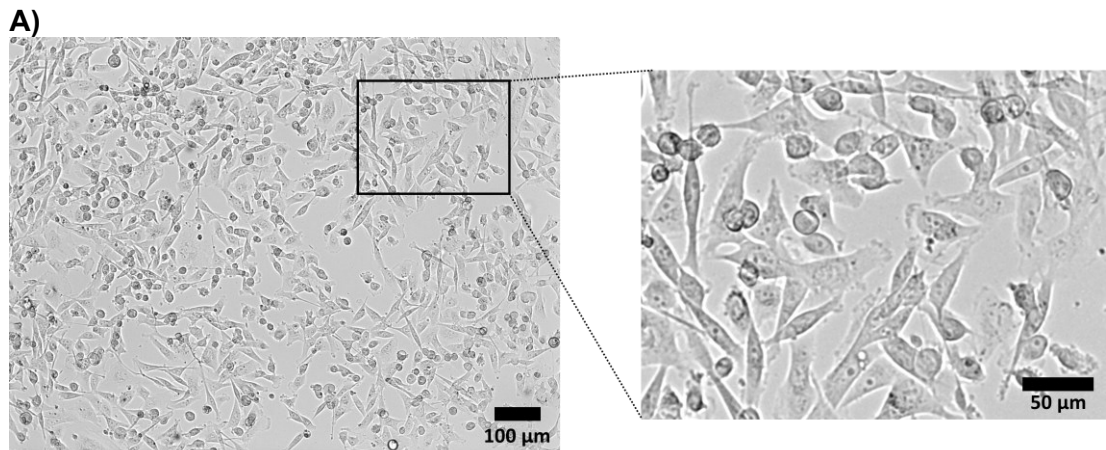
Figure 48 - Characterisation of MDA-MB-231 cells

A) Brightfield image of MDA-MB-231 cells. B) Immunofluorescent imaging in MDA-MB-231 cells revealed intracellular localisation of Cx43 (green). DAPI was used as a nuclear counterstain (blue). n = 5.

5.3   *Cell viability of MDA-MB-231 cells in response to DOX*

After the characterisation of the MDA-MB-231 triple negative breast cancer cells, studies were conducted with DOX. The morphology of the cells was altered in response to DOX, especially at concentrations of 3.0 µM and higher (Figure 49A). More gaps appeared between clusters of cells which was thought to be a result of cell death. Therefore cell viability assays were conducted and confirm a significant reduction of cell viability at 3.0 µM DOX in comparison to the control group ($p < 0.0001$). The development of a dose-response curve resulted in an IC50 value of 3.85 µM DOX.

A)

Control DMSO

0.1 µM 0.3 µM

1.0 µM 3.0 µM

10 µM 30 µM

100 µM

50 µm 100 µm
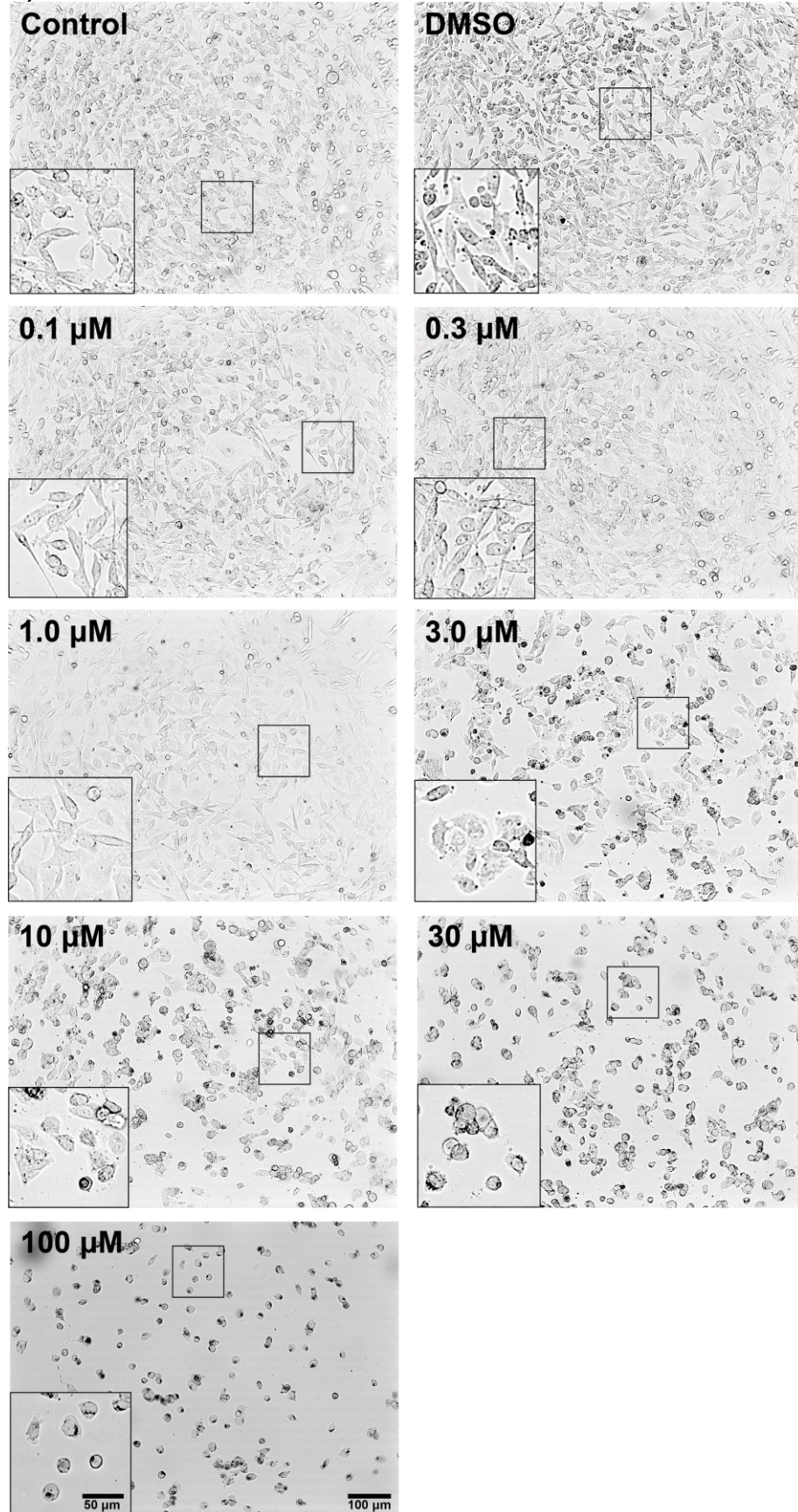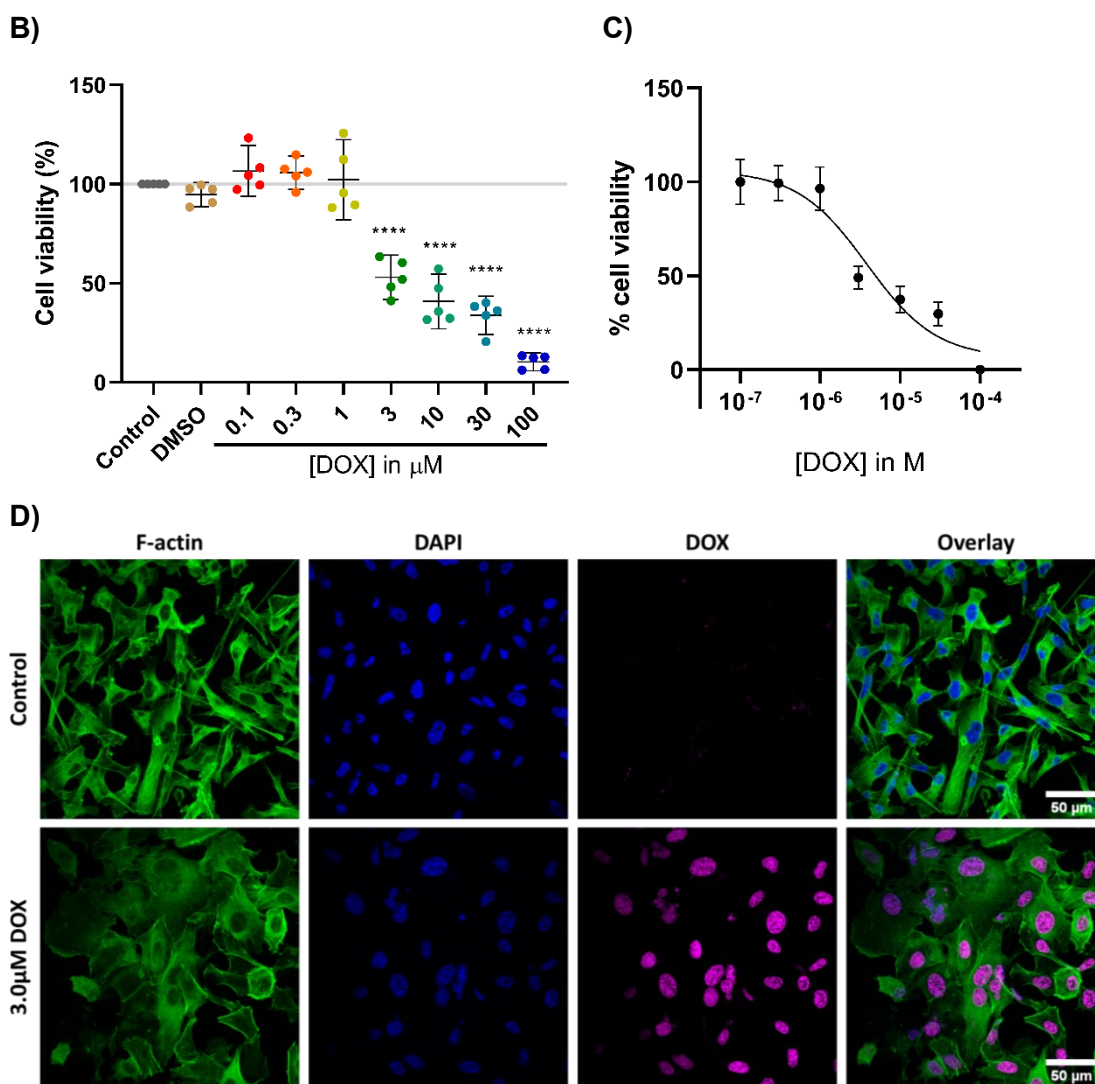
Figure 49 - Detrimental effects of DOX on MDA-MB-231 cells

A) *Representative brightfield images of 24-hour DOX (0-100 µM) treated MDA-MB-231 cells. Scalebar is 50 µm for original sized images and 25 µm for the zoomed in area. DOX concentrations over 3.0 µM resulted in morphological changes where the cells showed a more circular shape, indicating cell death.* **B)** *MTT assay revealed a significant decrease in cell viability at > 3.0 µM in comparison to the control group (**** $p \leq 0.0001$, n = 6).* **C)** *Dose response curve of MTT assay resulted in a IC50 of 3.85 µM (2.50 µM - 6.11 µM, 95% CI).* **D)** *Immunofluorescent images of DOX treated MDA-MB-231 cells for F-actin (green), DAPI (blue), and DOX (magenta) (n = 1).*

The autofluorescence properties of DOX had previously shown the localisation of the drug within the nuclear area of the endothelial and cardiac cells (see chapter 3). Identical experiments were conducted on the MDA-MB-231 cells in order to assess if the same phenomena appear within these cells. Figure 50A shows the nuclear accumulation of DOX in the nucleus, which becomes visible at a concentration of 1.0 µM (Figure 50B). Quantifications of the nuclear area confirmed the presence of DOX at a concentration of 0.3 µM with a significant increase at > 1.0 µM ($p < 0.0001$), while a significant decrease of the DAPI intensity was identified at 0.3 µM DOX in comparison to the control group ($p < 0.0001$, Figure 50C). This data supports the DNA-DOX interaction by forming a covalent bond with the guanine nucleotides. The next step was to determine whether DOX impacted the total Cx43 protein levels in MDA-MB-231 cells. The total Cx43 protein expression was evaluated and resulted in no significant differences in comparison to the control group ($p > 0.05$, Figure 50D-E).
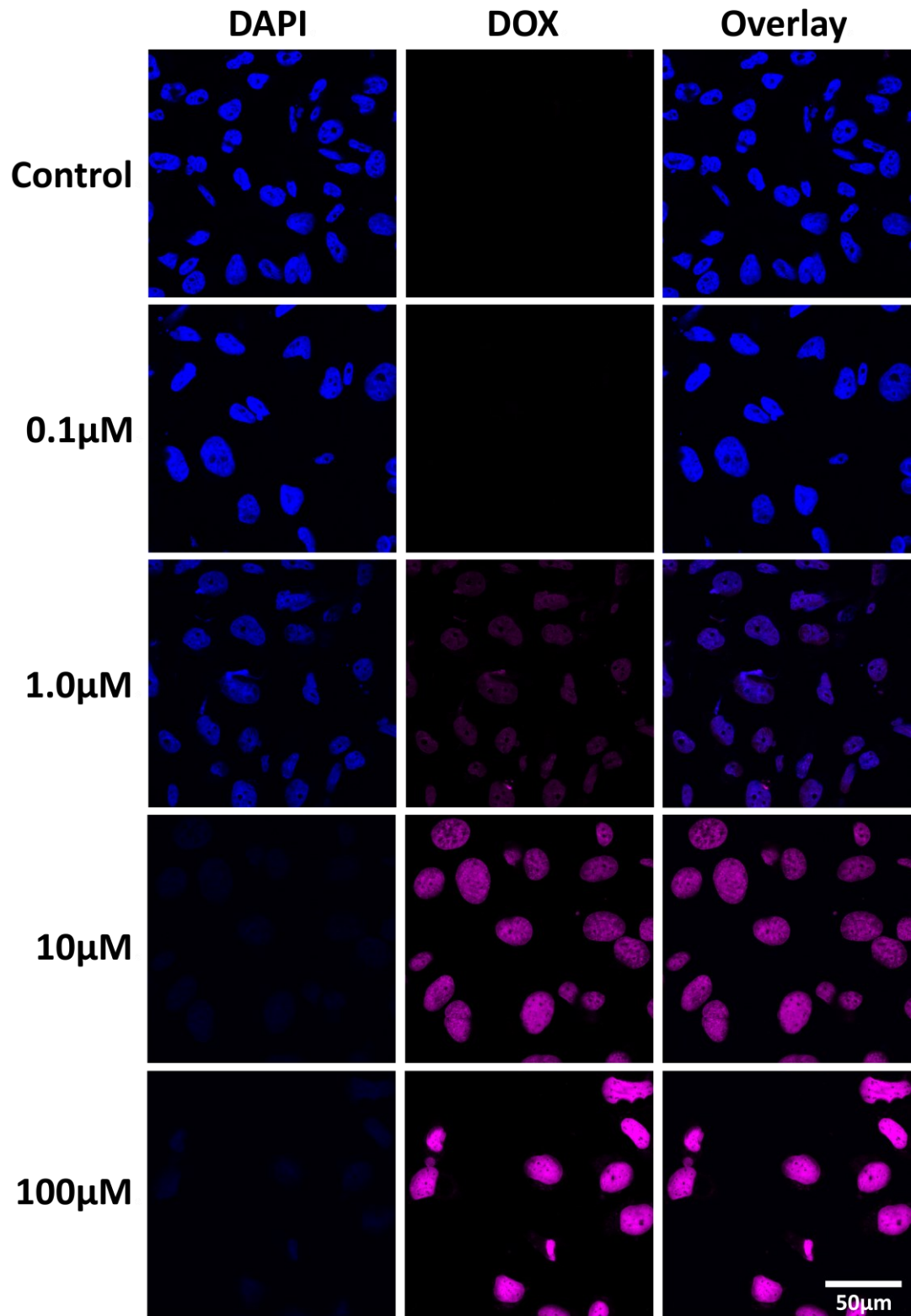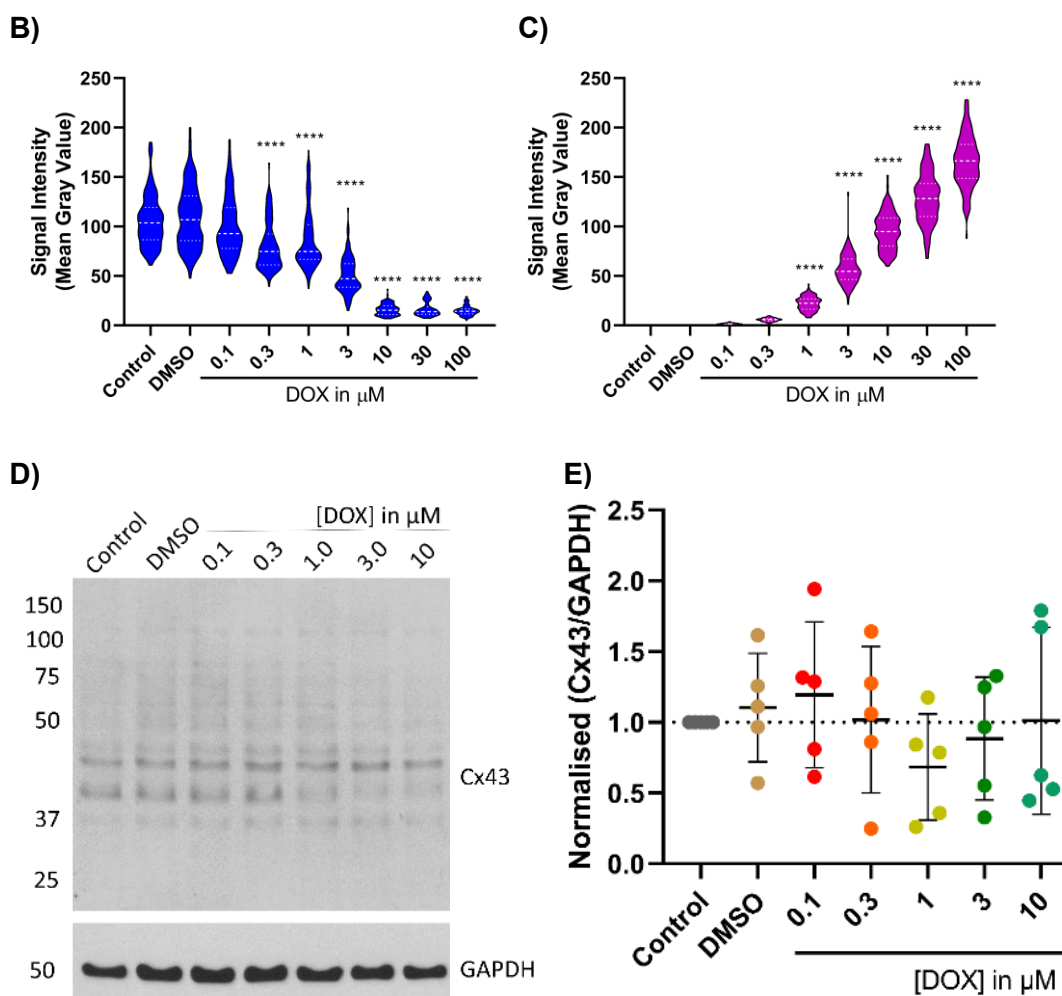
Figure 50 - Nuclear accumulation of DOX in MDA-MB-231 cells

A) Immunofluorescent imaging of MDA-MB-231 cells treated with DOX (0-100 µM) for 24 hours. DAPI (blue) was used as a nuclear counterstain and auto fluorescent properties of DOX was visualised (magenta). B) quantifications of the magenta and blue colour intensity in the nuclear regions revealed a significant DOX increase (C) nuclear localisation at > 1.0 µM (**** p ≤ 0.0001). In contrast, DAPI nuclear intensity decreased significantly at concentrations > 0.3 µM in comparison to the control group (**** p ≤ 0.0001). n = 5, for each n-number were 27 cells used for quantifications. D) Total Cx43 expression levels were determined by Western blotting and no changed in response to 24 hours DOX (0-100 µM) treatment were observed. E) Normalised total Cx43 expression levels to GAPDH (n = 5). The error bars represent ± 95% confidence interval

5.4   *Doxorubicin-mediated extracellular vesicle release in MDA-MB-231 cells*

The impact of DOX on the release of EVs and exosomal content from the MDA-MB-231 was assessed. Previous studies have shown the presence of EVs in fetal bovine serum and therefore result in difficulties in terms of researching EVs and exosomes (Lehrich *et al.*, 2018; Driedonks and Wilhaar et al., 2019; Lehrich and Liang et al., 2021).The first set of experiments was conducted to compare MDA-MB-231 cultured cells with and without the presence of serum before collecting the EVs. The serum cultured MDA-MB-231 cells showed a greater range of particle size (54-712nm) when compared to serum free (122-255nm) (Figure 51A). The greater range of the particle content is a result of the presence of serum and therefore future studies were conducted in serum free conditions. To measure the EVs and exosomes nanoparticle tracking analysis (NTA) was performed. NTA is a common technique that is used to measure particle diameter and concentration through both laser light scattering as well as Brownian motion. When MDA-MB-231 cells were treated with DOX there was a change of particle distribution within the media (Figure 51B). The control sample counted 1.29×10^8 and the DMSO sample 1.06×10^8. The particle number was significantly lower ($p < 0.0001$) in comparison to the DOX treated sample with 2.13×10^8, accounting for almost a two-fold increase in comparison to the control group (Figure 51C). This data indicates that DOX mediates release of particles from the MDA-MB-231 cells. The distribution of the particles size could be characterised with the D-values. The D90 value is the point in the distribution of size which contains 90% of the total sample volume. For example, a D90 of 150nm signifies that 90% of the sample has a size of ≤ 150 nm. This is similar to the D50 and D10 values. Interestingly only within the D10 value was a significant difference ($p < 0.0001$) observed between DMSO and DOX (Figure 51D). The span of the distribution, calculated by (D90 – D10) / D50, indicated how for the D90 and D10 points are

separated which is then normalised by the central point. No significant difference ($p > 0.05$) within the span was identified in comparison to DMSO, suggesting a similar window of particle size between the samples. The video of the NTA acquisition is displayed in Figure 51E and accessible through the QR-code in Figure 51F. The values of the particle distributions are shown in Table 13.
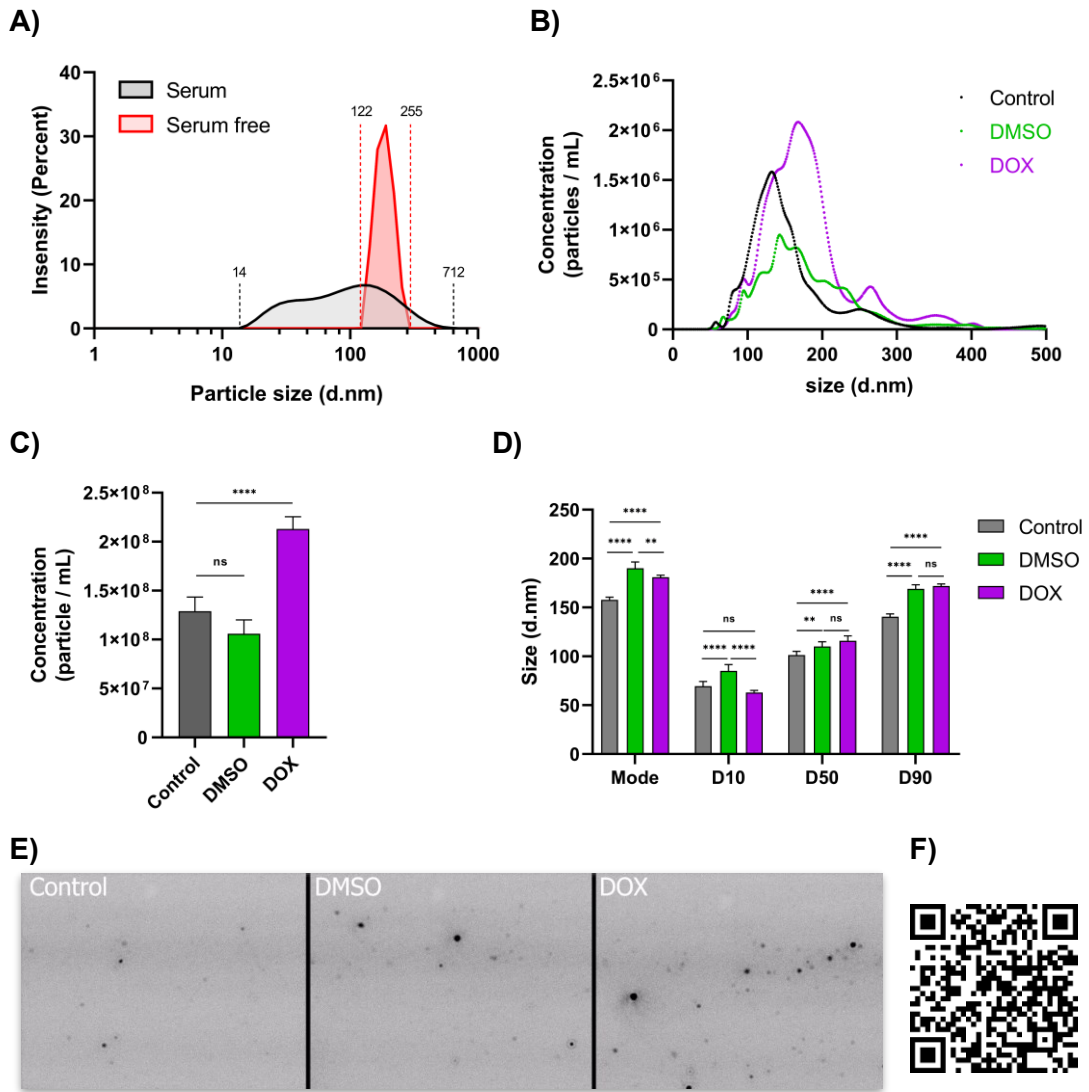
Figure 51 - DOX-mediated EV-release in MDA-MB-231 cells

*A) Nano-particle size range in the presence (14-712) and absence (122-255) of serum. B) NTA of collected EVs and exosomes from DOX and DMSO treated MDA-MB-231 cells. C) Concentration of particles / mL. D) Distribution of particles size with the mode, D10, D50, and D90. ** p ≤ 0.01, *** p ≤ 0.001, **** p ≤ 0.0001, ns = not significant. E) Representative image of NTA analysis with corresponding video which is accessible through the QR-code (F). n = 1.*

Table 13 – Distribution of nanoparticles in response to DOX

Parameter	Control	DMSO	DOX
D10 (in nm)	69	85	63
D50 (in nm)	101	110	116
D90 (in nm)	141	169	172
Mode (in nm)	158	190	181
Span (in nm)	140	168	171
particle number (x10^8)	1.29	1.06	2.13

5.5   *Cx43 knockout and overexpression studies*

To investigate the role of Cx43 in cancer cells for future studies SUM159 Cx43 knock out (KO) cells were acquired from Dr. T. Aasen from the Vall d'Hebron Institute of Research (VHIR) in Barcelona (Spain). SUM159 cells are also triple negative breast cancer cells from a mesenchymal origin. To evaluate the total Cx43 gap junctional protein levels within the wild type (WT) and KO cells, whole cell homogenates were used for Western blotting. As expected, Cx43 protein levels were present within the WT cell line and not in the KO cells (Figure 52).
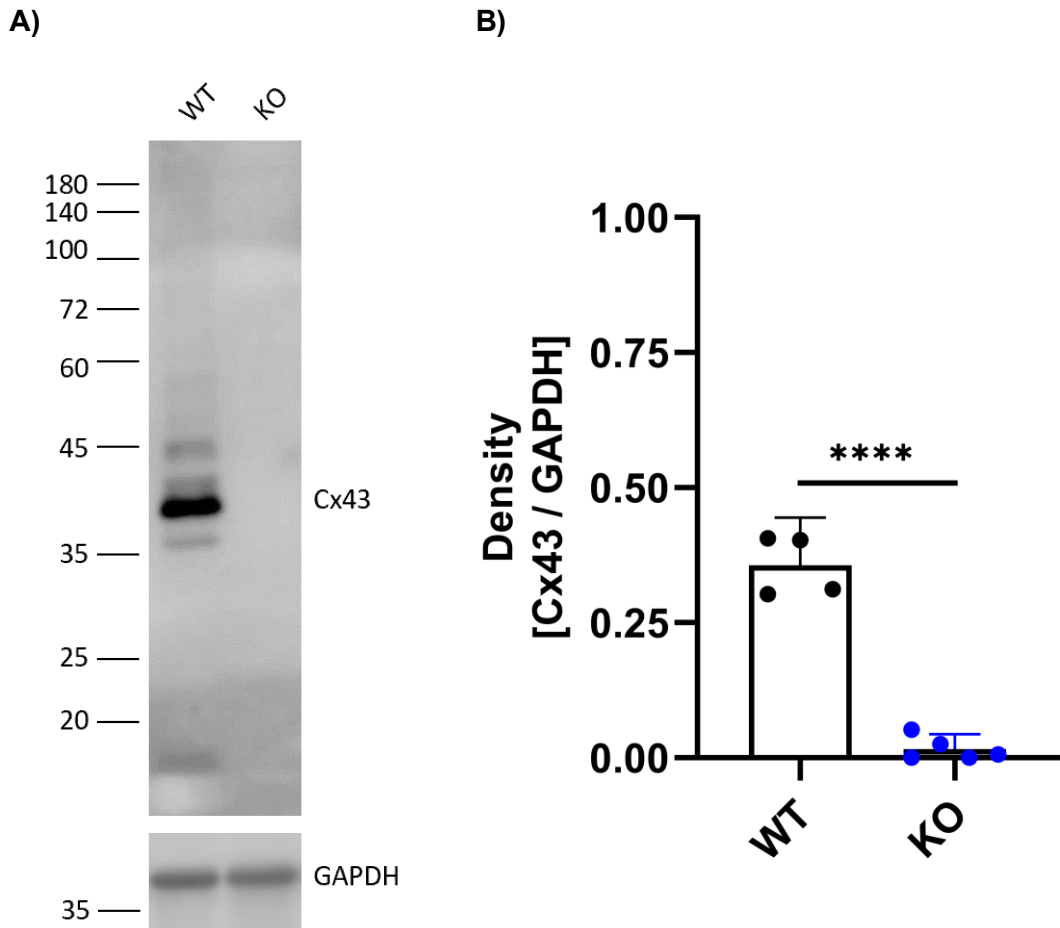
Figure 52 - Knockout of Cx43 in SUM-159 cells

A) *Western blot showing total Cx43 levels in WT and Cx43 KO SUM-159 cells.* **B)** *Levels of relative density, obtained from normalisation of Cx43 levels divided by GAPDH levels. **** p ≤ 0.0001, n = 5. WT; Wild-type, KO; Knockout.*

Next to studying Cx43 in KO models, it is also important to study overexpression models with green fluorescent protein (GFP) tagged Cx43. The pEGFP C1 Cx43 that was used in the overexpression studies was derived from Dr. H. Girão's group from the Faculty of Medicine of University of Coimbra (FMUC). The pEGFP C1 Cx43 plasmid was used for the transfections which was also previously used by the Xu group (Xu *et al*., 2012). Two different types of cell lines were used for the transfection, including the HEK293 and AC16 cells. The HEK293 line consists of an epithelial morphology from the kidney of a human embryo and is often used in studies concerning transfections. Two different techniques were compared to optimise a high transfection efficiency, including lipofectamine 2000 and 3000. Whole cell homogenates of transfected HEK293 and AC16 using lipofectamine 3000 showed a greater transfection efficiency in total GFP-Cx43 expression (Figure 53A-B).
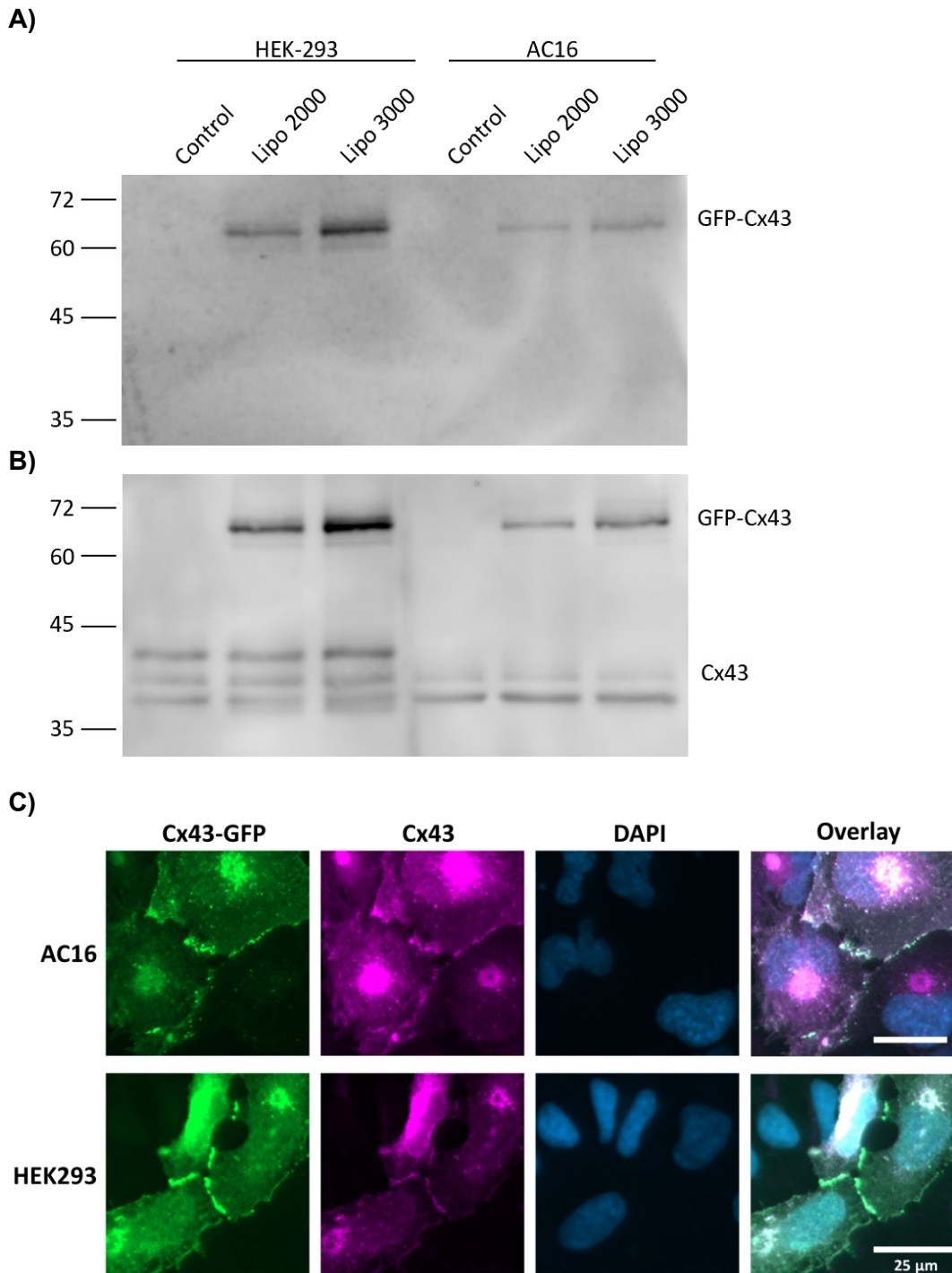
Figure 53 - Transfection of GFP-Cx43 in HEK293 and AC16 cells

Western blots for GFP-Cx43 (A) and native Cx43 (B) in transfected HEK293 and AC16 cells using lipofectamine 2000 and 3000. C) Immunofluorescent images of GFP-Cx43 (green) and endogenous Cx43 (magenta) in HEK293 and AC16 cells. DAPI was used as a nuclear counterstain (blue). The scalebar is 25 μm. n = 1.

5.6   *Discussion*

The aim of this chapter was to investigate the effect of DOX on breast cancer cells, total Cx43 protein levels, impact on the release of extracellular vesicles and exosomes and to optimise knockout as well as overexpression studies.

We have previously investigated the impact of DOX on different cardiovascular cell types (see Chapter 3). In this chapter we have focused on the impact of DOX on the cell viability on cancer cells and therefore experiments were conducted on MDA-MB-231 cells. These experiments revealed a IC50 value of 3.24 µM (2.29-4.58 µM) which could be supported by the Wen group, who identified a similar IC50 value (3.16 µM) (Wen *et al.*, 2018). This publication supports our findings on the impact of DOX on the MDA-MB-231 cell viability. An overview of the identified IC50 values of the cells is displayed in Table 14. A comparison has been created with our identified IC50 values to a cancer cell database (Figure 54) (Yang et al., 2013).

The cancer cell database showed responses to DOX ranging from an IC50 of 0.005 µM up to 38.8 µM, with a geometric mean of 0.17 µM. Given that DOX is applied as a chemotherapeutic agent for targeting cancer cells, it is interesting that our study revealed a more pronounced impact on the viability of cardiac cells. However, challenges arise when attempting to compare IC50 values. Assays conducted by other groups may result in variations, ranging from differences in assay types, cell confluency, serum starvation, treatment duration, the range of drug concentrations, and others. In 2019, a published study compared the IC50 values obtained from various cytotoxicity assays conducted in human glioblastoma cells (Damiani *et al.*, 2019). This paper showed the significant differences between cytotoxicity assays with their corresponding IC50 values and were not comparable. Nevertheless, our data

utilized identical assay conditions, drug concentration range, and treatment duration. Hence, the acquired IC50 values are suitable for intra-study comparisons but may not be directly comparable to those reported in the existing literature. Nonetheless, the IC50 values from the literature remain valuable for gaining insights into the toxicity profile of the drug.

Next to the identified difference in cell viability, variations were also observed on the total Cx43 protein levels between the cancer and cardiac cell types in response to DOX. A significant reduction of total Cx43 protein expression in the cardiac cells was characterised by using DOX (see chapter 3), where no significant reduction was observed in the MDA-MB-231 cells (see section 5.3). The differences in response to DOX on Cx43 could be different as the function of the protein could vary between cell types.

The effect of DOX on the release of extracellular and exosomes from MDA-MB-231 cells was investigated. Interestingly, increased particle numbers within the media were observed upon treatments with DOX (see section 5.4). Unfortunately, limited repetitions are available for this dataset and require more n-numbers. However, this data acquired from the NTA analysis could provide an indication of the effect of DOX upon particles within the media. The NTA provides information regarding the particle size distribution and concentration, but it has its limitations as no evidence of the origin of the nanoparticles is determined. For example, protein aggregates are also measured by the NTA analysis and could therefore interfere with the interpretation of the results (Filipe, Hawe and Jiskoot, 2010). In order to unravel whether the nanoparticles are extracellular vesicles or exosomes could the detection of specific proteins through Western blotting be useful. Examples of these proteins

include caveolar protein flotillin-1, tetraspanins CD63 & CD81, and endosomal trafficking protein Alix (Gemel *et al.*, 2019).

It has been confirmed that SUM-159 cells WT express the Cx43 protein as a depletion was discovered within the KO cells. The Cx43 KO triple negative breast cancer cell line could be used for future experiments to discover the role of Cx43 in DOX-mediated effects. Conversely, experiments involving the overexpression of GFP-Cx43 were successful on both HEK293 and AC16 cells, providing a promising foundation for future studies.

Table 14 - IC50 values of cardiac and cancer cell lines

Cell line	IC50 (DOX in µM)	Published pharmacological values (µM)	Reference
MDA-MB-231	3.24 (2.29-4.58)	3.16	(Wen *et al.*, 2018)
HUVEC	1.23 (1.01-1.50)	0.75	(Abou El Hassan *et al.*, 2003)
HCAEC	0.54 (0.42-0.70)	Not identified	N/A
hCF	0.37 (0.29-0.48)	Not identified	N/A
AC16	1.06 (0.86-1.31)	Not identified	N/A
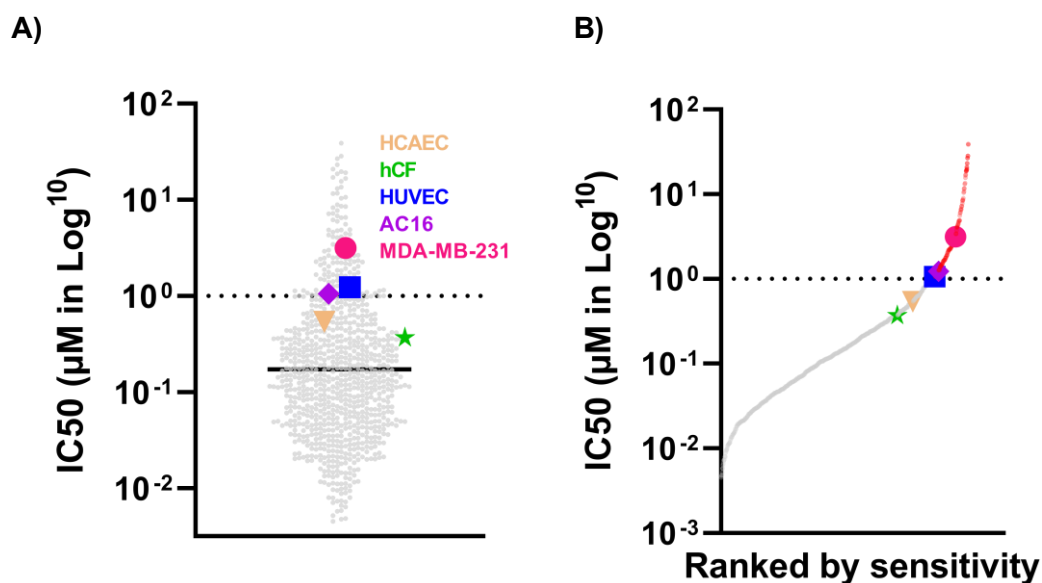
Figure 54 - Comparison of IC50 values of cancer cell types

*The IC50 values of DOX on HCAECs, hCFs, HUVECs, AC16, and MDA-MB-231 cells were compared to IC50 values of 870 different cancer cells. **A)** Scatter dot-plot of the IC50 values. **B)** Ranked by sensitivity of IC50 values from low to high. The dotted line at 1.02 µM indicates the max-screening concentration which was suggested by the database. The database was obtained from (Yang et al., 2013). N/A; Not Available.*

5.7   *Conclusion*

The cell viability following DOX treatment of the triple negative breast cancer cells MDA-MB-231 was higher when compared to the cardiac cell types. In addition, no significant reduction of total Cx43 protein levels was observed in MDA-MB-231 cells in response to DOX. This study suggests a DOX-mediated release of extracellular vesicles and/or exosomal content, which could potentially impact the heart and consequently contribute to DOX-induced cardiotoxicity. We have also confirmed the Cx43 KO in the triple negative breast cancer cells SUM-159 and achieved Cx43 overexpression in HEK293 as well as AC16 cells which could be used in future studies.

CHAPTER SIX:

GENERAL DISCUSSION

6.1   *General discussion*

This study evaluated the impact on the gap-junctional protein Cx43 in DOX-induced cardiotoxicity by using different cardiac cell types, Langendorff perfused rat hearts as well as 3D cardiac spheroid multicellular systems. The impact of DOX on cell viability were characterised highest amongst the cardiac fibroblasts followed by HCAECs, AC16s, and the MDA-MB-231 triple negative breast cancer cells. The greater toxic effect of DOX on the cardiac cell types in comparison to the breast cancer cells, illustrates the detrimental effects of the drug on the cardiovascular system. Whereas DOX has shown to reduce the total Cx43 protein levels in the cardiac cells, no change was observed in the cardiac spheroids. In contrast, studies on the Langendorff perfused rat hearts revealed an increase of the Cx43 levels alongside lateralisation. In addition, initial results indicate a DOX-mediated release of EVs from cancer cells which is currently work in progress. The release of EVs could be a potential mechanism of indirect DOX-induced cardiotoxicity.

There is a lack of automated drug-screening methods to measure cardiotoxic effects as stated by the 2022 ESC Guidelines on cardio-oncology (Lyon *et al.*, 2022). This research could potentially contribute to the search of methods and approach within this quest. An overview of the key findings within the project is illustrated in Figure 55.
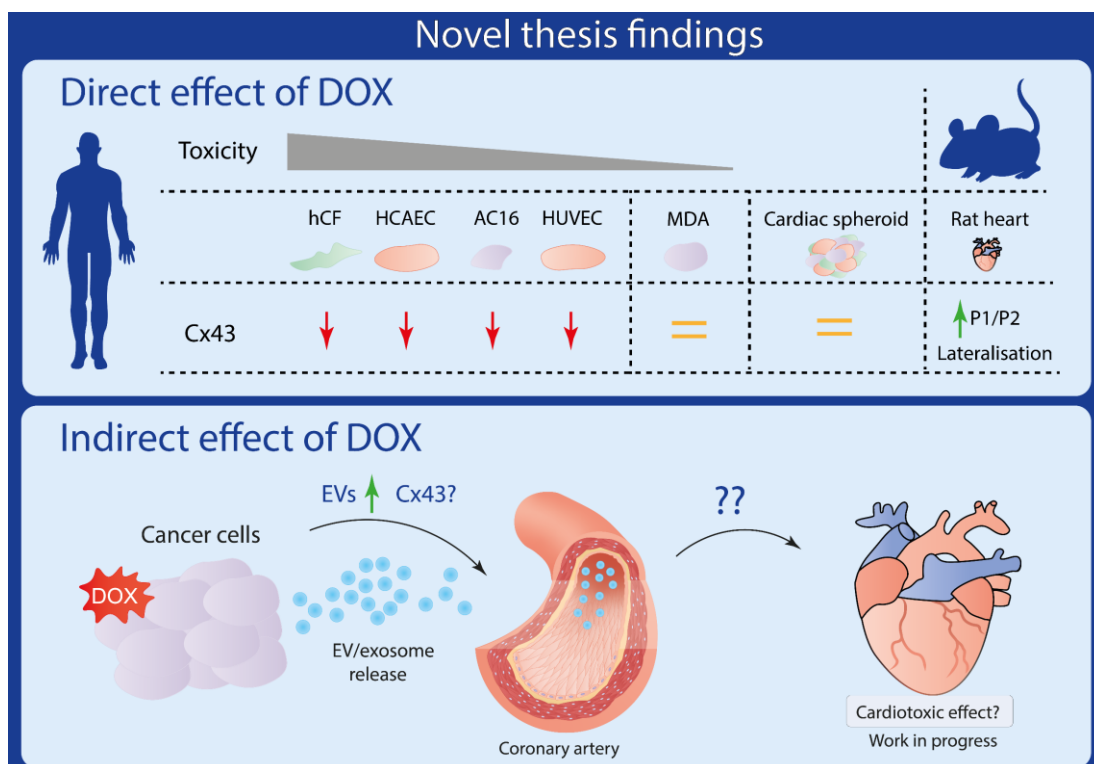
Figure 55 - Key novel findings of thesis

The direct effect of DOX on the toxicity from high to low was the following: hCFs, HCAECs, AC16s, HUVECs, and MDA-MB-231 cells. A decrease of Cx43 levels were observed in the hCFs, HCAECs, AC16s, and HUVECs but not in the MDA-MB-231 and cardiac spheroids. An increase of P1/P2 Cx43 levels were identified in Langendorff perfused rat hearts with DOX alongside a lateralisation. DOX could mediate a release of EVs which could potentially contribute to an indirect toxic effect to the heart.

6.2 The impact of DOX on Cx43 in cardiac tissue and cells

In our studies we used HCAECs to determine the effect of DOX on coronary endothelial cells and identified a significant reduction of total Cx43 protein levels (Figure 26). This has never been demonstrated before and the loss of the total Cx43 protein levels in HCAECs could result in a reduction of intercellular communication in the coronary endothelium and could thereby potentially contribute to a cardiotoxic effect. Our results were supported by the Hader group who previously revealed a detrimental impact of DOX on the human coronary vascular function (Hader *et al.*, 2019). Whether the decrease of Cx43 is as a result of enhanced protein degradation or a release through for example extracellular vesicles or exosomes is yet to be determined.

A reduction of total Cx43 protein levels in the cardiac cells identified in response to DOX at a concentration of 1.0 μM onwards (Figure 26, Figure 30, Figure 32). Therefore 1.0 μM DOX was used for the experiments concerning the ex-vivo Langendorff perfusion model. Interestingly, in contrast to a reduction in the AC16, hCFs, HCAECs, and HUVECs, increased protein levels of Cx43 were identified in the LV and RV tissue homogenates (Figure 47). The increased protein levels of DOX coincided with the lateralisation of the Cx43 protein. The lateralisation of Cx43 is associated with different phosphorylation states of the protein and therefore it is essential to use selective antibodies targeting specific phosphorylation sites. For future studies we would suggest to initially investigate the phosphorylation status of especially S368 and S373 (Jozwiak and Dhein, 2008; Dunn and Lampe, 2014; Del Ry *et al.*, 2015). Unfortunately, no high-quality phosphorylation site specific Cx43 antibodies are currently available.

Different approaches have been used to investigate and identify lateralisation. Lateralisation of Cx43 has previously been identified through colocalization studies of cadherin with Cx43 (Hesketh *et al.*, 2010; Himelman *et al.*, 2020; Rodríguez-Sinovas *et al.*, 2021). Cadherin is a plasma membrane protein that is present between adjacent cells and used as a marker for the intercalated discs (Gomes *et al.*, 2012). The Cx43 lateralisation in response to DOX could be conducted in future by using co-localisation experiments using cadherin with Cx43. Another strategy is to apply automated determination of Cx43 lateralisation in fluorescent images (Oliver-Gelabert *et al.*, 2020). This method is based on a software algorithm named MARTA (Myocyte Automatic Retrieval and Tissue Analyser) which uses cell masks, contouring individual cells in order to estimate the lateral Cx43 to total Cx43 ratio in ventricular tissue. The lateralisation of the Cx43 proteins has been associated to cardiac dysfunction and these results could thereby indicate a potential effect within DOX-induced cardiotoxicity (Hesketh *et al.*, 2010; Lucero *et al.*, 2020; Zheng *et al.*, 2020; Rodríguez-Sinovas *et al.*, 2021).

The effects regarding DOX-induced cardiotoxicity has been recently associated with targeting the mitochondria (Wu, Leung and Poon, 2022). The effect of ischaemia and reperfusion have been shown to cause a strong reduction in Cx43 protein expression, phosphorylation state, and a loss of localisation at the intercalated discs in rat hearts. These effects could be reduced by applying ischaemic preconditioning (Brandenburger *et al.*, 2014). Ischaemic preconditioning has been shown to prevent mitochondrial fragmentation and dysregulation, cardiomyocyte apoptosis, decreased Cx43 protein degradation and promotion of its plasma membrane localisation (Lin *et al.*, 2008; He *et al.*, 2020; Galán-Arriola *et al.*, 2021). Moreover, mitochondrial Cx43 (mCx43) could preserve cardioprotective effects

through the reduction of mitochondrial ROS during DOX-induced cardiotoxicity as blocking Cx43 translocation to the mitochondria ablated the protective effect (Pecoraro *et al.*, 2020). The protective role of Cx43 in the mitochondria is illustrated in Figure 56.
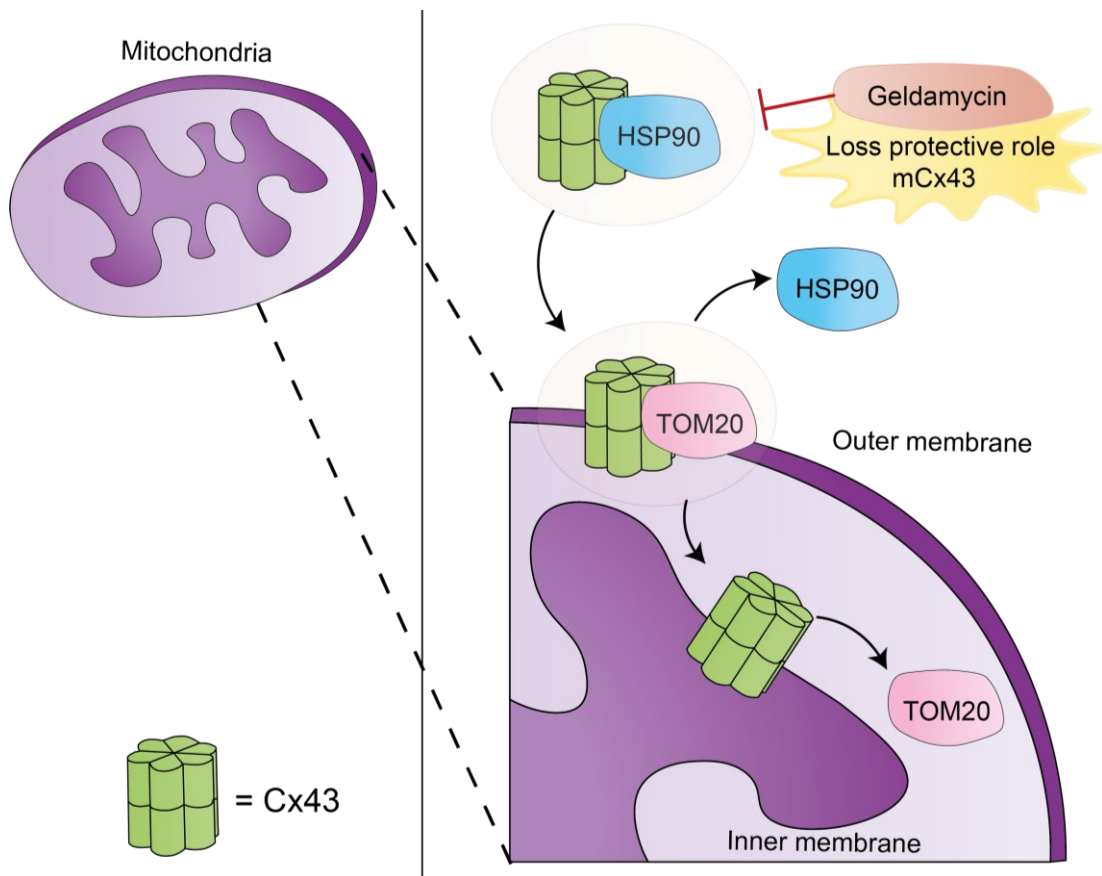
Figure 56 - The protective role of mitochondrial Cx43

Cx43 is transported to the outer mitochondrial membrane through HSP90 and thereafter further transported to the inner mitochondrial membrane by TOM20. Blocking of HSP90 by geldamycin, results in a reduced mCx43 expression and correlates with a loss of its protective role. Abbreviations: HSP90; Heat shock protein 90, TOM20; Mitochondrial import receptor subunit, mCx43; mitochondrial connexin 43.

6.3   *Spheroid models and screening for DOX-induce cardiotoxicity*

To overcome the lack of paracrine communication between the different cardiac cell types, were spheroids generated for studying DOX-induced cardiotoxicity. It would hold significant importance to optimise the imaging of the cardiac spheroids. This would allow the determinations of the ratio of the endothelial, fibroblast, and cardiomyocyte ratio within the 3D structure. Further optimisation experiments will be required to achieve increased spheroid clearance prior immunofluorescent imaging. The cell specific markers including vWF, cTn, α-SMC, and vimentin could be used to determine the ratio of different cell types within the spheroid. It is also mandatory to retrieve more information regarding the necrotic core of the spheroid, which is a well-known limitation of spheroid culture (King, 2012; Acland *et al.*, 2018). Another tool that could be applied to determine the cell population as well as to investigate the apoptotic cell number is fluorescence activated cell sorting (FACS) (Patra *et al.*, 2016; Tchoryk *et al.*, 2019).

In addition, the cardiac spheroids could be implemented in the fabrication of scaffold-free tubular cardiac constructs using a Bio-3D printer (Arai and Murata et al., 2018). By the use of human-induced pluripotent stem cell-derived cardiomyocytes 3D cardiac structures and heart-on-a-chip could be developed and used as a tool for drug research as well as investigating DOX-induced cardiotoxicity (Andrysiak, Stępniewski and Dulak, 2021). The cardiac spheroids using patient specific hiPSCs cardiomyocyte cells could be applied in the investigation of DOX-induced cardiotoxicity (Paik, Chandy and Wu, 2020).

6.4 The role of extracellular vesicles in DOX-induced cardiotoxicity

Our results have indicated that DOX could initiate a release of nanoparticles from the triple negative breast cancer MDA-MB-231 cells (Figure 51). Whether the nanoparticles are extracellular vesicles and/or exosomes must be investigated in future experiments. The origin of the particles could be evaluated by detecting specific proteins, including flotillin-1, Alix, and CD63 & CD81 (Gemel *et al.*, 2019). The role of exosomes and EVs has previously been identified to be involved with DOX-induced cardiotoxicity as previous studies have identified elevated number of EVs response from cancer cells (Yarana *et al.*, 2018, 2022; Martins-Marques *et al.*, 2020; Zhang *et al.*, 2022).

It would be interesting to discover the levels of Cx43 within the released particles to assess in response to DOX. The exosomes and EVs could be used in the treatments of HCAECs whether to investigate the impact on cell viability in response to DOX is associated with the levels of Cx43 and if the protein levels could be recovered. Furthermore, Cx43 also participates in the selective sorting of miRNAs into EV and could directly interact with specific miRNAs, including miR-133b (Martins-Marques *et al.*, 2022). Moreover, studies with exosomes and EVs released from cancer cells could be implemented within the Langendorff perfusion model in order to assess whether a cardiotoxic effect is introduced as well as changes in Cx43 protein expression. The role of Cx43 on the cardiotoxic effect, either in cell culture of cardiac cells or Langendorff perfusion could be evaluated with the optimised Cx43 WT and KO cancer cell models. The exosomes and EVs could also potentially be released from the cardiovascular cells and could therefore serve as an early diagnostic biomarker in DOX-induced cardiotoxicity.

6.5   *Could connexins be the key for therapeutic intervention strategies?*

The role of Cx43 in cancer and in the cardiovascular setting has been discussed in the previous sections. The importance of a better understanding of the role of connexins in cancer is critical in order to develop novel therapeutic strategies to improve cancer treatment (Bonacquisti and Nguyen, 2019; Nalewajska *et al.*, 2020). Moreover, understanding of the role of Cx43 in cardiac disease has resulted in the development of Cx43 mimetic peptides which have shown a reduction of cardiac injury in preclinical studies (Rusiecka *et al.*, 2020). A review was recently published by the Marsh group examining gap junctions and connexin peptides with their corresponding potential mechanisms through which they function (Marsh *et al.*, 2021).

Connexin-mimetic peptides contain homology with the connexin protein sequence and were originally designed as epitopes in order to produce connexin targeted antibodies but were not able to reduce connexin-related contractility in rabbits (Goodenough, Paul and Jesaitis, 1988; Meyer *et al.*, 1992; Chaytor, Evans and Griffith, 1997). Despite the unfavourable outcomes , were mimetic peptides characterised to inhibit gap junction channels (Becker *et al.*, 1995). GAP26 and GAP27 mimetic peptides target the extracellular loops of Cx43 and inhibit gap junctions, induce phosphorylation at S368, and increase intracellular Ca^{2+} levels (Martin, Wall and Griffith, 2005; De Bock *et al.*, 2012; Cotter *et al.*, 2018). The Leybaert group developed L2 peptides with a tyrosine aminotransferase (TAT) sequence to promote internalisation. The TAT-L2 has been shown to impact hemichannel functioning (Ponsaerts *et al.*, 2010). The GAP19 mimetic peptide changes Cx43 expression and prevents ischemia-reperfusion injury (Wang *et al.*, 2013). In addition, TAT-GAP19 reduces the development of arrhythmias (de Smet *et al.*, 2021).

A target towards the carboxyl terminus of Cx43 is alpha carboxyl terminus 1 (α-CT1) which is mimetic to the last 9 amino acids and is linked to the antennapedia sequence to promote cellular internalisation (Hunter *et al.*, 2005). As previously described in section 1.5.1, the carboxyl region functions as a PDZ domain and interacts with ZO-1. In this regard, the use of α-CT1 has been shown to inhibit ZO-1 binding and thereby increases the gap junction size, coupling, reduces hemichannel activity and has shown to limit ischaemia-reperfusion injury and development of arrhythmias (Rhett, Jourdan and Gourdie, 2011; Jiang *et al.*, 2019). A modification of α-CT1, named α-CT11 has also been shown to contain cardioprotective properties (Jiang *et al.*, 2019). The CT9 peptide is composed of the last 9 amino acids of α-CT11 which blocks the PDZ binding site, promotes phosphorylation at S368 and activates Cx43 hemichannels (De Bock *et al.*, 2012). An overview of different Cx43-mimetic peptides is displayed in Table 15 and the homology domains on Cx43 are illustrated in Figure 57.

Table 15 - Overview of Cx43-mimetic peptides

Peptide	Region	Properties	Reference
GAP26	64-76 (EL-1)	Blocking HC	(Chaytor et al., 1997; Chaytor *et al.*, 1999)
GAP27	201-211 (EL-2)	Blocking HC	(Chaytor et al., 1997; Chaytor *et al.*, 1999)
GAP21	201-210 (EL-2)	Blocking HC	(Cotter *et al.*, 2018, 2019)
L2	119-142 (IL)	Blocking HC	(Duffy *et al.*, 2002; Seki, Coombs, *et al.*, 2004; Seki, Duffy, *et al.*, 2004)
TAT-L2	119-142 (IL)	Blocking HC	(Ponsaerts *et al.*, 2010)
GAP19	128-136 (IL)	Blocking HC	(Wang *et al.*, 2013)
TAT-GAP19	128-136 (IL)	Blocking HC	(Abudara *et al.*, 2014)
α-CT1	374-382 (C-term)	Blocking HC	(Palatinus et al., 2011)
α-CT11	374-382 (C-term)	Stimulate GJ formation Enhance GJ Blocking HC	(Jiang *et al.*, 2019)
CT9	373-382 (C-term)	Blocking HC	(De Bock *et al.*, 2012)
TAT-CT10	373-382 (C-term)	Inhibiting GAP19	(Wang *et al.*, 2013)
JM2	231-245 (C-term)	Blocking HC	(Calder *et al.*, 2015)

Different Cx43 mimetic peptides are shown with their corresponding regions, properties, and corresponding references. Abbreviations: EL; extracellular loop, IL; intracellular loop, C-term; carboxyl terminus, GJ; gap-junction, HC; hemichannel. This table is adapted from (Marsh et al., 2021).
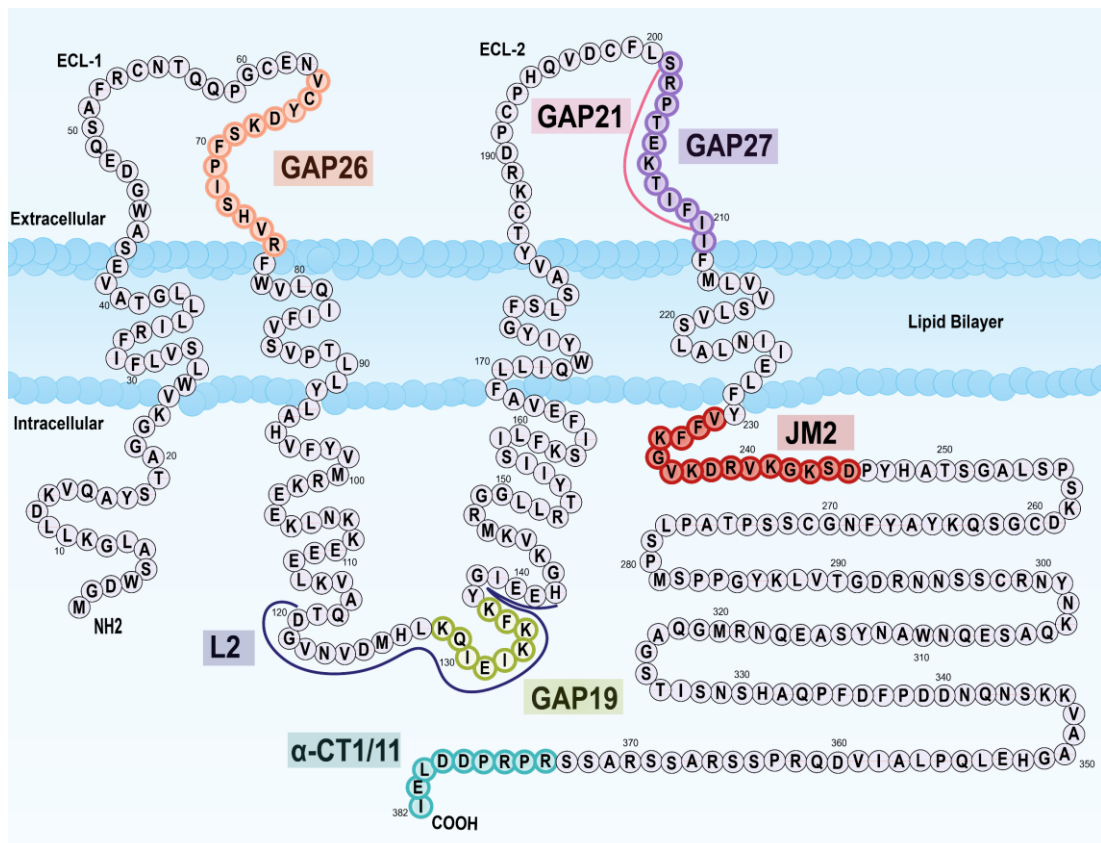
Figure 57 - Cx43 mimetic peptides

Overview of homology domains of the mimetic peptides within the Cx43 protein sequence. JM; juxtamembrane, α-CT; alpha carboxyl terminus.

6.6   Limitations of project - Specific work impacted by Covid-19

Limited work could be conducted regarding time-of-flight secondary ion mass spectrometry (ToF-SIMS) as a result of COVID-19. The IONTOFF training in Munster was cancelled and no access was granted to the Technology Innovation Centre (TIC) to use the machine. As a result was limited data was collected. The ToF-SIMS is discussed in the next section.

6.7 ToF-SIMS as a tool for screening for metabolic changes

Our studies have so far focussed to identify the effects of DOX on the expression and localisation of the gap-junctional protein Cx43 in cardiac cell types as well as its effect on the cell viability. Next to these investigations it is also important to look on the effect of DOX on metabolic changes and a useful tool for this identification is time of flight secondary ion mass spectrometry (ToF-SIMS). ToF-SIMS has become a beneficial analysis tool in providing information of biomolecule distribution on cellular and subcellular level.

In brief, the ToF-SIMS has three different operational modes, including surface spectroscopy, surface profiling, and depth profiling. The capability to detect ions and small biomolecules such as lipids, metabolites and peptides, without the requirement of labelling or chemical reagents (Denbigh and Lockyer, 2014; Passarelli et al., 2015; Urbini et al., 2017; Agüi-Gonzalez, Jähne et al., 2019). The aspects introduced new perspectives in the search of biomarkers in DOX-mediated cardiotoxicity. The ToF-SIMS process is initiated by a primary ion beam, impacting a solid surface to sputter and ionize secondary ions. These secondary ions are extracted and accelerated into a flight tube where their mass per charge (m/z) is determined by the time it is required to reach the detector, also known as the "time of flight". The detector analyses the intensity of the compounds and plots it versus m/z. The primary ion beam is focused on a selected field and pulses primary ions to the surface of the sample, pixel by pixel. This results in m/z intensity spectra for all pixels across the ROI. Intensity spectra for each individual compound can be translated into a coloured ion-image. A schematic overview of the ToF-SIMS principle is illustrated in Figure 58.
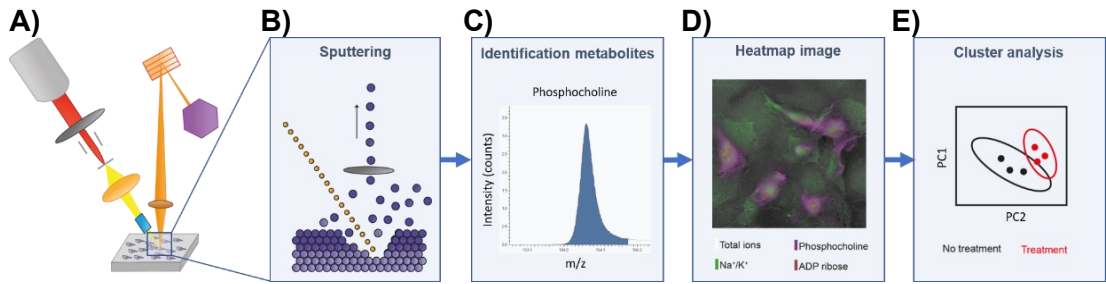
Figure 58 - Overview of time-of-flight secondary ion mass spectrophotometry
A) The energetic primary ion beam sputters the sample surface. B) Secondary ions are released towards the time of flight (ToF) reflector and detector. The separation is based on mass per charge (m/z) of the metabolites and result in peaks (C), and heatmap images (D). E) Data acquired by ToF-SIMS is processed by ion-imaging, spectral analysis, and multivariate analysis. This figure is adapted from (Hofmann et al., 2014; Agüi-Gonzalez, Jähne and Al., 2019).

Different metabolites were identified, such as glutamic acid fragments, potassium, sodium, calcium, DNA-ribose sugar, palmitic acid, oleic acid, and arachidonic acid. These different identified metabolites could be classified into different groups, such as amino acids, lipids, and nuclear markers. Normalised total intensity values were plotted from the positive and negative ion channel which are shown in Figure 59A-C. The collected intensity data from each pixel could be displayed in a heatmap in order to demonstrate its cellular localisation to confirm the identity of each metabolite. An example is shown in Figure 59D, whereby the intensity of the total secondary ions (white) and DNA ribose sugar (purple) are displayed. The total secondary ions display the cellular outlines, and the DNA ribose sugar shows the nucleus of the cell. Another example is shown in Figure 59D, the total secondary ions (white) is overlapped with potassium and sodium ions (green), phosphocholine (purple) and also DNA ribose sugar (red).

The wide variety of different types of metabolites were classified into amino acid fragments, nuclear markers, ions, fatty acids, and phospholipids (Table 16). The ToF-SIMS detected different metabolites without the requirement of labelling or chemical reagents and could therefore be a valuable tool in the search of biomarkers in DOX-mediated cardiotoxicity.

A) Amino acids
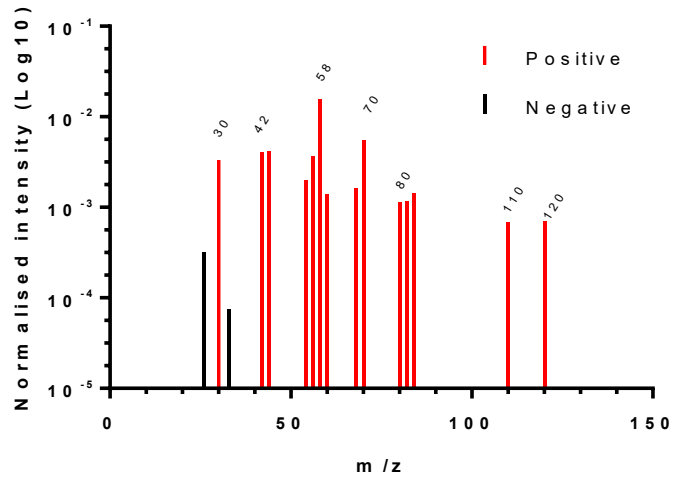
B) Lipids

C) Nuclear markers

D)

Total secondary ion image (white)
+ DNA ribose sugar (purple)

E)

Total secondary ion image (white)
+ Na/K (green)
+ Phosphocholine (purple)
+ DNA ribose sugar (red)
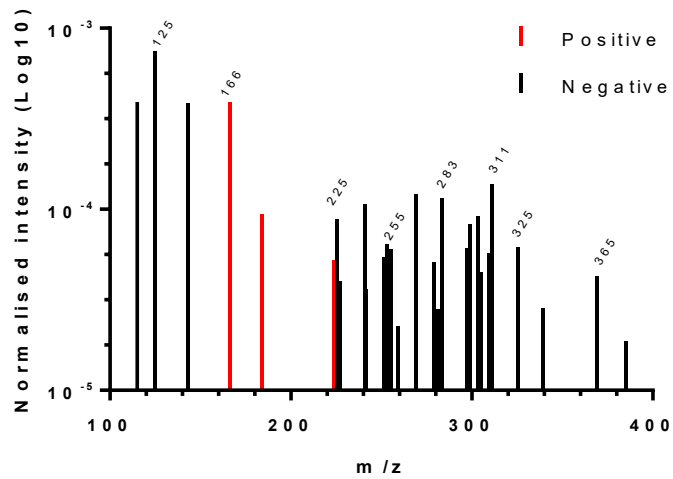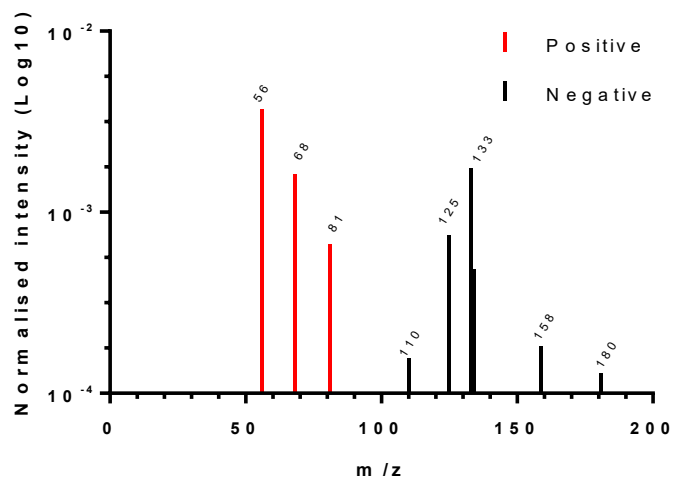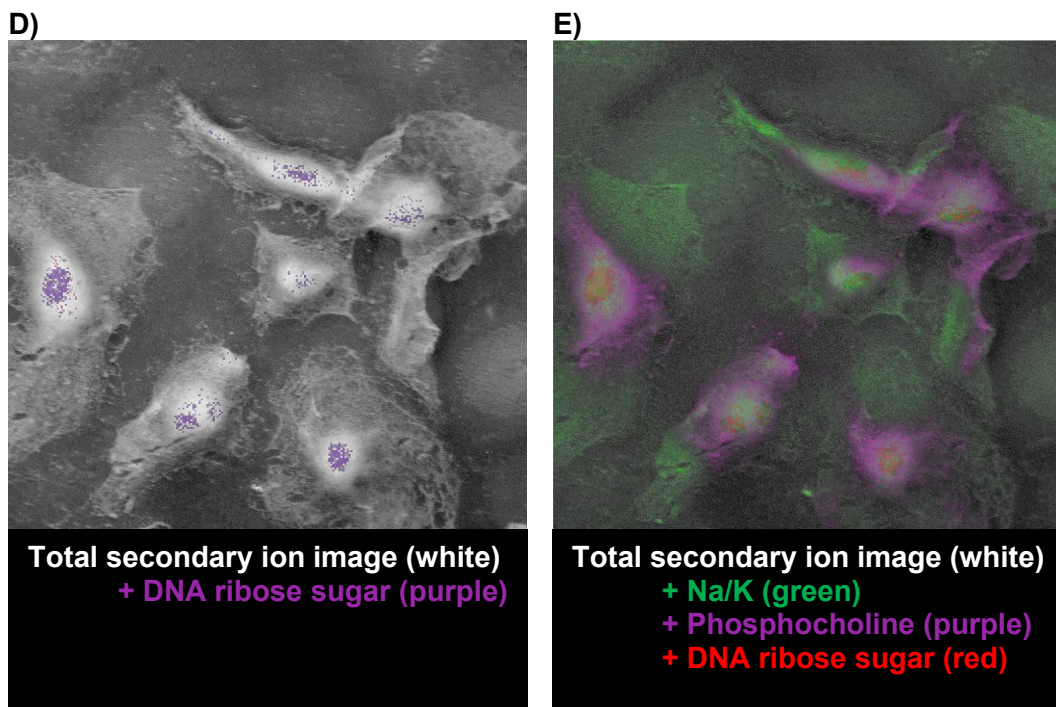
Figure 59 - Optimisation of identifying metabolites by using ToF-SIMS

*Identification of different metabolites in the positive and negative channels sorted by m/z. The metabolites include various amino acid fragments **(A)**, lipids **(B)**, and nuclear markers **(C)**. **D)** Total ion image (white) with DNA ribose sugar (magenta) to show the outline of the cells and the nuclear area. **E)** Total ion image (white) with Na/K ions (green), phosphocholine (purple), and DNA ribose sugar (red).*

Table 16 - ToF-SIMS identified metabolites in HCAECs

Classification	m/z	m/z theoretical	m/z measured	Formula	Name	Reference
Amino acid fragments	18	18.03	18.04	NH_4^+	All amino acids	(Urbini et al., 2017)
	58	58.07	58.07	$C_3H_8N^+$	Glutamic acid	
	84	84.04	84.04	$C_4H_6NO^+$	Glutamic acid	
	120	120.08	120.08	$C_8H_{10}N^+$	Phenylalanine	
	26	26.00	26.00	CN^-	Peptide backbone	
	32	32.98	32.98	HS^-	Cysteine	
	42	42.00	42.00	CNO^-	Peptide backbone	
Nuclear markers	56	56.0	56.06	$C_3H_4O^+$	Oxygenated hydrocarbon	(Passarelli et al., 2015)
	68	68.0	68.05	$C_4H_4O^+$	Oxygenated hydrocarbon	
	81	81.0	81.02	$C_5H_5O^+$	DNA ribose sugar	
	134	134.1	134.05	$C_5H_4N_5^-$	Adenine	
	158	158.9	158.93	$HP_2O_6^-$	Phosphate-oxygen fragment	
	180	180.9	180.91	$NaP_2O_6^-$	Phosphate-oxygen fragment	
Ions	17	17.00	17.00	$HO-$	Hydroxide	*No reference identified*
	19	19.00	19.00	$F-$	Fluoride	(Naraoka et al., 2015)
	19	19.02	19.02	H_3O^+	Hydronium	(Lanekoff et al., 2010)
	22	22.99	23.00	Na^+	Sodium	(Naraoka et al., 2015)
	38	38.36	38.97	$^{39}K^+$	Potassium-39	(Naraoka et al., 2015)
	39	39.96	39.97	Ca^+	Calcium	(Henss et al., 2013)
	30	30.97	30.97	P^-	Phosphorus	(Sodhi et al., 2018)

	31	31.97	31.97	S$^-$	Sulphur	*(Sodhi et al., 2018)*
	34	34.97	34.97	Cl$^-$	Chloride	*(Naraoka et al., 2015)*
	40	40.96	40.97	^{41}K$^+$	Potassium-41	*(Collin et al., 2019)*

Fatty acids	227	227.20	227.21	C$_{14}$H$_{27}$O$_2^-$	Myristic acid	*(Urbini et al., 2017)*
	253	254.23	254.25	C$_{16}$H$_{30}$O$_2^-$	Palmitoleic acid	
	255	255.23	255.23	C$_{16}$H$_{31}$O$_2^-$	Palmitic acid	
	279	279.23	279.24	C$_{18}$H$_{31}$O$_2^-$	Linoleic acid	
	281	281.25	281.25	C$_{18}$H$_{33}$O$_2^-$	Oleic acid	
	283	283.26	283.27	C$_{18}$H$_{35}$O$_2^-$	Stearic acid	
	303	303.23	303.25	C$_{20}$H$_{31}$O$_2^-$	Arachidonic acid	
	305	304.26	305.25	C$_{20}$H$_{32}$O$_2^-$	Dihomo-linoleic acid	

Phospholipids	166	166.06	166.06	C$_5$H$_{13}$NPO$_3^+$	Phosphocholine	*(Lanekoff et al., 2010)*
	184	184.07	184.08	C$_5$H$_{15}$NPO$_4^+$	Phosphocholine	*(Lanekoff et al., 2010)*
	224	224.10	224.10	C$_8$H$_{19}$NPO$_4^+$	Phosphocholine	*(Brunelle and Laprévote, 2009)*

Cx43 is involved in cell to cell communication and as such, is involved in the exchange and transport of ions, metabolites and second messengers (Brisset, Isakson and Kwak, 2009), which may have knock on effects in cellular dysregulation in the event of DOX-dependent dysregulation. Such changes in surface events can be sensitively detected using imaging mass spectrometry techniques. ToF-SIMS can provide information of not just metabolite levels and localisation, but also co-localisation studies can be performed with drugs. Metabolic changes upon drug treatment can be measured in the form ions, fatty acids, phospholipids and amino acid fragments (Denbigh and Lockyer, 2014; Passarelli *et al.*, 2015; Urbini *et al.*, 2017; Agüi-Gonzalez, Jähne and Al., 2019).

A recent extensive review writes regarding the use of mass spectrometry imaging in spheroids and how this tool could be applied in personalised medicine and drug discovery (Wang and Hummon, 2021). Therefore, we believe cardiac cells could individually be screened through ToF-SIMS analysis and in 3D spheroids models for metabolic changes identification in response to DOX. These results could give rise to shift the metabolic profile which could be then linked to the role of Cx43 in KO and overexpression models.

6.8   General conclusion

The treatment of cancer is widely associated with cardiovascular dysfunction, giving rise to a new discipline known as cardio-oncology. The anthracycline drug DOX is the most applied anti-cancer agent with manifestations of cardiac arrythmias and cardiomyopathy, however a better understanding of the molecular mechanism is required. The gap-junctional protein Cx43 is a key protein to maintain a physiological cardiac function and its remodelling is also associated with cardiac arrythmias and cardiomyopathy. This project investigated the impact of DOX on cardiac Cx43 by using ex-vivo, 3D cardiac spheroids, and primary cardiac and vascular cells.

Our findings indicated a DOX-mediated reduction of total Cx43 levels and a relocalisation in primary cardiac cells. In contrast, in ex-vivo Langendorff perfused rat hearts resulted in elevated phosphorylation and total Cx43 levels, coinciding with a lateralisation from the intercalated discs. Previous studies have shown a correlation between Cx43 lateralisation with cardiac arrythmias and cardiomyopathies. These early changes in response to DOX could contribute to the cardiovascular complications. In addition, DOX-treated hi-PSC derived cardiomyocytes revealed increased contraction frequencies, supporting the development of an arrhythmic phenotype. This data led to development of 3D-cardiac spheroids by using endothelial, fibroblasts, and hi-PSC derived cardiomyocytes. The spheroids showed a contractile phenotype, but post-analysis requires more optimisation to assess the impact of DOX on Cx43. Future experiments could further optimise the post-analysis of cardiac spheroids, assessing weather extracellular vesicles are released from cancer cells in response to DOX and could contribute to DOX-induced cardiotoxicity, to measure metabolic changes in response to DOX in single cells, tissues, and spheroids by using ToF-SIMS, and to use Cx43 overexpression and KO models.

REFERENCES

Aasen, T. *et al.* (2018) 'Connexins: Synthesis, post-translational modifications, and trafficking in health and disease', *International Journal of Molecular Sciences*. MDPI AG. Available at: https://doi.org/10.3390/ijms19051296.

Aasen, T. *et al.* (2019) 'Connexins in cancer: bridging the gap to the clinic', *Oncogene*. Nature Publishing Group, pp. 4429–4451. Available at: https://doi.org/10.1038/s41388-019-0741-6.

Abou El Hassan, M.A.I. *et al.* (2003) 'The new cardioprotector Monohydroxyethylrutoside protects against doxorubicin-induced inflammatory effects in vitro', *British Journal of Cancer*, 89(2), pp. 357–362. Available at: https://doi.org/10.1038/sj.bjc.6601022.

Abudara, V. *et al.* (2014) 'The connexin43 mimetic peptide Gap19 inhibits hemichannels without altering gap junctional communication in astrocytes', *Frontiers in Cellular Neuroscience*. Available at: https://doi.org/10.3389/fncel.2014.00306.

Acland, M. *et al.* (2018) 'Mass Spectrometry Analyses of Multicellular Tumor Spheroids', *Proteomics - Clinical Applications*, 12(3). Available at: https://doi.org/10.1002/prca.201700124.

Agrawal, K. (2019) 'Doxorubicin', in *xPharm: The Comprehensive Pharmacology Reference*, pp. 1–5. Available at: https://doi.org/10.1016/b978-008055232-3.61650-2.

Agudelo, D. *et al.* (2014) 'Intercalation of antitumor drug doxorubicin and its analogue by DNA duplex: Structural features and biological implications', *International Journal of Biological Macromolecules*, 66, pp. 144–150. Available at: https://doi.org/10.1016/j.ijbiomac.2014.02.028.

Agudelo, D. *et al.* (2016) 'Review on the binding of anticancer drug doxorubicin with DNA and tRNA: Structural models and antitumor activity', *Journal of Photochemistry and Photobiology*, 158, pp. 274–279. Available at: https://doi.org/10.1016/j.jphotobiol.2016.02.032.

Agüi-Gonzalez, P., Jähne, S. and Al., A. et (2019) 'SIMS imaging in neurobiology and cell biology', *Journal of Analytical Atomic Spectrometry*, 34(7), pp. 1355–1368.

Available at: https://doi.org/10.1039/c9ja00118b.

Ahmad, S., Martin, P.E.M. and Evans, W.H. (2001) 'Assembly of gap junction channels: mechanism, effects of calmodulin antagonists and identification of connexin oligomerization determinants', *European Journal of Biochemistry*, 268(16), pp. 4544–4552. Available at: https://doi.org/10.1046/j.1432-1327.2001.02380.x.

Akpek, M. *et al.* (2015) 'Protective effects of spironolactone against anthracycline-induced cardiomyopathy', *European Journal of Heart Failure*, 17(1), pp. 81–89. Available at: https://doi.org/10.1002/ejhf.196.

Alphandéry, E. *et al.* (2015) 'Cancer therapy using nanoformulated substances: scientific, regulatory and financial aspects', *Expert Review of Anticancer Therapy*, 15(10), pp. 1233–1255. Available at: https://doi.org/10.1586/14737140.2015.1086647.

Amani, J. *et al.* (2021) 'Cyclin-dependent kinase inhibitors (CDKIs) and the DNA damage response: The link between signaling pathways and cancer', *DNA Repair*, 102, p. 103103. Available at: https://doi.org/10.1016/j.dnarep.2021.103103.

Aminkeng, F. *et al.* (2015) 'A Coding Variant in RARG Confers Susceptibility to Anthracycline-Induced Cardiotoxicity in Childhood Cancer', *Nature Genetics*, 47(9), p. 1079. Available at: https://doi.org/10.1038/ng.3374.

Andrysiak, K., Stępniewski, J. and Dulak, J. (2021) 'Human-induced pluripotent stem cell-derived cardiomyocytes, 3D cardiac structures, and heart-on-a-chip as tools for drug research', *Pflugers Archiv European Journal of Physiology*, 473(7), pp. 1061–1085. Available at: https://doi.org/10.1007/s00424-021-02536-z.

Arai K, Murata D, Verissimo AR, Mukae Y, Itoh M, et al. (2018) 'Fabrication of scaffold-free tubular cardiac constructs using a Bio-3D printer', *PLOS ONE*, 13(12). Available at: https://doi.org/10.1371/journal.pone.0209162.

Armenian, S.H. *et al.* (2015) 'Recommendations for Cardiomyopathy Surveillance for Survivors of Childhood Cancer: A Report from the International Late Effects of Childhood Cancer Guideline Harmonization Group', *The Lancet. Oncology*, 16(3), pp. e123–e136. Available at: https://doi.org/10.1016/s1470-2045(14)70409-7.

Asencio-Barría, C. *et al.* (2019) 'Direct Intercellular Communications and Cancer: A

Snapshot of the Biological Roles of Connexins in Prostate Cancer', *Cancers*, 11(9), p. 1370. Available at: https://doi.org/10.3390/cancers11091370.

Aucher, A., Rudnicka, D. and Davis, D.M. (2013) 'MicroRNAs Transfer from Human Macrophages to Hepato-Carcinoma Cells and Inhibit Proliferation', *The Journal of Immunology*, 191(12), pp. 6250–6260. Available at: https://doi.org/10.4049/jimmunol.1301728.

Avila, M.S. *et al.* (2018) 'Carvedilol for Prevention of Chemotherapy-Related Cardiotoxicity: The CECCY Trial', *Journal of the American College of Cardiology*, 71(20), pp. 2281–2290. Available at: https://doi.org/10.1016/j.jacc.2018.02.049.

Awasthi, P., Foiani, M. and Kumar, A. (2015) 'ATM and ATR signaling at a glance', *Journal of Cell Science*, 128(23), pp. 4255–4262. Available at: https://doi.org/10.1242/jcs.169730.

Aziz, A.U.R. *et al.* (2019) 'Doxorubicin Induces ER Calcium Release via Src in Rat Ovarian Follicles', *Toxicological Sciences*, 168(1), pp. 171–178. Available at: https://doi.org/10.1093/toxsci/kfy284.

Barbosa, R.R. *et al.* (2018) 'Anthracycline-associated cardiotoxicity in adults: Systematic review on the cardioprotective role of beta-blockers', *Revista da Associacao Medica Brasileira*, 64(8), pp. 745–754. Available at: https://doi.org/10.1590/1806-9282.64.08.745.

Barenholz Y. (2012) 'Doxil®--the first FDA-approved nano-drug: lessons learned', *Journal of controlled release : official journal of the Controlled Release Society*, 160(2), pp. 117–134. Available at: https://doi.org/10.1016/j.jconrel.2012.03.020.

Battaglia, R.A. *et al.* (2018) 'Vimentin on the move: New developments in cell migration', *F1000Research*, 7. Available at: https://doi.org/10.12688/f1000research.15967.1.

Battisti, N.M.L. *et al.* (2021) 'Incidence of cardiotoxicity and validation of the Heart Failure Association-International Cardio-Oncology Society risk stratification tool in patients treated with trastuzumab for HER2-positive early breast cancer', *Breast Cancer Research and Treatment*, 188(1), pp. 149–163. Available at: https://doi.org/10.1007/s10549-021-06192-w.

Beauchamp, P. *et al.* (2020) '3D Co-culture of hiPSC-Derived Cardiomyocytes With Cardiac Fibroblasts Improves Tissue-Like Features of Cardiac Spheroids', *Frontiers in Molecular Biosciences*, 7, p. 14. Available at: https://doi.org/10.3389/fmolb.2020.00014/bibtex.

Bebelman, M.P. *et al.* (2018) 'Biogenesis and function of extracellular vesicles in cancer', *Pharmacology & Therapeutics*, 188, pp. 1–11. Available at: https://doi.org/10.1016/j.pharmthera.2018.02.013.

Becker, A. *et al.* (2016) 'Extracellular Vesicles in Cancer: Cell-to-Cell Mediators of Metastasis', *Cancer Cell*, 30(6), pp. 836–848. Available at: https://doi.org/10.1016/j.ccell.2016.10.009.

Becker, D.L. *et al.* (1995) 'Functional analysis of amino acid sequences in connexin43 involved in intercellular communication through gap junctions', *Journal of Cell Science*, 108(4), pp. 1455–1467. Available at: https://doi.org/10.1242/jcs.108.4.1455.

Bhatia, S. (2020) 'Genetics of Anthracycline Cardiomyopathy in Cancer Survivors: JACC: CardioOncology State-of-the-Art Review', *JACC. CardioOncology*, 2(4), p. 539. Available at: https://doi.org/10.1016/j.jaccao.2020.09.006.

Bielak-Zmijewska, A. *et al.* (2014) 'A comparison of replicative senescence and doxorubicin-induced premature senescence of vascular smooth muscle cells isolated from human aorta', *Biogerontology*, 15(1), pp. 47–64. Available at: https://doi.org/10.1007/s10522-013-9477-9/tables/1.

Blanco, J.G. *et al.* (2012) 'Anthracycline-Related Cardiomyopathy After Childhood Cancer: Role of Polymorphisms in Carbonyl Reductase Genes -- A Report From the Children's Oncology Group', *Journal of Clinical Oncology*, 30(13), p. 1415. Available at: https://doi.org/10.1200/jco.2011.34.8987.

Bloom, M.W. *et al.* (2016) 'Cancer Therapy–Related Cardiac Dysfunction and Heart Failure', *Circulation. Heart failure*, 9(1). Available at: https://doi.org/10.1161/circheartfailure.115.002661.

BNF (2023) *Doxorubicin hydrochloride*. Available at: https://bnf.nice.org.uk/drugs/doxorubicin-hydrochloride/#indications-and-dose (Accessed: 30 January 2023).

De Bock, M. *et al.* (2012) 'Connexin 43 hemichannels contribute to cytoplasmic Ca2+ oscillations by providing a bimodal Ca2+-dependent Ca2+ entry pathway', *The Journal of Biological Chemistry*, 287(15), pp. 12250–12266. Available at: https://doi.org/10.1074/jbc.m111.299610.

Bonacquisti, E.E. and Nguyen, J. (2019) 'Connexin 43 (Cx43) in cancer: Implications for therapeutic approaches via gap junctions', *Cancer Letters*, pp. 439–444. Available at: https://doi.org/10.1016/j.canlet.2018.10.043.

Bonadonna, G. *et al.* (1969) 'Clinical evaluation of adriamycin, a new antitumour antibiotic.', *British Medical Journal*, 3(5669), pp. 503–6. Available at: https://doi.org/10.1136/bmj.3.5669.503.

Bosch, X. *et al.* (2013) 'Enalapril and carvedilol for preventing chemotherapy-induced left ventricular systolic dysfunction in patients with malignant hemopathies', *Journal of the American College of Cardiology*, 61(23), pp. 2355–2362. Available at: https://doi.org/10.1016/j.jacc.2013.02.072.

Bosman, M. *et al.* (2021) 'Doxorubicin impairs smooth muscle cell contraction: Novel insights in vascular toxicity', *International Journal of Molecular Sciences*, 22(23), pp. 1–17. Available at: https://doi.org/10.3390/ijms222312812.

Braile, M. *et al.* (2020) 'VEGF-A in cardiomyocytes and heart diseases', *International Journal of Molecular Sciences*, 21(15), pp. 1–18. Available at: https://doi.org/10.3390/ijms21155294.

Brandenburger, T. *et al.* (2014) 'Remote ischemic preconditioning preserves Connexin 43 phosphorylation in the rat heart in vivo', *Journal of Translational Medicine*, 12(1), pp. 1–7. Available at: https://doi.org/10.1186/s12967-014-0228-8.

Breast cancer incidence (invasive) statistics - Cancer Research UK (2018). Available at: https://www.cancerresearchuk.org/health-professional/cancer-statistics/statistics-by-cancer-type/breast-cancer/incidence-invasive (Accessed: 10 August 2023).

Brisset, A.C., Isakson, B.E. and Kwak, B.R. (2009) 'Connexins in vascular physiology and pathology', *Antioxidants and Redox Signaling*, pp. 267–282. Available at: https://doi.org/10.1089/ars.2008.2115.

Brunelle, A. and Laprévote, O. (2009) 'Lipid imaging with cluster time-of-flight

secondary ion mass spectrometry', *Analytical and Bioanalytical Chemistry*, 393(1), pp. 31–35. Available at: https://doi.org/10.1007/s00216-008-2367-3.

Buss, J.L. and Hasinoff, B.B. (1993) 'The one-ring open hydrolysis product intermediates of the cardioprotective agent ICRF-187 (dexrazoxane) displace iron from iron-anthracycline complexes', *Agents and Actions*, 40(1–2), pp. 86–95. Available at: https://doi.org/10.1007/bf01976756.

Caballero, R.M. *et al.* (2022) 'Incidence of long-term cardiotoxicity and evolution of the systolic function in patients with breast cancer treated with anthracyclines', *Cardiology Journal*, 29(2), p. 228. Available at: https://doi.org/10.5603/cj.a2020.0062.

Cagel, M. *et al.* (2017) 'Doxorubicin: nanotechnological overviews from bench to bedside', *Drug Discovery Today*, pp. 270–281. Available at: https://doi.org/10.1016/j.drudis.2016.11.005.

Cailleau, R., Olivé, M. and Cruciger, Q.V.J. (1978) 'Long-term human breast carcinoma cell lines of metastatic origin: Preliminary characterization', *In Vitro*, 14(11), pp. 911–915. Available at: https://doi.org/10.1007/bf02616120.

Calder, B.W. *et al.* (2015) 'Inhibition of Connexin 43 Hemichannel-Mediated ATP Release Attenuates Early Inflammation During the Foreign Body Response', *Tissue Engineering. Part A*, 21(11–12), pp. 1752–1762. Available at: https://doi.org/10.1089/ten.tea.2014.0651.

Capranico, G. *et al.* (1992) 'Different patterns of gene expression of topoisomerase II isoforms in differentiated tissues during murine development', *Biochimica et Biophysica Acta (BBA) - Gene Structure and Expression*, 1132(1), pp. 43–48. Available at: https://doi.org/10.1016/0167-4781(92)90050-a.

Capranico, G., Marinello, J. and Chillemi, G. (2017) 'Type I DNA Topoisomerases', *Journal of Medicinal Chemistry*, 60(6), pp. 2169–2192. Available at: https://doi.org/10.1021/acs.jmedchem.6b00966.

Cardiac Muscle Tissue | GetBodySmart (2022). Available at: https://www.getbodysmart.com/circulatory-system/cardiac-muscle-tissue (Accessed: 29 June 2022).

Cardinale, D. *et al.* (2000) 'Left ventricular dysfunction predicted by early troponin I

release after high-dose chemotherapy', *Journal of the American College of Cardiology*, 36(2), pp. 517–522. Available at: https://doi.org/10.1016/s0735-1097(00)00748-8.

Cardinale, D. *et al.* (2004) 'Prognostic Value of Troponin I in Cardiac Risk Stratification of Cancer Patients Undergoing High-Dose Chemotherapy', *Circulation*, 109(22), pp. 2749–2754. Available at: https://doi.org/10.1161/01.cir.0000130926.51766.cc.

Cardinale, D. *et al.* (2015) 'Early detection of anthracycline cardiotoxicity and improvement with heart failure therapy', *Circulation*, 131(22), pp. 1981–1988. Available at: https://doi.org/10.1161/circulationaha.114.013777.

Cardinale, D. *et al.* (2017) 'Using biomarkers to predict and to prevent cardiotoxicity of cancer therapy', *Expert Review of Molecular Diagnostics*, 17(3), pp. 245–256. Available at: https://doi.org/10.1080/14737159.2017.1283219.

Cardinale, D. *et al.* (2018) 'Anthracycline-induced cardiotoxicity: A multicenter randomised trial comparing two strategies for guiding prevention with enalapril: The International CardioOncology Society-one trial', *European Journal of Cancer*, 94, pp. 126–137. Available at: https://doi.org/doi.org/10.1016/j.ejca.2018.02.005.

Cardinale, D. and Cipolla, C.M. (2016) 'Chemotherapy-induced cardiotoxicity: importance of early detection', *Expert Review of Cardiovascular Therapy*, 14(12), pp. 1297–1299. Available at: https://doi.org/10.1080/14779072.2016.1239528.

Cardinale, D., Iacopo, F. and Cipolla, C.M. (2020) 'Cardiotoxicity of Anthracyclines', *Frontiers in Cardiovascular Medicine*, 0, p. 26. Available at: https://doi.org/10.3389/fcvm.2020.00026.

Cardinale Daniela, D. and Sandri, M.T. (2010) 'Role of Biomarkers in Chemotherapy-Induced Cardiotoxicity', *Progress in Cardiovascular Diseases*, 53(2), pp. 121–129. Available at: https://doi.org/10.1016/j.pcad.2010.04.002.

Celsion (2005) *Celsion Treats First Patient in Phase I Clinical Trial of ThermoDox with Heat for Liver Cancer*. Available at: https://investor.celsion.com/static-files/ed09085a-7749-44af-b970-68616c8f155d (Accessed: 20 October 2022).

Cervantes, D.C. and Zurzolo, C. (2021) 'Peering into tunneling nanotubes-The path forward', *The EMBO Journal*, 40(8). Available at:

https://doi.org/10.15252/embj.2020105789.

Chakravarthy, P. *et al.* (2022) 'Imatinib-induced cardiotoxicity: A study to evaluate cardiac functions in patients on imatinib therapy for chronic myeloid leukemia', *Journal of Applied Hematology*, 13(2), pp. 71–75. Available at: https://doi.org/10.4103/joah.joah_9_21.

Chaytor, A.T. *et al.* (1999) 'The endothelial component of cannabinoid-induced relaxation in rabbit mesenteric artery depends on gap junctional communication', *The Journal of Physiology*, 520(2), pp. 539–550. Available at: https://doi.org/10.1111/j.1469-7793.1999.00539.x.

Chaytor, A.T., Evans, W.H. and Griffith, T.M. (1997) 'Peptides homologous to extracellular loop motifs of connexin 43 reversibly abolish rhythmic contractile activity in rabbit arteries', *The Journal of Physiology*, 503(1), pp. 99–110. Available at: https://doi.org/10.1111/j.1469-7793.1997.099bi.x.

Chen, C.C. *et al.* (2010) 'Effect of pravastatin on ventricular arrhythmias in infarcted rats: Role of connexin43', *Journal of Applied Physiology*, 109(2), pp. 541–552. Available at: https://doi.org/10.1152/japplphysiol.01070.2009.

Chen, G.L. *et al.* (1984) 'Nonintercalative antitumor drugs interfere with the breakage-reunion reaction of mammalian DNA topoisomerase II', *The Journal of Biological Chemistry*, 259(21), pp. 13560–13566.

Chen, Z. and Ai, D. (2016) 'Cardiotoxicity associated with targeted cancer therapies', *Molecular and Clinical Oncology*, 4(5), pp. 675–681. Available at: https://doi.org/10.3892/mco.2016.800.

Chow, E.J. *et al.* (2022) 'Late health outcomes after dexrazoxane treatment: A report from the Children's Oncology Group', *Cancer*, 128(4), pp. 788–796. Available at: https://doi.org/10.1002/cncr.33974.

Christoffersson, J. *et al.* (2018) 'A Cardiac Cell Outgrowth Assay for Evaluating Drug Compounds Using a Cardiac Spheroid-on-a-Chip Device', *Bioengineering*, 5(2), p. 36. Available at: https://doi.org/10.3390/bioengineering5020036.

Chu, T.F. *et al.* (2007) 'Cardiotoxicity Associated with the Tyrosine Kinase Inhibitor Sunitinib', *Lancet*, 370(9604), pp. 2011–2019. Available at:

https://doi.org/10.1016/s0140-6736(07)61865-0.

Classen, S., Olland, S. and Berger, J.M. (2003) 'Structure of the topoisomerase II ATPase region and its mechanism of inhibition by the chemotherapeutic agent ICRF-187', *Proceedings of the National Academy of Sciences of the United States of America*, 100(19), pp. 10629–10634. Available at: https://doi.org/10.1073/pnas.1832879100.

Collin, M. *et al.* (2019) 'ToF-SIMS depth profiling of altered glass', *npj Materials Degradation*, 3(1). Available at: https://doi.org/10.1038/s41529-019-0076-3.

Contreras, J.E. *et al.* (2003) 'Gating and regulation of connexin 43 (Cx43) hemichannels', *Proceedings of the National Academy of Sciences of the United States of America*, 100(20), pp. 11388–11393. Available at: https://doi.org/10.1073/pnas.1434298100.

Correia, A.S., Gärtner, F. and Vale, N. (2021) 'Drug combination and repurposing for cancer therapy: the example of breast cancer', *Heliyon*, 7(1). Available at: https://doi.org/10.1016/j.heliyon.2021.e05948.

Cotter, M.L. *et al.* (2018) 'Lipidated connexin mimetic peptides potently inhibit gap junction-mediated Ca2+-wave propagation', *American Journal of Physiology - Cell Physiology*, 315(2), pp. 141–154. Available at: https://doi.org/10.1152/ajpcell.00156.2017.

Cotter, M.L. *et al.* (2019) 'Channels and Transporters in Cell Signaling: The lipidated connexin mimetic peptide SRPTEKT-Hdc is a potent inhibitor of Cx43 channels with specificity for the pS368 phospho-isoform', *American Journal of Physiology - Cell Physiology*, 317(4), p. C825. Available at: https://doi.org/10.1152/ajpcell.00160.2019.

Coughlin, S.S. *et al.* (2020) 'Cardiovascular Disease among Breast Cancer Survivors', *Cardiovascular Disorder and Medicine*, 2(1), pp. 1–5. Available at: https://doi.org/10.31487/j.cdm.2020.01.01.

Curigliano, G. *et al.* (2020) 'Management of cardiac disease in cancer patients throughout oncological treatment: ESMO consensus recommendations', *Annals of oncology: official journal of the European Society for Medical Oncology*, 31(2), p. 171. Available at: https://doi.org/10.1016/j.annonc.2019.10.023.

Cutts, S.M. *et al.* (2005) 'The power and potential of doxorubicin-DNA adducts', *IUBMB Life*, 57(2), pp. 73–81. Available at: https://doi.org/10.1080/15216540500079093.

Daily , N.J. *et al.* (2017) 'Calcium Transient Assays for Compound Screening with Human iPSC-derived Cardiomyocytes: Evaluating New Tools', *Journal of Evolving Stem Cell Research*, 1(2), pp. 1–11. Available at: https://doi.org/10.14302/issn.2574-4372.jesr-16-1395.

Dalen, E.C. van *et al.* (2011) 'Cardioprotective interventions for cancer patients receiving anthracyclines', *The Cochrane Database of Systematic Reviews*, 2011(6), p. CD003917. Available at: https://doi.org/10.1002/14651858.cd003917.pub4.

Damiani, E. *et al.* (2019) 'How reliable are in vitro IC50 values? Values vary with cytotoxicity assays in human glioblastoma cells', *Toxicology Letters*, 302, pp. 28–34. Available at: https://doi.org/10.1016/j.toxlet.2018.12.004.

Dann, O. *et al.* (1971) 'Trypanocide Diamidine des 2-Phenyl-benzofurans, 2-Phenyl-indens und 2-Phenyl-indols', *Justus Liebigs Annalen der Chemie*, 749(1), pp. 68–89. Available at: https://doi.org/10.1002/jlac.19717490110.

Danson, S. *et al.* (2004) 'Phase I dose escalation and pharmacokinetic study of pluronic polymer-bound doxorubicin (SP1049C) in patients with advanced cancer', *British Journal of Cancer*, 90(11), pp. 2085–2091. Available at: https://doi.org/10.1038/sj.bjc.6601856.

Davidson, M.M. *et al.* (2005) 'Novel cell lines derived from adult human ventricular cardiomyocytes', *Journal of Molecular and Cellular Cardiology*, 39(1), pp. 133–147. Available at: https://doi.org/10.1016/j.yjmcc.2005.03.003.

Debela, D.T. *et al.* (2021) 'New approaches and procedures for cancer treatment: Current perspectives', *SAGE Open Medicine*, 9, p. 20503121211034370. Available at: https://doi.org/10.1177/20503121211034366.

Denbigh, J.L. and Lockyer, N.P. (2014) 'Materials Science and Technology ToF-SIMS as a tool for profiling lipids in cancer and other diseases ToF-SIMS as a tool for profiling lipids in cancer and other diseases'. Available at: https://doi.org/10.1179/1743284714Y.0000000648.

Denizot, F. and Lang, R. (1986) 'Rapid colorimetric assay for cell growth and survival. Modifications to the tetrazolium dye procedure giving improved sensitivity and reliability', *Journal of Immunological Methods*, 89(2), pp. 271–277. Available at: https://doi.org/10.1016/0022-1759(86)90368-6.

Desplantez, T. (2017) 'Cardiac Cx43, Cx40 and Cx45 co-assembling: Involvement of connexins epitopes in formation of hemichannels and Gap junction channels', *BMC Cell Biology*, 18(1), pp. 1–13. Available at: https://doi.org/10.1186/s12860-016-0118-4.

Dou, Y., Hynynen, K. and Allen, C. (2017) 'To heat or not to heat: Challenges with clinical translation of thermosensitive liposomes', *Journal of Controlled Release*, 249, pp. 63–73. Available at: https://doi.org/10.1016/j.jconrel.2017.01.025.

Dovmark, T.H. *et al.* (2017) 'Connexin-43 channels are a pathway for discharging lactate from glycolytic pancreatic ductal adenocarcinoma cells', *Oncogene*, 36(32), pp. 4538–4550. Available at: https://doi.org/10.1038/onc.2017.71.

Dovmark, T.H. *et al.* (2018) 'Normoxic cells remotely regulate the acid-base balance of cells at the hypoxic core of connexin-coupled tumor growths', *FASEB journal: official publication of the Federation of American Societies for Experimental Biology*, 32(1), pp. 83–96. Available at: https://doi.org/10.1096/fj.201700480r.

Driedonks, T.A.P., Nijen Twilhaar, M.K. and Nolte-'t Hoen, E.N.M. (2019) 'Technical approaches to reduce interference of Fetal calf serum derived RNA in the analysis of extracellular vesicle RNA from cultured cells', *Journal of Extracellular Vesicles*, 8(1). Available at: https://doi.org/10.1080/20013078.2018.1552059.

Drugs.com (2023) *Lipodox (Intravenous)*. Available at: https://www.drugs.com/cons/lipodox.html (Accessed: 14 August 2023).

Druhan, L., Fasan, O. and Copelan, O.R. (2015) 'Acute Heart Failure in a Patient with Acute Myeloid Leukemia following Daunorubicin Treatment: a Case Report', *Journal of Leukemia*, 3(2). Available at: https://doi.org/10.4172/2329-6917.1000185.

Drummond, G.R. *et al.* (2000) 'Transcriptional and posttranscriptional regulation of endothelial nitric oxide synthase expression by hydrogen peroxide', *Circulation Research*, 86(3), pp. 347–354. Available at: https://doi.org/10.1161/01.res.86.3.347.

Duffy, H.S. *et al.* (2002) 'pH-dependent intramolecular binding and structure involving Cx43 cytoplasmic domains', *The Journal of Biological Chemistry*, 277(39), pp. 36706–36714. Available at: https://doi.org/10.1074/jbc.m207016200.

Duggan, S.T. *et al.* (2011) 'Pegylated liposomal doxorubicin: A review of its use in metastatic breast cancer, ovarian cancer, multiple myeloma and AIDS-related Kaposis sarcoma', *Drugs*, 71(18), pp. 2531–2558. Available at: https://doi.org/10.2165/11207510-000000000-00000.

Dunk, C.E. *et al.* (2012) 'The molecular role of connexin 43 in human trophoblast cell fusion', *Biology of Reproduction*, 86(4). Available at: https://doi.org/10.1095/biolreprod.111.096925.

Dunn, C.A. and Lampe, P.D. (2014) 'Injury-triggered Akt phosphorylation of Cx43: A ZO-1-driven molecular switch that regulates gap junction size', *Journal of Cell Science*, 127(2), pp. 455–464. Available at: https://doi.org/10.1242/jcs.142497.

Duray, P.H., Cuono, C.B. and Madri, J.A. (1986) 'Demonstration of cutaneous doxorubicin extravasation by rhodamine-filtered fluorescence microscopy', *Journal of Surgical Oncology*, 31(1), pp. 21–25. Available at: https://doi.org/10.1002/jso.2930310104.

Epifantseva, I. and Shaw, R.M. (2018) 'Intracellular trafficking pathways of Cx43 gap junction channels', *Biochimica et Biophysica Acta - Biomembranes*, 1860(1), pp. 40–47. Available at: https://doi.org/10.1016/j.bbamem.2017.05.018.

Evans, W.H. and Martin, P.E.M. (2002) 'Gap junctions: Structure and function (review)', *Molecular Membrane Biology*, pp. 121–136. Available at: https://doi.org/10.1080/09687680210139839.

Fang, X. Bin *et al.* (2016) 'pH-sensitive micelles based on acid-labile pluronic F68–curcumin conjugates for improved tumor intracellular drug delivery', *International Journal of Pharmaceutics*, 502(1–2), pp. 28–37. Available at: https://doi.org/10.1016/j.ijpharm.2016.01.029.

Feaster, T.K. *et al.* (2021) 'Acute effects of cardiac contractility modulation on human induced pluripotent stem cell-derived cardiomyocytes', *Physiological Reports*, 9(21). Available at: https://doi.org/10.14814/phy2.15085.

Feijen, E.A.M. *et al.* (2019) 'Derivation of Anthracycline and Anthraquinone Equivalence Ratios to Doxorubicin for Late-Onset Cardiotoxicity', *JAMA Oncology*, 5(6), p. 864. Available at: https://doi.org/10.1001/jamaoncol.2018.6634.

Felker, G.M. *et al.* (2015) 'Serial high sensitivity cardiac troponin T measurement in acute heart failure: insights from the RELAX-AHF study', *European Journal of Heart Failure*, 17(12), pp. 1262–1270. Available at: https://doi.org/10.1002/ejhf.341.

Ferraro, F. *et al.* (2016) 'Weibel-Palade body size modulates the adhesive activity of its von Willebrand Factor cargo in cultured endothelial cells', *Scientific Reports*, 6, p. 32473. Available at: https://doi.org/10.1038/srep32473.

Figtree, G.A. *et al.* (2017) 'Vascularized Cardiac Spheroids as Novel 3D in vitro Models to Study Cardiac Fibrosis', *Cells Tissues Organs*, 204(3–4), pp. 191–198. Available at: https://doi.org/10.1159/000477436.

Filipe, V., Hawe, A. and Jiskoot, W. (2010) 'Critical evaluation of nanoparticle tracking analysis (NTA) by NanoSight for the measurement of nanoparticles and protein aggregates', *Pharmaceutical Research*, 27(5), pp. 796–810. Available at: https://doi.org/10.1007/s11095-010-0073-2.

Fontes, M.S.C. *et al.* (2012) 'Functional consequences of abnormal Cx43 expression in the heart', *Biochimica et Biophysica Acta - Biomembranes*, 1818(8), pp. 2020–2029. Available at: https://doi.org/10.1016/j.bbramem.2011.07.039.

Force, T. and Kolaja, K.L. (2011) 'Cardiotoxicity of kinase inhibitors: the prediction and translation of preclinical models to clinical outcomes', *Nature Reviews Drug Discovery*, 10(2), pp. 111–126. Available at: https://doi.org/10.1038/nrd3252.

Forrest, R.A. *et al.* (2012) 'Activation of DNA damage response pathways as a consequence of anthracycline-DNA adduct formation', *Biochemical pharmacology*, 83(12), pp. 1602–1612. Available at: https://doi.org/10.1016/j.bcp.2012.02.026.

Friedrichs, G.S., Patmore, L. and Bass, A. (2005) 'Non-clinical evaluation of ventricular repolarization (ICH S7B): Results of an interim survey of international pharmaceutical companies', *Journal of Pharmacological and Toxicological Methods*, 52(1), pp. 6–11. Available at: https://doi.org/10.1016/j.vascn.2005.05.001.

Gabizon, A. *et al.* (1989) 'Systemic administration of doxorubicin-containing

liposomes in cancer patients: a phase I study', *European Journal of Cancer & Clinical Oncology*, 25(12), pp. 1795–1803. Available at: https://doi.org/10.1016/0277-5379(89)90350-7.

Galán-Arriola, C. *et al.* (2021) 'Remote ischaemic preconditioning ameliorates anthracycline-induced cardiotoxicity and preserves mitochondrial integrity', *Cardiovascular Research*, 117(4), pp. 1132–1143. Available at: https://doi.org/10.1093/cvr/cvaa181.

Galán-Arriola, C. *et al.* (2022) 'Coronary microcirculation damage in anthracycline cardiotoxicity', *Cardiovascular Research*, 118(2), p. 531. Available at: https://doi.org/10.1093/cvr/cvab053.

Garcia-Pavia, P. *et al.* (2019) 'Genetic Variants Associated With Cancer Therapy-Induced Cardiomyopathy', *Circulation*, 140(1), pp. 31–41. Available at: https://doi.org/10.1161/circulationaha.118.037934.

Gemel, J. *et al.* (2019) 'Connecting Exosomes and Connexins', *Cancers*, 11(4), p. 476. Available at: https://doi.org/10.3390/cancers11040476.

Ghelli Luserna Di Rorà, A. *et al.* (2021) 'Exploring the ATR-CHK1 pathway in the response of doxorubicin-induced DNA damages in acute lymphoblastic leukemia cells', *Cell Biology and Toxicology*, 39(3), pp. 795–811. Available at: https://doi.org/10.1007/s10565-021-09640-x.

Giantris, A. *et al.* (1998) 'Anthracycline-induced cardiotoxicity in children and young adults', *Critical Reviews in Oncology/Hematology*, 27(1), pp. 53–68. Available at: https://doi.org/10.1016/s1040-8428(97)10007-5.

Gilula, N.B., Reeves, O.R. and Steinbach, A. (1972) 'Metabolic Coupling, Ionic Coupling and Cell Contacts', *Nature*, 235(5336), pp. 262–265. Available at: https://doi.org/10.1038/235262a0.

Gomes, J. *et al.* (2012) 'Electrophysiological abnormalities precede overt structural changes in arrhythmogenic right ventricular cardiomyopathy due to mutations in desmoplakin-A combined murine and human study', *European Heart Journal*, 33(15), pp. 1942–1953. Available at: https://doi.org/10.1093/eurheartj/ehr472.

Gong, K. *et al.* (2022) 'Gap junctions mediate glucose transfer to promote colon

cancer growth in three-dimensional spheroid culture', *Cancer Letters*, 531, pp. 27–38. Available at: https://doi.org/10.1016/j.canlet.2022.01.023.

Goodenough, D.A., Paul, D.L. and Jesaitis, L. (1988) 'Topological distribution of two connexin32 antigenic sites in intact and split rodent hepatocyte gap junctions.', *Journal of Cell Biology*, 107(5), pp. 1817–1824. Available at: https://doi.org/10.1083/jcb.107.5.1817.

Gottdiener, J.S. *et al.* (1981) 'Doxorubicin cardiotoxicity: Assessment of late left ventricular dysfunction by radionuclide cineangiography', *Annals of Internal Medicine*, 94(4–1), pp. 430–435. Available at: https://doi.org/10.7326/0003-4819-94-4-430.

Grein, A. *et al.* (1963) 'Descrizione e classificazione di un attinomicete (Streptomyces peucetius sp. nova) produttore di una sostanza attivita antitumorale: La daunomicina.', *Giorn Microbiol*, (11), pp. 109–118.

Grenier, M.A. and Lipshultz, S.E. (1998) 'Epidemiology of anthracycline cardiotoxicity in children and adults', *Seminars in Oncology*, 25(4 Suppl 10), pp. 72–85.

Gulati, G. *et al.* (2017) 'Neurohormonal Blockade and Circulating Cardiovascular Biomarkers During Anthracycline Therapy in Breast Cancer Patients: Results From the PRADA (Prevention of Cardiac Dysfunction During Adjuvant Breast Cancer Therapy) Study', *Journal of the American Heart Association*, 6(11). Available at: https://doi.org/10.1161/jaha.117.006513.

Guo, Y.H. and Yang, Y.Q. (2022) 'Atrial Fibrillation: Focus on Myocardial Connexins and Gap Junctions', *Biology*, 11(4), pp. 1–15. Available at: https://doi.org/10.3390/biology11040489.

Guo, Z. *et al.* (2021) 'Apolipoprotein M attenuates doxorubicin cardiotoxicity by regulating transcription factor EB', *bioRxiv*, 12(1), p. 426397. Available at: https://doi.org/10.1101/2021.01.12.426397.

Gupta, V. *et al.* (2018) 'Role of ACE inhibitors in anthracycline-induced cardiotoxicity: A randomized, double-blind, placebo-controlled trial', *Pediatric Blood and Cancer*, 65(11), pp. 2–7. Available at: https://doi.org/10.1002/pbc.27308.

Gurung, S. *et al.* (2021) 'The exosome journey: from biogenesis to uptake and intracellular signalling', *Cell Communication and Signaling: CCS*, 19(1), p. 47.

Available at: https://doi.org/10.1186/S12964-021-00730-1.

Haberichter, S.L. *et al.* (2005) 'Re-establishment of VWF-dependent Weibel-Palade bodies in VWD endothelial cells.', *Blood*, 105(1), pp. 145–52. Available at: https://doi.org/10.1182/blood-2004-02-0464.

Hader, S.N. *et al.* (2019) 'Detrimental effects of chemotherapy on human coronary microvascular function', *American Journal of Physiology-Heart and Circulatory Physiology*, 317(4), pp. H705–H710. Available at: https://doi.org/10.1152/ajpheart.00370.2019.

Hajduk, S.L. (1976) 'Demonstration of kinetoplast DNA in dyskinetoplastic strains of Trypanosoma equiperdum', *Science*, 191(4229), pp. 858–859. Available at: https://doi.org/10.1126/science.1251198.

Hannah Ritchie and Fiona Spooner et al. (2018) 'Causes of death', *Our World in Data* [Preprint]. Available at: https://ourworldindata.org/causes-of-death.

Harris, L. *et al.* (2002) 'Liposome-encapsulated doxorubicin compared with conventional doxorubicin in a randomized multicenter trial as first-line therapy of metastatic breast carcinoma', *Cancer*, 94(1), pp. 25–36. Available at: https://doi.org/10.1002/cncr.10201.

He, Q. *et al.* (2020) 'Repeated Remote Ischemic Conditioning Reduces Doxorubicin-Induced Cardiotoxicity', *JACC. CardioOncology*, 2(1), pp. 41–52. Available at: https://doi.org/10.1016/j.jaccao.2020.01.005.

Henss, A. *et al.* (2013) 'Applicability of ToF-SIMS for monitoring compositional changes in bone in a long-term animal model', *Journal of the Royal Society Interface*, 10(86). Available at: https://doi.org/10.1098/rsif.2013.0332.

Herrmann, J. *et al.* (2014) 'Evaluation and Management of Patients With Heart Disease and Cancer: Cardio-Oncology', *Mayo Clinic Proceedings*, 89(9), p. 1287. Available at: https://doi.org/10.1016/j.mayocp.2014.05.013.

Hesketh, G.G. *et al.* (2010) 'Ultrastructure and regulation of lateralized connexin43 in the failing heart', *Circulation Research*, 106(6), pp. 1153–1163. Available at: https://doi.org/10.1161/circresaha.108.182147.

Himelman, E. *et al.* (2020) 'Prevention of connexin-43 remodeling protects against

Duchenne muscular dystrophy cardiomyopathy', *Journal of Clinical Investigation*, 130(4), pp. 1713–1727. Available at: https://doi.org/10.1172/jci128190.

Hinz, B. *et al.* (2001) 'Alpha-smooth muscle actin expression upregulates fibroblast contractile activity', *Molecular Biology of the Cell*, 12(9), pp. 2730–2741. Available at: https://doi.org/10.1091/mbc.12.9.2730.

Hofmann, J.P., Rohnke, M. and Weckhuysen, B.M. (2014) 'Recent advances in secondary ion mass spectrometry of solid acid catalysts: large zeolite crystals under bombardment', *Physical Chemistry Chemical Physics*, 16(12), pp. 5465–5474. Available at: https://doi.org/10.1039/c3cp54337d.

Hole, L.D. *et al.* (2014) 'Diazoxide protects against doxorubicin-induced cardiotoxicity in the rat', *BMC Pharmacology and Toxicology*, 15(1), pp. 1–8. Available at: https://doi.org/10.1186/2050-6511-15-28.

Howerton, S.B., Nagpal, A. and Williams, L.D. (2003) 'Surprising roles of electrostatic interactions in DNA-ligand complexes', *Biopolymers*, 69(1), pp. 87–99. Available at: https://doi.org/10.1002/bip.10319.

Huang, R.P. *et al.* (2001) 'Connexin 43 (cx43) enhances chemotherapy-induced apoptosis in human glioblastoma cells', *International Journal of Cancer*, 92(1), pp. 130–138. Available at: https://doi.org/10.1002/1097-0215(200102)9999:9999<::AID-IJC1165>3.0.CO;2-G.

Huethorst, E. *et al.* (2022) 'Conventional rigid 2D substrates cause complex contractile signals in monolayers of human induced pluripotent stem cell-derived cardiomyocytes', *The Journal of Physiology*, 600(3), pp. 483–507. Available at: https://doi.org/10.1113/jp282228.

Hunter, A.W. *et al.* (2005) 'Zonula occludens-1 alters connexin43 gap junction size and organization by influencing channel accretion', *Molecular Biology of the Cell*, 16(12), pp. 5686–5698. Available at: https://doi.org/10.1091/mbc.E05-08-0737.

Jacobs, A.C. *et al.* (2013) 'Adenylate Kinase Release as a High-Throughput-Screening-Compatible Reporter of Bacterial Lysis for Identification of Antibacterial Agents', *Antimicrobial Agents and Chemotherapy*, 57(1), p. 26. Available at: https://doi.org/10.1128/aac.01640-12.

Jaffe, E.A. *et al.* (1973) 'Culture of human endothelial cells derived from umbilical veins. Identification by morphologic and immunologic criteria', *The Journal of Clinical Investigation*, 52(11), pp. 2745–2756. Available at: https://doi.org/10.1172/jci107470.

Jansen, J.A. *et al.* (2010) 'Cardiac connexins and impulse propagation', *Journal of Molecular and Cellular Cardiology*, 48(1), pp. 76–82. Available at: https://doi.org/10.1016/j.yjmcc.2009.08.018.

Jiang, J. *et al.* (2019) 'Interaction of α Carboxyl Terminus 1 Peptide With the Connexin 43 Carboxyl Terminus Preserves Left Ventricular Function After Ischemia-Reperfusion Injury', *Journal of the American Heart Association*, 8(16), p. e012385. Available at: https://doi.org/10.1161/jaha.119.012385.

Jirkovský, E. *et al.* (2021) 'Clinically Translatable Prevention of Anthracycline Cardiotoxicity by Dexrazoxane Is Mediated by Topoisomerase II Beta and Not Metal Chelation', *Circulation. Heart failure*, 14(11), p. e008209. Available at: https://doi.org/10.1161/circheartfailure.120.008209.

Jones, J.C. *et al.* (2021) 'Glucose-limiting conditions induce an invasive population of MDA-MB-231 breast cancer cells with increased connexin 43 expression and membrane localization', *Journal of Cell Communication and Signaling*, 15(2), pp. 223–236. Available at: https://doi.org/10.1007/s12079-020-00601-3.

Jozwiak, J. and Dhein, S. (2008) 'Local effects and mechanisms of antiarrhythmic peptide AAP10 in acute regional myocardial ischemia: electrophysiological and molecular findings', *Naunyn-Schmiedeberg's Archives of Pharmacology*, 378(5), pp. 459–470. Available at: https://doi.org/10.1007/s00210-008-0317-4.

Julyan, P.J. *et al.* (1999) 'Preliminary clinical study of the distribution of HPMA copolymers bearing doxorubicin and galactosamine', *Journal of Controlled Release*, 57(3), pp. 281–290. Available at: https://doi.org/10.1016/s0168-3659(98)00124-2.

Kalcheva, N. *et al.* (2007) 'Gap junction remodeling and cardiac arrhythmogenesis in a murine model of oculodentodigital dysplasia', *Proceedings of the National Academy of Sciences of the United States of America*, 104(51), pp. 20512–20516. Available at: https://doi.org/10.1073/pnas.0705472105.

Kalivendi, S. V. *et al.* (2001) 'Doxorubicin-induced apoptosis is associated with increased transcription of endothelial nitric-oxide synthase: Effect of antiapoptotic

antioxidants and calcium', *Journal of Biological Chemistry*, 276(50), pp. 47266–47276. Available at: https://doi.org/10.1074/jbc.m106829200.

Kapałczyńska, M. *et al.* (2018) '2D and 3D cell cultures – a comparison of different types of cancer cell cultures', *Archives of Medical Science: AMS*, 14(4), p. 910. Available at: https://doi.org/10.5114/aoms.2016.63743.

Karukstis, K.K. *et al.* (1998) 'Deciphering the fluorescence signature of daunomycin and doxorubicin', *Biophysical Chemistry*, 73(3), pp. 249–263. Available at: https://doi.org/10.1016/S0301-4622(98)00150-1.

Kauffman, M.K. *et al.* (2016) 'Fluorescence-Based Assays for Measuring Doxorubicin in Biological Systems', *Reactive Oxygen Species (Apex, N.C.)*, 2(6), p. 432. Available at: https://doi.org/10.20455/ros.2016.873.

Kciuk, M. *et al.* (2022) 'Cyclin-Dependent Kinase Synthetic Lethality Partners in DNA Damage Response', *International Journal of Molecular Sciences*, 23(7), p. 3555. Available at: https://doi.org/10.3390/ijms23073555.

Kciuk, M. *et al.* (2023) 'Doxorubicin - An Agent with Multiple Mechanisms of Anticancer Activity', *Cells*, p. 659. Available at: https://doi.org/10.3390/cells12040659.

Ke, X. *et al.* (2017) 'Synergistic dual-modified liposome improves targeting and therapeutic efficacy of bone metastasis from breast cancer', *Drug Delivery*, 24(1), pp. 1680–1689. Available at: https://doi.org/10.1080/10717544.2017.1396384.

Khan, T. and Gurav, P. (2017) 'PhytoNanotechnology: Enhancing Delivery of Plant Based Anti-cancer Drugs.', *Frontiers in Pharmacology*, 8, p. 1002. Available at: https://doi.org/10.3389/fphar.2017.01002.

Kim, D.Y. *et al.* (2019) 'Cardiovascular outcome of breast cancer patients with concomitant radiotherapy and chemotherapy: A 10-year multicenter cohort study', *Journal of Cardiology*, 74(2), pp. 175–181. Available at: https://doi.org/10.1016/j.jjcc.2019.02.001.

Kim, S.J. *et al.* (2011) 'Atrial remodeling and the substrate for atrial fibrillation in rat hearts with elevated afterload', *Circulation: Arrhythmia and Electrophysiology*, 4(5), pp. 761–769. Available at: https://doi.org/10.1161/circep.111.964783.

Kim, S.Y. *et al.* (2006) 'Doxorubicin-induced reactive oxygen species generation and

intracellular Ca2+ increase are reciprocally modulated in rat cardiomyocytes', *Experimental and Molecular Medicine*, 38(5), pp. 535–545. Available at: https://doi.org/10.1038/emm.2006.63.

King, M.R. (2012) 'Gather Round: In Vitro Tumor Spheroids as Improved Models of In Vivo Tumors', *Journal of Bioengineering & Biomedical Science*, 2(4). Available at: https://doi.org/10.4172/2155-9538.1000e109.

Kitsuka, T. *et al.* (2019) '2-Cl-C.OXT-A stimulates contraction through the suppression of phosphodiesterase activity in human induced pluripotent stem cell-derived cardiac organoids', *PLoS ONE*, 14(7), p. e0213114. Available at: https://doi.org/10.1371/journal.pone.0213114.

Koene, R.J. *et al.* (2016) 'Shared Risk Factors in Cardiovascular Disease and Cancer', *Circulation*, 133(11), pp. 1104–1114. Available at: https://doi.org/10.1161/circulationaha.115.020406.

Koepple, C. *et al.* (2021) 'Expression of Connexin43 Stimulates Endothelial Angiogenesis Independently of Gap Junctional Communication In Vitro', *International Journal of Molecular Sciences*, 22(14). Available at: https://doi.org/10.3390/ijms22147400.

Kopljar, I. *et al.* (2018) 'Development of a Human iPSC Cardiomyocyte-Based Scoring System for Cardiac Hazard Identification in Early Drug Safety De-risking', *Stem Cell Reports*, 11(6), pp. 1365–1377. Available at: https://doi.org/10.1016/j.stemcr.2018.11.007.

Kotamraju, S. *et al.* (2000) 'Doxorubicin-induced apoptosis in endothelial cells and cardiomyocytes is ameliorated by nitrone spin traps and ebselen. Role of reactive oxygen and nitrogen species', *Journal of Biological Chemistry*, 275(43), pp. 33585–33592. Available at: https://doi.org/10.1074/jbc.m003890200.

Kotini, M. *et al.* (2018) 'Gap junction protein Connexin-43 is a direct transcriptional regulator of N-cadherin in vivo', *Nature Communications*, 9(1), pp. 1–17. Available at: https://doi.org/10.1038/s41467-018-06368-x.

Kurz, E.U., Douglas, P. and Lees-Miller, S.P. (2004) 'Doxorubicin activates ATM-dependent phosphorylation of multiple downstream targets in part through the generation of reactive oxygen species', *Journal of Biological Chemistry*, 279(51), pp.

53272–53281. Available at: https://doi.org/10.1074/jbc.M406879200.

Kwok, J.C. and Richardson, D.R. (2000) 'The cardioprotective effect of the iron chelator dexrazoxane (ICRF-187) on anthracycline-mediated cardiotoxicity', *Redox Report*, 5(6), pp. 317–324. Available at: https://doi.org/10.1179/135100000101535898.

Laird, D.W. (2006) 'Life cycle of connexins in health and disease', *Biochemical Journal*, 394(3), pp. 527–543. Available at: https://doi.org/10.1042/bj20051922.

Laird, D.W. and Lampe, P.D. (2022) 'Cellular mechanisms of connexin-based inherited diseases', *Trends in Cell Biology*, 32(1), pp. 58–69. Available at: https://doi.org/10.1016/j.tcb.2021.07.007.

Lamarche, B.J., Orazio, N.I. and Weitzman, M.D. (2010) 'The MRN complex in double-strand break repair and telomere maintenance', *FEBS Letters*, 584(17), pp. 3682–3695. Available at: https://doi.org/10.1016/j.febslet.2010.07.029.

Lambiase, P.D. and Tinker, A. (2015) 'Connexins in the heart', *Cell and Tissue Research*, 360(3), pp. 675–684. Available at: https://doi.org/10.1007/s00441-014-2020-8.

Lampe, P.D. and Lau, A.F. (2004) 'The effects of connexin phosphorylation on gap junctional communication', *International Journal of Biochemistry and Cell Biology*, 36(7), pp. 1171–1186. Available at: https://doi.org/10.1016/s1357-2725(03)00264-4.

Lancellotti, P. *et al.* (2019) 'Cardio-Oncology Services: rationale, organization, and implementation', *European Heart Journal*, 40(22), pp. 1756–1763. Available at: https://doi.org/10.1093/eurheartj/ehy453.

Landon, C.D. *et al.* (2011) 'Nanoscale Drug Delivery and Hyperthermia: The Materials Design and Preclinical and Clinical Testing of Low Temperature-Sensitive Liposomes Used in Combination with Mild Hyperthermia in the Treatment of Local Cancer', *The Open Nanomedicine Journal*, 3, p. 38. Available at: https://doi.org/10.2174/1875933501103010038.

Lanekoff, I. *et al.* (2010) 'Time of flight mass spectrometry imaging of samples fractured in situ with a spring-loaded trap system', *Analytical Chemistry*, 82(15), pp. 6652–6659. Available at: https://doi.org/10.1021/ac101243b.

Lang, R.M. *et al.* (2015) 'Recommendations for Cardiac Chamber Quantification by Echocardiography in Adults: An Update from the American Society of Echocardiography and the European Association of Cardiovascular Imaging', *Journal of the American Society of Echocardiography*, 28(1), p. 1–39.e14. Available at: https://doi.org/10.1016/j.echo.2014.10.003.

Langendorff, O. (1897) 'Untersuchungen am überlebenden Säugethierherzen', *Archiv für die gesamte Physiologie des Menschen und der Tiere*, 66(7), pp. 355–400. Available at: https://doi.org/10.1007/bf01886524.

Lee, T.M., Lin, S.Z. and Chang, N.C. (2013) 'Both PKA and Epac Pathways Mediate N-Acetylcysteine-Induced Connexin43 Preservation in Rats with Myocardial Infarction', *PLoS ONE*, 8(8), p. e71878. Available at: https://doi.org/10.1371/journal.pone.0071878.

Lefrak, E.A. *et al.* (1973) 'A clinicopathologic analysis of adriamycin cardiotoxicity', *Cancer*, 32(2), pp. 302–314. Available at: https://doi.org/10.1002/1097-0142(197308)32:2<302::aid-cncr2820320205>3.0.co;2-2.

Lehrich, B.M. *et al.* (2018) 'Fetal bovine serum-derived extracellular vesicles persist within vesicle-depleted culture media', *International Journal of Molecular Sciences*, 19(11), p. 3538. Available at: https://doi.org/10.3390/ijms19113538.

Lehrich, B.M., Liang, Y. and Fiandaca, M.S. (2021) 'Foetal bovine serum influence on in vitro extracellular vesicle analyses', *Journal of Extracellular Vesicles*, 10(3), p. e12061. Available at: https://doi.org/10.1002/jev2.12061.

Leithe, E., Mesnil, M. and Aasen, T. (2018) 'The connexin 43 C-terminus: A tail of many tales', *Biochimica et Biophysica Acta Biomembranes*, 1860(1), pp. 48–64. Available at: https://doi.org/10.1016/j.bbamem.2017.05.008.

Leybaert, L. *et al.* (2017) 'Connexins in Cardiovascular and Neurovascular Health and Disease: Pharmacological Implications.', *Pharmacological Reviews*, 69(4), pp. 396–478. Available at: https://doi.org/10.1124/pr.115.012062.

Li, D. *et al.* (2014) 'Isolation and culture of adult mouse cardiomyocytes for cell signaling and in vitro cardiac hypertrophy', *Journal of Visualized Experiments*, (87), pp. 2–9. Available at: https://doi.org/10.3791/51357.

Li, J. *et al.* (2019) 'Collaborative assembly of doxorubicin and galactosyl diblock glycopolymers for targeted drug delivery of hepatocellular carcinoma', *Biomaterials Science*, 8(1), pp. 189–200. Available at: https://doi.org/10.1039/c9bm01604j.

Liao, Y. *et al.* (2001) 'Endothelial cell-specific knockout of connexin 43 causes hypotension and bradycardia in mice', *Proceedings of the National Academy of Sciences of the United States of America*, 98(17), pp. 9989–9994. Available at: https://doi.org/10.1073/pnas.171305298.

Lin, J.H.C. *et al.* (2008) 'A central role of connexin 43 in hypoxic preconditioning', *Journal of Neuroscience*, 28(3), pp. 681–695. Available at: https://doi.org/10.1523/jneurosci.3827-07.2008.

Linscheid, N. *et al.* (2020) 'Quantitative Proteomics of Human Heart Samples Collected In Vivo Reveal the Remodeled Protein Landscape of Dilated Left Atrium Without Atrial Fibrillation', *Molecular & cellular proteomics: MCP*, 19(7), pp. 1132–1144. Available at: https://doi.org/10.1074/mcp.RA119.001878.

Liston, D.R. and Davis, M. (2017) 'Clinically Relevant Concentrations of Anticancer Drugs: A Guide for Nonclinical Studies', *Clinical Cancer Research*, 23(14), pp. 3489–3498. Available at: https://doi.org/10.1158/1078-0432.ccr-16-3083.

Liu, C. *et al.* (2022) 'Generating 3D human cardiac constructs from pluripotent stem cells', *eBioMedicine*, 76, p. 103813. Available at: https://doi.org/10.1016/j.ebiom.2022.103813.

Liu, D. *et al.* (2015) 'Infection by Cx43 adenovirus increased chemotherapy sensitivity in human gastric cancer BGC-823 cells: not involving in induction of cell apoptosis', *Gene*, 574(2), pp. 217–224. Available at: https://doi.org/10.1016/j.gene.2015.08.052.

Liu, Z. *et al.* (2017) 'Vascular disease-causing mutation, smooth muscle α-actin R258C, dominantly suppresses functions of α-actin in human patient fibroblasts', *Proceedings of the National Academy of Sciences of the United States of America*, 114(28), pp. e5569–e5578. Available at: https://doi.org/10.1073/pnas.1703506114.

López-Dávila, A.J. *et al.* (2021) 'Cytotoxicity of snake venom Lys49 PLA2-like myotoxin on rat cardiomyocytes ex vivo does not involve a direct action on the contractile apparatus', *Scientific Reports*, 11(1), p. 19452. Available at: https://doi.org/10.1038/s41598-021-98594-5.

Lucero, C.M. *et al.* (2020) 'Cardiac remodeling and arrhythmogenesis are ameliorated by administration of Cx43 mimetic peptide Gap27 in heart failure rats', *Scientific Reports*, 10(1). Available at: https://doi.org/10.1038/s41598-020-63336-6.

Lynen, F. and Wieland, U. (1937) 'Über die Giftstoffe des Knollenblätterpilzes. IV', *Justus Liebigs Annalen der Chemie*, 533(1), pp. 93–117. Available at: https://doi.org/10.1002/jlac.19385330105.

Lyon, A.R. *et al.* (2020) 'Baseline cardiovascular risk assessment in cancer patients scheduled to receive cardiotoxic cancer therapies: a position statement and new risk assessment tools from the Cardio-Oncology Study Group of the Heart Failure Association of the European Society', *European Journal of Heart Failure*, 22(11), pp. 1945–1960. Available at: https://doi.org/10.1002/ejhf.1920.

Lyon, A.R. *et al.* (2022) '2022 ESC Guidelines on cardio-oncology developed in collaboration with the European Hematology Association (EHA), the European Society for Therapeutic Radiology and Oncology (ESTRO) and the International Cardio-Oncology Society (IC-OS)', *European Heart Journal*, 0, pp. 1–133. Available at: https://doi.org/10.1093/eurheartj/ehac244.

Ma, J.W. *et al.* (2020) 'Inhibition of connexin 43 attenuates oxidative stress and apoptosis in human umbilical vein endothelial cells', *BMC Pulmonary Medicine*, 20(1). Available at: https://doi.org/10.1186/s12890-019-1036-y.

Macedo, A.V.S. *et al.* (2019) 'Efficacy of Dexrazoxane in Preventing Anthracycline Cardiotoxicity in Breast Cancer', *JACC. CardioOncology*, 1(1), pp. 68–79. Available at: https://doi.org/10.1016/j.jaccao.2019.08.003.

Mamas, M.A. and Matetic, A. (2022) 'How Common Is Pre-Existing Cardiovascular Disease in Cancer Patients: What Do We Know? Does It Matter?', *JACC: CardioOncology*, 4(2), pp. 254–257. Available at: https://doi.org/10.1016/j.jaccao.2022.05.001.

Mamoshina, P., Rodriguez, B. and Bueno-Orovio, A. (2021) 'Toward a broader view of mechanisms of drug cardiotoxicity', *Cell Reports. Medicine*, 2(3), p. 100216. Available at: https://doi.org/10.1016/j.xcrm.2021.100216.

Marinello, J., Delcuratolo, M. and Capranico, G. (2018) 'Anthracyclines as Topoisomerase II Poisons: From Early Studies to New Perspectives.', *International*

Journal of Molecular Sciences, 19(11), p. 3480. Available at: https://doi.org/10.3390/ijms19113480.

Marsh, S.R. *et al.* (2021) 'Peptidic connexin43 therapeutics in cardiac reparative medicine', *Journal of Cardiovascular Development and Disease*, 8(5), p. 52. Available at: https://doi.org/10.3390/jcdd8050052.

Martin, P.E.M., Wall, C. and Griffith, T.M. (2005) 'Effects of connexin-mimetic peptides on gap junction functionality and connexin expression in cultured vascular cells', *British Journal of Pharmacology*, 144(5), pp. 617–627. Available at: https://doi.org/10.1038/sj.bjp.0706102.

Martins-Marques, T. *et al.* (2015) 'Ischaemia-induced autophagy leads to degradation of gap junction protein connexin43 in cardiomyocytes', *Biochemical Journal*, 467(2), pp. 231–245. Available at: https://doi.org/10.1042/bj20141370.

Martins-Marques, T. *et al.* (2020) 'Myocardial infarction affects Cx43 content of extracellular vesicles secreted by cardiomyocytes', *Life Science Alliance*, 3(12), pp. 1–16. Available at: https://doi.org/10.26508/lsa.202000821.

Martins-Marques, T. *et al.* (2022) 'Cx43-mediated sorting of miRNAs into extracellular vesicles', *EMBO reports*, 23(7), p. e54312. Available at: https://doi.org/10.15252/embr.202154312.

Max Roser and Hannah Ritchie et al. (2021) 'Burden of disease', *Our World in Data* [Preprint]. Available at: https://ourworldindata.org/burden-of-disease.

MDA-MB-231 - HTB-26 | ATCC (no date). Available at: https://www.atcc.org/products/htb-26#detailed-product-images.

Medina-Leyte, D.J. *et al.* (2020) 'Use of human umbilical vein endothelial cells (HUVEC) as a model to study cardiovascular disease: A review', *Applied Sciences*, 10(3), p. 938. Available at: https://doi.org/10.3390/app10030938.

Meyer, R.A. *et al.* (1992) 'Inhibition of gap junction and adherens junction assembly by connexin and A-CAM antibodies.', *Journal of Cell Biology*, 119(1), pp. 179–189. Available at: https://doi.org/10.1083/jcb.119.1.179.

Michela, P. *et al.* (2015) 'Role of connexin 43 in cardiovascular diseases', *European Journal of Pharmacology*, pp. 71–76. Available at:

https://doi.org/10.1016/j.ejphar.2015.10.030.

Miller, K.D. *et al.* (2022) 'Cancer treatment and survivorship statistics, 2022', *CA: A Cancer Journal for Clinicians*, 72(5), pp. 409–436. Available at: https://doi.org/10.3322/caac.21731.

Mirams, G.R. *et al.* (2011) 'Simulation of multiple ion channel block provides improved early prediction of compounds' clinical torsadogenic risk', *Cardiovascular Research*, 91(1), pp. 53–61. Available at: https://doi.org/10.1093/cvr/cvr044.

Mitry, M.A. and Edwards, J.G. (2016) 'Doxorubicin induced heart failure: Phenotype and molecular mechanisms', *International Journal of Cardiology. Heart & Vasculature*, 10, pp. 17–24. Available at: https://doi.org/10.1016/j.ijcha.2015.11.004.

Mobaraki, M. and Faraji et al. (2017) 'Molecular Mechanisms of Cardiotoxicity: A Review on Major Side-effect of Doxorubicin', *Indian Journal of Pharmaceutical Sciences*, 79(3), pp. 335–344. Available at: https://doi.org/10.4172/pharmaceutical-sciences.1000235.

Mooney, L. *et al.* (2015) 'Effects of acute and chronic sunitinib treatment on cardiac function and calcium/calmodulin-dependent protein kinase II', *British Journal of Pharmacology*, 172(17), pp. 4342–4354. Available at: https://doi.org/10.1111/bph.13213.

Mosmann, T. (1983) 'Rapid colorimetric assay for cellular growth and survival: Application to proliferation and cytotoxicity assays', *Journal of Immunological Methods*, 65(1–2), pp. 55–63. Available at: https://doi.org/10.1016/0022-1759(83)90303-4.

Mulkearns-Hubert, E.E., Reizes, O. and Lathia, J.D. (2020) 'Connexins in Cancer: Jekyll or Hyde?', *Biomolecules*, 10(12). Available at: https://doi.org/10.3390/BIOM10121654.

Murphy, S.F. *et al.* (2016) 'Connexin 43 inhibition sensitizes chemoresistant glioblastoma cells to temozolomide', *Cancer Research*, 76(1), pp. 139–149. Available at: https://doi.org/10.1158/0008-5472.can-15-1286.

Musil, L.S. *et al.* (1990) 'Differential phosphorylation of the gap junction protein connexin43 in junctional communication-competent and -deficient cell lines', *Journal*

of Cell Biology, 111(5), pp. 2077–2088. Available at: https://doi.org/10.1083/jcb.111.5.2077.

Musil, L.S. and Goodenough, D.A. (1993) 'Multisubunit assembly of an integral plasma membrane channel protein, gap junction connexin43, occurs after exit from the ER', *Cell*, 74(6), pp. 1065–1077. Available at: https://doi.org/10.1016/0092-8674(93)90728-9.

Mustroph, J., Neef, S. and Maier, L.S. (2017) 'CaMKII as a target for arrhythmia suppression', *Pharmacology and Therapeutics*, 176, pp. 22–31. Available at: https://doi.org/10.1016/j.pharmthera.2016.10.006.

Nalewajska, M. *et al.* (2020) 'Connexins-Therapeutic Targets in Cancers', *International Journal of Molecular Sciences*, 21(23), p. 9119. Available at: https://doi.org/10.3390/ijms21239119.

Naraoka, H. *et al.* (2015) 'ToF-SIMS analysis of carbonaceous particles in the sample catcher of the Hayabusa spacecraft Planetary science', *Earth, Planets and Space*, 67(1). Available at: https://doi.org/10.1186/s40623-015-0224-0.

Narikawa, M. *et al.* (2019) 'Doxorubicin induces trans-differentiation and MMP1 expression in cardiac fibroblasts via cell death-independent pathways', *PLoS ONE*, 14(9), pp. 1–17. Available at: https://doi.org/10.1371/journal.pone.0221940.

Negro, A., Brar, B.K. and Lee, K.F. (2004) 'Essential roles of Her2/erbB2 in cardiac development and function', *Recent Progress in Hormone Research*, 59, pp. 1–12. Available at: https://doi.org/10.1210/rp.59.1.1.

Nguyen, L.S. *et al.* (2022) 'Systematic analysis of drug-associated myocarditis reported in the World Health Organization pharmacovigilance database', *Nature Communications*, 13(1), p. 25. Available at: https://doi.org/10.1038/s41467-021-27631-8.

NHS England (2020) 'Clinical Commissioning Policy: Dexrazoxane for preventing cardiotoxicity in children and young people (under 25 years) receiving high-dose anthracyclines or related drugs for the treatment of cancer'.

Nicholls, C., Li, H. and Liu, J.P. (2012) 'GAPDH: A common enzyme with uncommon functions', *Clinical and Experimental Pharmacology and Physiology*, 39(8), pp. 674–

679. Available at: https://doi.org/10.1111/j.1440-1681.2011.05599.x.

Nie, X. *et al.* (2017) 'An appropriate loading control for western blot analysis in animal models of myocardial ischemic infarction', *Biochemistry and Biophysics Reports*, 12(August), pp. 108–113. Available at: https://doi.org/10.1016/j.bbrep.2017.09.001.

O'Brien, M.E.R. *et al.* (2004) 'Reduced cardiotoxicity and comparable efficacy in a phase III trial of pegylated liposomal doxorubicin HCl (CAELYX™/Doxil®) versus conventional doxorubicin for first-line treatment of metastatic breast cancer', *Annals of Oncology*, 15(3), pp. 440–449. Available at: https://doi.org/10.1093/annonc/mdh097.

Oliver-Gelabert, A. *et al.* (2020) 'Automatic Quantification of Cardiomyocyte Dimensions and Connexin 43 Lateralization in Fluorescence Images', *Biomolecules*, 10(9), p. 1334. Available at: https://doi.org/10.3390/biom10091334.

Oltolina, F. *et al.* (2015) 'Human Cardiac Progenitor Spheroids Exhibit Enhanced Engraftment Potential', *PLoS ONE*, 10(9). Available at: https://doi.org/10.1371/journal.pone.0137999.

Ongstad, E. and Kohl, P. (2016) 'Fibroblast-myocyte coupling in the heart: Potential relevance for therapeutic interventions', *Journal of Molecular and Cellular Cardiology*, pp. 238–246. Available at: https://doi.org/10.1016/j.yjmcc.2016.01.010.

Pabst, A.M. *et al.* (2016) 'Influence of porcine-derived collagen matrix on endothelial progenitor cells: an in vitro study', *Odontology*, 104(1), pp. 19–26. Available at: https://doi.org/10.1007/s10266-014-0186-x.

Padget, K., Pearson, A. and Austin, C. (2000) 'Quantitation of DNA topoisomerase IIα and β in human leukaemia cells by immunoblotting', *Leukemia*, 14(11), pp. 1997–2005. Available at: https://doi.org/10.1038/sj.leu.2401928.

Paik, D.T., Chandy, M. and Wu, J.C. (2020) 'Patient and disease–specific induced pluripotent stem cells for discovery of personalized cardiovascular drugs and therapeutics', *Pharmacological Reviews*, 72(1), pp. 320–342. Available at: https://doi.org/10.1124/pr.116.013003.

Palatinus, J.A., Rhett, J.M. and Gourdie, R.G. (2011) 'Enhanced PKCε mediated phosphorylation of connexin43 at serine 368 by a carboxyl-terminal mimetic peptide

is dependent on injury', *Channels*, 5(3), pp. 236–240. Available at: https://doi.org/10.4161/chan.5.3.15834.

Paolini, G. V., Lyons, R.A. and Laflin, P. (2010) 'How desirable are your IC50s? A way to enhance screening-based decision making', *Journal of Biomolecular Screening*, 15(10), pp. 1183–1193. Available at: https://doi.org/10.1177/1087057110384402.

Passarelli, M.K. *et al.* (2015) 'Single-Cell Analysis: Visualizing Pharmaceutical and Metabolite Uptake in Cells with Label-Free 3D Mass Spectrometry Imaging', *Analytical Chemistry*, 87(13), pp. 6696–6702. Available at: https://doi.org/10.1021/acs.analchem.5b00842.

Passini, E. *et al.* (2017) 'Human in silico drug trials demonstrate higher accuracy than animal models in predicting clinical pro-arrhythmic cardiotoxicity', *Frontiers in Physiology*, 8(SEP), p. 668. Available at: https://doi.org/10.3389/fphys.2017.00668.

Patra, B. *et al.* (2016) 'Drug testing and flow cytometry analysis on a large number of uniform sized tumor spheroids using a microfluidic device', *Scientific Reports*, 6, pp. 1–12. Available at: https://doi.org/10.1038/srep21061.

Pecoraro, M. *et al.* (2015) 'Doxorubicin-Mediated Cardiotoxicity: Role of Mitochondrial Connexin 43', *Cardiovascular Toxicology*, 15(4), pp. 366–376. Available at: https://doi.org/10.1007/S12012-014-9305-8.

Pecoraro, M. *et al.* (2017) 'Cardiotoxic effects of short-term doxorubicin administration: Involvement of connexin 43 in calcium impairment', *International Journal of Molecular Sciences*, 18(10). Available at: https://doi.org/10.3390/ijms18102121.

Pecoraro, M. *et al.* (2020) 'Doxorubicin-induced oxidative and nitrosative stress: Mitochondrial connexin 43 is at the crossroads', *International Journal of Molecular Medicine*, 46(3), pp. 1197–1209. Available at: https://doi.org/10.3892/ijmm.2020.4669.

Petrov, V. V., Fagard, R.H. and Lijnen, P.J. (2002) 'Stimulation of Collagen Production by Transforming Growth Factor-β1 During Differentiation of Cardiac Fibroblasts to Myofibroblasts', *Hypertension*, 39(2 I), pp. 258–263. Available at: https://doi.org/10.1161/hy0202.103268.

Pleschke, J.M. *et al.* (2000) 'Poly(ADP-ribose) binds to specific domains in DNA damage checkpoint proteins', *Journal of Biological Chemistry*, 275(52), pp. 40974–40980. Available at: https://doi.org/10.1074/jbc.M006520200.

Pokrywczynska, M. *et al.* (2016) 'Isolation, expansion and characterization of porcine urinary bladder smooth muscle cells for tissue engineering', *Biological Procedures Online*, 18(1). Available at: https://doi.org/10.1186/s12575-016-0047-9.

Polonchuk, L. *et al.* (2017) 'Cardiac spheroids as promising in vitro models to study the human heart microenvironment.', *Scientific Reports*, 7(1), p. 7005. Available at: https://doi.org/10.1038/s41598-017-06385-8.

Polontchouk, L. *et al.* (2001) 'Effects of chronic atrial fibrillation on gap junction distribution in human and rat atria', *Journal of the American College of Cardiology*, 38(3), pp. 883–891. Available at: https://doi.org/10.1016/S0735-1097(01)01443-7.

Pondé, N.F., Lambertini, M. and De Azambuja, E. (2016) 'Twenty years of anti-HER2 therapy-associated cardiotoxicity', *ESMO Open*, 1(4), p. e000073. Available at: https://doi.org/10.1136/esmoopen-2016-000073.

Ponikowski, P. *et al.* (2016) '2016 ESC Guidelines for the diagnosis and treatment of acute and chronic heart failureThe Task Force for the diagnosis and treatment of acute and chronic heart failure of the European Society of Cardiology (ESC)', *European Heart Journal*, 37(27), pp. 2129–2200. Available at: https://doi.org/10.1093/eurheartj/ehw128.

Ponsaerts, R. *et al.* (2010) 'Intramolecular loop/tail interactions are essential for connexin 43-hemichannel activity', *FASEB journal: official publication of the Federation of American Societies for Experimental Biology*, 24(11), pp. 4378–4395. Available at: https://doi.org/10.1096/fj.09-153007.

Press, E.R. *et al.* (2017) 'Induction of cell death and gain-of-function properties of connexin26 mutants predict severity of skin disorders and hearing loss', *Journal of Biological Chemistry*, 292(23), pp. 9721–9732. Available at: https://doi.org/10.1074/jbc.m116.770917.

Qian, T. *et al.* (2020) 'Adaptable pulsatile flow generated by quantitative imaging of stem-cell derived cardiomyocytes for disease modeling', *bioRxiv*, 3(20), p. 752. Available at: https://doi.org/10.1101/2020.03.20.000752.

Qiu, S. *et al.* (2021) 'Risk Factors for Anthracycline-Induced Cardiotoxicity', *Frontiers in Cardiovascular Medicine*, 8, p. 736854. Available at: https://doi.org/10.3389/fcvm.2021.736854.

Regenold, M. *et al.* (2022) 'Turning down the heat: The case for mild hyperthermia and thermosensitive liposomes', *Nanomedicine: Nanotechnology, Biology and Medicine*, 40, p. 102484. Available at: https://doi.org/10.1016/j.nano.2021.102484.

Rembiałkowska, N. *et al.* (2020) 'Doxorubicin Assisted by Microsecond Electroporation Promotes Irreparable Morphological Alternations in Sensitive and Resistant Human Breast Adenocarcinoma Cells', *Applied Sciences*, 10(8), p. 2765. Available at: https://doi.org/10.3390/app10082765.

Revel, J.P. and Karnovsky, M.J. (1967) 'Hexagonal array of subunits in intercellular junctions of the mouse heart and liver', *Journal of Cell Biology*, 33(3), pp. C7-12. Available at: https://doi.org/10.1083/jcb.33.3.c7.

Rhett, J.M., Jourdan, J. and Gourdie, R.G. (2011) 'Connexin 43 connexon to gap junction transition is regulated by zonula occludens-1', *Molecular Biology of the Cell*, 22(9), pp. 1516–1528. Available at: https://doi.org/10.1091/mbc.E10-06-0548.

Richards, D.J. *et al.* (2017) 'Inspiration from heart development: Biomimetic development of functional human cardiac organoids', *Biomaterials*, 142, pp. 112–123. Available at: https://doi.org/10.1016/j.biomaterials.2017.07.021.

Roca, J. and Wang, J.C. (1994) 'DNA transport by a type II DNA topoisomerase: Evidence in favor of a two-gate mechanism', *Cell*, 77(4), pp. 609–616. Available at: https://doi.org/10.1016/0092-8674(94)90222-4.

Rodríguez-Sinovas, A. *et al.* (2021) 'Connexins in the Heart: Regulation, Function and Involvement in Cardiac Disease', *International Journal of Molecular Sciences*, 22(9), p. 4413. Available at: https://doi.org/10.3390/ijms22094413.

Rucker-Martin, C. *et al.* (2006) 'Chronic hemodynamic overload of the atria is an important factor for gap junction remodeling in human and rat hearts', *Cardiovascular Research*, 72(1), pp. 69–79. Available at: https://doi.org/10.1016/j.cardiores.2006.06.016.

Ruff, S.E. *et al.* (2020) 'Roles for MDC1 in cancer development and treatment', *DNA*

Repair, 95, pp. 1–23. Available at: https://doi.org/10.1016/j.dnarep.2020.102948.

Rusiecka, O.M. *et al.* (2020) 'Canonical and non-canonical roles of connexin43 in cardioprotection', *Biomolecules*, 10(9), pp. 1–22. Available at: https://doi.org/10.3390/biom10091225.

Del Ry, S. *et al.* (2015) 'Altered expression of connexin 43 and related molecular partners in a pig model of left ventricular dysfunction with and without dipyrydamole therapy', *Pharmacological Research*, 95–96, pp. 92–101. Available at: https://doi.org/10.1016/j.phrs.2015.03.015.

Salat-Canela, C. *et al.* (2014) 'Internal translation of the connexin 43 transcript', *Cell Communication and Signaling: CCS*, 12(1), p. 31. Available at: https://doi.org/10.1186/1478-811x-12-31.

Salat-Canela, C. *et al.* (2015) 'Post-transcriptional regulation of connexins', *Biochemical Society Transactions*, 43, pp. 465–470. Available at: https://doi.org/10.1042/bst20150033.

Sandri, M.I. *et al.* (1996) 'Differential expression of the topoisomerase II alpha and beta genes in human breast cancers.', *British Journal of Cancer*, 73(12), pp. 1518–24. Available at: https://doi.org/10.1038/bjc.1996.286.

Sanguinetti, M.C. *et al.* (1995) 'A mechanistic link between an inherited and an acquird cardiac arrthytmia: HERG encodes the IKr potassium channel', *Cell*, 81(2), pp. 299–307. Available at: https://doi.org/10.1016/0092-8674(95)90340-2.

Schmid, C. *et al.* (2021) 'Ion Channel Expression and Electrophysiology of Singular Human (Primary and Induced Pluripotent Stem Cell-Derived) Cardiomyocytes', *Cells*, 10(12), p. 3370. Available at: https://doi.org/10.3390/cells10123370.

Schmidtmann, M. (1925) 'Über die intracelluläre Wasserstoffionenkonzentration unter physiologischen und einigen pathologischen Bedingungen', *Zeitschrift für die gesamte experimentelle Medizin*, 45(1), pp. 714–742. Available at: https://doi.org/10.1007/bf02626087.

Schultz, F. *et al.* (2019) 'Cardiomyocyte–myofibroblast contact dynamism is modulated by connexin-43', *The FASEB Journal*, 33(9), pp. 10453–10468. Available at: https://doi.org/10.1096/fj.201802740RR.

Schütz, C.A. *et al.* (2013) 'Therapeutic nanoparticles in clinics and under clinical evaluation', *Nanomedicine*, 8(3), pp. 449–467. Available at: https://doi.org/10.2217/nnm.13.8.

Seki, A., Coombs, W., *et al.* (2004) 'Loss of electrical communication, but not plaque formation, after mutations in the cytoplasmic loop of connexin43', *Heart Rhythm*, 1(2), pp. 227–233. Available at: https://doi.org/10.1016/j.hrthm.2004.03.066.

Seki, A., Duffy, H.S., *et al.* (2004) 'Modifications in the biophysical properties of connexin43 channels by a peptide of the cytoplasmic loop region.', *Circulation Research*, 95(4), pp. 22–29. Available at: https://doi.org/10.1161/01.res.0000140737.62245.c5.

Severs, N.J. (1990) 'The cardiac gap junction and intercalated disc', *International Journal of Cardiology*, 26(2), pp. 137–173. Available at: https://doi.org/10.1016/0167-5273(90)90030-9.

Severs, N.J. *et al.* (2004) 'Gap junction alterations in human cardiac disease', *Cardiovascular Research*, pp. 368–377. Available at: https://doi.org/10.1016/j.cardiores.2003.12.007.

Severs, N.J. (2009) 'Connexins in the heart', in *Connexins: A Guide*. Humana Press, pp. 435–456. Available at: https://doi.org/10.1007/978-1-59745-489-6_21.

Seymour, L.W. *et al.* (2002) 'Hepatic drug targeting: phase I evaluation of polymer-bound doxorubicin', *Journal of Clinical Oncology: official journal of the American Society of Clinical Oncology*, 20(6), pp. 1668–1676. Available at: https://doi.org/10.1200/jco.2002.20.6.1668.

Seymour, L.W. *et al.* (2009) 'Phase II studies of polymer-doxorubicin (PK1, FCE28068) in the treatment of breast, lung and colorectal cancer', *International Journal of Oncology*, 34(6), pp. 1629–1636. Available at: https://doi.org/10.3892/ijo_00000293.

Shaikh, F. *et al.* (2016) 'Cardioprotection and Second Malignant Neoplasms Associated With Dexrazoxane in Children Receiving Anthracycline Chemotherapy: A Systematic Review and Meta-Analysis', *JNCI: Journal of the National Cancer Institute*, 108(4). Available at: https://doi.org/10.1093/JNCI/DJV357.

Sharma, P. and Gentile, C. (2021) 'Cardiac Spheroids as in vitro Bioengineered Heart Tissues to Study Human Heart Pathophysiology', *JoVE (Journal of Visualized Experiments)*, 2021(167), p. e61962. Available at: https://doi.org/10.3791/61962.

Shaw, R.M. *et al.* (2007) 'Microtubule plus-end-tracking proteins target gap junctions directly from the cell interior to adherens junctions', *Cell*, 128(3), pp. 547–560. Available at: https://doi.org/10.1016/j.cell.2006.12.037.

Shen, C. *et al.* (2018) 'Doxorubicin and indocyanine green loaded superparamagnetic iron oxide nanoparticles with PEGylated phospholipid coating for magnetic resonance with fluorescence imaging and chemotherapy of glioma', *International Journal of Nanomedicine*, 14, pp. 101–117. Available at: https://doi.org/10.2147/ijn.s173954.

Shi, Y., Li, X. and Yang, J. (2022) 'Cx43 upregulation in HUVECs under stretch via TGF-β1 and cytoskeletal network', *Open Medicine*, 17(1), p. 463. Available at: https://doi.org/10.1515/med-2022-0432.

Silva, E.F. *et al.* (2017) 'DNA-doxorubicin interaction: New insights and peculiarities', *Biopolymers*, 107(3). Available at: https://doi.org/10.1002/bip.22998.

Singh, D. *et al.* (2005) 'Connexin 43 interacts with zona occludens-1 and -2 proteins in a cell cycle stage-specific manner', *Journal of Biological Chemistry*, 280(34), pp. 30416–30421. Available at: https://doi.org/10.1074/jbc.m506799200.

Sjöstrand, F.S., Andersson-Cedergren, E. and Dewey, M.M. (1958) 'The ultrastructure of the intercalated discs of frog, mouse and guinea pig cardiac muscle', *Journal of Ultrastructure Research*, 1(3), pp. 271–287. Available at: https://doi.org/10.1016/s0022-5320(58)80008-8.

de Smet, M.A.J. *et al.* (2021) 'Cx43 hemichannel microdomain signaling at the intercalated disc enhances cardiac excitability', *The Journal of Clinical Investigation*, 131(7), p. e137752. Available at: https://doi.org/10.1172/jci137752.

Smit, K.F. *et al.* (2018) 'Helium alters the cytoskeleton and decreases permeability in endothelial cells cultured in vitro through a pathway involving Caveolin-1', *Scientific Reports*, 8(1), p. 4768. Available at: https://doi.org/10.1038/s41598-018-23030-0.

Smyth, J.W. and Shaw, R.M. (2013) 'Autoregulation of connexin43 gap junction formation by internally translated isoforms', *Cell Reports*, 5(3), pp. 611–618. Available

at: https://doi.org/10.1016/j.celrep.2013.10.009.

Soares, A.R. *et al.* (2015) 'Gap junctional protein Cx43 is involved in the communication between extracellular vesicles and mammalian cells', *Scientific Reports*, 5(1), p. 13243. Available at: https://doi.org/10.1038/srep13243.

Soares, C.P. *et al.* (2012) '2D and 3D-organized cardiac cells shows differences in cellular morphology, adhesion junctions, presence of myofibrils and protein expression', *PLoS ONE*, 7(5). Available at: https://doi.org/10.1371/journal.pone.0038147.

Sodhi, R.N.S. *et al.* (2018) 'ToF-SIMS and other surface spectroscopies applied to the study of ancient artifacts: Preliminary investigation of a tetradrachm of Claudius', *Journal of Vacuum Science & Technology B, Nanotechnology and Microelectronics*, 36(3), p. 03F104. Available at: https://doi.org/10.1116/1.5013613.

Solan, J.L. and Lampe, P.D. (2007) 'Key connexin 43 phosphorylation events regulate the gap junction life cycle', *The Journal of membrane biology*, 217(206), pp. 35–41. Available at: https://doi.org/10.1007/s00232-007-9035-y.Key.

Solan, J.L. and Lampe, P.D. (2020) 'Src Regulation of Cx43 Phosphorylation and Gap Junction Turnover', *Biomolecules*, 10(12), pp. 1–18. Available at: https://doi.org/10.3390/biom10121596.

Sousa, A.M. *et al.* (2007) 'Smooth muscle α-actin expression and myofibroblast differentiation by TGFβ are dependent upon MK2', *Journal of Cellular Biochemistry*, pp. 1581–1592. Available at: https://doi.org/10.1002/jcb.21154.

Srinivas, M., Verselis, V.K. and White, T.W. (2018) 'Human diseases associated with connexin mutations', *Biochimica et Biophysica Acta - Biomembranes*, 1860(1), pp. 192–201. Available at: https://doi.org/10.1016/j.bbamem.2017.04.024.

Steinherz, L.J. *et al.* (1991) 'Cardiac Toxicity 4 to 20 Years After Completing Anthracycline Therapy', *JAMA: The Journal of the American Medical Association*, 266(12), pp. 1672–1677. Available at: https://doi.org/10.1001/jama.1991.03470120074036.

Stoltzfus, K.C. *et al.* (2020) 'Fatal heart disease among cancer patients', *Nature Communications*, 11(1). Available at: https://doi.org/10.1038/s41467-020-15639-5.

Stone, J.R. *et al.* (2021) 'Monitoring for Chemotherapy-Related Cardiotoxicity in the Form of Left Ventricular Systolic Dysfunction: A Review of Current Recommendations', *American Society of Clinical Oncology*, 17(5), pp. 228–236. Available at: https://doi.org/10.1200/op.20.00924.

Stroemlund, L.W. *et al.* (2015) 'Gap junctions - Guards of excitability', *Biochemical Society Transactions*, pp. 508–512. Available at: https://doi.org/10.1042/bst20150059.

Strongman, H. *et al.* (2019) 'Medium and long-term risks of specific cardiovascular diseases in survivors of 20 adult cancers: a population-based cohort study using multiple linked UK electronic health records databases.', *Lancet*, 394(10203), pp. 1041–1054. Available at: https://doi.org/10.1016/s0140-6736(19)31674-5.

Sugita, S. *et al.* (2019) 'Photoelasticity-based evaluation of cellular contractile force for phenotypic discrimination of vascular smooth muscle cells', *Scientific Reports*, 9(1), pp. 1–9. Available at: https://doi.org/10.1038/s41598-019-40578-7.

Suzuki, T. *et al.* (1997) 'DNA staining for fluorescence and laser confocal microscopy', *Journal of Histochemistry and Cytochemistry*, 45(1), pp. 49–53. Available at: https://doi.org/10.1177/002215549704500107.

Swenson, C.E. *et al.* (2001) 'Liposome technology and the development of Myocet™ (liposomal doxorubicin citrate)', *The Breast*, 10(2), pp. 1–7. Available at: https://doi.org/10.1016/s0960-9776(01)80001-1.

Takahashi, N. *et al.* (2012) 'New therapeutic target for the non-electrophysiological signaling in atrial fibrosis and fibrillation such as inflammation', *Journal of Arrhythmia*, 28(3), pp. 145–154. Available at: https://doi.org/10.1016/j.joa.2012.05.001.

Tan, L.L. and Lyon, A.R. (2018) 'Role of Biomarkers in Prediction of Cardiotoxicity During Cancer Treatment', *Current Treatment Options in Cardiovascular Medicine*, p. 55. Available at: https://doi.org/10.1007/s11936-018-0641-z.

Tchoryk, A. *et al.* (2019) 'Penetration and uptake of nanoparticles in 3D tumor spheroids', *Bioconjugate Chemistry*, 30(5), pp. 1371–1384. Available at: https://doi.org/10.1021/acs.bioconjchem.9b00136.

Teleki, I. *et al.* (2014) 'Correlations of differentially expressed gap junction connexins

cx26, cx30, cx32, cx43 and cx46 with breast cancer progression and prognosis', *PLoS ONE*, 9(11). Available at: https://doi.org/10.1371/journal.pone.0112541.

Telli, M.L. *et al.* (2008) 'Cardiotoxicity associated with the cancer therapeutic agent sunitinib malate', *Annals of Oncology*, 19(9), pp. 1613–1618. Available at: https://doi.org/10.1093/annonc/mdn168.

Tewey, K.M. *et al.* (1984) 'Adriamycin-induced DNA damage mediated by mammalian DNA topoisomerase II', *Science*, 226(4673), pp. 466–468. Available at: https://doi.org/10.1126/science.6093249.

Thakur, V. *et al.* (2021) 'Changes in Stress-Mediated Markers in a Human Cardiomyocyte Cell Line under Hyperglycemia', *International journal of molecular sciences*, 22(19), p. 10802. Available at: https://doi.org/10.3390/ijms221910802.

Thévenin, A.F. *et al.* (2013) 'Proteins and mechanisms regulating gap-junction assembly, internalization, and degradation', *Physiology*, 28(2), pp. 93–116. Available at: https://doi.org/10.1152/physiol.00038.2012.

Thorn, C.F. *et al.* (2011) 'Doxorubicin pathways: pharmacodynamics and adverse effects.', *Pharmacogenetics and Genomics*, 21(7), pp. 440–6. Available at: https://doi.org/10.1097/fpc.0b013e32833ffb56.

Tishchenko, A. *et al.* (2020) 'Cx43 and Associated Cell Signaling Pathways Regulate Tunneling Nanotubes in Breast Cancer Cells', *Cancers*, 12(10), pp. 1–25. Available at: https://doi.org/10.3390/cancers12102798.

Torchilin, V.P. (2001) 'Structure and design of polymeric surfactant-based drug delivery systems', *Journal of Controlled Release*, 73(2–3), pp. 137–172. Available at: https://doi.org/10.1016/s0168-3659(01)00299-1.

Torchilin, V.P. (2002) 'PEG-based micelles as carriers of contrast agents for different imaging modalities', *Advanced Drug Delivery Reviews*, 54(2), pp. 235–252. Available at: https://doi.org/10.1016/s0169-409X(02)00019-4.

Touyz, R.M. and Herrmann, J. (2018) 'Cardiotoxicity with vascular endothelial growth factor inhibitor therapy', *NPJ Precision Oncology*, 2(1). Available at: https://doi.org/10.1038/s41698-018-0056-z.

Trexler, E.B. *et al.* (1996) 'Voltage gating and permeation in a gap junction

hemichannel', *Proceedings of the National Academy of Sciences of the United States of America*, 93(12), pp. 5836–5841. Available at: https://doi.org/10.1073/pnas.93.12.5836.

Tscheschner, H. *et al.* (2019) 'CaMKII activation participates in doxorubicin cardiotoxicity and is attenuated by moderate GRP78 overexpression', *PLoS ONE*, 14(4), pp. 1–20. Available at: https://doi.org/10.1371/journal.pone.0215992.

Tsuchiya, H. and Mizogami, M. (2013) 'Interaction of local anesthetics with biomembranes consisting of phospholipids and cholesterol: Mechanistic and clinical implications for anesthetic and cardiotoxic effects', *Anesthesiology Research and Practice*, 2013, p. 297141. Available at: https://doi.org/10.1155/2013/297141.

Turley, H. *et al.* (1997) 'The distribution and expression of the two isoforms of DNA topoisomerase II in normal and neoplastic human tissues.', *British Journal of Cancer*, 75(9), pp. 1340–6. Available at: https://doi.org/10.1038/bjc.1997.227.

Urbini, M. *et al.* (2017) 'ToF-SIMS and principal component analysis of lipids and amino acids from inflamed and dysplastic human colonic mucosa', *Analytical and Bioanalytical Chemistry*, 409(26), pp. 6097–6111. Available at: https://doi.org/10.1007/s00216-017-0546-9.

Valdebenito, S. *et al.* (2018) 'The Novel Roles of Connexin Channels and Tunneling Nanotubes in Cancer Pathogenesis', *International Journal of Molecular Sciences*, 19(5). Available at: https://doi.org/10.3390/ijms19051270.

Valle, J.W. *et al.* (2011) 'A phase 2 study of SP1049C, doxorubicin in P-glycoprotein-targeting pluronics, in patients with advanced adenocarcinoma of the esophagus and gastroesophageal junction', *Investigational New Drugs*, 29(5), pp. 1029–1037. Available at: https://doi.org/10.1007/s10637-010-9399-1.

Varga, Z. V. *et al.* (2015) 'Drug-induced mitochondrial dysfunction and cardiotoxicity', *American Journal of Physiology - Heart and Circulatory Physiology*, 309(9), pp. H1453–H1467. Available at: https://doi.org/10.1152/ajpheart.00554.2015.

Vasey, P.A., Kaye, S.B., Morrison, R., Twelves, C.J., Wilson, P., Duncan, R., Thomson, A.H., Murray, L.S., Hilditch, T.E., Murray, T., Burtles, S.S., Fraier, D., Frigerio, E., & Cassidy, J. (1999) 'Phase I clinical and pharmacokinetic study of PK1 [N-(2-hydroxypropyl)methacrylamide copolymer doxorubicin]: first member of a new

class of chemotherapeutic agents-drug-polymer conjugates. Cancer Research Campaign Phase I/II Committee.', *Clinical Cancer Research*, 5(1), pp. 83–94.

Verselis, V.K. *et al.* (2009) 'Loop gating of connexin hemichannels involves movement of pore-lining residues in the first extracellular loop domain', *Journal of Biological Chemistry*, 284(7), pp. 4484–4493. Available at: https://doi.org/10.1074/jbc.m807430200.

Vigevani, A. and Williamson, M.J. (1981) 'Doxorubicin', *Analytical Profiles of Drug Substances and Excipients*, 9(C), pp. 245–274. Available at: https://doi.org/10.1016/s0099-5428(08)60143-4.

Wang, D.G. *et al.* (2014) 'Cx43 in mesenchymal stem cells promotes angiogenesis of the infarcted heart independent of gap junctions', *Molecular Medicine Reports*, 9(4), pp. 1095–1102. Available at: https://doi.org/10.3892/mmr.2014.1923.

Wang, G. *et al.* (2018) 'Upregulation of connexin43 by glucose deprivation in H9c2 cells via the extracellular signal-regulated kinase/mitogen-activated protein kinase signaling pathway', *Molecular Medicine Reports*, 17(1), pp. 729–734. Available at: https://doi.org/10.3892/mmr.2017.7967.

Wang, H.H. *et al.* (2008) 'Activation of endothelial cells to pathological status by down-regulation of connexin43', *Cardiovascular Research*, 79(3), pp. 509–518. Available at: https://doi.org/10.1093/cvr/cvn112.

Wang, N. *et al.* (2013) 'Selective inhibition of Cx43 hemichannels by Gap19 and its impact on myocardial ischemia/reperfusion injury', *Basic Research in Cardiology*, 108(1), pp. 1–16. Available at: https://doi.org/10.1007/s00395-012-0309-x.

Wang, W.K. *et al.* (2014) 'Connexin 43 suppresses tumor angiogenesis by down-regulation of vascular endothelial growth factor via hypoxic-induced factor-1α', *International Journal of Molecular Sciences*, 16(1), pp. 439–451. Available at: https://doi.org/10.3390/ijms16010439.

Wang, X. *et al.* (2010) 'Animal cells connected by nanotubes can be electrically coupled through interposed gap-junction channels.', *Proceedings of the National Academy of Sciences of the United States of America*, 107(40), pp. 17194–9. Available at: https://doi.org/10.1073/pnas.1006785107.

Wang, Y. and Hummon, A.B. (2021) 'MS imaging of multicellular tumor spheroids and organoids as an emerging tool for personalized medicine and drug discovery', *Journal of Biological Chemistry*, 297(4), p. 101139. Available at: https://doi.org/10.1016/j.jbc.2021.101139.

Watanabe, M. and Okada, T. (2018) 'Langendorff Perfusion Method as an Ex Vivo Model to Evaluate Heart Function in Rats', *Methods in molecular biology (Clifton, N.J.)*, 1816, pp. 107–116. Available at: https://doi.org/https://doi.org/10.1007/978-1-4939-8597-5_8.

Wei, L. *et al.* (2015) 'Dissecting the mechanisms of doxorubicin and oxidative stress-induced cytotoxicity: The involvement of actin cytoskeleton and ROCK1', *PLoS ONE*, 10(7), pp. 1–18. Available at: https://doi.org/10.1371/journal.pone.0131763.

Wen, S. hsuan *et al.* (2018) 'Sulbactam-enhanced cytotoxicity of doxorubicin in breast cancer cells', *Cancer Cell International*, 18(1), pp. 1–18. Available at: https://doi.org/10.1186/s12935-018-0625-9.

Wilkinson, E.L., Sidaway, J.E. and Cross, M.J. (2016) 'Cardiotoxic drugs Herceptin and doxorubicin inhibit cardiac microvascular endothelial cell barrier formation resulting in increased drug permeability.', *Biology Open*, 5(10), pp. 1362–1370. Available at: https://doi.org/10.1242/bio.020362.

Wojcik, T. *et al.* (2015) 'Comparative endothelial profiling of doxorubicin and daunorubicin in cultured endothelial cells', *Toxicology in Vitro*, 29(3), pp. 512–521. Available at: https://doi.org/10.1016/j.tiv.2014.12.009.

Wong, B. (2011) 'Color blindness', *Nature Methods*, 8(6), p. 441. Available at: https://doi.org/10.1038/nmeth.1618.

Wu, B. Bin, Leung, K.T. and Poon, E.N.Y. (2022) 'Mitochondrial-Targeted Therapy for Doxorubicin-Induced Cardiotoxicity', *International Journal of Molecular Sciences*, 23(3), p. 1912. Available at: https://doi.org/10.3390/ijms23031912.

Xu, H.J. *et al.* (2012) 'S262A mutation abolishes protective effects of connexin 43 against hypothermic preservation-induced injury in cardiomyocytes', *Journal of Heart and Lung Transplantation*, 31(6), pp. 663–669. Available at: https://doi.org/10.1016/j.healun.2012.03.004.

Xu, L. *et al.* (2020) 'Cardioprotective Effects and Duration of Beta Blocker Therapy in Anthracycline-Treated Patients: A Systematic Review and Meta-analysis', *Cardiovascular toxicology*, 20(1), pp. 11–19. Available at: https://doi.org/10.1007/s12012-019-09558-1.

Xu, Z. *et al.* (2009) 'Cardiotoxicity of tyrosine kinase inhibitors in chronic myelogenous leukemia therapy', *Hematology Reports*, 1(1), p. e4. Available at: https://doi.org/10.4081/hr.2009.e4.

Yang, F., Kemp, C.J. and Henikoff, S. (2013) 'Doxorubicin enhances nucleosome turnover around promoters', *Current Biology*, 23(9), pp. 782–787. Available at: https://doi.org/10.1016/j.cub.2013.03.043.

Yang, W. *et al.* (2013) 'Genomics of Drug Sensitivity in Cancer (GDSC): a resource for therapeutic biomarker discovery in cancer cells', *Nucleic Acids Research*, 41(D1), pp. D955–D961. Available at: https://doi.org/10.1093/nar/gks1111.

Yao, F. *et al.* (2015) 'Nanopore Single-Molecule Analysis of DNA−Doxorubicin Interactions', *Analylical Chemistry*, 87, p. 33. Available at: https://doi.org/10.1021/ac503926g.

Yarana, C. *et al.* (2018) 'Extracellular vesicles released by cardiomyocytes in a doxorubicin-induced cardiac injury mouse model contain protein biomarkers of early cardiac injury', *Clinical Cancer Research*, 24(7), pp. 1644–1653. Available at: https://doi.org/10.1158/1078-0432.CCR-17-2046/87384/AM/EXTRACELLULAR-VESICLES-RELEASED-BY-CARDIOMYOCYTES.

Yarana, C. *et al.* (2022) 'Extracellular Vesicles Released after Doxorubicin Treatment in Rats Protect Cardiomyocytes from Oxidative Damage and Induce Pro-Inflammatory Gene Expression in Macrophages', *International Journal of Molecular Sciences*, 23(21), pp. 1–17. Available at: https://doi.org/10.3390/ijms232113465.

Yin, Z. *et al.* (2016) 'miR-320a mediates doxorubicin-induced cardiotoxicity by targeting VEGF signal pathway', *Aging*, 8(1), pp. 192–207. Available at: https://doi.org/10.18632/aging.100876.

Yuan, D. *et al.* (2015) 'Connexin 43 expressed in endothelial cells modulates monocyte-endothelial adhesion by regulating cell adhesion proteins', *Molecular Medicine Reports*, 12(5), pp. 7146–7152. Available at:

https://doi.org/10.3892/mmr.2015.4273.

Zamai, L. *et al.* (1996) 'Supravital exposure to propidium iodide identifies apoptotic cells in the absence of nucleosomal DNA fragmentation', *Cytometry*, 23(4), pp. 303–311. Available at: https://doi.org/10.1002/(sici)1097-0320(19960401)23:4<303::aid-cyto6>3.0.co;2-h.

Zamorano, J.L. *et al.* (2016) '2016 ESC Position Paper on cancer treatments and cardiovascular toxicity developed under the auspices of the ESC Committee for Practice Guidelines: The Task Force for cancer treatments and cardiovascular toxicity of the European Society of Cardiology', *European Heart Journal*, 37(36), pp. 2768–2801. Available at: https://doi.org/10.1093/eurheartj/ehw211.

Zeglinski, M. *et al.* (2011) 'Trastuzumab-induced cardiac dysfunction: A "dual-hit"', *Experimental & Clinical Cardiology*, 16(3), p. 70.

Zhang, G. *et al.* (2022) 'Understanding the Protective Role of Exosomes in Doxorubicin-Induced Cardiotoxicity', *Oxidative Medicine and Cellular Longevity*, 2022(2852251). Available at: https://doi.org/10.1155/2022/2852251.

Zhang, L. and Yu, D. (2019) 'Exosomes in cancer development, metastasis, and immunity', *Biochimica et Biophysica Acta Reviews on cancer*, 1871(2), pp. 455–468. Available at: https://doi.org/10.1016/j.bbcan.2019.04.004.

Zhang, Y. *et al.* (2014) 'Doxorubicin Induces Sarcoplasmic Reticulum Calcium Regulation Dysfunction via the Decrease of SERCA2 and Phospholamban Expressions in Rats', *Cell Biochemistry and Biophysics*, 70(3), pp. 1791–1798. Available at: https://doi.org/10.1007/s12013-014-0130-2.

Zhang, Z. *et al.* (2014) 'Magnetic resonance imaging-visible and pH-sensitive polymeric micelles for tumor targeted drug delivery', *Journal of Biomedical Nanotechnology*, 10(2), pp. 216–226. Available at: https://doi.org/10.1166/jbn.2014.1729.

Zhang, Z. *et al.* (2016) 'Role of myoendothelial gap junctions in the regulation of human coronary artery smooth muscle cell differentiation by laminar shear stress', *Cellular Physiology and Biochemistry*, 39(2), pp. 423–437. Available at: https://doi.org/10.1159/000445636.

Zheng, L. *et al.* (2020) 'Inhibition of Pyk2 and Src activity improves Cx43 gap junction intercellular communication', *Journal of Molecular and Cellular Cardiology*, 149(February), pp. 27–40. Available at: https://doi.org/10.1016/j.yjmcc.2020.09.004.

Zhou, S., Heller, L.J. and Wallace, K.B. (2001) 'Interference with calcium-dependent mitochondrial bioenergetics in cardiac myocytes isolated from doxorubicin-treated rats', *Toxicology and Applied Pharmacology*, 175(1), pp. 60–67. Available at: https://doi.org/10.1006/taap.2001.9230.

Zhou, Z. and Li, M. (2022) 'Targeted therapies for cancer', *BMC Medicine*, 20(1), p. 90. Available at: https://doi.org/10.1186/s12916-022-02287-3.

Zibara, K. *et al.* (2015) 'Anti-angiogenesis therapy and gap junction inhibition reduce MDA-MB-231 breast cancer cell invasion and metastasis in vitro and in vivo', *Scientific Reports*, 5, p. 12598. Available at: https://doi.org/10.1038/srep12598.

APPENDICES

I. *Python script: Protein normalisation*

main.py
csv_loc.py
csv_name.py
csv_open.py
csv_output.py
BCA_calculation.py

main.py

```python
1   # The data acquired from the BCA should be saved as a CSV file
2   # The top row of the CSV file has to be the column labels
3   # The file should only contain one set of data (multiple data sets in one? save as
different CSV files)
4
5
6   # importing functions from other files
7   import csv_open as csv_open
8   import csv_name as csv_name
9   import csv_loc as csv_loc
10   import csv_output as csv_output
11   import BCA_calculation as BCA_calculation
12
13
14   # choose min to normalise to lowest concentration (pick an integer or select "min")
15   NORM_FACTOR = "min"
16
17
18   # pick amount of uL as desired final volume
19   TOTAL_VOLUME = 70
20
21
```

```
22   # path to start searching the files
23   PATH = 'F:/2021/BCA_assays'
24
25
26   csv = csv_open.csv_open(PATH)
27   csv_name = csv_name.csv_name(csv)
28   loc = csv_loc.location(csv)
29    data = BCA_calculation.BCA_calc(loc, csv, csv_name, NORM_FACTOR,
TOTAL_VOLUME)
30   csv_output.csv_output(loc, TOTAL_VOLUME, csv_name, data)
```

csv_loc.py
```
1   def location(csv):
2     loc = csv.split('/')
3     loc = '/'.join(loc[0:-1])  # merging all except last one in list
4     loc = loc + "/"
5     return(loc)
```

csv_name.py
```
1   def csv_name(csv):  # Retreive name of csv file
2     csv_name = csv.split(".csv")
3     csv_name = csv_name[0].split("/")
4     csv_name = csv_name[-1]
5     return(csv_name)
```

csv_open.py
```
1   from tkinter import filedialog
2   def csv_open(PATH):
3     csv = filedialog.askopenfile(initialdir=PATH, title='select file',
4                     filetypes=(('csv files', '.csv'), ('all files', '*.*')))
5     csv = csv.name
6     return(csv)
```

csv_output.py
```
1   def csv_output(loc, TOTAL_VOLUME, csv_name, data):
```

```
2
3      # csv filename
4      csv_new = loc + str(TOTAL_VOLUME) + "uL_Normalised_" + csv_name +
".csv"
5
6      # create new csv file in same directory as selected
7      data.to_csv(csv_new)
8      print("generated csv output !")
```

BCA_calculation.py

```
1    import pandas as pd
2    from decimal import *
3
4    def BCA_calc(loc, csv, csv_name, NORM_FACTOR, TOTAL_VOLUME):
5
6        df = pd.read_csv(loc + csv_name + ".csv")
7
8        # How to take data from one column as a LIST
9        mean_conc = df["MeanConc"].dropna().values
10        names = df["Sample"].dropna().values
11
12        if  NORM_FACTOR == "min":
13            normal_factor = min(mean_conc)
14        else:
15            normal_factor = NORM_FACTOR
16
17        SB_factor = 0.75
18        Dilution_Factor = TOTAL_VOLUME * SB_factor
19
20        Sample = df["Sample"]
21        Sample = Sample.dropna()
22        ID = Sample.tolist()
23        Sample = Sample.tolist()
24
25        normalized_concs = []
```

```python
26    for conc in mean_conc:
27        # Creating the result for EACH element
28        normalized_conc = normal_factor / conc * Dilution_Factor
29        # save result into empty list
30        normalized_concs.append(normalized_conc)
31
32    Vol_LB = []
33    for normalized_conc in normalized_concs:
34        Vol_LBuffer = (TOTAL_VOLUME * SB_factor) - normalized_conc
35        Vol_LB.append(Vol_LBuffer)
36
37    Vol_SB = []
38    for normalized_conc in normalized_concs:
39        Vol_SBuffer = TOTAL_VOLUME * (1 - SB_factor)
40        Vol_SB.append(Vol_SBuffer)
41
42    y = 0
43
44    for y in range(len(Sample)):
45        # Decimal numbering
46        Vol_LB[y] = Decimal(Vol_LB[y]).quantize(Decimal('.01'),
rounding=ROUND_DOWN)
47        Vol_SB[y] = Decimal(Vol_SB[y]).quantize(Decimal('.01'),
rounding=ROUND_DOWN)
48        normalized_concs[y] =
Decimal(normalized_concs[y]).quantize(Decimal('.01'), rounding=ROUND_DOWN)
49
50        # Back to float
51        Vol_LB[y] = float(Vol_LB[y])
52        Vol_SB[y] = float(Vol_SB[y])
53        normalized_concs[y] = float(normalized_concs[y])
54
55        y = y + 1
56
57    z = 0
```

```
58    output = []
59
60    for z in range(len(Sample)):
61        output.append(Sample[z])
62        output.append(Vol_SB[z])
63        output.append(Vol_LB[z])
64        output.append(normalized_concs[z])
65        z = z + 1
66
67    data = pd.DataFrame(list(zip(ID, Vol_SB, Vol_LB, normalized_concs)),
68                    columns=['ID', 'Vol_SB', 'Vol_LB', 'Vol_Sample'])
69    data.set_index(['ID'], inplace=True)
70    return(data)
```

II. Python script: Processing LIF files from SP8 confocal

This script will only work when images are acquired in the RGB (red green blue) mode.

1. Pre-processing

1.1 Importing libraries that are used within the script

```python
import pandas as pd
import glob
import os
import fnmatch
```

1.2 Selecting the lif file

```python
lif = [os.path.join(dirpath, f) # used to select a file
    for dirpath, dirnames, files in os.walk('F://2021/Confocal') # Folder to search in
    for f in fnmatch.filter(files, '*.lif')] # type of files to search for
lif = lif[-4] # Select the lif file
lif # Printing the selected lif file
```

1.3 Get location and name of the selected lif file

```python
lif = lif.split('\\')
lif_name = lif[-1]
lif = '/'.join(lif[0:-1])
print("lif = " + lif)
print("lif_name = "+ lif_name)
# lif = location of the lif file
# lif_name = name of the lif file
```

lif = F://2021/Confocal
lif_name = SMC MEG 290521.lif

1.4 Import linked CSV file of the selected lif file

Important to do beforehand:

1. Open lif file in Image J with metadata file

2. Save metadata file as CSV in the same folder as the lif file and does not change the name

```python
filename = lif_name.split('.lif')
filename = filename[0]
csv = lif_name.split('.lif')
csv = csv[0]
csv = lif + '/' + "Original Metadata - " + filename + ".csv"
print("csv file: " + csv)
```

csv file: F://2021/Confocal/Original Metadata - SMC MEG 290521.csv

2. Output preparation

2.1 Creating folder for output

```python
# Get location lif
loc_lif = lif.split('/')
loc_lif = '/'.join(loc_lif[0:-1]) + '/'
loc_lif

# Create new folder with name of lif file
new_folder = lif + "/" + lif_name
new_folder = new_folder.strip("lif")
new_folder = new_folder.strip(".")


def createFolder(loc):
    try:
        if not os.path.exists(loc):
            os.makedirs(loc)

        print("Folder created successfully:  " + new_folder)
    except OSError:
        print ('Error: Creating directory. ' +  new_folder)


createFolder(new_folder) # Creates a folder in the current directory called data
```

2.2 Creating a list image names from csv file

```python
df = pd.read_csv(csv) # creating pandas dataframe
filt = df['Key'].str.contains('Series ')
df['Filter'] = filt
csv_names = df[filt]
csv_list = csv_names['Value'].values.tolist()
```

2.3 Creating a general library

Select here scalebar width, height, font, colour, and the type of output

```python
select = 'selectImage'

save = "saveAs"
close = "close"
split = '"Split Channels"'
merge = '"Merge Channels..."'
run = "run"
scale = '"Scale Bar..."'
Open = "open" + '("'
close_stack = "close" + '("stack")'

C1 = 'C1-'
C2 = 'C2-'
C3 = 'C3-'

C6_mag = "(C6_magenta)"
C3_green = "(C3_green)"
C2_blue = "(C2_blue)"
C1_red = "(C1_red)"

c1 = 'c1=['
c2 = 'c2=['
c3 = 'c3=['
c6 = 'c6=['

cm = ""
cl = ", "
cb = ")"
cf = "("

rgbc = '"RGB Color"'
rgb = '"RGB"'
mag = '"Replace Red with Magenta"'
png = '"PNG"'
```

```
ftype = ".png"

analysis = "MGB" # Type of colour representation (RGB / MGB / GB / RB / MB / RG
B_green / MGB_green / RGB_red)

#scalebar
width = 'width=50 '
height = 'height=12 '
font = 'font=28 '
color = 'color=White background=None location=[Lower Right] bold overlay'
scalebar = width + height + font + color + cm

# For montage
stack = 'run' + "(" + "'Images to Stack'" + ',' + "'method=[Scale (smallest)] name=Stac
k title=[] use'" + ')'
montage_4 = 'run' + "(" + "'Make Montage...'" + ', ' + "'columns=4 rows=1 scale=1.0 fi
rst=1 last=4 increment=1 border=2 font=0 label'"+ ')'
montage_3 = 'run' + "(" + "'Make Montage...'" + ', ' + "'columns=3 rows=1 scale=1.0 fi
rst=1 last=3 increment=1 border=2 font=0 label'"+ ')'
```

3. Define functions for output

3.1 RGB = Red Green Blue

```
def RGB(lif, img, loc, loc2, loc_montage):
    a = select + cf + cm + lif + img + cm + cb
    b = run + cf + split + cb
    c = select + cf + cm + C1 + lif + img + cm + cb
    d = run + cf + rgbc + cb
    f = save + cf + png + cl + cm + loc + lif + img + C1_red + cm + cb
    f1 = select + cf + cm + C2 + lif + img + cm + cb
    g = run + cf + rgbc + cb
    h = save + cf + png + cl + cm + loc + lif + img + C2_blue + cm + cb
    i = run + cf + rgbc + cb
    i1 = select + cf + cm + C3 + lif + img + cm + cb
    j = save + cf + png + cl + cm + loc + lif + img + C3_green + cm + cb
    j1 = run + cf + rgbc + cb
    k = run + cf + merge + cl + cm + c2 + lif + img + C3_green + ftype+ ']' + ' ' + c3 + lif
+ img + C2_blue + ftype + ']' + ' ' + c1 + lif + img + C1_red + ftype + ']' + ' ' + 'keep' +
cm + cb
    l = select + cf + rgb + cb
    m = run + cf + scale + cl + cm + scalebar + cb
    n = save + cf + png + cl + cm + loc + lif + img + '(rgb)' + ftype + cm + cb
```

```
o = select + cf + cm + lif + img + C1_red + ftype + cm + cb
p = close + cf + cm + lif + img + C1_red + ftype + cm + cb
o2 = select + cf + cm + lif + img + C2_blue + ftype + cm + cb
p2 = close + cf + cm+ lif + img + C2_blue + ftype + cm + cb
o3 = select + cf + cm + lif + img + C3_green + ftype + cm + cb
p3 = close + cf + cm +lif + img + C3_green + ftype + cm + cb
o4 = select + cf + cm + lif + img + '(rgb)' + ftype + cm + cb
s = close + cf + cm + lif + img + '(rgb)' + ftype + cm + cb

M = Open + loc2 + lif + img + C1_red + ftype + cm + cb
M1 = Open + loc2 + lif + img + C2_blue + ftype + cm + cb
M2 = Open + loc2 + lif + img + C3_green + ftype + cm + cb
M3 = Open + loc2 + lif + img + '(rgb)' + ftype + cm + cb

O = stack
O1 = montage_4
O2 = 'saveAs' + cf + png + cl + cm + loc_montage + lif + img + '_Montage.png' + c
m + cb
O3 = close + cf + cm + lif + img + '_Montage.png' + cm + cb

N = close + cf + cm + lif + img + C1_red + ftype + cm + cb
N1 = close + cf + cm + lif + img + C2_blue + ftype + cm + cb
N2 = close + cf + cm + lif + img + C3_green + ftype + cm + cb
N3 = close + cf + cm + lif + img + '(rgb)' + ftype + cm + cb
N4 = close_stack


with open(loc + lif_txt + "_RGB.txt","a") as ff:
    ff.write(a + "\n" +
            b + "\n" +
            c + "\n" +
            d + "\n" +
            f + "\n" +
            f1 + "\n" +
            g + "\n" +
            h + "\n" +
            i + "\n" +
            i1 + "\n" +
            j + "\n" +
            j1 + "\n" +
            k + "\n" +
            l + "\n" +
            m + "\n" +
            n + "\n" +
            o + "\n" +
```

```
            p + "\n" +
            o2 + "\n" +
            p2 + "\n" +
            o3 + "\n" +
            p3 + "\n" +
            o4 + "\n" +
            s + "\n" +

            M + "\n" +
            M1 + "\n" +
            M2 + "\n" +
            M3 + "\n" +

            O + "\n" +
            O1 + "\n" +
            O2 + "\n" +
            O3 + "\n" +

            N + "\n" +
            N1 + "\n" +
            N2 + "\n" +
            N3 + "\n" +
            N4 + "\n" + "\n" + "\n")
```

3.2 MGB = Magenta Green Blue

```python
def MGB(lif, img, loc, loc2, loc_montage):
    a = select + cf + cm + lif + img + cm + cb
    b = run + cf + split + cb
    c = select + cf + cm + C1 + lif + img + cm + cb
    d = run + cf + rgbc + cb
    e = run + cf + mag + cb
    f = save + cf + png + cl + cm + loc + lif + img + C6_mag + cm + cb
    f1 = select + cf + cm + C2 + lif + img + cm + cb
    g = run + cf + rgbc + cb
    h = save + cf + png + cl + cm + loc + lif + img + C2_blue + cm + cb
    i = run + cf + rgbc + cb
    i1 = select + cf + cm + C3 + lif + img + cm + cb
    j = save + cf + png + cl + cm + loc + lif + img + C3_green + cm + cb
    j1 = run + cf + rgbc + cb
    k = run + cf + merge + cl + cm + c2 + lif + img + C3_green + ftype+ ']' + ' ' + c3 + lif
 + img + C2_blue + ftype + ']' + ' ' + c6 + lif + img + C6_mag + ftype + ']' + ' ' + 'keep'
+ cm + cb
```

```
l = select + cf + rgb + cb
m = run + cf + scale + cl + cm + scalebar + cb
n = save + cf + png + cl + cm + loc + lif + img + '(mgb)' + ftype + cm + cb
o = select + cf + cm + lif + img + C6_mag + ftype + cm + cb
p = close + cf + cm + lif + img + C6_mag + ftype + cm + cb
o2 = select + cf + cm + lif + img + C2_blue + ftype + cm + cb
p2 = close + cf + cm+ lif + img + C2_blue + ftype + cm + cb
o3 = select + cf + cm + lif + img + C3_green + ftype + cm + cb
p3 = close + cf + cm +lif + img + C3_green + ftype + cm + cb
o4 = select + cf + cm + lif + img + '(mgb)' + ftype + cm + cb
s = close + cf + cm + lif + img + '(mgb)' + ftype + cm + cb

M = Open + loc2 + lif + img + C6_mag + ftype + cm + cb
M1 = Open + loc2 + lif + img + C2_blue + ftype + cm + cb
M2 = Open + loc2 + lif + img + C3_green + ftype + cm + cb
M3 = Open + loc2 + lif + img + '(mgb)' + ftype + cm + cb

O = stack
O1 = montage_4
O2 = 'saveAs' + cf + png + cl + cm + loc_montage + lif + img + '_Montage.png' + c
m + cb
O3 = close + cf + cm + lif + img + '_Montage.png' + cm + cb

N = close + cf + cm + lif + img + C6_mag + ftype + cm + cb
N1 = close + cf + cm + lif + img + C2_blue + ftype + cm + cb
N2 = close + cf + cm + lif + img + C3_green + ftype + cm + cb
N3 = close + cf + cm + lif + img + '(mgb)' + ftype + cm + cb
N4 = close_stack

with open(loc + lif_txt + "_MGB.txt","a") as ff:
    ff.write(a + "\n" +
            b + "\n" +
            c + "\n" +
            d + "\n" +
            e + "\n" +
            f + "\n" +
            f1 + "\n" +
            g + "\n" +
            h + "\n" +
            i + "\n" +
            i1 + "\n" +
            j + "\n" +
            j1 + "\n" +
            k + "\n" +
            l + "\n" +
```

```
        m + "\n" +
        n + "\n" +
        o + "\n" +
        p + "\n" +
        o2 + "\n" +
        p2 + "\n" +
        o3 + "\n" +
        p3 + "\n" +
        o4 + "\n" +
        s + "\n" +

        M + "\n" +
        M1 + "\n" +
        M2 + "\n" +
        M3 + "\n" +

        O + "\n" +
        O1 + "\n" +
        O2 + "\n" +
        O3 + "\n" +

        N + "\n" +
        N1 + "\n" +
        N2 + "\n" +
        N3 + "\n" +
        N4 + "\n" + "\n" + "\n")
```

3.3 GB = Green Blue

```
def GB(lif, img, loc, loc2, loc_montage):

    a = select + cf + cm + lif + img + cm + cb
    b = run + cf + split + cb
    f1 = select + cf + cm + C2 + lif + img + cm + cb
    h = save + cf + png + cl + cm + loc + lif + img + C3_green + cm + cb
    i1 = select + cf + cm + C1 + lif + img + cm + cb
    j = save + cf + png + cl + cm + loc + lif + img + C2_blue + cm + cb
    k = run + cf + merge + cl + cm + c3 + lif + img + C2_blue + ftype+ ']' + ' ' + c2 + lif
+ img + C3_green + ftype + ']' + ' ' + 'create' + cm + cb
    m = run + cf + scale + cl + cm + scalebar + cb
    n = save + cf + png + cl + cm + loc + lif + img + '(gb)' + ftype + cm + cb
    s = close + cf + cm + lif + img + '(gb)' + ftype + cm + cb
```

```python
    M = Open + loc2 + lif + img + C3_green + ftype + cm + cb
    M1 = Open + loc2 + lif + img + C2_blue + ftype + cm + cb
    M3 = Open + loc2 + lif + img + '(gb)' + ftype + cm + cb

    O = stack
    O1 = montage_3
    O2 = 'saveAs' + cf + png + cl + cm + loc_montage + lif + img + '_Montage.png' + c
m + cb
    O3 = close + cf + cm + lif + img + '_Montage.png' + cm + cb

    N = close + cf + cm + lif + img + C3_green + ftype + cm + cb
    N1 = close + cf + cm + lif + img + C2_blue + ftype + cm + cb
    N3 = close + cf + cm + lif + img + '(gb)' + ftype + cm + cb
    N4 = close_stack

    with open(loc + lif_txt + "_GB.txt","a") as ff:
        ff.write(a + "\n" +
              b + "\n" +
              f1 + "\n" +
              h + "\n" +
              i1 + "\n" +
              j + "\n" +
              k + "\n" +
              m + "\n" +
              n + "\n" +
              s + "\n" +

              M + "\n" +
              M1 + "\n" +
              M3 + "\n" +

              O + "\n" +
              O1 + "\n" +
              O2 + "\n" +
              O3 + "\n" +

              N + "\n" +
              N1 + "\n" +
              N3 + "\n" +
              N4 + "\n" + "\n" + "\n")
```

3.4 RB = Red Blue

```python
def RB(lif, img, loc, loc2, loc_montage):
```

```
a = select + cf + cm + lif + img + cm + cb
b = run + cf + split + cb
f3 = select + cf + cm + C1 + lif + img + cm + cb
h = save + cf + png + cl + cm + loc + lif + img + C1_red + cm + cb
i1 = select + cf + cm + C2 + lif + img + cm + cb
j = save + cf + png + cl + cm + loc + lif + img + C2_blue + cm + cb
k = run + cf + merge + cl + cm + c1 + lif + img + C1_red + ftype+ ']' + ' ' + c3 + lif +
img + C2_blue + ftype + ']' + ' ' + 'create' + cm + cb
m = run + cf + scale + cl + cm + scalebar + cb
o2 = select + cf + cm + lif + img + C2_blue + ftype + cm + cb
p2 = close + cf + cm+ lif + img + C2_blue + ftype + cm + cb
o3 = select + cf + cm + lif + img + C1_red + ftype + cm + cb
p3 = close + cf + cm+ lif + img + C1_red + ftype + cm + cb
n = save + cf + png + cl + cm + loc + lif + img + '(rb)' + ftype + cm + cb
s = close + cf + cm + lif + img + '(rb)' + ftype + cm + cb

M = Open + loc2 + lif + img + C1_red + ftype + cm + cb
M1 = Open + loc2 + lif + img + C2_blue + ftype + cm + cb
M3 = Open + loc2 + lif + img + '(rb)' + ftype + cm + cb

O = stack
O1 = montage_3
O2 = 'saveAs' + cf + png + cl + cm + loc_montage + lif + img + '_Montage.png' + c
m + cb
O3 = close + cf + cm + lif + img + '_Montage.png' + cm + cb

N = close + cf + cm + lif + img + C1_red + ftype + cm + cb
N1 = close + cf + cm + lif + img + C2_blue + ftype + cm + cb
N3 = close + cf + cm + lif + img + '(rb)' + ftype + cm + cb
N4 = close_stack

with open(loc + lif_txt + "_RB.txt","a") as ff:
    ff.write(a + "\n" +
            b + "\n" +
            f3 + "\n" +
            h + "\n" +
            i1 + "\n" +
            j + "\n" +
            k + "\n" +
            m + "\n" +
            n + "\n" +
            s + "\n" +

            M + "\n" +
```

```
            M1 + "\n" +
            M3 + "\n" +

            O + "\n" +
            O1 + "\n" +
            O2 + "\n" +
            O3 + "\n" +

            N + "\n" +
            N1 + "\n" +
            N3 + "\n" +
            N4 + "\n" + "\n" + "\n")
```

3.5 MB = Magenta Blue

```
def MB(lif, img, loc, loc2, loc_montage):

    a = select + cf + cm + lif + img + cm + cb
    b = run + cf + split + cb
    f3 = select + cf + cm + C1 + lif + img + cm + cb
    f4 = run + cf + mag + cb
    h = save + cf + png + cl + cm + loc + lif + img + C6_mag + cm + cb
    i1 = select + cf + cm + C2 + lif + img + cm + cb
    j = save + cf + png + cl + cm + loc + lif + img + C2_blue + cm + cb
    k = run + cf + merge + cl + cm + c6 + lif + img + C6_mag + ftype+ ']' + ' ' + c3 + lif
+ img + C2_blue + ftype + ']' + ' ' + 'create' + cm + cb
    m = run + cf + scale + cl + cm + scalebar + cb
    o2 = select + cf + cm + lif + img + C2_blue + ftype + cm + cb
    p2 = close + cf + cm+ lif + img + C2_blue + ftype + cm + cb
    o3 = select + cf + cm + lif + img + C6_mag + ftype + cm + cb
    p3 = close + cf + cm+ lif + img + C6_mag + ftype + cm + cb
    n = save + cf + png + cl + cm + loc + lif + img + '(mb)' + ftype + cm + cb
    s = close + cf + cm + lif + img + '(mb)' + ftype + cm + cb

    M = Open + loc2 + lif + img + C6_mag + ftype + cm + cb
    M1 = Open + loc2 + lif + img + C2_blue + ftype + cm + cb
    M3 = Open + loc2 + lif + img + '(mb)' + ftype + cm + cb

    O = stack
    O1 = montage_3
    O2 = 'saveAs' + cf + png + cl + cm + loc_montage + lif + img + '_Montage.png' + c
m + cb
    O3 = close + cf + cm + lif + img + '_Montage.png' + cm + cb
```

```python
    N = close + cf + cm + lif + img + C6_mag + ftype + cm + cb
    N1 = close + cf + cm + lif + img + C2_blue + ftype + cm + cb
    N3 = close + cf + cm + lif + img + '(mb)' + ftype + cm + cb
    N4 = close_stack

    with open(loc + lif_txt + "_MB.txt","a") as ff:
        ff.write(a + "\n" +
              b + "\n" +
              f3 + "\n" +
              f4 + "\n" +
              h + "\n" +
              i1 + "\n" +
              j + "\n" +
              k + "\n" +
              m + "\n" +
              n + "\n" +
              s + "\n" +

              M + "\n" +
              M1 + "\n" +
              M3 + "\n" +

              O + "\n" +
              O1 + "\n" +
              O2 + "\n" +
              O3 + "\n" +

              N + "\n" +
              N1 + "\n" +
              N3 + "\n" +
              N4 + "\n" + "\n" + "\n")
```

3.6 RGB_green = Red Green Blue minus green

```python
def RGB_green(lif, img, loc, loc2, loc_montage):

    a = select + cf + cm + lif + img + cm + cb
    b = run + cf + split + cb
    f1 = select + cf + cm + C3 + lif + img + cm + cb
    f2 = close + cf + cb
    f3 = select + cf + cm + C1 + lif + img + cm + cb
    h = save + cf + png + cl + cm + loc + lif + img + C1_red + cm + cb
```

```python
    i1 = select + cf + cm + C2 + lif + img + cm + cb
    j = save + cf + png + cl + cm + loc + lif + img + C2_blue + cm + cb
    k = run + cf + merge + cl + cm + c1 + lif + img + C1_red + ftype+ ']' + ' ' + c3 + lif +
img + C2_blue + ftype + ']' + ' ' + 'create' + cm + cb
    m = run + cf + scale + cl + cm + scalebar + cb
    o2 = select + cf + cm + lif + img + C2_blue + ftype + cm + cb
    p2 = close + cf + cm+ lif + img + C2_blue + ftype + cm + cb
    o3 = select + cf + cm + lif + img + C1_red + ftype + cm + cb
    p3 = close + cf + cm+ lif + img + C1_red + ftype + cm + cb
    n = save + cf + png + cl + cm + loc + lif + img + '(rb)' + ftype + cm + cb
    s = close + cf + cm + lif + img + '(rb)' + ftype + cm + cb

    M = Open + loc2 + lif + img + C1_red + ftype + cm + cb
    M1 = Open + loc2 + lif + img + C2_blue + ftype + cm + cb
    M3 = Open + loc2 + lif + img + '(rb)' + ftype + cm + cb

    O = stack
    O1 = montage_3
    O2 = 'saveAs' + cf + png + cl + cm + loc_montage + lif + img + '_Montage.png' + c
m + cb
    O3 = close + cf + cm + lif + img + '_Montage.png' + cm + cb

    N = close + cf + cm + lif + img + C1_red + ftype + cm + cb
    N1 = close + cf + cm + lif + img + C2_blue + ftype + cm + cb
    N3 = close + cf + cm + lif + img + '(rb)' + ftype + cm + cb
    N4 = close_stack

    with open(loc + lif_txt + "_RGB_green.txt","a") as ff:
        ff.write(a + "\n" +
                b + "\n" +
                f1 + "\n" +
                f2 + "\n" +
                f3 + "\n" +
                h + "\n" +
                i1 + "\n" +
                j + "\n" +
                k + "\n" +
                m + "\n" +
                n + "\n" +
                s + "\n" +

                M + "\n" +
                M1 + "\n" +
                M3 + "\n" +
```

```
            O + "\n" +
            O1 + "\n" +
            O2 + "\n" +
            O3 + "\n" +

            N + "\n" +
            N1 + "\n" +
            N3 + "\n" +
            N4 + "\n" + "\n" + "\n")
```

3.7 MGB_green = Magenta Green Blue minus green

```
def MGB_green(lif, img, loc, loc2, loc_montage):

    a = select + cf + cm + lif + img + cm + cb
    b = run + cf + split + cb
    c = select + cf + cm + C1 + lif + img + cm + cb
    d = run + cf + rgbc + cb
    e = run + cf + mag + cb
    f = save + cf + png + cl + cm + loc + lif + img + C6_mag + cm + cb
    f1 = select + cf + cm + C3 + lif + img + cm + cb
    f2 = close + cf + cb
    f3 = select + cf + cm + C2 + lif + img + cm + cb
    f4 = run + cf + rgbc + cb
    h = save + cf + png + cl + cm + loc + lif + img + C2_blue + cm + cb
    k = run + cf + merge + cl + cm + c6 + lif + img + C6_mag + ftype+ ']' + ' ' + c3 + lif
+ img + C2_blue + ftype + ']' + ' ' + 'create' + cm + cb
    m = run + cf + scale + cl + cm + scalebar + cb
    n = save + cf + png + cl + cm + loc + lif + img + '(mb)' + ftype + cm + cb
    s = close + cf + cm + lif + img + '(mb)' + ftype + cm + cb

    M = Open + loc2 + lif + img + C6_mag + ftype + cm + cb
    M1 = Open + loc2 + lif + img + C2_blue + ftype + cm + cb
    M3 = Open + loc2 + lif + img + '(mb)' + ftype + cm + cb

    O = stack
    O1 = montage_3
    O2 = 'saveAs' + cf + png + cl + cm + loc_montage + lif + img + '_Montage.png' + c
m + cb
    O3 = close + cf + cm + lif + img + '_Montage.png' + cm + cb

    N = close + cf + cm + lif + img + C6_mag + ftype + cm + cb
    N1 = close + cf + cm + lif + img + C2_blue + ftype + cm + cb
```

```python
N3 = close + cf + cm + lif + img + '(mb)' + ftype + cm + cb
N4 = close_stack

with open(loc + lif_txt + "_MGB_green.txt","a") as ff:
    ff.write(a + "\n" +
            b + "\n" +
            c + "\n" +
            d + "\n" +
            e + "\n" +
            f + "\n" +
            f1 + "\n" +
            f2 + "\n" +
            f3 + "\n" +
            f4 + "\n" +
            h + "\n" +
            k + "\n" +
            m + "\n" +
            n + "\n" +
            s + "\n" +

            M + "\n" +
            M1 + "\n" +
            M3 + "\n" +

            O + "\n" +
            O1 + "\n" +
            O2 + "\n" +
            O3 + "\n" +

            N + "\n" +
            N1 + "\n" +
            N3 + "\n" +
            N4 + "\n" + "\n" + "\n")
```

3.8 RGB_red = Red Green Blue minus red

```python
def RGB_red(lif, img, loc, loc2, loc_montage):

    a = select + cf + cm + lif + img + cm + cb
    b = run + cf + split + cb
    f1 = select + cf + cm + C1 + lif + img + cm + cb
    f2 = close + cf + cb
    f3 = select + cf + cm + C3 + lif + img + cm + cb
```

```python
    h = save + cf + png + cl + cm + loc + lif + img + C3_green + cm + cb
    i1 = select + cf + cm + C2 + lif + img + cm + cb
    j = save + cf + png + cl + cm + loc + lif + img + C2_blue + cm + cb
    k = run + cf + merge + cl + cm + c2 + lif + img + C3_green + ftype+ ']' + ' ' + c3 + lif
 + img + C2_blue + ftype + ']' + ' ' + 'create' + cm + cb
    m = run + cf + scale + cl + cm + scalebar + cb
    o2 = select + cf + cm + lif + img + C3_green + ftype + cm + cb
    p2 = close + cf + cm+ lif + img + C3_green + ftype + cm + cb
    o3 = select + cf + cm + lif + img + C2_blue + ftype + cm + cb
    p3 = close + cf + cm+ lif + img + C2_blue + ftype + cm + cb
    n = save + cf + png + cl + cm + loc + lif + img + '(gb)' + ftype + cm + cb
    s = close + cf + cm + lif + img + '(gb)' + ftype + cm + cb

    M = Open + loc2 + lif + img + C3_green + ftype + cm + cb
    M1 = Open + loc2 + lif + img + C2_blue + ftype + cm + cb
    M2 = Open + loc2 + lif + img + '(gb)' + ftype + cm + cb

    O = stack
    O1 = montage_3
    O2 = 'saveAs' + cf + png + cl + cm + loc_montage + lif + img + '_Montage.png' + c
m + cb
    O3 = close + cf + cm + lif + img + '_Montage.png' + cm + cb

    N = close + cf + cm + lif + img + C3_green + ftype + cm + cb
    N1 = close + cf + cm + lif + img + C2_blue + ftype + cm + cb
    N3 = close + cf + cm + lif + img + '(gb)' + ftype + cm + cb
    N4 = close_stack

    with open(loc + lif_txt + "_RGB_red.txt","a") as ff:
        ff.write(a + "\n" +
                b + "\n" +
                f1 + "\n" +
                f2 + "\n" +
                f3 + "\n" +
                h + "\n" +
                i1 + "\n" +
                j + "\n" +
                k + "\n" +
                m + "\n" +
                n + "\n" +
                s + "\n" +
                m + "\n" +

                M + "\n" +
                M1 + "\n" +
```

```
        M2 + "\n" +

        O + "\n" +
        O1 + "\n" +
        O2 + "\n" +
        O3 + "\n" +

        N + "\n" +
        N1 + "\n" +
        N3 + "\n" +
        N4 + "\n" + "\n" + "\n")
```

4. Creating a text file with the script to run

The script in the text file can be copied into Image J

1. Select Plugins
2. Select New
3. Select Macro

Run the script with all the images opened in colourized hyperstack mode. Make sure all images are opened.

In [69]:

```
lif = lif_name + " - "
loc = new_folder + "/"
lif_txt = lif.split(".lif - ")
lif_txt = lif_txt[0]

loc2 = new_folder + "/"
loc2 = loc2.split('//')
loc2 = ("/").join(loc2)
loc2

x=0

if analysis == "MGB":
    createFolder(new_folder + "/MGB/")
    createFolder(new_folder + "/MGB/Montage/")

    loc = new_folder + "/MGB/"
    loc2 = loc2 + "MGB/"
    loc_montage = loc2 + "Montage/"
```

```python
elif analysis == "RGB":
    createFolder(new_folder + "/RGB/")
    createFolder(new_folder + "/RGB/Montage/")

    loc = new_folder + "/RGB/"
    loc2 = loc2 + "RGB/"
    loc_montage = loc2 + "Montage/"



elif analysis == "GB":
    createFolder(new_folder + "/GB/")
    createFolder(new_folder + "/GB/Montage/")

    loc = new_folder + "/GB/"
    loc2 = loc2 + "GB/"
    loc_montage = loc2 + "Montage/"



elif analysis == "RB":
    createFolder(new_folder + "/RB/")
    createFolder(new_folder + "/RB/Montage/")

    loc = new_folder + "/RB/"
    loc2 = loc2 + "RB/"
    loc_montage = loc2 + "Montage/"



elif analysis == "RG":
    createFolder(new_folder + "/RG/")
    createFolder(new_folder + "/RG/Montage/")

    loc = new_folder + "/RG/"
    loc2 = loc2 + "RG/"
    loc_montage = loc2 + "Montage/"



elif analysis == "MG":
    createFolder(new_folder + "/MG/")
    createFolder(new_folder + "/MG/Montage/")

    loc = new_folder + "/MG/"
```

```python
        loc2 = loc2 + "MG/"
        loc_montage = loc2 + "Montage/"



    elif analysis == "MB":
        createFolder(new_folder + "/MB/")
        createFolder(new_folder + "/MB/Montage/")

        loc = new_folder + "/MB/"
        loc2 = loc2 + "MB/"
        loc_montage = loc2 + "Montage/"



    elif analysis == "RGB_green":
        createFolder(new_folder + "/RGB_green/")
        createFolder(new_folder + "/RGB_green/Montage/")

        loc = new_folder + "/RGB_green/"
        loc2 = loc2 + "RGB_green/"
        loc_montage = loc2 + "Montage/"



    elif analysis == "MGB_green":
        createFolder(new_folder + "/MGB_green/")
        createFolder(new_folder + "/MGB_green/Montage/")

        loc = new_folder + "/MGB_green/"
        loc2 = loc2 + "MGB_green/"
        loc_montage = loc2 + "Montage/"



    elif analysis == "RGB_red":
        createFolder(new_folder + "/RGB_red/")
        createFolder(new_folder + "/RGB_red/Montage/")

        loc = new_folder + "/RGB_red/"
        loc2 = loc2 + "RGB_red/"
        loc_montage = loc2 + "Montage/"
```

```python
    else:
        print("no folder created")
        pass


#### for each image create script for software
for x in range(len(csv_list)):
    img = csv_list[x]

    if analysis == "MGB":
        print("magenta green blue")
        MGB(lif, img, loc, loc2, loc_montage)
        x = x + 1

    elif analysis == "RGB":
        print("red green blue")
        RGB(lif, img, loc, loc2, loc_montage)
        x = x + 1

    elif analysis == "GB":
        print("green blue")
        GB(lif, img, loc, loc2, loc_montage)
        x = x + 1

    elif analysis == "RB":
        print("red blue")
        RB(lif, img, loc, loc2, loc_montage)
        x = x + 1

    elif analysis == "RG":
        print("red green")
        RG(lif, img, loc, loc2, loc_montage)
        x = x + 1

    elif analysis == "MG":
        print("magenta green")
        MG(lif, img, loc, loc2, loc_montage)
        x = x + 1

    elif analysis == "MB":
        print("magenta blue")
        MB(lif, img, loc, loc2, loc_montage)
        x = x + 1

    elif analysis == "RGB_green":
```

```python
        print("RGB_green")
        RGB_green(lif, img, loc, loc2, loc_montage)
        x = x + 1

    elif analysis == "MGB_green":
        print("MGB_green")
        MGB_green(lif, img, loc, loc2, loc_montage)
        x = x + 1

    elif analysis == "RGB_red":
        print("RGB_red")
        RGB_red(lif, img, loc, loc2, loc_montage)
        x = x + 1

    else:
        print("No correct input?")
        pass
```